

# **AN INTEGRATED MODEL FOR FORCE PREDICTION IN PERIPHERAL MILLING OPERATIONS**

by

**Guiping Zou**

B.A.Sc Dalian University of Technology, 1985  
M.A.Sc Dalian University of Technology, 1988  
Ph.D Dalian University of Technology, 1995

A THESIS SUBMITTED IN PARTIAL FULLFILLMENT OF THE  
REQUIREMENTS FOR THE DEGREE OF

DOCTOR OF PHILOSOPHY

in

The Faculty of Graduate Studies

(Mechanical Engineering)

THE UNIVERSITY OF BRITISH COLUMBIA  
(VANCOUVER)

January 2011

© Guiping Zou, 2011

## **Abstract**

This thesis is primarily concerned with the modeling of peripheral milling operations and, in particular, with cutting force prediction. The models developed incorporate novel approaches to deal with the difficulties described regarding edge geometry and chip thickness. The major contributions are outlined below.

The first step in the analysis has been the development of models for small chip thickness. The model for cutting with a large cutting edge radius or chamfer (compared to chip thickness) is formulated as an Upper Bound where the primary and secondary zones are defined from a previous slip-line field model. This has the advantage of providing both force and moment equilibrium together with a realistic rake face stress situation. The second major contribution of the thesis lies in the formulation of a new model of oblique cutting and the direct application of this to the milling process. The new upper bound model that incorporates force equilibrium parallel to the cutting edge is proposed for oblique cutting operations. The energy approach is framed in terms of the normal shear angle and two fundamental variables that characterize the energy requirements of the oblique cutting process.

Since the process of surface generation requires the analysis of entry and exit phenomenon, the attention has been directed towards simple slip-line field models of ploughing with single and double cutting edges. The analysis includes the influence of ploughing length on the ploughing/cutting transition. Finally the thesis presents the modeling of milling forces using the oblique cutting method as outlined and adding to the ploughing forces calculated from the new model. In addition, the model incorporates

suitable material constitutive equations so that the influence of strain, strain rate, and temperature effects can be accounted for as chip thickness varies. The Upper Bound model at this stage is also able to incorporate the influence of surface slope and the kinematics of the process.

The models developed have been tested with a variety of end mills on several work materials. These tests clearly demonstrate the need to account for the secondary factors not normally included in the modeling process.

## **Preface**

A version of chapter 3 has been published. Zou, G. P., Yellowley, I., and Seethaler, R. J., 2009. A new approach to the modeling of oblique cutting processes, *Int. J. of Machine Tools and Manufacture*, 49, 701-707. I am responsible for the formulations and algorithms, the development of software, the numerical computations, the draft of the paper and further modifications. Prof. Yellowley is responsible for proposing the methodology, checking formulations, writing paper, replying to the reviewers and finalizing the paper. Prof. Seethaler is responsible for deriving the formulations related to the parameter identifications, and modifying the paper, also.

A version of chapter 4 has been published. Zou, G. P., Yellowley, I., and Seethaler, R. J., 2010. The extension of a simple predictive model for orthogonal cutting to include flow below the cutting edge, *Proceedings of the Institution of Mechanical Engineers, Part B: Journal of Engineering Manufacture*, special issue for 36 MATADOR, submitted. Zou, G. P., Yellowley, I., and Seethaler, R. J., 2010. Extension of a simple predictive model for orthogonal cutting to include below the cutting edge, 36 MATADOR Conf., Manchester, UK. I conducted research on deriving the formulations, compiling Maple optimization program, numerical computations, and writing the draft. Prof. Yellowley proposed the methodology, modified paper and replied to the reviewer. Prof. Seethaler checked formulations, modified the paper and presented to 36 MATADOR.

# Table of Contents

<b>Abstract.....</b>	<b>ii</b>
<b>Preface.....</b>	<b>iv</b>
<b>Table of Contents .....</b>	<b>v</b>
<b>List of Tables .....</b>	<b>ix</b>
<b>List of Figures.....</b>	<b>x</b>
<b>Nomenclature .....</b>	<b>xviii</b>
<b>Acknowledgements .....</b>	<b>xxv</b>
<b>1 Introduction.....</b>	<b>1</b>
<b>1.1 Overview .....</b>	<b>1</b>
<b>1.2 Objective and Scope of Thesis .....</b>	<b>6</b>
<b>1.3 Outline.....</b>	<b>8</b>
<b>2 Literature Survey.....</b>	<b>10</b>
<b>2.1 Introduction.....</b>	<b>10</b>
<b>2.2 Basic Mechanics of Metal Cutting.....</b>	<b>10</b>
2.2.1 Shear Plane Models .....	11
2.2.2 Slip Line Field .....	13
2.2.3 Upper Bound Method .....	21
2.2.4 Material Separation.....	23
2.2.5 Finite Element Modeling of Machining .....	24
<b>2.3 Oblique Cutting Models .....</b>	<b>26</b>
<b>2.4 Analysis of Practical Milling Tools.....</b>	<b>30</b>
2.4.1 Modeling of Milling Forces.....	33
2.4.2 Modeling of Ploughing Forces .....	37
<b>2.5 Conclusions.....</b>	<b>44</b>
<b>3 A New Approach to the Modeling of Oblique Cutting Processes.....</b>	<b>46</b>
<b>3.1 Introduction.....</b>	<b>46</b>

<b>3.2</b>	<b>Analysis</b> .....	<b>46</b>
<b>3.3</b>	<b>Special Cases</b> .....	<b>53</b>
3.3.1	Zero SLIP .....	53
3.3.2	SLIP Approaching Unity .....	54
<b>3.4</b>	<b>Relationship between the Major Parameters</b> .....	<b>55</b>
3.4.1	SLIP and RATIO .....	55
3.4.2	SLIP and Angle of Chip Flow on the Rake Face.....	56
<b>3.5</b>	<b>Model Calibration from Measurement of Cutting Forces</b> .....	<b>58</b>
<b>3.6</b>	<b>Comparison with Existing Experimental Tests</b> .....	<b>60</b>
<b>3.7</b>	<b>Conclusions</b> .....	<b>64</b>
<b>4</b>	<b>The Modeling of Tool Edge Ploughing Forces in Milling Operations</b> .....	<b>66</b>
<b>4.1</b>	<b>Introduction</b> .....	<b>66</b>
<b>4.2</b>	<b>Predictive Model for Orthogonal Cutting to Include Flow below the Cutting Edge</b> .....	<b>67</b>
4.2.1	Upper-Bound Formulation.....	67
4.2.2	Optimization Procedure .....	71
4.2.3	Force Prediction.....	72
4.2.4	Adapting the Predictive Model for Radiused Edge Tools .....	75
4.2.5	Case Studies of Predictive Cutting Model.....	76
4.2.5.1	Optimized Upper Bound Geometries .....	76
4.2.5.2	Validating the Proposed Model with Experimental Data .....	78
4.2.6	Parameter Studies of Predictive Cutting Model .....	81
4.2.6.1	Influence of Chamfer Angle on Cutting Forces.....	81
4.2.6.2	Influence of Chamfered Land Length on Cutting Forces .....	82
<b>4.3</b>	<b>Ploughing Models</b> .....	<b>83</b>
4.3.1	Single Edge Ploughing Model .....	83
4.3.2	Double Edge Ploughing Model .....	85
4.3.3	Ploughing Model with Rounded Edge Tool .....	88
4.3.4	Ploughing Model Applications .....	89
4.3.4.1	Effect of Attack Angle.....	89
4.3.4.2	Edge Radius Effects.....	90
<b>4.4</b>	<b>Transition of Ploughing to Cutting Processes</b> .....	<b>90</b>

4.4.1	Effect of Sliding Distance on the Single Edge Ploughing Model.....	91
4.4.2	Effect of Sliding Distance on Double Edge Ploughing Model.....	93
4.4.3	Discussion on the Entry and Exit Milling Processes .....	94
4.4.4	Validating Entry and Exit with Worn Tool Milling Operations.....	95
<b>4.5</b>	<b>Conclusions.....</b>	<b>97</b>
<b>5</b>	<b>A New Predictive Model for Peripheral Milling Operations.....</b>	<b>99</b>
<b>5.1</b>	<b>Introduction.....</b>	<b>99</b>
<b>5.2</b>	<b>The Development of a Methodology to Estimate Milling Forces.....</b>	<b>100</b>
<b>5.3</b>	<b>The Estimation of Oblique Cutting Forces.....</b>	<b>102</b>
5.3.1	Deformation Energy Dissipation on the Shear Plane .....	102
5.3.2	Friction Energy Dissipation at the Tool-chip Interface .....	104
<b>5.4</b>	<b>The Influence of Work Hardening on the Average Normal Stress in the Shear Plane.....</b>	<b>106</b>
<b>5.5</b>	<b>The Estimation of Edge Force Components.....</b>	<b>109</b>
<b>5.6</b>	<b>The Effect of Work Surface Slope.....</b>	<b>110</b>
5.6.1	Surface Slope Formations.....	110
5.6.2	Frictionless Orthogonal Cutting .....	112
5.6.3	Oblique Cutting Model.....	113
<b>5.7</b>	<b>Force Prediction Based on the Shear Plane Forces .....</b>	<b>114</b>
<b>5.8</b>	<b>Kinematics of Helical End Milling Tools.....</b>	<b>116</b>
5.8.1	Coordinate System and Velocity Relationship.....	117
5.8.2	Helical Tool Velocity Profile.....	119
5.8.3	Continuous Shear.....	123
5.8.4	Special Case: Frictionless.....	124
<b>5.9</b>	<b>Cutting Force Prediction for a General Helical Tooth Milling Cutter .....</b>	<b>127</b>
<b>5.10</b>	<b>Conclusions.....</b>	<b>131</b>
<b>6</b>	<b>Experimental Validation of the Predictive Model .....</b>	<b>133</b>
<b>6.1</b>	<b>Introduction.....</b>	<b>133</b>
<b>6.2</b>	<b>Experimental Setup .....</b>	<b>133</b>
<b>6.3</b>	<b>Edge Radius Measurement .....</b>	<b>135</b>
<b>6.4</b>	<b>Identification of the Constitutive Parameters .....</b>	<b>139</b>

<b>6.5</b>	<b>Detailed Validation of the Proposed Model.....</b>	<b>148</b>
6.5.1	Validating Simulation Results for Aluminum Alloy .....	151
6.5.2	Validating Simulation Results for Titanium Alloy with 3/8” SGS Cutter	160
6.5.3	Validating Simulation Results for Titanium Alloy with 3/16” SGS Cutter.... .....	168
6.5.4	Validating Simulation Results for Steel .....	180
<b>6.6</b>	<b>Conclusions.....</b>	<b>184</b>
<b>7</b>	<b>Conclusions.....</b>	<b>185</b>
7.1	Dissertation Overview .....	185
7.2	Major Contributions.....	186
	<b>Bibliography .....</b>	<b>188</b>
	<b>Appendices.....</b>	<b>200</b>
	Appendix A: Experimental Tests .....	200
	Appendix B: Dynamometer Calibration .....	202

## List of Tables

Table 3.1 SLIP and RATIO from experimental data (Brown and Armarego (1964)).....	62
Table 3.2 SLIP and RATIO from experimental data (Pal and Koenigsberger (1968)).....	62
Table 3.3 Average values of RATIO and SLIP extracted from experimental data.....	62
Table 6.1 The range of cutting tests undertaken.....	134
Table 6.2 Cutter information .....	136
Table 6.3 The cutting operations and measured edge radii .....	136
Table 6.4 Workpiece material properties .....	143
Table 6.5 The measured forces at the midpoint of central cuts .....	144
Table 6.6 Identified J-C constitutive parameters for aluminum alloy, titanium alloy and steel..	144
Table AA.1 Milling tests for aluminum alloy .....	200
Table AA.2 Milling tests for titanium alloy with 2 teeth 3/8” end mill cutter .....	200
Table AA.3 Milling tests for titanium alloy with 2 teeth 3/16” end mill cutter .....	201
Table AA.4 Milling tests for AISI 4140 steel .....	201
Table AB.1 Identified parameters used for charge amplifiers (Kistler Model 5004).....	202

# List of Figures

Figure 1.1 Edge radius of milling tools .....	3
Figure 1.2 Milling parameters .....	3
Figure 1.3 Schematic showing 3 phases of milling .....	4
Figure 1.4 Chip load and force relationship .....	4
Figure 1.5 Milling operations .....	5
Figure 2.1 Single shear plane model .....	12
Figure 2.2 Lee and Shaffer's slip-line field solution .....	14
Figure 2.3 Oxley's thin zone model .....	15
Figure 2.4 Kudo's slip line field.....	16
Figure 2.5 Oxley's parallel zone model .....	17
Figure 2.6 Dewhurst model .....	19
Figure 2.7 Geometry of the basic model .....	20
Figure 2.8 Equilibrium of chip .....	21
Figure 2.9 Force in oblique cutting with single edge tool .....	28
Figure 2.10 Face milling geometry .....	31
Figure 2.11 End milling geometry.....	31
Figure 2.12 Milling types .....	32
Figure 2.13 Milling forces.....	34
Figure 2.14 Scheme of forces acting on the face and flank surface of the tool.....	37
Figure 2.15 Endres' dual-mechanism approach .....	39
Figure 2.16 The division of slip-line field (Fang 2003) .....	40
Figure 2.17 Ren and Altintas's model (2000) .....	40
Figure 2.18 Schematic of Waldorf's ploughing force model (1998).....	41
Figure 2.19 Manjunathaiah and Endres's geometric model of edge radius tool (2000).....	43
Figure 3.1 The oblique cutting process .....	48
Figure 3.2 Power and derivative with different assumptions regarding the formulation of rake face force .....	52
Figure 3.3 Normal shear angle versus inclination angle (RATIO=1) .....	55
Figure 3.4 The relationship between SLIP and RATIO with varying inclination and normal shear angles .....	56

Figure 3.5 SLIP as a function of normalized flow angle.....	58
Figure 3.6 The influence of normal rake angle on chip flow angle.....	61
Figure 3.7 Comparison of the predicted chip flow angle with experimental results (Moufki et al. (2000)) .....	63
Figure 3.8 Comparison of the predicted chip flow angle with experimental results (Pal and Koenigsberger (1968)).....	63
Figure 3.9 Comparison of the predicted chip flow angle at various normal rake angles with experimental data from several investigators .....	64
Figure 4.1 Proposed slip-line field for orthogonal cutting chamfer tools.....	67
Figure 4.2 Hodograph of the proposed slip-line field .....	68
Figure 4.3 Moment equilibrium of chip .....	69
Figure 4.4 Force equilibrium on the tool-rake face .....	73
Figure 4.5 Force equilibrium for chamfered tool .....	74
Figure 4.6 Upper bound field for radiused edge.....	75
Figure 4.7 Upper bound solutions for the case of $\gamma_1=-70^\circ$ , $\gamma_2=0^\circ$ , $\beta_s=40^\circ$ .....	77
Figure 4.8 Upper bound solutions for different chamfer angles.....	77
Figure 4.9 Calculation of normal stress on chamfer using two extreme cases of field geometry .....	77
Figure 4.10 Comparison of predicted cutting forces with experimental results.....	78
Figure 4.11 Variation of cutting and thrust forces versus uncut chip thickness.....	80
Figure 4.12 Change in force ratio as uncut chip thickness increases .....	80
Figure 4.13 Cutting force $F_c$ versus chamfer angle for the rake angle of $-10^\circ$ , $0^\circ$ and $10^\circ$ .....	81
Figure 4.14 Thrust force $F_T$ versus chamfer angle for the rake angle of $-10^\circ$ , $0^\circ$ and $10^\circ$ .....	82
Figure 4.15 Variation of cutting force $F_C$ and thrust force $F_T$ with respect to chamfer length .....	83
Figure 4.16 Slip-line field for single edge ploughing model.....	84
Figure 4.17 Double edge slip-line field.....	85
Figure 4.18 Hodograph.....	86
Figure 4.19 Round edge tool ploughing geometry .....	88
Figure 4.20 Specific cutting power versus attack angle .....	89
Figure 4.21 Specific ploughing power with respect to ploughing depth.....	90
Figure 4.22 Specific power versus sliding distance for attack angle $\lambda_s=35^\circ$ .....	91

Figure 4.23 Specific power versus sliding distance for attack angle $\lambda_s=45^\circ$ .....	92
Figure 4.24 Specific power versus sliding distance for attack angle $\lambda_s=55^\circ$ .....	92
Figure 4.25 Slip-line field variation with sliding distance for attack angle $\lambda_s=35^\circ$ .....	93
Figure 4.26 Slip-line field variation with attack angle for sliding distance $l_{slide}=2h_0$ .....	93
Figure 4.27 Specific power versus sliding distance for $\gamma_1=55^\circ$ , $\gamma_2=80^\circ$ and $L_{ED}=0.5 h_0$ .....	93
Figure 4.28 Slip-line field with different sliding distance for ploughing angle $\gamma_1=55^\circ$ , $\gamma_2=80^\circ$ .....	94
Figure 4.29 Simulation of micromilling processes.....	97
Figure 5.1 Diagram of predictive model .....	102
Figure 5.2 Coordinate system of oblique cutting .....	105
Figure 5.3 Normal shear plane for oblique cutting.....	106
Figure 5.4 Slope variation in milling.....	111
Figure 5.5 Orthogonal model with surface slope .....	112
Figure 5.6 Shear angle relationship with RATIO.....	113
Figure 5.7 Force diagram for the shear plane .....	116
Figure 5.8 Geometry of helical tool system .....	117
Figure 5.9 Basic geometry of helical pitch.....	120
Figure 5.10 Tangential velocity of the segment .....	121
Figure 5.11 Plan view of chip.....	123
Figure 5.12 Power change versus depth of cut a and helical angle i .....	126
Figure 5.13 Power change versus tool radius R and helical angle i .....	126
Figure 5.14 Geometry of helical tooth .....	128
Figure 6.1 Mounted cutter samples .....	135
Figure 6.2 SEM image for Cutter A .....	137
Figure 6.3 SEM image for Cutter B .....	137
Figure 6.4 SEM image for Cutter C .....	137
Figure 6.5 SEM image for Cutter D .....	138
Figure 6.6 SEM image for Cutter E.....	138
Figure 6.7 Forces acting on the rake face and shear plane .....	141
Figure 6.8 Centerline cutting force comparison as feedrate changes for central cutting aluminum alloy (cutter A).....	145

Figure 6.9 Centerline cutting force comparison as feedrate changes for central cutting titanium alloy (cutter B).....	145
Figure 6.10 Centerline cutting force as feedrate changes for slotting of steel (cutter D).....	146
Figure 6.11 Predicted shear angle versus uncut chip thickness for central cutting aluminum alloy (cutter A).....	146
Figure 6.12 Predicted shear angle versus uncut chip thickness for central cutting titanium alloy (cutter B).....	147
Figure 6.13 Predicted shear angle versus uncut chip thickness for slotting steel (cutter D).....	147
Figure 6.14 Velocity profile for cutting aluminum alloy (Cutter A).....	149
Figure 6.15 Velocity profile for cutting titanium alloy (Cutter B and C).....	149
Figure 6.16 Velocity profile for cutting titanium alloy (Cutter E).....	150
Figure 6.17 Velocity profile for cutting steel (Cutter D).....	150
Figure 6.18 Measured and predicted forces $F_x$ and $F_y$ for up milling of aluminum alloy ( $V_f=3.95$ in/min, Cutter A).....	151
Figure 6.19 Measured and predicted forces $F_x$ and $F_y$ for up milling of aluminum alloy ( $V_f=7.9$ in/min, Cutter A).....	152
Figure 6.20 Measured and predicted force $F_x$ and $F_y$ for down milling of aluminum alloy ( $V_f=1.28$ in/min, Cutter A).....	152
Figure 6.21 Measured and predicted force $F_x$ and $F_y$ for down milling of aluminum alloy ( $V_f=2.56$ in/min, Cutter A).....	153
Figure 6.22 Measured and predicted force $F_x$ and $F_y$ for down milling of aluminum alloy ( $V_f=3.95$ in/min, Cutter A).....	153
Figure 6.23 Measured and predicted force $F_x$ and $F_y$ for down milling of aluminum alloy ( $V_f=6.75$ in/min, Cutter A).....	154
Figure 6.24 Measured and predicted forces $F_x$ and $F_y$ for central cutting aluminum alloy ( $V_f=1.28$ in/min, Cutter A).....	154
Figure 6.25 Measured and predicted forces $F_x$ and $F_y$ for central cutting aluminum alloy ( $V_f=2.56$ in/min, Cutter A).....	155

Figure 6.26 Measured and predicted forces $F_x$ and $F_y$ for central cutting aluminum alloy ( $V_f=4.4$ in/min, Cutter A).....	155
Figure 6.27 Measured and predicted forces $F_x$ and $F_y$ for central cutting aluminum alloy ( $V_f=6.75$ in/min, Cutter A).....	156
Figure 6.28 Measured and predicted forces $F_x$ and $F_y$ for central cutting aluminum alloy ( $V_f=7.9$ in/min, Cutter A).....	156
Figure 6.29 Force comparison with and without considering ploughing force on central cutting aluminum alloy ( $V_f=1.28$ in/min, Cutter A) .....	157
Figure 6.30 Force comparison with and without considering ploughing force on central cutting aluminum alloy ( $V_f=2.56$ in/min, Cutter A) .....	157
Figure 6.31 Force comparison with and without considering slope effect on central cutting aluminum alloy ( $V_f=7.9$ in/min, Cutter A) .....	158
Figure 6.32 Force comparison with and without considering slope effect on up milling aluminum alloy ( $V_f=7.9$ in/min, Cutter A).....	158
Figure 6.33 Measured and predicted forces $F_x$ and $F_y$ for slotting (center jump of depth of cut) aluminum alloy at different feeding velocities (Cutter A).....	159
Figure 6.34 Measured and predicted forces $F_x$ and $F_y$ for down milling of titanium alloy ( $V_f=0.75$ in/min, Cutter C).....	160
Figure 6.35 Measured and predicted forces $F_x$ and $F_y$ for down milling of titanium alloy ( $V_f=1.5$ in/min, Cutter C).....	160
Figure 6.36 Measured and predicted forces $F_x$ and $F_y$ for down milling of titanium alloy ( $V_f=2.2$ in/min, Cutter C).....	161
Figure 6.37 Measured and predicted forces $F_x$ and $F_y$ for up milling of titanium alloy ( $V_f=0.75$ in/min, Cutter C).....	161
Figure 6.38 Measured and predicted forces $F_x$ and $F_y$ for up milling of titanium alloy ( $V_f=1.5$ in/min, Cutter C).....	162
Figure 6.39 Measured and predicted forces $F_x$ and $F_y$ for up milling of titanium alloy ( $V_f=4.4$ in/min, Cutter C).....	162
Figure 6.40 Measured and predicted forces $F_x$ and $F_y$ for central cutting titanium alloy ( $V_f=0.75$ in/min, Cutter B).....	163
Figure 6.41 Measured and predicted forces $F_x$ and $F_y$ for central cutting titanium alloy ( $V_f=1.5$ in/min, Cutter B).....	163

Figure 6.42 Measured and predicted forces $F_x$ and $F_y$ for central cutting titanium alloy ( $V_f=2.2$ in/min, Cutter B).....	164
Figure 6.43 Measured and predicted forces $F_x$ and $F_y$ for central cutting titanium alloy ( $V_f=3.95$ in/min, Cutter B).....	164
Figure 6.44 Measured and predicted forces $F_x$ and $F_y$ for central cutting titanium alloy ( $V_f=4.4$ in/min, Cutter B).....	165
Figure 6.45 Force comparison with and without considering ploughing force for central cutting titanium alloy ( $V_f=0.75$ in/min, Cutter B).....	166
Figure 6.46 Force comparison with and without considering ploughing force for up milling of titanium alloy ( $V_f=0.75$ in/min, Cutter C).....	166
Figure 6.47 Force comparison with and without considering ploughing force for down milling of titanium alloy ( $V_f=0.75$ in/min, Cutter C).....	167
Figure 6.48 Force comparison with and without considering slope effect for up milling of titanium alloy ( $V_f=4.4$ in/min, Cutter C).....	167
Figure 6.49 Force comparison with and without considering slope effect for central cutting titanium alloy ( $V_f=4.4$ in/min, Cutter B) .....	168
Figure 6.50 Measured and predicted forces $F_x$ and $F_y$ for down milling of titanium alloy ( $V_f=0.75$ in/min, Cutter E).....	169
Figure 6.51 Measured and predicted forces $F_x$ and $F_y$ for down milling of titanium alloy ( $V_f=1.5$ in/min, Cutter E).....	169
Figure 6.52 Measured and predicted forces $F_x$ and $F_y$ for down milling of titanium alloy ( $V_f=2.2$ in/min, Cutter E).....	170
Figure 6.53 Measured and predicted forces $F_x$ and $F_y$ for down milling of titanium alloy ( $V_f=2.56$ in/min, Cutter E).....	170
Figure 6.54 Measured and predicted forces $F_x$ and $F_y$ for up milling of titanium alloy ( $V_f=1.5$ in/min, Cutter E).....	171
Figure 6.55 Measured and predicted forces $F_x$ and $F_y$ for up milling of titanium alloy ( $V_f=1.5$ in/min, Cutter E).....	171
Figure 6.56 Measured and predicted forces $F_x$ and $F_y$ for up milling of titanium alloy ( $V_f=2.2$ in/min, Cutter E).....	172
Figure 6.57 Measured and predicted forces $F_x$ and $F_y$ for up milling of titanium alloy ( $V_f=2.56$ in/min, Cutter E).....	172

Figure 6.58 Measured and predicted forces $F_x$ and $F_y$ for central cutting titanium alloy ( $V_f=0.75$ in/min, Cutter E).....	173
Figure 6.59 Measured and predicted forces $F_x$ and $F_y$ for central cutting titanium alloy ( $V_f=1.5$ in/min, Cutter E).....	173
Figure 6.60 Measured and predicted forces $F_x$ and $F_y$ for central cutting titanium alloy ( $V_f=2.2$ in/min, Cutter E).....	174
Figure 6.61 Measured and predicted forces $F_x$ and $F_y$ for central cutting titanium alloy ( $V_f=2.56$ in/min, Cutter E).....	174
Figure 6.62 Comparison of the predicted forces with and without considering ploughing force for down milling of titanium alloy ( $V_f=0.75$ in/min, Cutter E).....	175
Figure 6.63 Comparison of the predicted forces with and without considering ploughing force for up milling of titanium alloy ( $V_f=0.75$ in/min, Cutter E).....	176
Figure 6.64 Comparison of the predicted forces with and without considering ploughing force for central cutting titanium alloy ( $V_f=0.75$ in/min, Cutter E).....	176
Figure 6.65 Comparison of the predicted forces with and without considering slope effect for down milling of titanium alloy ( $V_f=2.56$ in/min, Cutter E) .....	177
Figure 6.66 Comparison of the predicted forces with and without considering slope effect for up milling of titanium alloy ( $V_f=2.56$ in/min, Cutter E) .....	177
Figure 6.67 Comparison of the predicted forces with and without considering slope effect for central cutting titanium alloy ( $V_f=2.56$ in/min, Cutter E).....	178
Figure 6.68 Comparison of the effect of velocity profile for down milling of titanium alloy ( $V_f=2.56$ in/min, Cutter E).....	178
Figure 6.69 Comparison of the effect of velocity profile for up milling of titanium alloy ( $V_f=2.56$ in/min, Cutter E).....	179
Figure 6.70 Comparison of the effect of velocity profile for central cutting titanium alloy ( $V_f=2.56$ in/min, Cutter E).....	179
Figure 6.71 Measured and predicted forces $F_x$ and $F_y$ for slotting of steel ( $V_f=0.75$ in/min, Cutter D).....	180

Figure 6.72 Measured and predicted forces $F_x$ and $F_y$ for slotting of steel ( $V_f=1.28$ in/min, Cutter D).....	181
Figure 6.73 Measured and predicted forces $F_x$ and $F_y$ for slotting of steel ( $V_f=1.5$ in/min, Cutter D).....	181
Figure 6.74 Measured and predicted forces $F_x$ and $F_y$ for slotting of steel ( $V_f=2.2$ in/min, Cutter D).....	182
Figure 6.75 Measured and predicted forces $F_x$ and $F_y$ for slotting of steel ( $V_f=2.56$ in/min, Cutter D).....	182
Figure 6.76 Measured and predicted forces $F_x$ and $F_y$ for slotting of steel ( $V_f=3.95$ in/min, Cutter D).....	183
Figure 6.77 Comparison of force prediction with and without considering edge force for slotting of steel ( $V_f=0.75$ in/min, Cutter D) .....	183
Figure AA.1 Geometry of central cutting titanium alloy by 3/16” end mill cutter .....	201
Figure AB.1 Calibration of the dynamometer in x direction.....	203
Figure AB.2 Calibration of dynamometer in y direction.....	203
Figure AB.3 Calibration of dynamometer in z direction.....	204

## Nomenclature

$a$	Axial depth of cut
$a_2$	Penetration depth
$A$	Material constant of Johnson-Cook model
$A_c$	Plastic contact area on the rake face
$A_s$	Area of shear plane
$A_s^e$	Elemental area of shear plane
$B$	Material constant of Johnson-Cook model
$C_m$	Material constant of Johnson-Cook model
$d$	Radial depth of cut
$D$	Tool diameter
$ds_1$	Elemental length along the slip-line $\alpha$
$ds_2$	Elemental length along the slip-line $\beta$
$E$	Young's modulus
$F_C$	Principal cutting force
$F'_C$	Cutting force for orthogonal cutting
$F_{CE}$	Edge force component in the principal cutting direction
$F_C^e$	Elemental principal cutting force
$F_{C,elastic}$	Elastic force component in the cutting direction
$F'_{CE}$	Edge force component in the cutting direction for orthogonal cutting
$F'_{CH}$	Cutting force component in orthogonal cutting for high negative rake cutting
$F_{CP}$	Ploughing force component in the principal cutting direction
$F'_{CP}$	Ploughing force component in the cutting direction for orthogonal cutting
$F_{CS}$	Sharp tool cutting force
$F_f$	Resultant friction force acting on the rake face
$F_{f,elastic}$	Elastic friction force acting on the tool-chip interface
$F_{ft}$	Friction force component parallel to the cutting edge on the rake face

$F_{fr}$	Friction force component normal to the cutting edge on the rake face
$F_N$	Normal force acting on elastic region of rake face
$F_R$	Lateral force
$F_r$	Radial force component in milling
$F_{RE}$	Edge force component in the lateral direction
$F_R^e$	Elemental lateral force
$F_{RP}$	Ploughing force component in the lateral direction
$F_S$	Resultant shear force
$F_{sr}$	Shear force component normal to the cutting edge in the shear plane
$F_{st}$	Shear force component parallel to the cutting edge in the shear plane
$F_S^e$	Elemental resultant shear force
$F_t$	Tangential force component in milling
$F_T$	Thrust force
$F_T'$	Thrust force for orthogonal cutting
$F_{TE}$	Edge force component in the transverse direction
$F_T^e$	Elemental transverse cutting force
$F'_{TE}$	Edge force component in the transverse direction for orthogonal cutting
$F_{T,elastic}$	Elastic contact force component along the vertical direction
$F'_{TH}$	Thrust force component in orthogonal cutting for high negative rake cutting
$F_{TP}$	Ploughing force component in the transverse direction
$F'_{TP}$	Ploughing force component in the transverse direction for orthogonal cutting
$F_{TS}$	Sharp tool thrust force
$F_x$	Milling force component in the x direction
$F_y$	Milling force component in the y direction
$F_z$	Milling force component in the z direction
$G_c$	Fracture toughness
$h$	Instantaneous uncut chip thickness in milling operations

$h_0$	Uncut chip thickness
$h_1$	Chip thickness
$h_{av}$	Average chip thickness in milling operations
$h_{cr}$	Critical uncut chip thickness
$h_m$	Minimum chip thickness
$i$	Inclination angle
$k$	Shear flow stress
$k^e$	Elemental shear yield stress
$K$	Thermal diffusivity
$k_{AB}^N$	Shear yield stress in normal shear plane
$K_{cf}$	Normal force coefficient on the clearance face
$K_f$	Rake face force coefficient
$L$	Fan radius of ploughing model; Height of primary deformation zone for chamfer model
$l$	Length of cut
$L_C$	Chip-tool contact length
$lc$	Chip length
$L_{chmf}$	Chamfer land length
$L_E$	Elastic contact length
$L_e$	Equivalent tool cutting length
$l^N$	Normal shear plane length
$L_P$	Plastic contact length
$l_s$	Shear plane length
$l_{slide}$	Sliding distance
$m$	Material constant of Johnson-Cook model
$n$	Material constant of Johnson-Cook model
$N$	Normal force on the rake face for orthogonal cutting
$N_e$	Number of segment for helical tool
$N_{EF}$	Normal force acting on chamfer plane
$n_{eq}$	Equivalent work hardening term
$N_f$	Number of teeth

$N_s$	Normal force acting on the shear plane
$p$	Hydrostatic pressure
$P$	Total power consuming
$P_f$	Rate of energy dissipation by friction force
$P_{shear}$	Continuous volume shear power
$P_{shear}^e$	Element continuous volume shear power
$P_s$	Shear plane plasticity energy dissipation rate
$P_T$	Total power consumption for chamfer tool
$r$	Chip thickness ratio; Nose radius
$r_1$	Ratio of tangential to radial cutting force
$r_2$	Ratio of tangential to radial parasitic force
$r_e$	Tool edge radius
$R$	Tool radius; Height of secondary deformation zone for chamfer model
$RPM$	Spindle speed [rev/min]
$R_i$	Inside chip radius
$R_o$	Outside chip radius
$R_{tool}$	Tool resultant cutting force
$S$	Specific heat
$S_t$	Feed per tooth
$T$	Temperature
$T_l$	Temperature at the lower boundary of shear zone
$T_u$	Temperature at the upper boundary of shear zone
$u_r$	Chip flow velocity in the radial direction
$u_t$	Chip flow velocity in the tangential direction
$u_x$	Chip flow velocity in the x direction
$u_y$	Chip flow velocity in the y direction
$u_z$	Chip flow velocity in the z direction
$u_{x'}$	Chip flow velocity in the x' direction
$u_{y'}$	Chip flow velocity in the y' direction
$u_{z'}$	Chip flow velocity in the z' direction

$V_0$	Cutting velocity
$V_C$	Chip velocity on the rake face
$V_C^e$	Elemental chip velocity on the rake face
$V_{cn}$	Component of chip velocity normal to the cutting edge on the rake face
$V_{cn}^e$	Elemental component of chip velocity normal to the cutting edge on the rake face
$V_{ct}$	Component of chip velocity parallel to the cutting edge on the rake face
$V_{ct}^e$	Elemental component of chip velocity parallel to the cutting edge on the rake face
$V_f$	Table feeding velocity
$V_i$	Interference volume
$V_S$	Shear velocity on the shear plane
$V_S^e$	Elemental shear velocity on the shear plane
$V_S^N$	Shear velocity component along normal shear plane
$V_{sn}$	Component of shear velocity normal to the cutting edge in the shear plane
$V_{sn}^e$	Elemental component of shear velocity normal to the cutting edge in the shear plane
$V_{st}$	Component of shear velocity parallel to the cutting edge in the shear plane
$V_{st}^e$	Elemental component of shear velocity parallel to the cutting edge in the shear plane
$w$	Width of cut
$x$	Fraction of the cutting power transformed to heat; Elastic sliding distance relative to the plastic point B on the rake face for chamfer model; Global coordinate direction x
$x'$	Local coordinate direction $x'$
$y$	Global coordinate direction y
$y'$	Local coordinate direction $y'$
$z$	Distance between the plastic point B and $F_N$ for chamfer model; Global coordinate direction z

$z'$	Local coordinate direction $z'$
$z_e$	Height of the element
$z_h$	Height of linear tangential velocity equal to constant tangential velocity
$\beta$	Friction angle
$\beta_A$	Average friction angle
$\beta_N$	Normal friction angle
$\beta_s$	Elastic friction angle
$\delta$	Fan angle of ploughing model
$\delta_s$	Surface slope
$\delta_s^e$	Elemental surface slope
$\Delta T$	Increased temperature
$\varepsilon$	Strain
$\dot{\varepsilon}$	Strain rate
$\dot{\varepsilon}_0$	Reference strain rate
$\varepsilon_{AB}^N$	Normal shear plane strain along middle shear zone
$\dot{\varepsilon}_{AB}^N$	Normal shear plane strain rate along middle shear zone
$\dot{\varepsilon}_p$	Equivalent strain rate
$\dot{\varepsilon}_{rr}, \dot{\varepsilon}_{\theta\theta}, \dot{\varepsilon}_{r\theta}$	Tension and shear strain rates
$\phi$	Shear angle
$\phi_N$	Normal shear angle
$\phi_{N0}$	Normal shear angle when $\delta_s=0$
$\gamma$	Rake angle
$\gamma_1$	Chamfer angle; Rake angle for single edge ploughing model
$\gamma_2$	Chamfer tool rake angle
$\gamma_{ave}$	Equivalent rake angle
$\gamma_e$	Effective rake angle
$\gamma_N$	Normal rake angle
$\gamma_{oblique}$	Oblique cutting strain

$\dot{\gamma}_{oblique}$	Strain rate of oblique cutting
$\gamma_v$	Velocity rake angle
$\eta_c$	Chip flow angle
$\eta_s$	Shear flow angle
$\eta_s^e$	Elemental shear flow angle
$\lambda$	Runout angle
$\lambda_s$	Attack angle
$\mu$	Coefficient of friction
$\mu_{cf}$	Friction coefficient on the clearance face
$\theta$	Angle between the resultant force and the shear plane
$\theta_N$	Angle between the resultant force and the normal shear plane
$\rho$	Material density; Magnitude of runout; Ploughing bulge angle
$\sigma$	Yield stress; Normal stress distribution on the tool rake face
$\sigma_{AB}^N$	Yield stress in normal shear plane
$\sigma_B$	Normal force at point B for chamfer tool model
$\sigma_{N,GF}$	Normal force acting at the plastic region GF for chamfer tool model
$\sigma_y$	Yield stress
$\Omega$	Spindle speed
$\psi$	Tool rotation angle; Approach angle
$\psi_1$	Central cut entry angle
$\psi_2$	Central cut exit angle
$\psi_e$	Effective approach angle
$\psi_{en}$	Entry angle
$\psi_{ex}$	Exit angle
$\psi_L$	Helix pitch rotation angle
$\psi_s$	Immersion angle

## **Acknowledgements**

I take this opportunity to express my sincere gratitude to my supervisors, Dr. Ian Yellowley and Dr. Rudolf Seethaler, for their expert guidance, valuable suggestions and advice throughout the course of this thesis. I also thank them for their financial support during the years of my doctoral program. A heart-felt thanks to Prof. Yellowley for his kindness and care throughout the doctoral program, although he is retired, he has still spent a great deal of time guiding the direction of my research. I am very grateful to Dr. Rudolf Seethaler for his help in the design and implementation of the experimental program which was conducted to verify the modeling process.

I would like to thank technicians Markus Fengler and Erik Wilson for their help in testing.

I would like to thank my wife Ping Lu and son Jie Zou for their sacrifices, endless inspiration and patience without which this work would not have been completed.

# 1 Introduction

## 1.1 Overview

Milling is a commonly used machining operation in the aerospace, automobile and die-mold industries. The milling operation removes material by feeding a workpiece past a rotating single or multiple teeth cutter; the process is versatile and allows large amounts of material to be removed quickly. Competition in the manufacturing market requires the use of efficient and cost-effective planning systems and the optimization of process plans; both require the availability of good physical models of the machining processes. Many of the current machining models, whether for force, power, surface finish or tool life are expressed in empirical form and the required constants must be determined experimentally. These models are useful and necessary; however, the resulting equations and parameters are often restricted to a particular operation and condition tested. There is clearly considerable scope to improve the accuracy and validity of the process models on the basis of the fundamental physics and mechanics. The need for quantitative machining performance information has been recognized by many researchers and by industry (Armarego et al. 1995; Armarego 2000; Chiou et al. 2005; Wang et al. 2004; and Li and Shin 2006). Due to the wide variety of machining operations and numerous factors influencing each operation, the development of models for the prediction of machining performance presents a formidable task.

In milling, as in other machining operations, the work material goes through a severe deformation process, at very high deformation strain (up to 4), strain rate (up to  $10^6$  1/s), and temperatures (up to 1000 °C). A major challenge in describing the milling

## 1 Introduction

forces analytically is the computation of the flow stress in the primary shear zone. The experimental methods commonly used to determine flow stress data through tensile and/or compression tests are not able to represent deformation behavior in these ranges of strain, strain rate, and temperature (Jaspers and Dautzenberg 2002). Jaspers and Dautzenberg (2002) conducted experiments using a Split Hopkinson's Pressure Bar (SHPB) test to obtain the Johnson-Cook and Zerilli-Armstrong constitutive equations for AISI 1045 steel and 6082-T6 aluminum alloy. Sartkulvanich et al. (2004) proposed an approach to estimate the flow stress data using an orthogonal slot milling test. Finding approaches to describe the general complex milling operations with an accurate and reliable constitutive model is still a challenge.

The milling process usually involves chip thicknesses that are small and variable; such chip thicknesses are often too small to promote cutting and instead result in either sliding or ploughing (Liu et. al. 2004). It is well known that the cutting tool is not perfectly sharp, and that there is always an edge radius at the cutting edge of a "sharp" tool; in addition, tool wear is a natural and inevitable process for all cutting tools that further degrades the cutting edge. The edge is thought to play a significant role in the cutting forces, especially in milling where the radius of the edge relative to the chip thickness will be much higher. The major difference between micro and conventional end milling operations, (from the perspective of this work), is that as the size of a tool decreases, the sharpness of the tool cannot be improved proportionally due to limitations in the tool fabrication processes and the need to provide some degree of strength at the tool edge. Figure 1.1 shows the edge radius of the milling tools, which can exert considerable influence on the cutting forces. Macro-chip formulation models are based on

## 1 Introduction

the assumption that the cutting tool completely removes the surface of the work piece (i.e., no material flows under the tool or is displaced sideward). On the other hand, the micro milling chip thickness is of the same order as tool edge radius and the same assumption cannot be made.

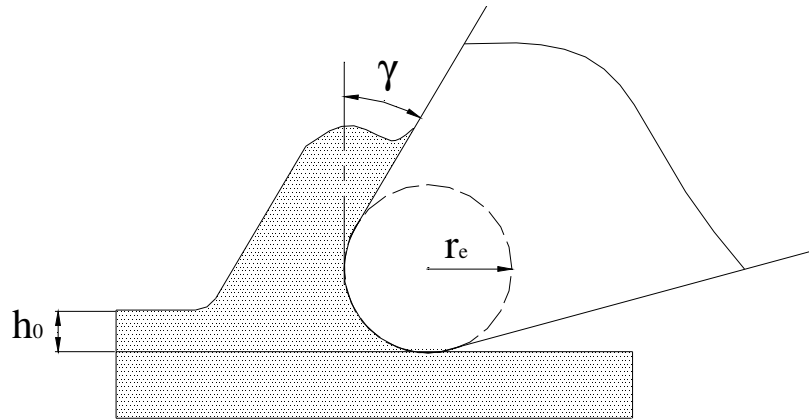


**Figure 1.1 Edge radius of milling tools**

The instantaneous chip thickness in milling can be approximated as

$$h(\psi) = S_i \sin \psi \quad (1.1)$$

where  $\psi$  is the angle of immersion (shown in Figure 1.2).

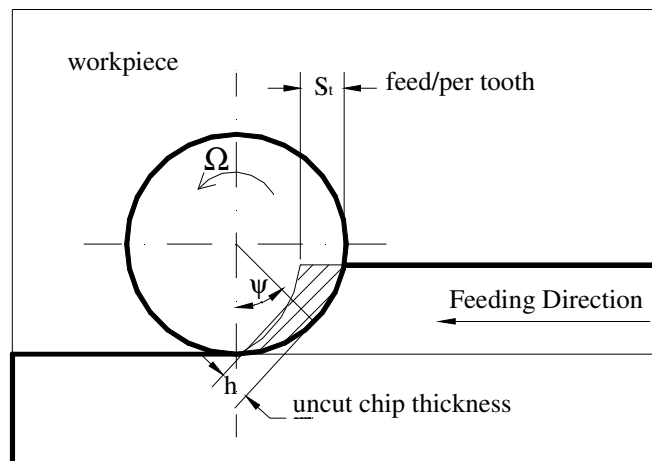


**Figure 1.2 Milling parameters**

## 1 Introduction

However, in reality the cutting process only proceeds once the elastic deflection and initial ploughing process have been completed, (see Figure 1.3 below which depicts the 3 stages).

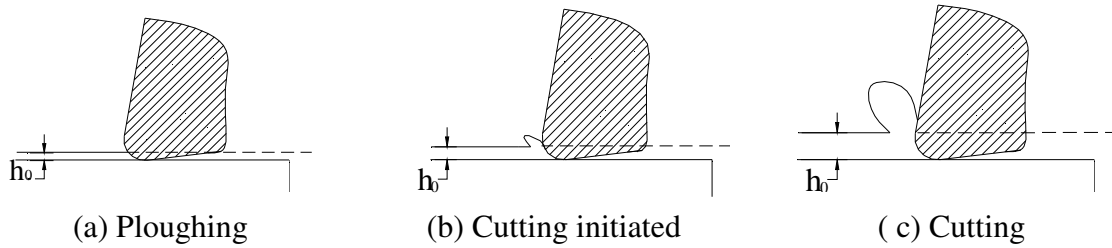


**Figure 1.3 Schematic showing 3 phases of milling**

Liu et al. (2004, 2006, and 2007) experimentally examined chip formulation and micro-cutting forces. They concluded that sudden change in thrust force corresponded to the shift from ploughing to cutting and hence occurred at what is termed the critical chip thickness. This sudden change in thrust forces was explained by a shifting from a ploughing/sliding process to normal cutting as shown in Figure 1.4. The same pattern of change in force and physical explanation has been reported in the milling of titanium alloy with worn tools by Yellowley et al. (1992).

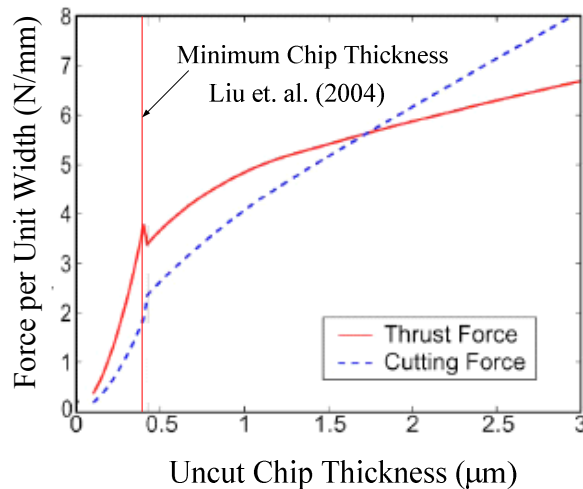


**Figure 1.4 Chip load and force relationship**

## 1 Introduction

In examining the peripheral milling processes one must differentiate between the up and down milling modes, (as shown in Figure 1.5). One expects that the entry and exit effects will be quite different between the down milling and up milling processes and need to be modeled with different fields. In addition, the work surface slope and the uncut chip thickness continuously vary in the milling processes somewhat resembling wave removing in dynamic cutting. The slope is a function of the cutter diameter and the feedrate in milling operations and is positive for up-milling and negative for down-milling. The effect of slope on the milling operations has been examined by previous authors (Pandey and Shan 1972; Altintas 1986). Pandey and Shan (1972) examined the slope change due to the advancement of shear plane, while Altintas (1986) only considered the chip thickness variation, more research is needed to study the effect of the total surface slope on the forces in milling operations as well as the relationship between the shear angle and the surface slope.

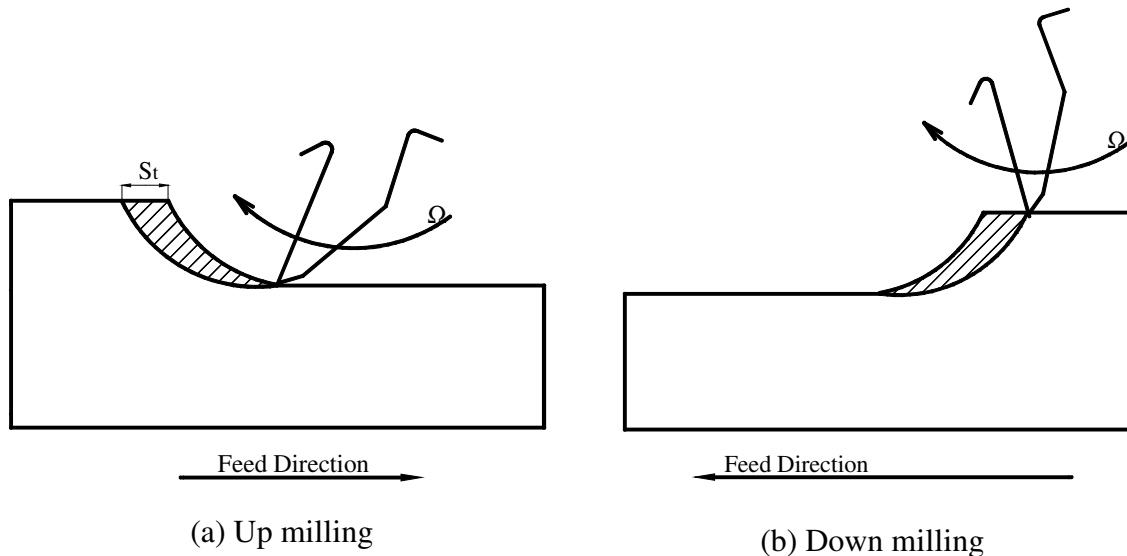


**Figure 1.5 Milling operations**

### 1.2 Objective and Scope of Thesis

Milling forces for a particular tool-workpiece pair are related to a variety of parameters, such as, width of cut, chip thickness, tool edge radius, constrained kinematics of the chip, cutting velocity, and milling type. Such parameters are difficult to incorporate in a conventional mechanistic modeling approach. This thesis intends to estimate the expected contribution of these influences so as to extend the applicability of a conventional modeling approach. Specific areas of concentration are stated as follows:

- 1) Practical milling cutters have significant edge radius and wear during their active life. Since the milling chip thicknesses are very small and variable, surface integrity and cutting forces are greatly influenced by the process at the tool edge. Traditionally, the majority of the modeling effort has concentrated on the deformation of the chip material. More recently a strong interest in understanding the physics of the process occurring at the cutting edge and below the tool has emerged. In addition, it is important to study all the milling force generation processes by considering the influences of the entry and exit processes.
- 2) Helical end milling tools have non-straight cutting edges and non-planar rake faces. Non-straight cutting edges cause the kinematic constraint in the cutting process. A kinematically admissible velocity field for the analysis of helical tools needs to be investigated to estimate the size of this influence.
- 3) Since helical milling cutters have non-planar rake faces and complex tool edge geometry, it is not possible to experimentally determine the shear angle from the chip geometry. This requires the development of an oblique cutting model that obviates the necessity for accurate shear angle data during calibration.

## 1 Introduction

- 4) Unlike the normal oblique cutting processes, the surface inclination to the cutting direction and the uncut chip thickness continuously vary in the milling processes (either increasing in up milling or decreasing in down milling). The usual shear plane force models show no dependence on the surface slope. In order to estimate the milling forces with sufficient accuracy, the influence of surface slope on the equilibrium value of shear angle needs to be investigated and included in a realistic milling model.
- 5) In practice no tool is perfectly sharp and the cutting edge always has a finite radius with corresponding forces acting at the cutting edge. In addition, due to wear, possible deformation of the cutting edge and perhaps the surface generation, additional forces will exist in this region. Because these forces are not considered to contribute to the chip removal process they are collectively referred to as the edge force. It is difficult to measure the edge force directly, especially in milling where the chip thickness is variable. The author investigates the design of a series of experimental tests and the development of a realistic methodology to identify the material properties and the characteristics of the primary shear zone based on the measured milling forces that avoid as much as possible the influence of edge forces and slope on the forces used for calibration. (The changes expected from these are incorporated in the final force equations).
- 6) The thesis attempts to develop a simple predictive model for milling operations that includes the considerations for the complex milling cutter edge geometries, the influence of tool edge radius, kinematics and the surface slope. It also incorporates realistic material models to cope with varying values of strain, strain

## 1 Introduction

rate and temperature. The model considers both the conventional chip formation aspects of the process as well as subsurface flow.

### 1.3 Outline

The chapters in this thesis are arranged as follows. Chapter 2 provides a review of metal cutting theory and milling operations. Basic orthogonal and oblique metal cutting models based on a single shear plane, slip-line fields, upper bound methods, and FEM approaches are introduced. The characteristics of milling operations, chip thickness models, edge forces and ploughing effects are presented.

Chapter 3 presents a new upper-bound model that incorporates force equilibrium parallel to the cutting edge for oblique cutting operations. The energy approach is framed in terms of the normal shear angle and two new fundamental variables that characterize the energy requirements of the oblique cutting process. *SLIP* is a kinematic variable and is defined as the ratio of the shear velocity imparted to the chip on the shear plane parallel to the cutting edge, to the incoming velocity in the same direction. *RATIO* is a force based variable and is defined as the ratio of the friction force on the rake face to the resultant shear force in the shear plane. Calibration of the model for either real time identification purposes or for process planning/optimization requires experimental force data but no shear angle data making it very suitable for the analysis of cutting operations with non-straight cutting edges.

Chapter 4 describes the extension of a simple predictive model for orthogonal cutting to accommodate flow under the cutting edge. The model utilizes an upper bound approach combined with primary and secondary boundaries that guarantee both force and moment equilibrium of the chip. Next, single and double edge ploughing models are

## 1 Introduction

developed to study the ploughing process, ploughing/cutting transition and minimum chip thickness. The issues of entry and exit of milling operations are discussed, also.

Chapter 5 presents a predictive force model for peripheral milling operations based on the integration of the newly developed oblique cutting model and the incorporation of edge effects together with the adoption of a realistic material model, surface slope and admissible velocity profile.

Chapter 6 presents the validation processes of the proposed model. The cutter edge radius is measured by scanning electron microscope (SEM). The predictive results are compared with experimental results for various workpiece materials, tool diameters, feeding velocities, and milling types.

Chapter 7 points out the development and contribution of the present works; in particular recommends the importance of the second order effects in peripheral milling simulations.

## **2 Literature Survey**

### **2.1 Introduction**

The milling operation is a metal cutting process that uses a rotating cutter that normally has multiple teeth. The process is usually oblique and a varying chip thickness is presented to the cutting edges. Chip formation in milling is the central issue that must be addressed in order to progress to a consideration of the practical variables of cutting force, tool wear and tool life, chatter, and tool breakage. The analysis of cutting forces generated during machining has been a popular research topic and from a practical point of view, force measurements have been shown to be valuable in the monitoring of cutting processes. This chapter provides a brief review of the previous research related to the modeling of machining operations. First, the fundamental physics and mechanics of metal cutting are discussed. Second, previous research covering the 3D cutting models, (especially the equivalent orthogonal models), is presented. Third, the modeling of practical milling operations is discussed. Special attention is given to the characteristics of milling operations, chip kinematics, cutting and edge force components and the incorporation of the ploughing effect within the analysis of milling processes.

### **2.2 Basic Mechanics of Metal Cutting**

The purpose of metal cutting process is to remove material and in doing so to create a new surface. The majority of modeling effort has concentrated on the deformation of the chip material and ignores the secondary factors. Researchers in this field have attempted to develop theories of the cutting process that can predict important

## 2 Literature Survey

cutting parameters without the need for empirical formulation. The following sections briefly review previous works based upon shear plane models, slip-line fields, simple upper bound models, and FEM analysis.

### 2.2.1 Shear Plane Models

The most widely used model is that proposed by Ernst and Merchant (1941) and Merchant (1944, 1945). The model describes shearing of incoming material as it passes through the primary shear zone. Earlier work by Piispanen (1937), considered that the shear process of metal is similar to cutting a deck of stacked cards; the cards being inclined at the effective shear plane angle. As the cards approach the tool, they are forced to slide over each other due to resistive force provided by the tool. Merchant (1944) was the first to attempt to analyze the process and attempt to obtain a relationship between the shear angle and other variables. He began the metal cutting analysis by making certain assumptions, as follows

- 1) The tool is perfectly sharp and there is no contact along the clearance face;
- 2) The shear surface is a plane extending upward from the cutting edge to the free surface;
- 3) The chip is in a state of quasi-static equilibrium;
- 4) There is a constant coefficient of friction on the tool rake face;
- 5) The shear and normal stresses along the shear plane and tool are uniform. The forces acting between the chip and tool acting on the tool face, the shear plane and in the direction of relative work/tool velocity are shown in a free body diagram in Figure 2.1. The following relations follow from the assumption of equilibrium

## 2 Literature Survey

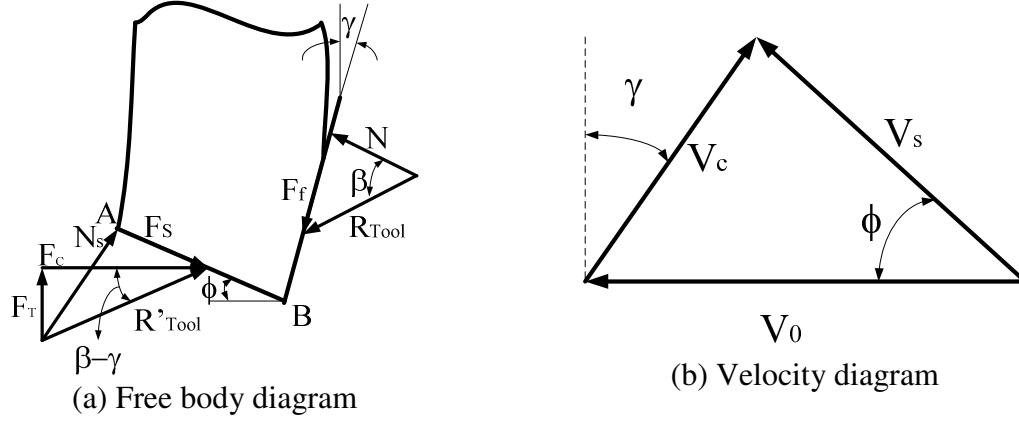


**Figure 2.1 Single shear plane model**

$$\begin{aligned} F_s &= F_C \cdot \cos \phi - F_T \cdot \sin \phi \\ N_s &= F_T \cdot \cos \phi + F_C \cdot \sin \phi \end{aligned} \quad (2.1)$$

where  $\beta$  is the friction angle and  $\mu$  the coefficient of friction given by

$$\begin{aligned} \beta &= \tan^{-1}(\mu) \\ F_f &= F_C \cdot \sin \gamma + F_T \cdot \cos \gamma \\ N &= F_C \cdot \cos \gamma - F_T \cdot \sin \gamma \\ \mu &= \frac{F_f}{N} \end{aligned} \quad (2.2)$$

Assuming that there is only sliding friction on the rake face and that there is a thin primary shear deformation area, then the power consuming force and the thrust force can be formulated as follows

$$\begin{aligned} F_C &= h_0 w k \left[ \frac{\cos(\beta - \gamma)}{\sin \phi \cdot \cos(\phi + \beta - \gamma)} \right] \\ F_T &= h_0 w k \left[ \frac{\sin(\beta - \gamma)}{\sin \phi \cdot \cos(\phi + \beta - \gamma)} \right] \end{aligned} \quad (2.3)$$

where  $w$  is the width of cut and  $h_0$  is the uncut chip thickness. The shear angle may be found experimentally by considering the material volume continuity

## 2 Literature Survey

$$\phi = \tan^{-1} \left( \frac{r \cdot \cos \gamma}{1 - r \cdot \sin \gamma} \right) \quad (2.4)$$

where  $r$  is the cutting ratio, or chip thickness ratio

$$r = \frac{h_0}{h_1} = \frac{\sin \phi}{\cos(\phi - \gamma)} \quad (2.5)$$

and  $h_1$  is the chip thickness.

The velocity diagram is shown in Figure 2.1b. The cutting velocity,  $V_0$ , is the velocity of the tool relative to the workpiece and is parallel to  $F_c$ . The chip velocity,  $V_c$ , is the velocity of the chip relative to the workpiece and is directed along the tool face. The shear velocity  $V_s$  is the velocity of chip relative to the workpiece; this component is directed along the shear plane.

$$\begin{aligned} V_c &= \frac{\sin \phi}{\cos(\phi - \gamma)} V_0 \\ V_s &= \frac{\cos \gamma}{\cos(\phi - \gamma)} V_0 \end{aligned} \quad (2.6)$$

### 2.2.2 Slip Line Field

Lee and Shaffer (1951) were the first researchers to apply engineering plasticity to solve the metal cutting problem; their slip line field is shown in Figure 2.2. The Lee and Shaffer model makes the following assumptions:

- 1) The work material is rigid-perfectly plastic;
- 2) The field is in a state of plain strain;
- 3) The cutting zone approximates a constant stress field;
- 4) No elastic contact is apparent, (hence the final boundary is stress free).

## 2 Literature Survey

Because the state of stress in ABC is uniform, a single Mohr circle diagram was used for its representation as shown in Figure 2.3. Since the maximum stress that can be withstood is  $k = \tau_y$ , the radius of the circle is  $k$ . Further, since there is no force across AC then the Mohr circle passes through the origin. There are two possible circles satisfying these conditions, one in which all normal stress components are tensile and the other in which are compressive; the latter is the appropriate one. Based on the Mohr circle, the Lee and Shaffer solution gives the following expression for the shear angle

$$\phi + \beta - \gamma = \frac{\pi}{4} \quad (2.7)$$

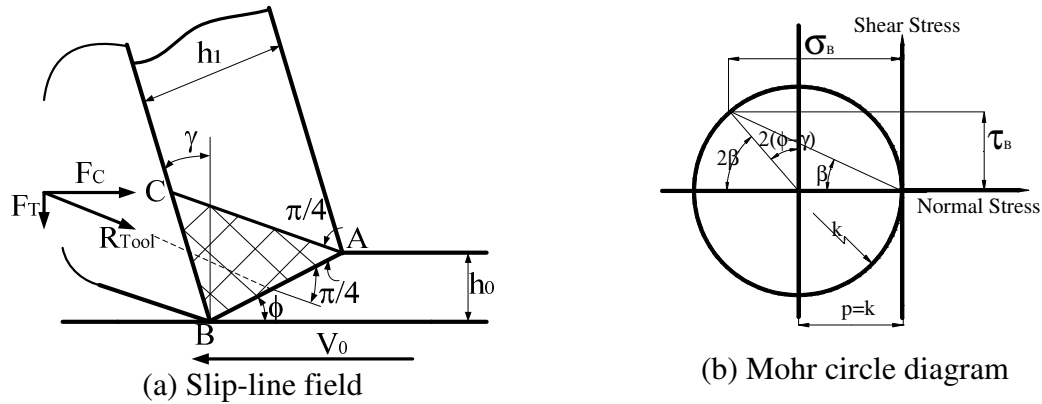


**Figure 2.2 Lee and Shaffer's slip-line field solution**

Oxley (1961, 1963) applied a simplified slip-line field to a thin zone model in metal cutting as shown in Figure 2.3. The deformation zone was assumed to be bounded by straight and parallel slip lines at an angle of  $\phi$  to the direction of motion, and the point A to be a negligible distance from the free surface. The approximation allows one to consider that the stresses acting on the shear plane are uniform. Oxley used the modified Hencky relationships with a work-hardening term to describe the stress condition in the plastic zone as:

## 2 Literature Survey

$$\begin{cases} p + 2k\psi + \int \frac{\partial k}{\partial s_2} ds_1 = \text{const} & \text{along line } \alpha \\ p - 2k\psi + \int \frac{\partial k}{\partial s_1} ds_2 = \text{const} & \text{along line } \beta \end{cases} \quad (2.8)$$

where  $p$  is the hydrostatic stress,  $k$  is the yield stress,  $\psi$  is the slip line counter-clockwise rotation angle,  $ds_1$  and  $ds_2$  are elemental length along the slip lines  $\alpha$  and  $\beta$ , respectively, and  $\psi$  is the angle between a tangent to the slip line  $\alpha$  at any point and a reference axis. The method first involves finding two expressions for the hydrostatic stress at point B; one applying the modified Hencky relationships along the shear plane, the other considering the stress between the chip and tool. The assumed stress distribution is shown in Figure 2.3b. From these expressions, the relationship for the angle  $\theta$ , between the resultant cutting force and the shear plane, is obtained as

$$\theta = \tan^{-1} \left[ \frac{1}{2} + \frac{\pi}{4} - \phi + \left( 1 + \frac{h'}{h} \right) \frac{\cos 2(\phi - \gamma)}{2 \tan \beta} - \frac{\sin 2(\phi - \gamma)}{2} \right] \quad (2.9)$$

and  $\theta = \phi + \beta - \gamma$

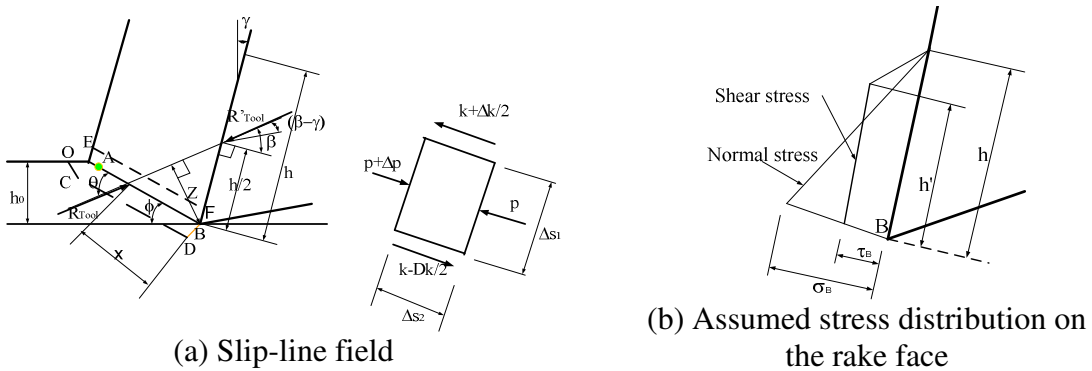


**Figure 2.3 Oxley's thin zone model**

Kudo (1965) suggested a slip-line field solution that included the possibility of curl by replacing the straight slip-lines of Lee and Shaffer with curved slip-lines (Figure 2.4). The suggested field satisfies the kinematic requirements of chip flow but the



## 2 Literature Survey

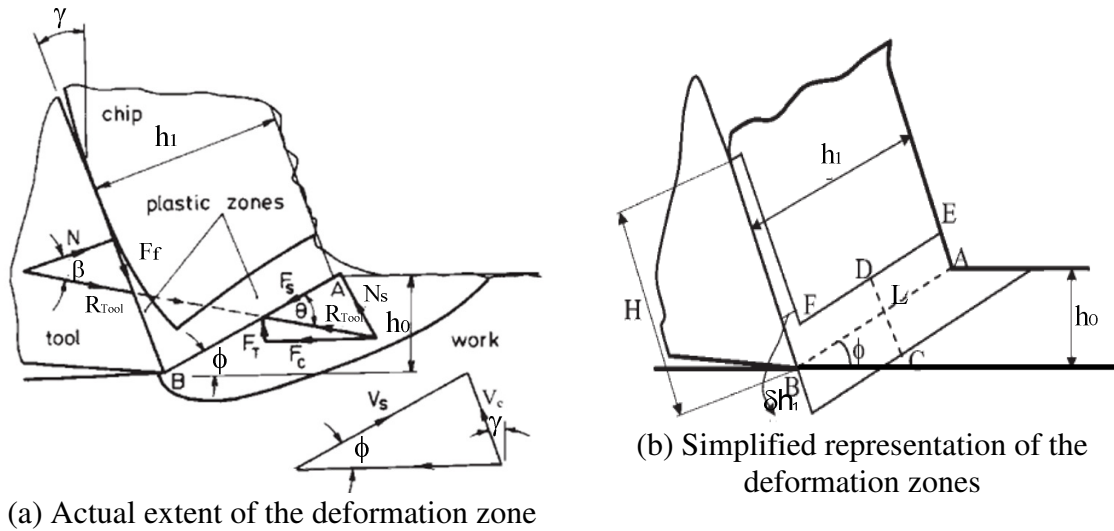


**Figure 2.5 Oxley's parallel zone model**

In the configuration shown in Figure 2.5, the slip-line in the primary shear zone along the direction AB is an  $\alpha$  slip-line and the slip-line in the secondary shear zone along the chip face is a  $\beta$  slip-line. Assuming that the strain along AB is uniform, equal to one half the strain in the primary shear zone, and further assuming that the temperature and strain rate are uniform along AB, the shear stress along AB is calculated from the material model. This is used to obtain the shear force as well as the power dissipated in the primary shear zone. The partition of heat between the chip and the workpiece is obtained by using the results of Boothroyd (1965). Again assuming a uniform distribution of the normal stress along the rake face, the tool-chip contact length is obtained so that the moment of the normal force about the point B equals to the moment of the resultant force along the shear plane. The normal stress  $\sigma_n$  and the shear stress  $\tau_{int}$  on the rake face are obtained from the corresponding forces and the contact length. The normal stress on the rake face can be obtained in a different manner by assuming that the  $\alpha$  slip-line in the primary shear zone turns to meet the tool perpendicular to the rake face. Assuming that

## 2 Literature Survey

there is sticking friction at the tool-chip interface, the shear strength of the chip ( $k_{chip}$ ) at the average temperature of the tool chip interface should be equal to  $\tau_{int}$  is taken to be correct shear plane angle.

Dewhurst (1978) proposed a non-unique solution for machining with chip curling. Dewhurst noted that other investigators, notably Oxley and coworkers, have taken the view that an understanding of the process can only be attained by considering the distribution of temperature in the deformation zone as well as the influence of strain-rate and strain hardening of the deforming material. With this premise however the problem becomes analytically intractable so that theoretically unjustifiable assumptions about the mode of deformation are needed in order to obtain solutions. For example, in their investigation of the friction conditions along the tool face, Oxley and Hastings (1976) were forced to make assumptions about the thickness of the deformation zone and the contact length between the tool and the chip. Moreover, the known solutions ignore one of the most basic experimental facts that the chip emerges from the deforming zone with significant angular velocity. Deriving and analyzing the mixed stress and velocity boundary conditions in the deforming zone, Dewhurst was able to construct his slip-line field justifying these comments. The physical model and corresponding hodograph are shown in Figures 2.6a and 2.6b respectively. Analyzing this velocity hodograph, Dewhurst concluded that the slip-line field could satisfy a range of values of rake angles. Therefore only three conditions  $F_1 = F_2 = M = 0$  (the force components that maintain chip equilibrium) remain to determine the value of four parameters  $\psi$ ,  $\theta$ ,  $\eta$ , and  $p_A$  (which is the hydrostatic pressure). As a result, infinite numbers of solutions exist for every value of the rake angle and shear stress. Further, Dewhurst concluded that the major theorems

## 2 Literature Survey

of engineering plasticity couldn't be applied to analyze machining due to the lack of defined boundary conditions. Also, if strain hardening is included, the solution is in principle poorer since the uniqueness theorem then does not apply to any steady-state process. Maity and Das (2001) applied Dewhurst's model to consider both slipping and sticking friction zones on the tool rake face. This model is possible to obtain statically as well as kinematically admissible solutions to the Kudo's slip line field (Kudo 1965) with the assumption of an elastic zone at the chip-tool interface. They showed that the stress boundary conditions can be satisfied by assuming an exponential distribution of normal stress in the elastic region. The method can introduce more realistic friction effect into the plastic slip line field.

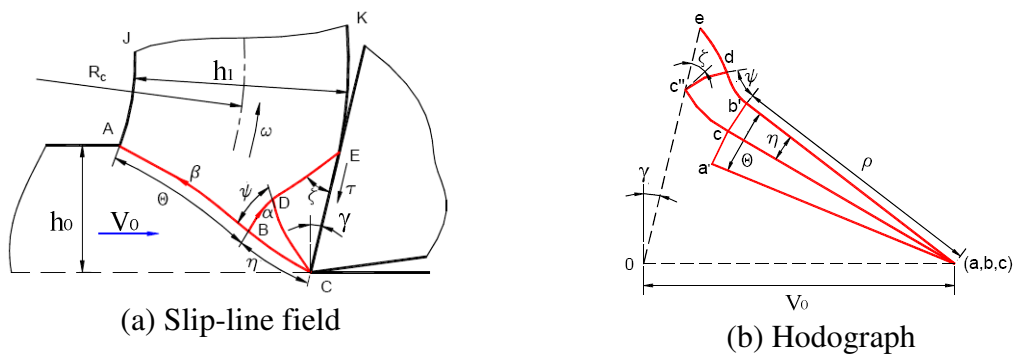


**Figure 2.6 Dewhurst model**

Dewhurst and Collins (1978) also developed a matrix technique for solving a certain class of mixed boundary value problems of slip line field. The procedure is based on power series representation of the solution of governing equations first used by Ewing (1967), and a vector representation of slip-lines and a system of matrix operators developed by Collins (1968, 1970). A universal slip line model and its associated hodograph for restricted contact machining have been presented by Fang et. al. (2001). It has been shown that the previously developed slip line models (Johnson (1962), Lee and



## 2 Literature Survey

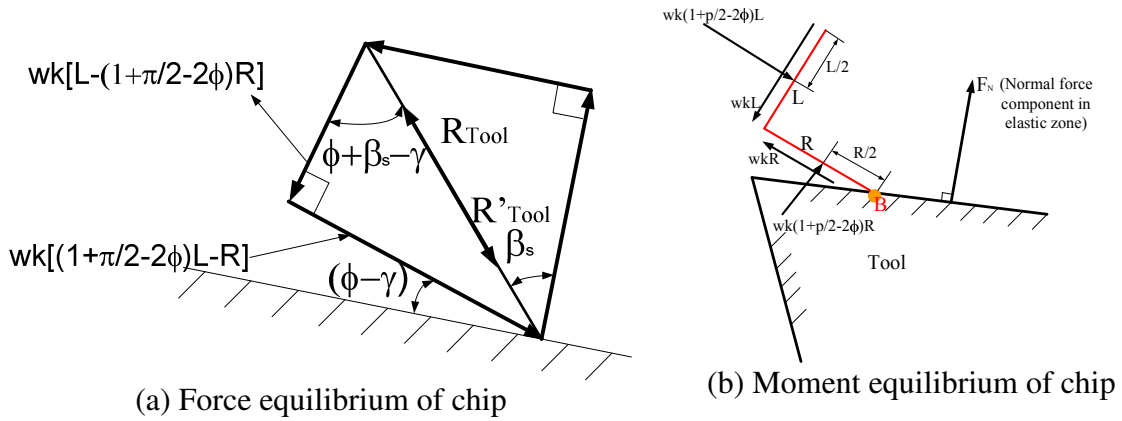


**Figure 2.8 Equilibrium of chip**

The relationship of  $R$ ,  $L$  and shear angle  $\phi$  is given by Yellowley (1987) as

$$\tan(\phi + \beta_s - \gamma) = \frac{(1 + \pi/2 - 2\phi) - (R/L)}{1 - (1 + \pi/2 - 2\phi)(R/L)} \quad (2.10)$$

In which  $\beta_s$  is the angle of friction in elastic contact zone on the rake face,  $R/L$  is the ratio of the height of the secondary deformation zone to the primary deformation zone.

The model is based on the fundamental mechanics of the process, (it satisfies force equilibrium, moment equilibrium, the known tribology of the sticking and sliding zones and stress continuity on the rake face).

### 2.2.3 Upper Bound Method

The upper bound theorem states that the rate of total energy associated with any kinematically admissible velocity field defines an upper bound to the actual rate of total energy required for the deformation (Bower 2010). Hence, for a given class of kinematically admissible velocity fields, the velocity field that minimizes the rate of total

## 2 Literature Survey

energy is the lowest upper bound, and therefore is nearest to the actual solution. Here, the kinematically admissible velocity field is used to denote a velocity field that satisfies the incompressibility requirement for a rigid-plastic material and the prescribed velocity boundary conditions. The best-known approach to machining using a similar methodology is that due to Merchant (1945) hence leading to a shear angle equation in the form (2.11).

$$\phi = \frac{\pi}{4} + \frac{\gamma}{2} - \frac{\beta}{2} \quad (2.11)$$

Rowe and Spick (1967) avoided the introduction of an elastic friction coefficient and were thus able to take a more conventional upper bound approach where the resultant force acting on the rake face is assumed to derive from plastic work. The resulting shear angle relationship is stated as

$$\cos \gamma \cdot \cos(2\phi - \gamma) - m \cdot \chi \cdot \sin^2 \phi = 0 \quad (2.12)$$

where  $m$  is the ratio of shear stress on rake face over the shear yield stress of the chip material during cutting,  $\chi$  is the ratio of uncut chip thickness and contact length on the rake face. DeChiffre (1977) in similar fashion, attempted to find a simpler expression by replacing the shear angle with the chip compression ratio and the friction coefficient by the chip contact length. This simplification yielded an expression that is equivalent to the one obtained by Rowe and Spick. Mittal and Juneja (1982) proposed a theoretical solution for the determination of shear angle for controlled contact orthogonal cutting based on Merchant's minimum energy approach. Stephenson and Agapiou (1997) provided a detailed discussion about minimum work and uniqueness assumptions applied to the cutting problem where they conclude that minimum work is an acceptable line of attack.

### 2.2.4 Material Separation

In the traditional approach, machining models account only for the energy consumed in the primary and secondary deformation zones. The energy used to separate the chip from the metal just ahead of the cutting tool tip is almost always ignored as being small, (based on simple surface energy calculations, Shaw 1997), that relating to flow around and under the edge is also usually ignored but has been addressed by several authors, (Masuko 1953; Albrecht 1960; Palmer and Yeo 1963; and Johnson 1967).

Recently, Atkins (2003, 2005, and 2006) has contended that the fracture terms are important in any cutting analysis. Atkins argued that ductile fracture mechanics can be used to explain chip formation in ductile metals by incorporating fracture toughness, (as the specific work of surface creation) into the machining model. This approach adds a constant term in the force expression that gives rise to the “so called” size effect in force, (as opposed to material strength). This approach was also shown to account for the observed trends in shear angles with decrease in uncut chip thickness. Atkins has gone further and suggested cutting as a way to establish fracture toughness values of materials (2005). Atkins (2005) cited the work associated with the chip separation criterion in finite element simulations of machining to be orders of magnitude different from that associated with chemical surface energy or solid surface tension, and comparable to fracture toughness values. Following this approach then the cutting force can be formulated as follows, (the final constant term in the equation corresponds to the work of surface creation)

$$F_c = \left( \frac{kh_0 w}{Q} \right) \frac{\cos \gamma}{\sin \phi \cdot \cos(\phi - \gamma)} + \frac{G_c w}{Q} \quad (2.13)$$

## 2 Literature Survey

where  $G_c$  is the fracture toughness,  $Q$  is a friction correction factor given by

$$Q = [1 - (\sin \beta \cdot \sin \phi / (\cos(\beta - \gamma) \cdot \cos(\phi - \gamma)))] \quad (2.14)$$

Wyeth (2009) applied Atkins's theory to investigate the orthogonal cutting of Nylon 66. It was shown that a better correlation was found with the inclusion of separation energy as proposed by Atkins (2003) with that of models did not consider the separation energy. Williams et al. (2010) and Patel et al. (2009) extended the fracture mechanics to study the case where the tool tip touches the crack tip and so obviate the need for cracks to precede the tool. Cutting analysis incorporating shear yielding on a slip plane in addition to fracture toughness  $G_c$  have been applied to cutting polymers. The results also show that the inclusion of the fracture energy  $G_c$  form a good base for describing data for cutting polymers.

### 2.2.5 Finite Element Modeling of Machining

The application of Finite Element (FE) models of the machining process aids in both qualitative and quantitative understanding of metal cutting behavior. The main advantage in using the finite element method is that various material models and complex boundary conditions can be simulated. The information delivered by the finite element simulation is more detailed than that obtained from analytical or mechanistic models. The FE models can simultaneously provide:

- 1) Detailed information on chip formation, shear angle, flow stress and interaction with the cutting tool;
- 2) Strain and strain rate during machining;
- 3) The temperature distribution in the chip/tool/workpiece interface;
- 4) Cutting forces;

## 2 Literature Survey

### 5) The stress distribution within the tool itself.

The difficulties of accurate FE modeling of cutting processes, even for conventional machining derive from the need to have detailed constitutive equations for the work material, and to have realistic contact conditions on the rake face. Clearly there will often be the need to iterate, and often effects such as strain gradients and history will be difficult to accommodate. The researcher must also decide upon a suitable chip separation criteria and FE modeling will be time consuming, because of the remeshing process. The accuracy of the results depends largely upon the representation of workpiece and tool material properties. Several authors have examined the extent of these difficulties. Jaspers and Dautzenberg (2002), Shi and Liu (2004) and Sartkulvanich et al. (2004) studied the effects of different material constitutive models. Sartkulvanich et al. (2005) published a flow stress database, known as Material Database for Machining Simulation (MADAMS), established with inputs from several research groups. Guo et al. (2005) proposed an internal state variable plasticity-based approach to predict the strain rate history and temperature effects. Pantale et al. (2004) adopted the damage constitutive law in models allowing defining advanced simulations of the tool's penetration into the workpiece and chip formation. Ozel and Zeren (2004, 2006) proposed an improved Oxley model to characterize work material flow stress and friction in the primary and secondary deformation zones around the cutting edge by utilizing orthogonal cutting tests. Iwata et al. (1984) proposed an equivalent strain criterion for simulating the crack propagation at the tool-tip. Ng et al. (2002) employed the conditional link element to simulate the tool-tip crack propagation. They showed importance of the failure and crack propagation criteria in FEM modeling of machining processes.

### 2.3 Oblique Cutting Models

Although the idealized orthogonal process is a close approximation to many actual machining operations, it is clear that many practical operations dictate the consideration of obliquity. The three-dimensional plastic flow in oblique cutting is considerably more complex than orthogonal cutting. Noteworthy attempts to extend the mechanics of orthogonal cutting to the oblique cutting process have been made by Merchant (1944), Stabler (1951), Shaw et al. (1952), Brown and Armarego (1964), Pal and Koenigsberger (1968), Zorev (1966), Spaans (1970), Morcos (1980), Lin et al. (1982), Hu et al. (1986), Rubenstein (1983), Lau and Rubenstein (1983), Vinuvinod and Jin (1995). Most of these analyses attempt to predict three important variables- chip flow angle, shear angle and forces. These in turn are functions of tool geometry and machining conditions such as rake angle, inclination angle, coefficient of friction etc. There has been an ongoing debate on the equivalent rake angle that would influence the mechanics of oblique machining similar to the rake angle in orthogonal machining. Some consider the velocity rake to be significant (Kronenberg 1966), while some others consider the effective rake to be significant (Shaw et al. 1952), while a third group considers the normal rake to be significant (Brown and Armarego (1964), Armarego and Brown (1969), and Armarego (2000)). The thin shear zone model for “classical” oblique cutting is an extension of the orthogonal case using similar assumptions. To derive relations for forces  $F_C$ ,  $F_T$ , and  $F_R$  in terms of stress in the shear plane, the following assumptions were made (Armarego and Brown 1969)

- 1) The tool tip is sharp and no rubbing or ploughing forces act on the tip;
- 2) The stress distributions on the shear plane are uniform;

## 2 Literature Survey

- 3) The resultant force  $R_{Tool}$  acting on the chip at the shear plane is equal, opposite and collinear to the force acting on the chip at the rake face.

As for orthogonal cutting the resultant force can be considered to act as two components in the shear plane ( $F_s$  and  $N_s$ ) and two components on the rake face ( $F_f$  and  $N$ ). The shear force  $F_s$  is inclined at the same direction of shear flow velocity ( $\eta_s$ ) in the shear plane. Similarly, the friction  $F_f$  is at the same direction of chip flow angle ( $\eta_c$ ) on the rake face. By resolving the resultant force in a plane perpendicular to the cutting edge and along the cutting edge, the following equations have been developed (Armarego 2000)

$$\begin{aligned}
 F_C &= \frac{kh_0w}{\sin \phi_N} \left( \frac{\cos(\beta_N - \gamma_N) + \tan i \cdot \tan \eta_c \cdot \sin \beta_N}{\sqrt{\cos^2(\phi_N + \beta_N - \gamma_N) + \tan^2 \eta_c \cdot \sin^2 \beta_N}} \right) \\
 F_T &= \frac{kh_0w}{\sin \phi_N \cdot \cos i} \left( \frac{\sin(\beta_N - \gamma_N)}{\sqrt{\cos^2(\phi_N + \beta_N - \gamma_N) + \tan^2 \eta_c \cdot \sin^2 \beta_N}} \right) \\
 F_R &= \frac{kh_0w}{\sin \phi_N} \left( \frac{\cos(\beta_N - \gamma_N) \cdot \tan i - \tan \eta_c \cdot \sin \beta_N}{\sqrt{\cos^2(\phi_N + \beta_N - \gamma_N) + \tan^2 \eta_c \cdot \sin^2 \beta_N}} \right)
 \end{aligned} \tag{2.15}$$

The shear angle and friction angle are given by

$$\tan \phi_N = \frac{r \cdot \left( \frac{\cos \eta_c}{\cos i} \right) \cos \gamma_N}{1 - \left( \frac{\cos \eta_c}{\cos i} \right) \sin \gamma_N}, \quad \tan \beta_N = \tan \beta \cdot \cos \eta_c \tag{2.16}$$

where  $r=l_c/l$  is chip length ratio,  $l_c$  is the chip length, and  $l$  is the length of cut (Song 2006). The collinearity condition provides a means of relating the force and velocities in oblique cutting. The condition assumes the friction force on the rake face is collinear to the chip velocity direction and that the shear force in the shear plane is collinear to the

## 2 Literature Survey

shear velocity direction. When the collinearity conditions are satisfied, the following equations must be met to find the chip flow angle  $\eta_c$  (Armarego 2000)

$$\tan(\phi_N + \beta_N) = \frac{\tan i \cdot \cos \gamma_N}{\tan \eta_c - \sin \gamma_N \cdot \tan i} \quad (2.17)$$

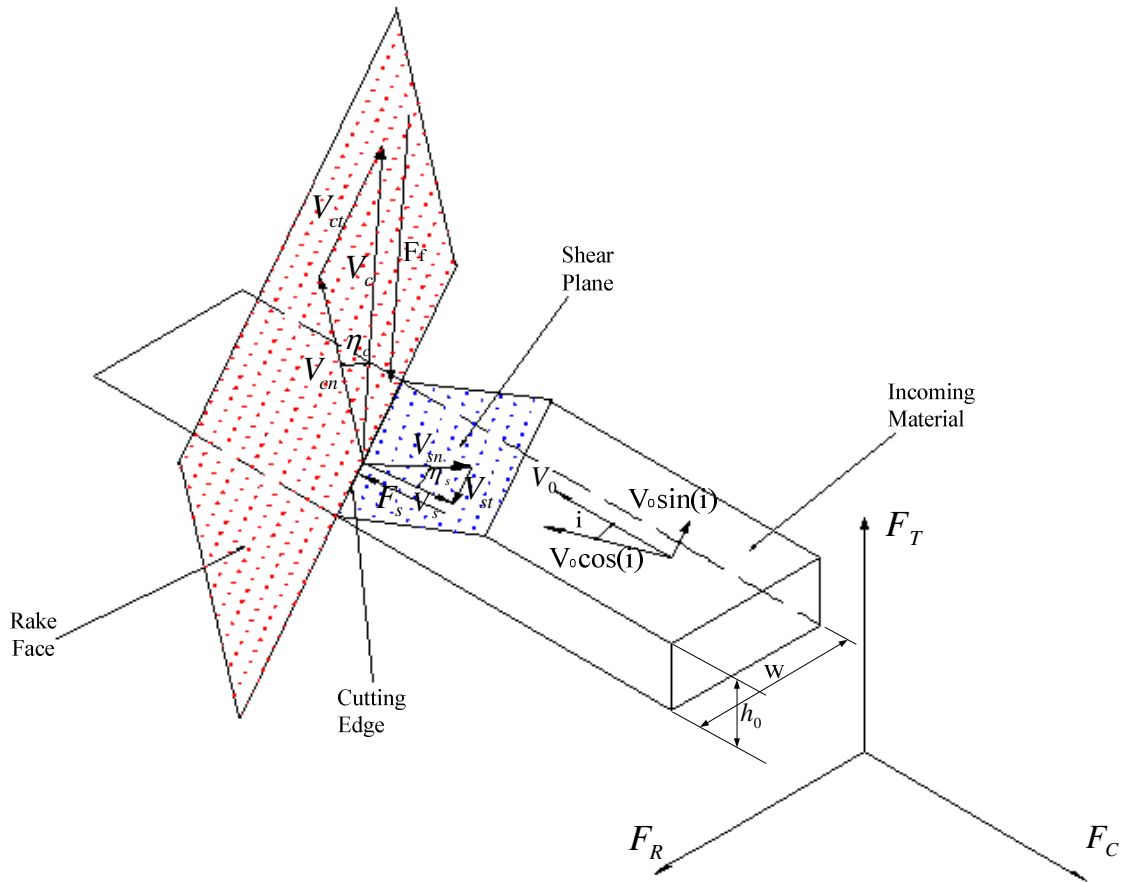


**Figure 2.9 Force in oblique cutting with single edge tool**

Predictive oblique cutting analyses have been proposed by Lin and Oxley (1972), Lin (1978), Lin et al. (1982) and Hu et al. (1986). They assumed that the flow in the plane normal to the cutting edge could be treated as plane strain deformation with the Oxley orthogonal cutting model being used to predict the chip geometry and the associated forces referred to this plane. To relate these values to the three-dimensional values, collinearity is assumed. The forces  $F_C$  and  $F_T$  can be determined from the

## 2 Literature Survey

orthogonal theory; based on Stabler's rule, the radial force  $F_R$  is then found as (Oxley 1989)

$$F_R = \frac{F_C (\sin i - \cos i \cdot \sin \gamma_N \cdot \tan \eta_c) - F_T \cos \gamma_N \cdot \tan \eta_c}{\sin i \cdot \sin \gamma_N \cdot \tan \eta_c + \cos i} \quad (2.18)$$

Eqn. (2.18) must be satisfied in order that the resultant cutting force lies in the plane normal to the tool cutting face that contains the resultant frictional force acting in the chip direction. A model of oblique cutting for viscoplastic materials was developed by Moufki et al. (2000, 2004). The thermomechanical properties and the inertia effects were accounted for so as to describe the material flow in the primary shear zone. The results show that a good correlation with the experimental measurements.

Some authors have also pursued an energy approach or traditional upper bound methods to oblique cutting (Usui et al. 1978; Usui and Hirota 1978; Tai et al. 1994; Chang 1998; Fuh and Change 1995; Stephenson and Wu 1988; Shamoto and Altintas 1999; Seethaler and Yellowley 1997 and Sedeh et al. 2002, 2003, 2004). Traditional upper bound analyses of oblique cutting generally make an assumption to calculate the friction area at the chip-tool interface. Seethaler and Yellowley (1997) proposed a methodology to calculate the area of cut on the rake face by obeying force equilibrium, which results in

$$A_f = \frac{A_s \sin \beta_e}{\cos(\phi_e - \gamma_e + \beta_e)} \quad (2.19)$$

where  $A_f$  is the area of chip plastic deformation on the rake face,  $A_s$  is the area of shear plane.

The effective rake angle  $\gamma_e$  and effective shear angle  $\phi_e$  are measured in the plane containing the cutting direction and chip flow direction. The friction angle  $\beta_e$  depends on

## 2 Literature Survey

the material properties and on the amount of work hardening present. In the absence of work-hardening and the presence of sticking friction, it can be written as (Seethaler and Yellowley 1997)

$$\tan \beta_e = \frac{1}{1 + \pi/2 - 2\gamma_e} \quad (2.20)$$

The optimized unknown parameters are the magnitude of chip velocity and chip flow angle  $\eta_c$ . Sedeh et al. (2002, 2003, 2004) extended Seethaler and Yellowley's approach to sharp corner and flat face nose radius tools and introduced a robust approach for calculation of the uncut chip area.

### 2.4 Analysis of Practical Milling Tools

The two most common milling processes found in production are face milling and peripheral milling (or end milling). Figure 2.10 and 2.11 show the difference between these two types. The symbols for face milling shown in Figure 2.10 are described as

$F_t$	Tangential force	$R$	Tool radius
$F_{th}$	Thrust force	$a$	Axial depth of cut
$F_r$	Radial force	$S_t$	Feed per tooth
$F_z$	Axial force	$\psi$	Cutter rotation angle
$F_x$	Feed force	$\psi_1$	Entry angle
$F_y$	Normal force	$\psi_2$	Exit angle
$T_c$	Cutting torque	$\psi_s$	Swept angle
		$\Psi_e$	Chip flow angle

## 2 Literature Survey

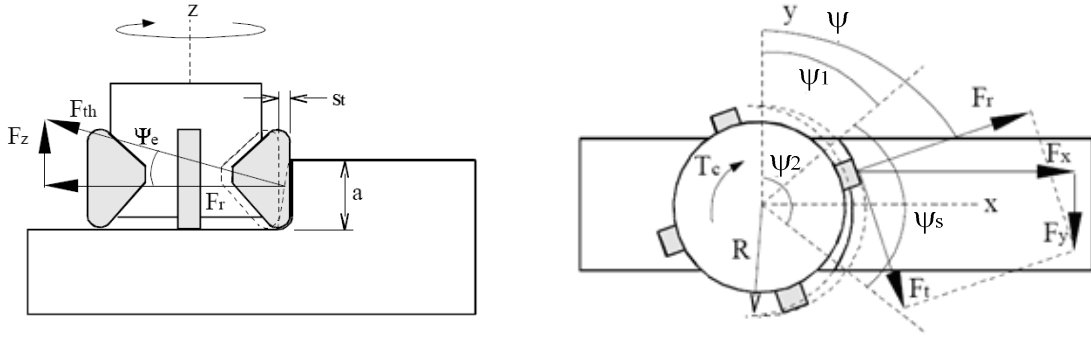


**Figure 2.10 Face milling geometry**

Figure 2.11 shows the workpiece geometry for end milling with the following symbols:

$i$	Helical angle	$D$	Tool diameter
$a$	Axial depth of cut	$d$	Radial depth of cut
$S_t$	Feed per tooth	$\Omega$	Spindle speed
		$\psi$	Cutter rotation angle

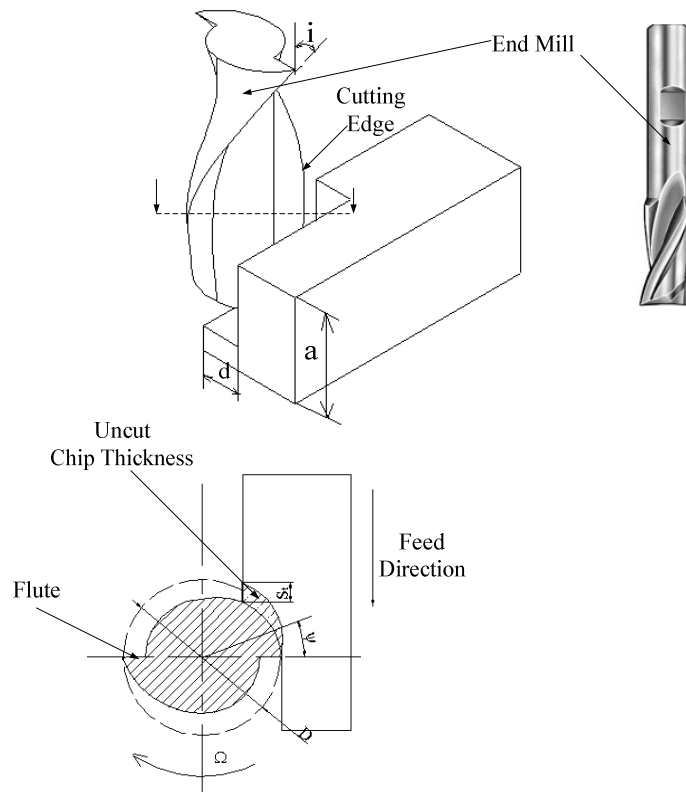


**Figure 2.11 End milling geometry**

## 2 Literature Survey

Face milling generates a surface that is perpendicular to the axis of cutter rotation; in the usual case the cutter both enters and exits the workpiece with a finite chip thickness and the axial depth of cut is relatively low. End milling cutters have cutting edges located on both the end of face of the cutter and (usually in helical form) on the periphery of the cutter body; they usually have relatively high depths of cut and may often be used with little or no end/face cutting. Normal peripheral or end milling can be classified as up milling and down milling (see Figure 2.12). In up milling, the cutter enters with zero chip thickness and exits with a chip thickness which is dependent upon the width of cut and cutter radius. In down milling, the cutter exits with zero chip thickness. For small widths of cut this leads to very different force directions and the mechanics of cutting can be quite different, as one approaches widths close to the cutter diameter then the processes become similar.

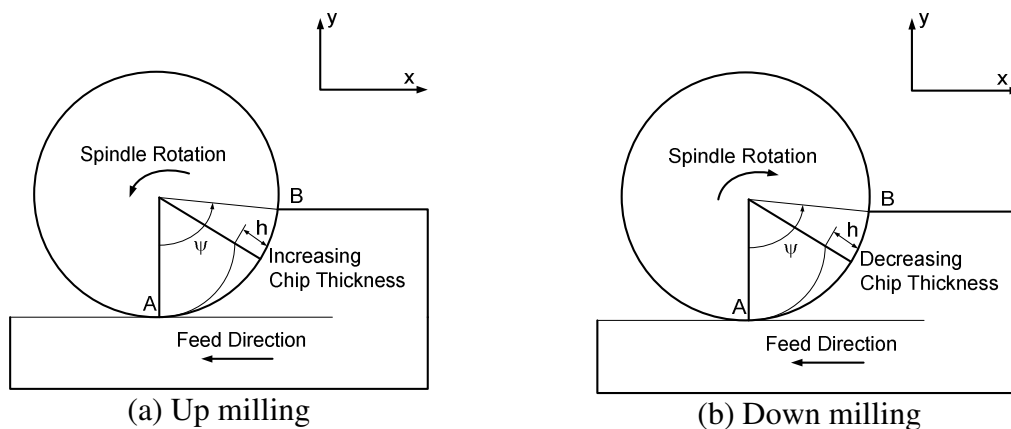


**Figure 2.12 Milling types**

The earliest analysis of the kinematics of milling processes was carried out by Martellotti (1941). Martellotti showed that the true path of milling cutter path is trochoidal and the equations describing the tooth path are given by

## 2 Literature Survey

$$\begin{cases} x = \pm \frac{N_f S_t}{2\pi} \psi + R \sin \psi \\ y = R(1 - \cos \psi) \end{cases} \quad (2.21)$$

where  $x$  and  $y$  are the coordinates of a point along the cutter path,  $N_f$  is the number of cutter teeth, the plus and minus signs apply to up and down milling, respectively.

Martellotti showed that the tooth path is almost circular for light feeds, and the circular tooth path approximation may be invoked if the radius of the cutter is much larger than the feed per tooth. This approximation simplifies the analysis of the process, and in practice, the necessary conditions of the radius being larger than the feed per tooth is usually satisfied. Using this approximation the formulation of the chip thickness can be derived as (Martellotti 1941)

$$h = S_t \cdot \sin \psi \quad (2.22)$$

### 2.4.1 Modeling of Milling Forces

The forces acting upon a single straight tooth in up and down milling are shown in Figure 2.13. It is customary to resolve the radial and tangential force components parallel to the feed direction ( $x$ ) and perpendicular to the feed ( $y$ ). In the simplest case it is assumed that the tangential component may be calculated by multiplying the instantaneous area of cut by the specific cutting pressure ( $K$ ) and that the radial component will be proportional to the tangential component (the constant  $r$  is often used to denote the ratio of radial to tangential components). Some authors have assumed these parameters to be functions of chip thickness (Koenigsberger and Sabberwal 1961; Fu et al. 1984; Kapoor et al. 1998; Ranganath et al. 2007; Feng and Su 2001). Since the chip thickness in peripheral milling is generally very low then it would seem logical, as a first

## 2 Literature Survey

improvement on a linear model of cutting forces, to consider the edge forces, (nose and flank), which are known to constitute a significant proportion of total forces at such conditions (Zorev 1966; Spaans 1970; Yellowley 1985; Armarego 2000). For steady state cutting, the instantaneous tangential and radial forces acting on a straight single tooth-milling cutter are given by (Yellowley 1985, 1988)

$$\begin{cases} F_t = KaS_t \left( \sin \psi + \frac{h^*}{S_t} \right) \\ F_r = KaS_t \left( r_1 \sin \psi + r_2 \frac{h^*}{S_t} \right) \end{cases} \quad (2.23)$$

where  $r_1$  and  $r_2$  are the tangential to radial cutting forces ratios of the cutting and parasitic components, respectively. The parameters  $K$ ,  $r_1$ ,  $r_2$  and  $h^*$  are assumed to be constant for a tool-workpiece pair. The empirical parameters  $K$  and  $r_1$  contain the information regarding the work material's shear yield stress, coefficient of friction, shear angle and the tool geometry, while parameters  $r_2$  and  $h^*$  are related to the ratio of energy consumption in the nose area and the remainder, as well as the stress situation which is quite different from rake to clearance faces. The torque is related to the tangential force component through the radius of the cutter

$$T_C = R \cdot F_t \quad (2.24)$$

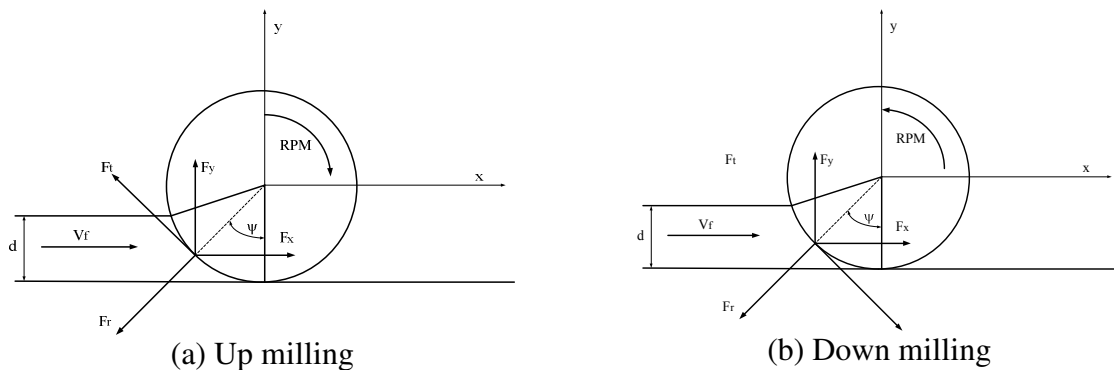


**Figure 2.13 Milling forces**

## 2 Literature Survey

To decompose the cutting forces  $F_t$  and  $F_r$  into the  $x$  and  $y$  directions, the instantaneous cutting forces in the  $x$  and  $y$  directions with a single cutting edge can be expressed as

(a) Up milling

$$\begin{aligned} F_x &= F_t \cos \psi + F_r \sin \psi \\ F_y &= F_r \cos \psi - F_t \sin \psi \end{aligned} \quad (2.25)$$

(b) Down milling

$$\begin{aligned} F_x &= F_r \sin \psi - F_t \cos \psi \\ F_y &= F_r \cos \psi + F_t \sin \psi \end{aligned} \quad (2.26)$$

The periodic, intermittent nature of the cutting force in milling lends itself to frequency domain analysis. The convention for representing cutting forces in milling operations can be written as (Yellowley 1985)

$$\begin{aligned} F_t &= KaS_t \left[ a_0 + \sum_{k=1}^{\infty} (a_k \cos k\psi + b_k \sin k\psi) \right] \\ F_x &= KaS_t \left[ a_{x0} + \sum_{k=1}^{\infty} (a_{xk} \cos k\psi + b_{xk} \sin k\psi) \right] \\ F_y &= KaS_t \left[ a_{y0} + \sum_{k=1}^{\infty} (a_{yk} \cos k\psi + b_{yk} \sin k\psi) \right] \end{aligned} \quad (2.27)$$

The equivalent Fourier series for the cutting force  $F_x$  and  $F_y$  in helical end milling cutter can be expressed in the form of

## 2 Literature Survey

$$\begin{aligned}
 F_x &= \frac{1}{k_\beta} \int_0^\alpha \{a_{x0} + \sum_{k=1}^{\infty} [a_{xk} \cos(k(\psi + \alpha_1)) + b_{xk} \sin(k(\psi + \alpha_1))]\} d\alpha_1 \\
 &= a \left[ ah_{x0} + \sum_{k=1}^{\infty} (ah_{xk} \cos k\psi + bh_{xk} \sin k\psi) \right] \\
 F_y &= \frac{1}{k_\beta} \int_0^\alpha \{a_{y0} + \sum_{k=1}^{\infty} [a_{yk} \cos k(\psi + \alpha_1) + b_{yk} \sin k(\psi + \alpha_1)]\} d\alpha_1 \\
 &= a \left\{ ah_{y0} + \sum_{k=1}^{\infty} [ah_{yk} \cos k\psi + bh_{yk} \sin k\psi] \right\}
 \end{aligned} \tag{2.28}$$

where

$$\alpha = \frac{a \cdot \tan \eta}{R}, \quad k_\beta = \frac{\tan i}{R} \tag{2.29}$$

These equations indicate that it is possible to relate the Fourier coefficients of helical cutter to the Fourier coefficients of an equivalent straight cutter as follows

$$\begin{aligned}
 ah_{x0} &= a_{x0}, \quad ah_{xk} = \frac{a_{xk}}{k\alpha} \sin k\alpha + \frac{b_{xk}}{k\alpha} (1 - \cos k\alpha) \\
 bh_{xk} &= \frac{b_{xk}}{k\alpha} \sin k\alpha - \frac{a_{xk}}{k\alpha} (1 - \cos k\alpha)
 \end{aligned} \tag{2.30}$$

and

$$\begin{aligned}
 ah_{y0} &= a_{y0}, \quad ah_{yk} = \frac{k\alpha}{2} \left( a_{yk} \frac{\sin k\alpha}{1 - \cos k\alpha} - b_{yk} \right) \\
 bh_{yk} &= \frac{k\alpha}{2} \left( a_{yk} + b_{yk} \frac{\sin k\alpha}{1 - \cos k\alpha} \right)
 \end{aligned} \tag{2.31}$$

It should be pointed out that the period of the fundamental frequency of the Fourier series is at the spindle rotation frequency.

Gygax (1980) developed a convolution operator for the multi-tooth milling force analysis in the frequency domain. Yellowley et al. (1992), Seethaler (1997) have used frequency domain analysis of milling forces in order to arrive at efficient identification techniques for swept angles of cut and wear from in-situ measured cutting forces.

Seethaler and Yellowley (1999), Zheng et al. (1997) and Wang and Huang (2004) applied frequency domain analysis to estimate the cutter runout in milling operations.

### 2.4.2 Modeling of Ploughing Forces

In practice no tool is perfectly sharp and the cutting edge always has a finite radius with corresponding forces acting at the cutting edge. In addition wear and deformation of the cutting edge will cause additional forces to exist in this region. Because these forces are not considered to contribute to the chip removal process they may be collectively referred to as the ploughing force. Since it is extremely difficult to measure the ploughing force directly, indirect methods have been used to estimate its magnitude, e.g. the extrapolation method (Zorev 1966). Figure 2.14 shows a scheme of forces acting on the rake face and flank surfaces of a free-cutting tool, the normal force  $N$  and the tangential force  $F$ , which together give the resultant force  $R_{Tool,s}$ , act on rake face  $OB$ . The normal force  $N_{cf}$  and the tangential force  $F_{cf}$ , which together give the resultant  $R_{Tool,cf}$ , act on the clearance surface  $OA$ .

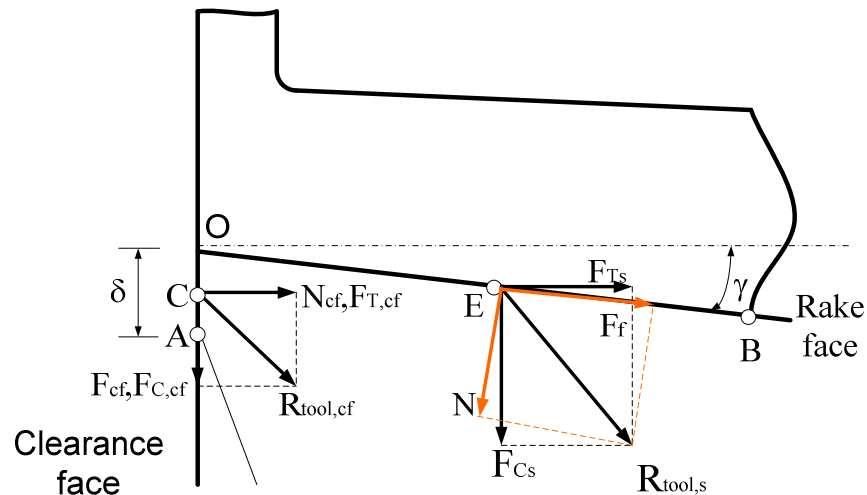


Figure 2.14 Scheme of forces acting on the face and flank surface of the tool

## 2 Literature Survey

Force  $R_{Tool,s}$  and  $R_{Tool,cf}$  added together give the cutting and thrust forces as

$$\begin{aligned} F_C &= F_{CS} + F_{C,cf} \\ F_T &= F_{TS} + F_{T,cf} \end{aligned} \quad (2.32)$$

where  $F_{CS}$  and  $F_{TS}$  are the projections of the force  $R_{Tool,s}$  onto the vertical and horizontal force on the tool face;  $F_{C,cf}$  and  $F_{T,cf}$  are the projections of the force  $R_{Tool,cf}$  on the vertical and horizontal projections of the force acting on the clearance surface, or so called edge force. It is possible to find the tangential and normal forces on the clearance surface by extrapolating the experimentally obtained relationships for the vertical and horizontal projections of the cutting force with varying depths of cut. It is noted that the extrapolating methods require maintaining shear angle  $\phi$  constant when varying uncut chip thickness to find edge forces.

Endres et al. (1995) proposed a dual-mechanism approach to address the chip removal and edge ploughing mechanisms. The geometry local to the cutting edge and along the clearance face is shown in Figure 2.15a, which includes primary, secondary and tertiary shear zones. The geometric relations of the dual-mechanism approach can be visualized using a diagram similar to that of Merchant's (1944) force circle diagram represented by Masuko (1953) and Albrecht (1960). The dual-mechanism approach is shown in Figure 2.15b and displays the forces as follows

$$N = K_f A_c, F_f = \mu N \quad (2.33)$$

and

$$N_{cf} = K_{cf} V_i, F_{cf} = \mu_{cf} N_{cf} \quad (2.34)$$

where  $K_f$  and  $\mu$  are the rake face force coefficient and friction, respectively.  $K_{cf}$  and  $\mu_{cf}$  are the normal and friction coefficients on a clearance face;  $V_i$  is the interference volume.

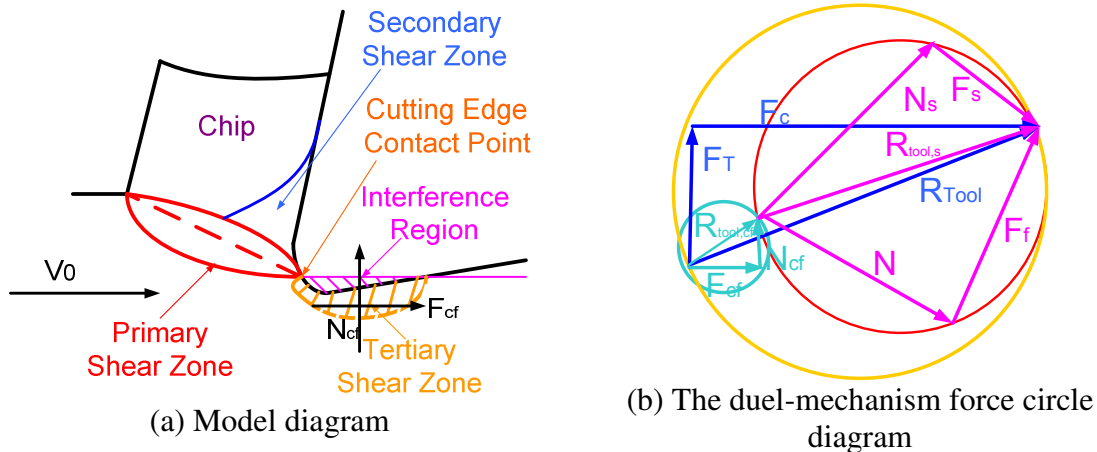


**Figure 2.15 Endres' dual-mechanism approach**

Shi and Ramalingam (1991) proposed a slip-line field for orthogonal cutting with chip breaker and flank wear. For a worn tool, the slip-line field includes a primary deformation zone with finite thickness; two secondary shear zones, one along the rake face and the other along the flank face; a predeformation zone; a curled chip and a flank face system. Fang (2003) presented a comprehensive slip-line model for machining with a round edge tool based upon the flat material flow theory (without stable built-up edge). In this model, the entire region of chip formation is composed of three shear zones (termed as the primary, secondary, and tertiary shear zones), three transition regions, and a material “pre-flow” region as shown in Figure 2.16. The tertiary shear zone is directly caused by the rounded edge of the tool. The round cutting edge BN is approximated by two straight chords SB and SN to simplify the mathematical formulation. Point S is the stagnation point of flow of material. The entire slip-line field is divided into 27 sub-regions; since the model accounts for the chip up-curling effect; the slip-lines are curved with different slip-line angles that introduce numerous model coefficients that need to be





## 2 Literature Survey

The forces in this model are determined from the forces acting along the shear plane (line AB), and the bottom of the build-up region (line CA). The stresses in the slip-line field are found based on the equilibrium conditions that require

$$p + 2k\psi = \text{const} \quad (2.37)$$

along an  $\alpha$  slip-line, and

$$p - 2k\psi = \text{const} \quad (2.38)$$

along a  $\beta$  slip-line where  $p$  is the hydrostatic pressure and  $\psi$  is the counter-clockwise angle through which the slip-line has rotated. Since no normal or tangential stresses act on the free surface,  $p$  is equal to  $k$  on that surface. The slip-line has rotated by  $-\xi$  on the shear plane, resulting in

$$p = k(1 + 2\xi) \quad (2.39)$$

Along CA, the slip-lines have rotated by  $-(\xi + \delta)$  resulting in

$$p = k(1 + 2\xi + 2\delta) \quad (2.40)$$

The shearing forces in the cutting (parallel to  $V_0$ ) and thrust (normal to  $V_0$ ) directions are determined from the shear angle  $\phi$  and Eqn. (2.37)

$$\begin{aligned} F_{Cs} &= \frac{kh_0w}{\sin\phi} [\cos\phi + (1 + 2\xi)\sin\phi] \\ F_{Ts} &= \frac{kh_0w}{\sin\phi} [(1 + 2\xi)\sin\phi - \cos\phi] \end{aligned} \quad (2.41)$$

The forces along CA are found to be

$$\begin{aligned} F_{CP} &= \frac{k\omega R}{\sin\eta} [\cos 2\eta \cdot \cos(\phi - \delta + \eta) + (1 + 2\xi + 2\delta + \sin 2\omega) \cdot \sin(\phi - \delta + \eta)] \\ F_{TP} &= \frac{k\omega R}{\sin\eta} [(1 + 2\xi + 2\delta + \sin 2\eta) \cdot \cos(\phi - \delta + \eta) - \cos 2\omega \cdot \sin(\phi - \delta + \eta)] \end{aligned} \quad (2.42)$$

The total cutting and thrust forces can then be found

## 2 Literature Survey

$$\begin{aligned} F_C &= F_{Cs} + F_{CP} \\ F_T &= F_{Ts} + F_{TP} \end{aligned} \quad (2.43)$$

Based on Connolly and Rubenstein's (1968) cutting model, Manjunathaiah and Endres (2000) set up a simple geometrical and machining force model to include the edge radius effect by conducting a force balance on the lower boundary of the deformation zone, as shown in Figure 2.19. It employs a shear zone instead of a shear plane and includes the deformation region below the tool edge radius. This model calculates strain and strain rate, and in the force prediction it includes an explicit effect of the ploughing component due to edge radius. The force prediction, in the model, does not treat the chip formation force component and ploughing force component as independent of each other like many researchers (Masuko, 1953; Albrecht, 1960; Endres et al., 1995; Waldorf et al. 1995), but couples the two components through the shear angle  $\phi$ . Therefore, an increase of the force, due to the increase in edge radius, is not completely attributed to the ploughing mechanism, but partly also because of an increased chip formation force arising from a smaller shear angle.

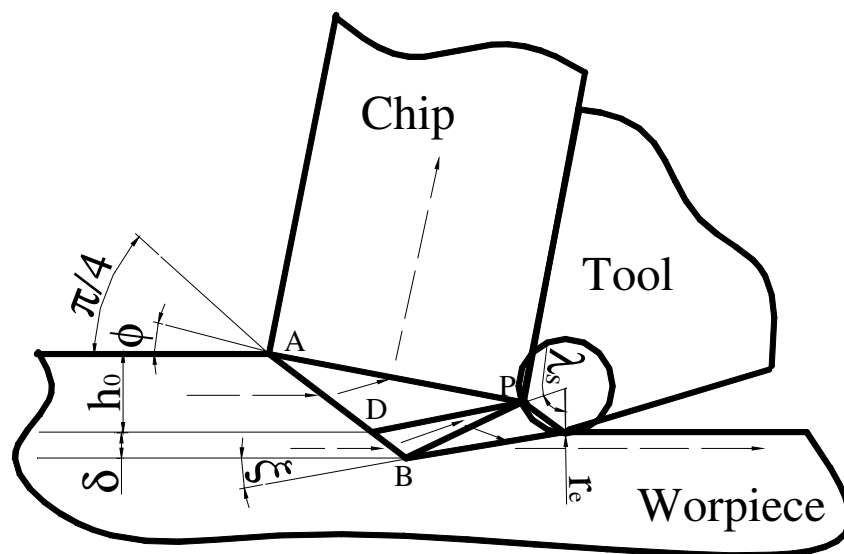


**Figure 2.19** Manjunathaiah and Endres's geometric model of edge radius tool (2000)

### 2.5 Conclusions

The effects of ploughing or rubbing due to rounded cutting edges and worn tools have been shown to significantly affect process outputs such as part quality and cutting forces. The ploughing phenomenon has generated considerable research aimed at gaining a fundamental understanding of the mechanisms involved. The majority of the modeling efforts have concentrated on the application of slip line fields. The basic problem with most slip line field applications to metal cutting has been the need to either ignore elastic contact or to incorporate this in an approximate way with the plastic zone. The extension of fields around the nose of the tool is even more challenging since in this region one has a singularity due to separation, and the strain, strain rate and temperature distributions on each side of the boundary between chip and finished surface are difficult to estimate. An early attempt to model the nose region was proposed by Oxley (1989) and further developed by Zhang et al. (1991), and Ren and Altintas (2000) for the analysis of chamfer tools. The metal flow resulting from the field, originally developed for the analysis of polishing operations, leads to the necessity to allow a second “chip” to exit below the tool, (the field exit velocity is not that of the work). Waldorf et al. (1998) developed a later slip line field which accommodates the ploughing action at the tool edge. The geometry of the field includes a raised prow and a stable build-up of workpiece material adhered to the cutting edge which acts to divert the coming flow either into the chip or into the workpiece. The model requires extensive experiments to calibrate unknown parameters. Manjunathaiah and Endres (2000) extended Connolly and Rubenstein’s (1968) sharp tool model to the analysis of rounded edge tools. The geometry of the zone in this case is very approximate, (it is not a slip line field), and

## 2 Literature Survey

hence some of the assumptions regarding (normal) stress on the boundaries can be questioned. Not surprisingly then, (again), significant experimental data is required to calibrate the model. Given the previous comments, the author believes that there is value in examining the extension of a thick zone slip line field model which includes elastic contact forces to incorporate flow under the tool edge.

Most of the oblique cutting models in the literature concentrated on force equilibrium, using orthogonal cutting as a base and very often by defining the equivalent parameters as a convenience in understanding this more complex process. Some researchers have also pursued an upper bound approach. There is a split between the more conventional UB approach and those that use the notion of apparent friction coefficient to give solution that parallels the Merchant solution of orthogonal cutting. If one wishes to obviate the need to use the apparent friction coefficient in the UB approach, one must use a force balance to obtain the area of cut on the rake face. The disadvantage to the latter approach is the need to estimate normal stress on the tool rake face. It would seem that the increased complexity of oblique cutting could be used to advantage here through the balancing of shear stresses along the tool edge to achieve the same result with more realistic assumptions.

Considerable progress has been made in the calculation of the forces acting upon helical milling cutters based on both the empirical and mechanistic approaches. The author believes that there is still scope to examine the important entry and exit processes and to examine the role that the non-straight cutting edge will exert through the added kinematic constraint on chip flow.

## **3 A New Approach to the Modeling of Oblique Cutting Processes**

### **3.1 Introduction**

The majority of practical cutting tools have both non-straight cutting edges and non-planar rake faces. It is of great importance to build an oblique cutting model to be able to analyze such complex kinematically constrained tools (primarily milling, drilling, and tapping operations). This chapter describes a new upper-bound model that incorporates force equilibrium parallel to the cutting edge for the oblique cutting operations. In addition to the normal shear angle, two new fundamental variables *RATIO* (force-based variable) and *SLIP* (kinematic variable) are introduced to characterize the energy requirements of the oblique cutting processes. Calibration of the model for either real time identification purposes or for process planning/optimization requires experimental data but no shear angle data. This is very important for complex milling, drilling and tapping operations, since these operations will not yield geometry data for determining shear angle. The relationships among major parameters over a wide range of obliquity and normal rake angles are discussed. Finally, this chapter demonstrates the success of the model using existing experimental data.

### **3.2 Analysis**

Traditional Upper Bound analyses of oblique cutting utilize the normal shear angle, the angle of chip flow in the rake face and the apparent coefficient of friction on the rake face. The energy approach to be presented here utilizes force equilibrium to determine the friction area/force on the rake face; the approach was first suggested by

### 3 A New Approach to the Modeling of Oblique Cutting Processes

Seethaler and Yellowley (1997) and extended by Sedeh et al (2002, 2004). Fortunately the oblique cutting process allows force equilibrium to be applied directly in the direction parallel to the cutting edge, (in essence now comparing shearing forces on the shear and rake faces and so there is no need to make uncomfortable assumptions regarding rake face normal stress as is necessary in the simpler case of orthogonal cutting).

The energy approach is framed in terms of the normal shear angle and the following two variables that derive directly from force and kinematic considerations:

*SLIP* is the ratio of the edgewise shear velocity imparted to the chip on the shear plane parallel to the cutting edge versus the incoming velocity along the cutting edge. It is expected that improving efficiency on the rake face will reduce *SLIP* and lead to higher chip velocities; a *SLIP* of unity implies that the chip flows perpendicular to the tool edge.

*RATIO* is the ratio of the friction force on the rake face to the resultant shearing force on the shear plane. *RATIO* is a complicated variable that needs to be determined experimentally. *RATIO* is dependent upon material properties at the relevant conditions on each plane, as well as the stress distributions on these planes and the elastic contact conditions of the rake face.

$$SLIP = \frac{V_{st}}{V_0 \sin i}, \quad RATIO = \frac{F_f}{F_s} \quad (3.1)$$

The power consumed in oblique cutting is given by

$$P = k \cdot A_s \cdot V_s + k \cdot RATIO \cdot A_s \cdot V_c \quad (3.2)$$

where  $A_s$  is the area of the shear plane,  $V_s$  is the resultant shear velocity on the shear plane,  $V_c$  is the resultant chip velocity on the rake face. The shear area  $A_s$  is derived as

$$A_s = \frac{wh_0}{\sin \phi_N \cdot \cos i} \quad (3.3)$$

### 3 A New Approach to the Modeling of Oblique Cutting Processes

where  $w$  is the width of cut,  $h_0$  is the depth of cut.

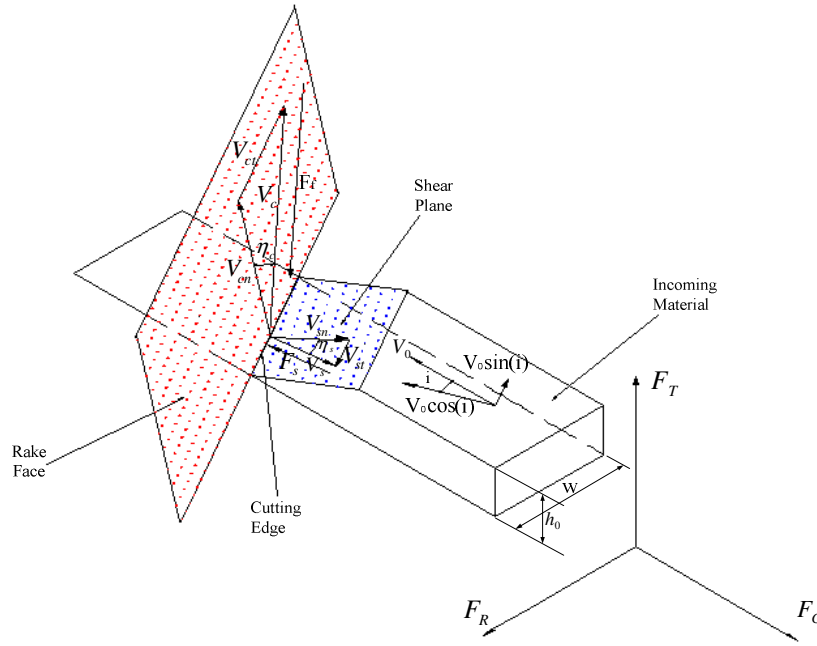


**Figure 3.1** The oblique cutting process

The resultant velocities and components on the two planes (see Figure 3.1) are given as follows:

$$\begin{aligned} V_{cn} &= \frac{V_0 \cos i \cdot \sin \phi_N}{\cos(\phi_N - \gamma_N)}, & V_{ct} &= (1 - SLIP) \cdot V_0 \sin i \\ V_{sn} &= \frac{V_0 \cos i \cdot \cos \gamma_N}{\cos(\phi_N - \gamma_N)}, & V_{st} &= SLIP \cdot V_0 \sin i \end{aligned} \quad (3.4)$$

where  $i$  is the inclination angle,  $\phi_N$  is the normal shear angle, and  $\gamma_N$  is the normal rake angle.

The power consumed in the process is assumed to be a minimum and an upper bound solution for the normal shear angle in terms of tool geometry, *SLIP* and *RATIO* obtained. In this case however it is necessary to be able to estimate either the area of contact on the rake face, or the *RATIO* directly. Rather than make an estimate based on

### 3 A New Approach to the Modeling of Oblique Cutting Processes

approximate normal stress as suggested by Seethaler and Yellowley (1997), one can simply balance force in the direction of the tool edge, this results in

$$F_{\tan} = k \cdot A_s \sin \eta_s = k \cdot A_c \cdot \sin \eta_c \quad (3.5)$$

Thus

$$RATIO = \frac{\sin \eta_s}{\sin \eta_c} = \frac{V_{st} V_c}{V_{ct} V_s} = \frac{SLIP}{(1 - SLIP)} \frac{V_c}{V_s} \quad (3.6)$$

where  $A_s$  and  $A_c$  are the area of plastic deformation on the shear plane and rake face, respectively and where  $\eta_s$  and  $\eta_c$  are the shear flow and chip angle angles, respectively.

Given the relationship between forces and velocities derived in equation (3.6) then the power requirements of the process may be rewritten as follows:

$$P = F_s \cdot V_s + F_f \cdot V_c = V_s F_s \left(1 + \frac{(1 - SLIP)}{SLIP} RATIO^2\right) \quad (3.6)$$

The ratio of rake face work to shear plane work is then given by

$$R_w = \frac{(1 - SLIP)}{SLIP} RATIO^2 \quad (3.7)$$

It is well known that in orthogonal cutting the ratio of work is remarkably constant. The only influence being seen through normal rake angle (Zorev 1966).

The upper-bound problem can be mathematically defined as the dual problem which seeks the smallest value of  $P(SLIP, \phi_N)$ . The problem was formulated as a constrained minimization problem as follows

$$\begin{aligned} &\text{Minimize} && P(SLIP, \phi_N) \\ &\text{Subject to:} && RATIO = \frac{V_{st} \cdot V_c}{V_{ct} \cdot V_s} \\ &&& 0 \leq \phi_N \leq \frac{\pi}{4} + \frac{\gamma_N}{2} \\ &&& 0 \leq SLIP \leq 1 \end{aligned} \quad (3.8)$$

### 3 A New Approach to the Modeling of Oblique Cutting Processes

where the constraint  $0 \leq \phi_N \leq \frac{\pi}{4} + \frac{\gamma_N}{2}$  was suggested by Brown and Armarego (1964); the maximum normal shear angle  $(\frac{\pi}{4} + \frac{\gamma_N}{2})$  corresponds to the frictionless case.

The nonlinear optimization was carried out using Maple (2010). The tolerance allowed on the objective function was  $10^{-9}$ , while the tolerance on the state variables (*SLIP* and  $\phi_N$ ) was  $10^{-6}$ .

It would be advantageous, for real time applications, if it was possible to obtain a solution for the Upper Bound problem without resort to a general purpose non-linear optimization process. The major difficulty with seeking a closed form solution is that of the defining of variables in such a manner as to be able to define their relationship with the normal shear angle. In the model described here it is assumed that the *SLIP* is constant for one workpiece-tool pair but that *RATIO* will have a relationship with both normal rake angle and with the shear angle. (The data available reveals that *RATIO* varies relatively little with shear angle but one should still account for the non-zero nature of the derivative in the formulation). Since the lateral force balance is always an active constraint to the optimization then in this case the best manner of modeling *RATIO* through the examination of this constraint may be determined.

At small values of inclination angle the resultant velocities on the shear plane and rake face are approximately equal to the normal components, thus in this case

$$\frac{V_c}{V_s} \approx \frac{V_{cn}}{V_{sn}} = \frac{\sin \phi_N}{\cos \gamma_N} \quad (3.9)$$

or

$$RATIO \approx \frac{SLIP}{(1 - SLIP)} \frac{\sin \phi_N}{\cos \gamma_N} \quad (3.10)$$

### 3 A New Approach to the Modeling of Oblique Cutting Processes

Then friction force  $F_f$  can be approximated as

$$F_f \approx \frac{SLIP}{(1 - SLIP)} \frac{k \cdot w \cdot h_0}{\cos i \cdot \cos \gamma_N} \quad (3.11)$$

So it is expected that the rake face resultant force must be simply proportional to the uncut chip area.

For large values of inclination angle  $i$  ( $i \geq 30^\circ$ ), the situation is more complex, the relationship between  $V_c$  and  $V_s$  can be written as

$$\left[ \frac{V_c}{V_s} \right]^2 = \left\{ \frac{[SLIP \cdot \sin i]^2 + \left[ \frac{\cos i \cdot \sin \phi_N}{\cos(\phi_N - \gamma_N)} \right]^2}{[(1 - SLIP) \cdot \sin i]^2 + \left[ \frac{\cos i \cdot \cos \gamma_N}{\cos(\phi_N - \gamma_N)} \right]^2} \right\} \quad (3.12)$$

In this case there are large and constant tangential force components acting on both the shear plane and rake face, as a result the ratio of resultant velocities varies little and the assumption can be made as follows

$$\left[ \frac{V_c}{V_s} \right] \approx \text{Constant} \quad (3.13)$$

Hence

$$\frac{1 - SLIP}{SLIP} \text{RATIO} \approx \text{Constant} \quad (3.14)$$

It is then assumed that *RATIO* remains approximately constant and that the derivative of *RATIO* with respect to normal shear angle in searching for a minimum value may be ignored. The rake face resultant force in this case can be formulated as

$$F_f = \frac{SLIP}{1 - SLIP} \cdot \text{CONST} \cdot \frac{w \cdot h_0 \cdot k}{\cos i \cdot \sin \phi_N} \quad (3.15)$$

### 3 A New Approach to the Modeling of Oblique Cutting Processes

The validity of the approximations presented are easily seen by substituting the two approximations for resultant rake face force into the power equation, differentiating with respect to normal shear angle and comparing the shear angles at which a minimum power requirement is expected with the actual power curve. Figure 3.2 shows the results for a small and large inclination angle. In each case the overall power is shown together with the derivative of power with respect to normal shear angle calculated according to the two simplified approaches described. As expected the two approximations each work well in predicting the value of shear angle at which power is minimized provided they are used in the correct circumstances. It should also be noted that at small values of *SLIP* and *RATIO* there is little difference between the two results, (since rake face work is small).

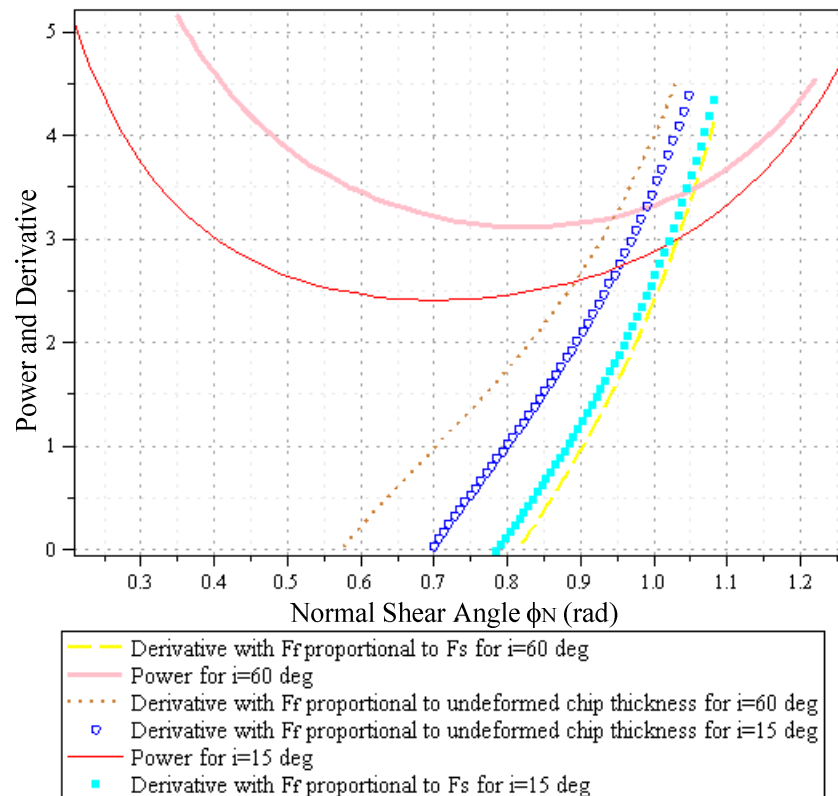


**Figure 3.2 Power and derivative with different assumptions regarding the formulation of rake face force**

### 3.3 Special Cases

The boundaries of oblique cutting are reached when *SLIP* is zero (and *RATIO* is zero) and when *SLIP* is unity, (and *RATIO* is infinite). It is instructive to examine these boundaries to ascertain the range of behaviours to be expected from oblique cutting.

#### 3.3.1 Zero *SLIP*

When *SLIP* is zero, then to satisfy force equilibrium, there can be no force on the rake face parallel to the tool edge. The velocity of the chip in that direction is  $V_0 \sin(i)$  and hence non-zero for any degree of obliquity. It must be concluded that the *RATIO* is zero and there is no resultant friction force on the rake face when *SLIP* is zero. Given the preceding conclusions from force equilibrium along the tool edge, the final solution is trivial, being simply equivalent to minimising the shear energy in orthogonal cutting, (rake face power is zero). The complete solution in this case is given by:

$$SLIP = 0, \text{RATIO} = 0, 2\phi_N - \gamma_N = \frac{\pi}{2} \quad (3.16)$$

The chip flow angle in the rake face is given as

$$\eta_c = \tan^{-1} \left( \frac{\tan i \cdot \cos(\phi_N - \gamma_N)}{\sin \phi_N} \right) \quad (3.17)$$

Substituting Eqn. (3.16) into Eqn. (3.17), then

$$\phi_N - \gamma_N = \pi/2 - \phi_N \quad (3.18)$$

and

$$\eta_c = \tan^{-1} \left( \tan i \frac{\sin \phi_N}{\sin \phi_N} \right) = i \quad (3.19)$$

Therefore the Stabler solution (Stabler 1951) is always valid for this special case, (this has been indicated by other authors (Seethaler and Yellowley 1997, Sedeh et al. 2002) as friction approaches zero but here the result and the reasons for the result are easily proven once force equilibrium is applied).

### 3.3.2 *SLIP* Approaching Unity

In the case where *SLIP* approaches unity then, by definition, the chip must flow perpendicular to the cutting edge, and from force equilibrium one must then conclude that the *RATIO* approaches infinity as the *SLIP* approaches unity.

In the normal case of  $\left[ \frac{V_{st}}{V_{sn}} \right] < 1$ , one may then approximate the power as follows

$$\begin{aligned}
 P &= \frac{h_0 w}{\cos i \cdot \sin \phi_N} \left\{ V_C \cdot \text{RATIO} + V_{sn} \left( 1 + 0.5 \left[ \frac{V_{st}}{V_{sn}} \right]^2 \right) \right\} \\
 &= \frac{h_0 w}{\sin \phi_N} \left\{ \frac{V_0 \cdot \sin \phi_N}{\cos(\phi_N - \gamma_N)} \cdot \text{RATIO} + \frac{V_0 \cdot \cos \gamma_N}{\cos(\phi_N - \gamma_N)} \right\} \\
 &\quad + \frac{1}{2} \frac{h_0 w}{\sin \phi_N} \frac{V_0 \cdot \sin^2 i \cdot \cos(\phi_N - \gamma_N)}{\cos \gamma_N}
 \end{aligned} \tag{3.20}$$

The first term in equation (3.20) represents the power requirements of the equivalent orthogonal process; the second term is much smaller and is generally decreasing with increasing  $\phi_N$  in the region where the orthogonal model shows a minimum energy condition. One thus expects the minimum energy to be found at slightly higher values of normal shear angle than that found in the equivalent orthogonal case. Figure 3.3 shows the variation of the normal shear angle with respect to inclination angle for normal rake angles of  $0^\circ$ ,  $+20^\circ$  and  $-20^\circ$ , respectively. It is seen that the shear angle in oblique cutting, (even for large values of inclination), takes on values that are only

slightly higher than those for orthogonal cutting. This finding is consistent with the discussion of equation (3.20) and very useful in establishing the expected trends between the practical variables.

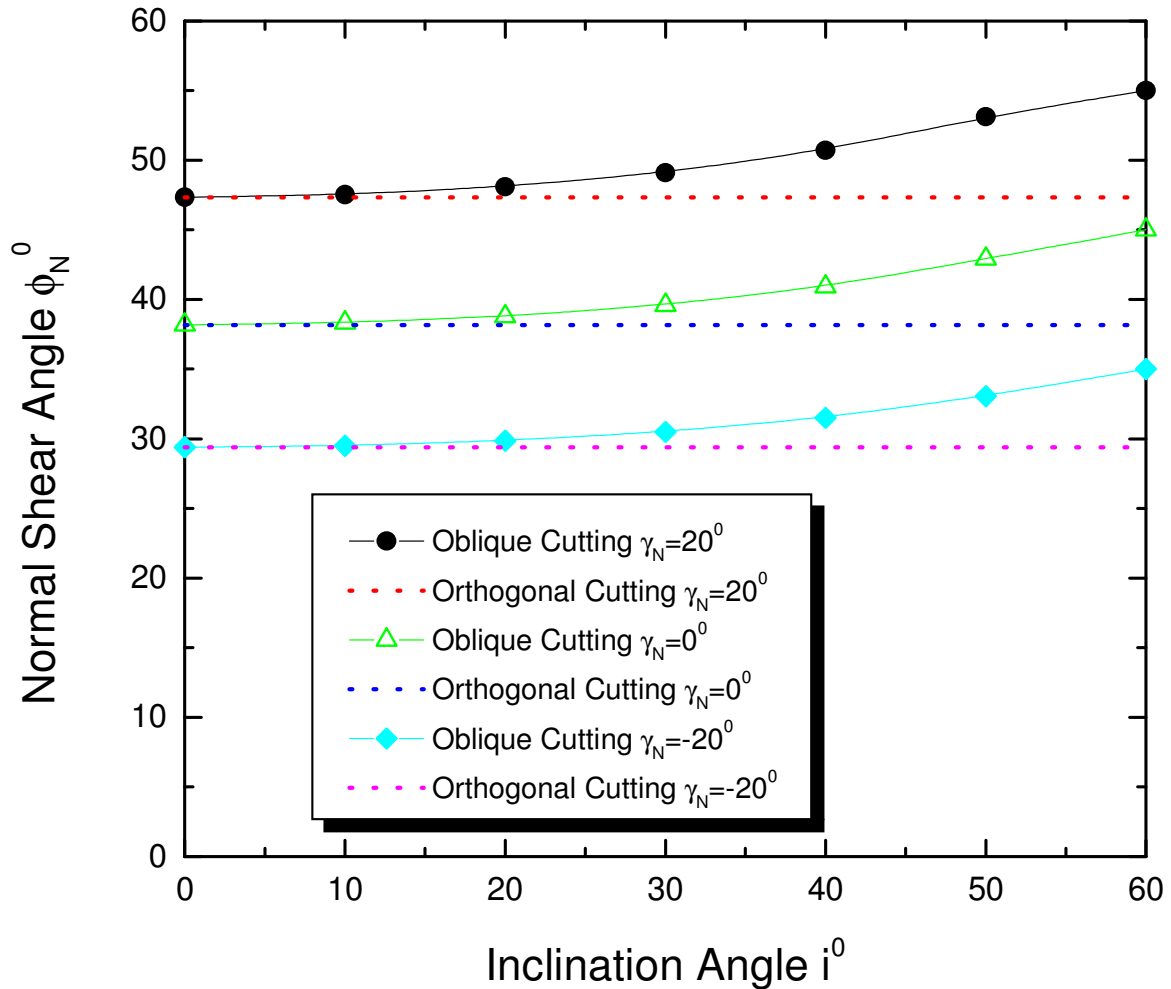


Figure 3.3 Normal shear angle versus inclination angle (*RATIO*=1)

### 3.4 Relationship between the Major Parameters

#### 3.4.1 *SLIP* and *RATIO*

There is a close relationship between the *RATIO* and amount of *SLIP*; this occurs as a results of force equilibrium where the degree of *SLIP* is related to the force available on the rake face to balance the parallel component on the shear plane causing the slip.

The relationship is reinforced by the fact that the optimal value of shear angle is related to the *RATIO*, (and hence *SLIP*), also. Figure 3.4 demonstrates just how little variation there is in the relationship between these variables for large changes in tool geometry.

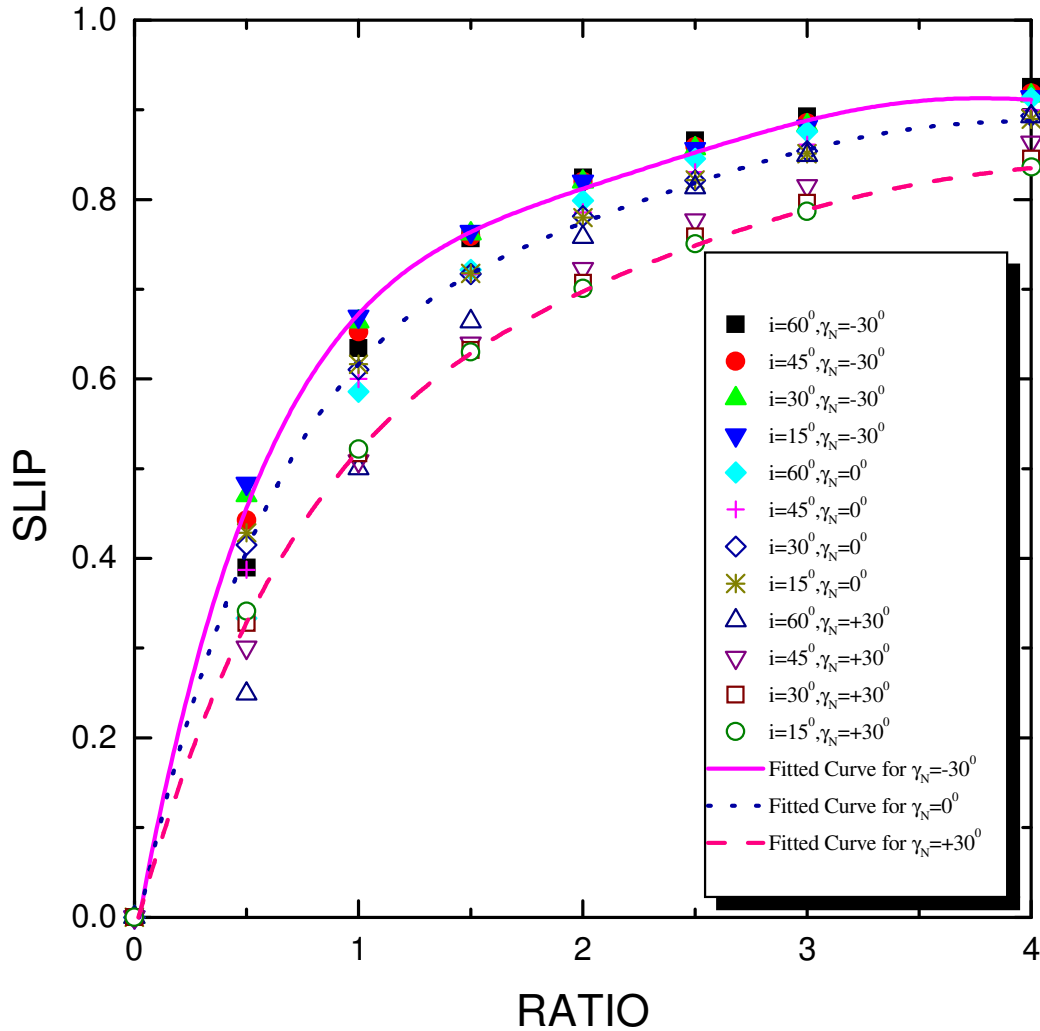


**Figure 3.4** The relationship between *SLIP* and *RATIO* with varying inclination and normal shear angles

### 3.4.2 *SLIP* and Angle of Chip Flow on the Rake Face

The angle of chip flow in the rake face is given by

### 3 A New Approach to the Modeling of Oblique Cutting Processes

$$\tan \eta_c = \frac{V_{ct}}{V_{cn}} = \frac{(1 - SLIP) \cdot V_0 \sin i}{\frac{V_0 \cos i \cdot \sin \phi_N}{\cos(\phi_N - \gamma_N)}} \quad (3.21)$$

thus

$$\frac{\tan \eta_c}{\tan i} = \frac{(1 - SLIP) \cos(\phi_N - \gamma_N)}{\sin \phi_N} \quad (3.22)$$

It can be expected that the ratio of the angle tangents will be approximately constant as inclination angle changes (normal shear angle varies little), and to be determined almost uniquely by the *SLIP*. Fortunately the influence of normal rake angle is also small over the practical range.

Figure 3.5 shows the relationship that result over the entire practical range (including a 60 degree range of both normal rake angle and inclination angle). The fitted curve is given by

$$SLIP = 1.00928 - 0.47799 \left( \frac{\eta_c}{i} \right) - 0.53039 \left( \frac{\eta_c}{i} \right)^2 \quad (3.23)$$

and is accurate enough for most practical purposes. (The relationships for individual normal rake angles have been calculated where accuracy is essential; this is only necessary in exceptional circumstances or at extreme values of rake and inclination angle).

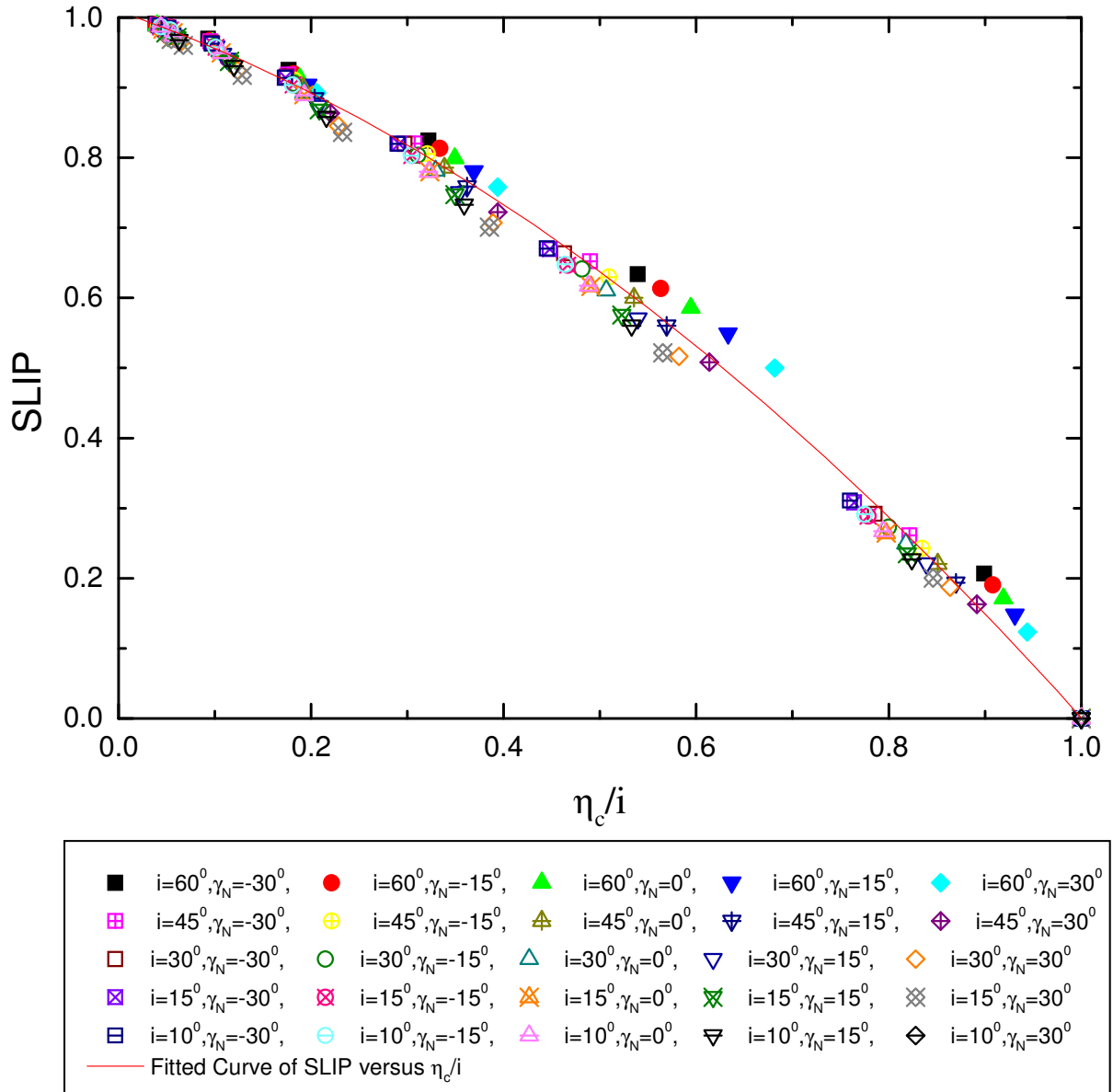


Figure 3.5 *SLIP* as a function of normalized flow angle

### 3.5 Model Calibration from Measurement of Cutting Forces

To validate the model described in this paper, *SLIP*, *RATIO*, normal shear angle,  $\phi_N$ , and shear yield stress,  $k$ , need to be obtained from measured values of cutting force.

### 3 A New Approach to the Modeling of Oblique Cutting Processes

Cutting forces are usually measured with a three-axis dynamometer that provides magnitude and direction of the resultant cutting force on the work piece.

By resolving the cutting force into the plane of the rake face, the chip flow direction on the rake face,  $\eta_c$ , is obtained. One particularly appealing feature of the model presented here is that if the chip flow angle,  $\eta_c$ , with the inclination angle,  $i$ , is normalized, then a unique relationship between  $\eta_c/i$  and  $SLIP$  can be obtained. This relationship is shown in Figure 3.5.

Once  $SLIP$  has been found, the shear angle can be derived as follows

$$\tan \eta_c = \frac{V_{ct}}{V_{cn}} = \frac{(1 - SLIP) \cdot V_0 \sin i}{\frac{V_0 \cos i \cdot \sin \phi_N}{\cos(\phi_N - \gamma_N)}} \quad (3.24)$$

$$\therefore \tan \phi_N = \frac{\tan i \cdot \cos \gamma_N \cdot (1 - SLIP)}{\tan \eta_c + \tan i \cdot \sin \gamma_N \cdot (SLIP - 1)}$$

Subsequently,  $RATIO$  is obtained from the force balance in the tangential flow direction

$$RATIO = \frac{\sin \eta_s}{\sin \eta_c} = \frac{V_{st} V_c}{V_{ct} V_s} \quad (3.25)$$

Finally, the shear yield stress is found from the power consuming force,  $F_C$

$$k = \frac{F_C V_0}{A_s (V_s + RATIO \cdot V_c)} \quad (3.26)$$

### 3.6 Comparison with Existing Experimental Tests

The model is intended to be used in the analysis of practical processes, particularly milling. Some approximations are necessary to allow a basic set of data to be used for calibration then the resulting equations reused to cover a variety of applications over a wide range of cutting conditions. At the same time the practical applications envisaged usually allow some tolerance for reasonable approximations (tool wear and end condition may influence the forces at small chip thickness quite significantly). The assumptions made are stated as follows:

- a) The shear yield stress on the shear plane may be assumed constant for one work/tool pair over a reasonable range of cutting conditions and tool geometry.
- b) *SLIP* may be assumed constant for one work tool pair with a constant value of normal rake angle over a reasonable range of cutting conditions. This may be seen when examining typical chip flow data where the normalized chip flow angle is constant as the inclination angle changes. The behavior depicted in Figures 3.5 and 3.6 implies almost constant *SLIP* with only small changes in *SLIP* resulting from large changes in normal rake angle. Since there are only small changes in normal shear angle, one also expects relatively small changes in *RATIO* as shown in Figure 3.4.
- c) Edge forces in particular would defeat these assumptions if small chip thicknesses were considered during the calibration stage with no accounting made of their presence. The data examined here will then utilize large values of chip thickness so that the edge forces will not play a large role. Clearly in milling operations methods must be devised to compensate for these components.

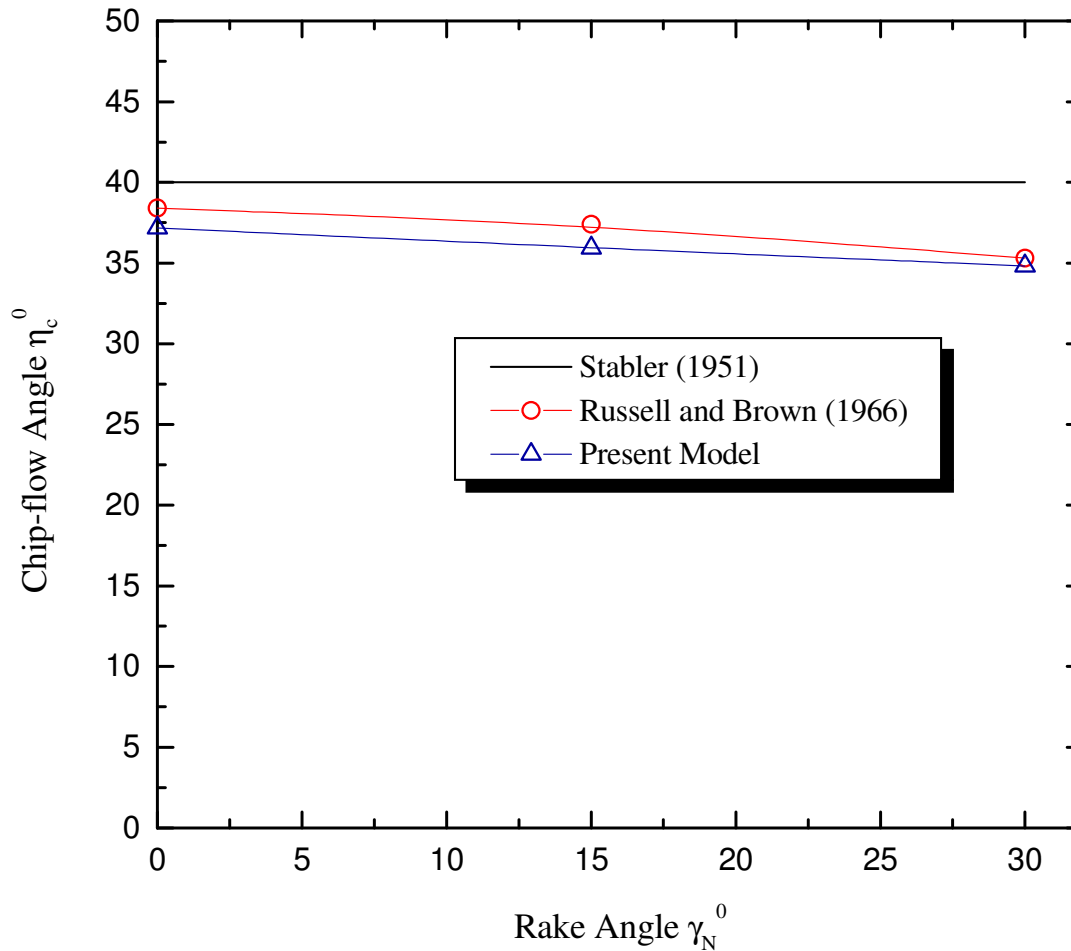


**Figure 3.6 The influence of normal rake angle on chip flow angle**

Table 3.1 and 3.2 show values of *SLIP* and *RATIO* calculated from previously published data ( Brown and Armarego (1964) for SAE 1008 steel with a normal rake angle of 20 degrees and Pal and Koenigsberger for Aluminium Alloy and a normal rake angle of 10 degrees). It is seen that there is a fair amount of scatter in the data, this is specially evident in the calculated values for low inclination angles. This occurs as a result of the relatively small velocity vector along the edge. At the same time of course any errors introduced will lead to only small changes in force at the same conditions, (and for the same reason).

**Table 3.1 *SLIP* and *RATIO* from experimental data (Brown and Armarego (1964))**

$h_0$ (mm)	$i$ (deg)	$F_C$ (N)	$F_T$ (N)	$F_R$ (N)	$\eta_c$ (deg)	<i>SLIP</i>	<i>RATIO</i>	$k$ (MPa)
0.2032	10	1112.1	609.4	112.1	5.0	0.6083	1.1296	601.1
	20	1112.0	609.4	161.0	13.6	0.4185	0.6054	795.6
	30	1156.6	589.4	224.2	22.3	0.3461	0.4711	876.7
	40	1223.3	645.0	302.5	29.2	0.3742	0.5736	837.7

**Table 3.2 *SLIP* and *RATIO* from experimental data (Pal and Koenigsberger (1968))**

$i$ (deg)	$F_C$ (N)	$F_T$ (N)	$F_R$ (N)	$\eta_c$ (deg)	<i>SLIP</i>	<i>RATIO</i>	$k$ (MPa)
10	977.25	555.12	62.83	8.6	0.1883	0.1776	495.6
20	966.18	499.25	151.18	16.0	0.2656	0.2813	454.9
30	971.72	482.83	194.02	26.5	0.1632	0.1661	489.7
40	972.79	420.89	273.10	35.9	0.1478	0.1649	483.2
50	976.71	428.39	330.75	43.0	0.2112	0.2815	426.2

Table 3.3 shows the average values of *SLIP* and *RATIO* from published data (Brown and Armarego (1964), Russell and Brown (1966), Moufki et al. (2000), and Pal and Koenigsberger (1968)) for different materials and rake angles; the average values of *SLIP* are then used to recalculate the chip flow angle. The results are shown in Figures 3.7, 3.8 and 3.9 where it is seen that the influence of averaging on the chip flow angle is negligible.

**Table 3.3 Average values of *RATIO* and *SLIP* extracted from experimental data**

Material	Experimental Data	Rake Angle $\gamma_N$ (deg)	<i>SLIP</i>	<i>RATIO</i>
SAE 1008 Steel	Brown and Armarego (1964)	20	0.4368	0.6955
AA65S-T6 Aluminum	Russell and Brown (1966)	15	0.1628	0.1580
		30	0.2573	0.3426
AISI 4142 Steel	Moufki et al. (2000)	0	0.2694	0.2528
Aluminum Alloy	Pal and Koenigsberger (1968)	10	0.195	0.234

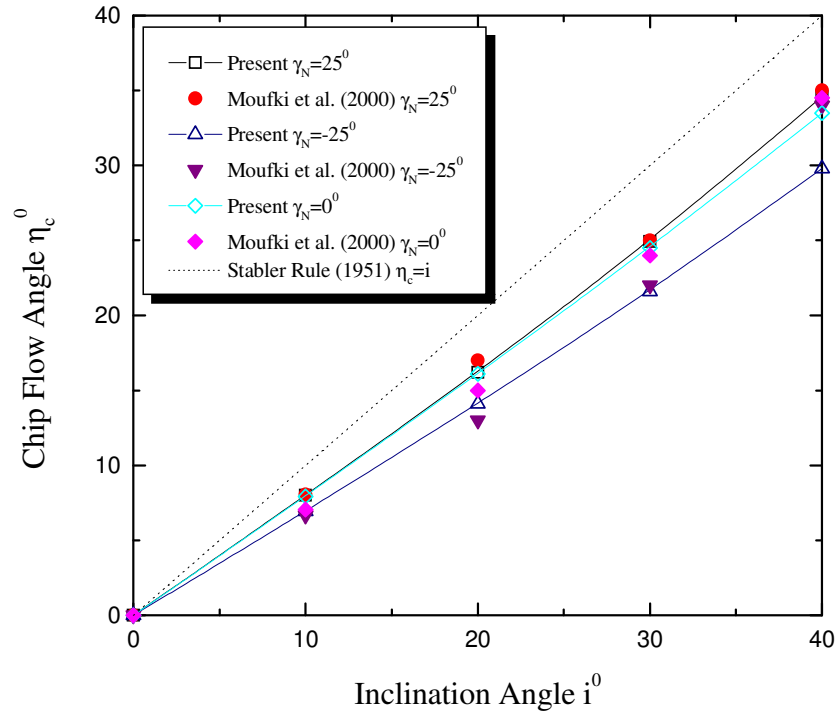


Figure 3.7 Comparison of the predicted chip flow angle with experimental results (Moufki et al. (2000))

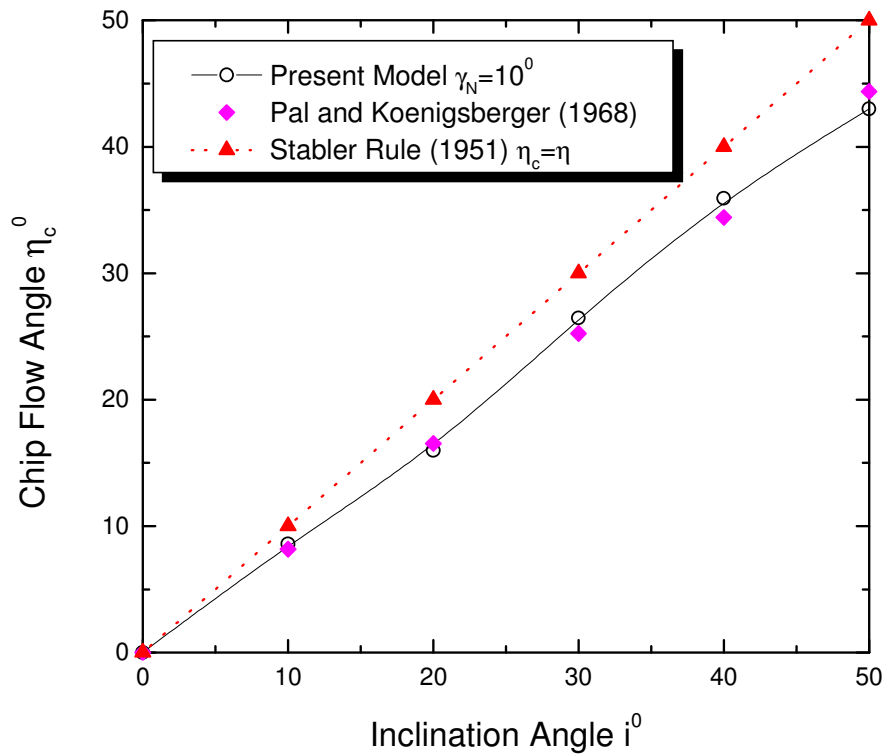
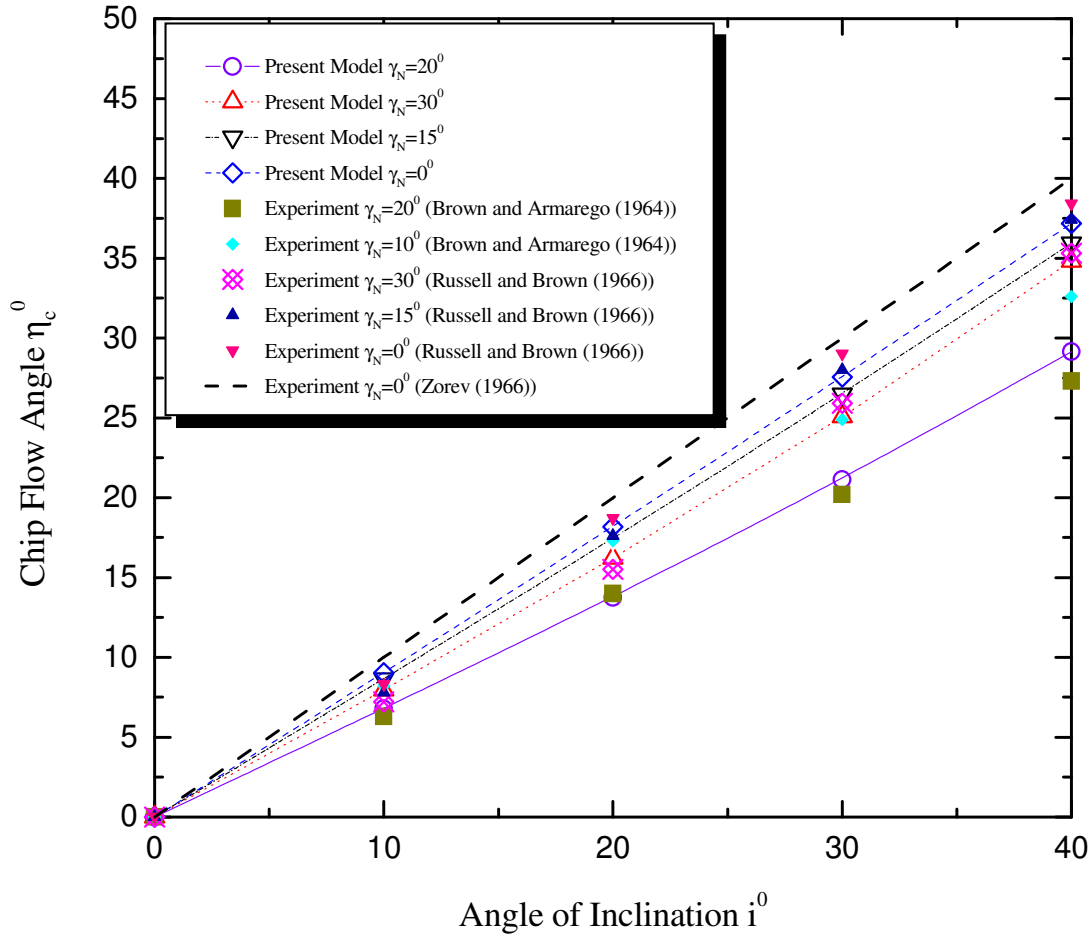


Figure 3.8 Comparison of the predicted chip flow angle with experimental results (Pal and Koenigsberger (1968))



**Figure 3.9 Comparison of the predicted chip flow angle at various normal rake angles with experimental data from several investigators**

### 3.7 Conclusions

This chapter has described the development of a new upper bound model for oblique cutting. The analysis replaces the normal variables of chip flow angle and apparent coefficient of friction with basic variables relating to the kinematics (*SLIP*) and forces in the two main deformation zones, (*RATIO*). The relationship between *SLIP* and *RATIO* is easily found through force equilibrium parallel to the tool edge thus avoiding any assumptions regarding rake face stress or the ratio of stresses on the shear plane. The

### 3 A New Approach to the Modeling of Oblique Cutting Processes

model avoids the need for shear angle data, relying instead on experimental force data for calibration and an internal optimization routine to find the normal shear angle. The decision to avoid the necessity of having shear angle data is driven by the realization that the normal shear angle is difficult to measure when tools have obliquity and non-straight cutting edges. The influence of constraint and obliquity on the expected value of normal shear angle along the tool edge is assessed. The model allows the prediction of chip flow angle and in this regard it is proved that the Stabler's law (1951) must result when *RATIO* is zero. This chapter also demonstrates the use of the model with the simplifying assumptions of constant *SLIP*, in the prediction of chip flow angle. Good agreement with measured chip flow angle from the published data is demonstrated.

## **4 The Modeling of Tool Edge Ploughing Forces in Milling Operations**

### **4.1 Introduction**

As mentioned previously, the milling process exhibits small average values of chip thickness and, in the case of peripheral milling, a chip thickness that goes to zero at either entry or exit. It is likely then that one must examine both the influence of edge effects during cutting and the process of entering and exit where one may encounter elastic contact and ploughing as well as cutting. It is to be expected that the previous history of cutting or rubbing will influence the plastic field and forces, hence up milling and down milling should not yield similar results in the area where ploughing and cutting are to be expected, (based on chip thickness alone).

This chapter describes two simple models to examine the entry and exit stages of milling. The models are approximated and intended to provide a better understanding of the shape and magnitude of the forces during these periods. This chapter also introduces a model to estimate the ploughing components during actual cutting; the model extends a previous slip-line field to include flow under the tool edge. And although phrased as an Upper Bound approach it preserves both force and moment equilibrium of the chip. The author will first introduce the basic theoretical analysis of both the transient rubbing/cutting process and that of cutting with a radiused edge before making comparison with experiment and finally attempting to quantify the conditions for the rubbing cutting transition.

## 4.2 Predictive Model for Orthogonal Cutting to Include Flow below the Cutting Edge

This section deals with the development of an upper-bound method coupled with a simple predictive model proposed by Yellowley (1987) to analyze flow around and under the tool edge. Optimization techniques are applied to optimize the velocity field and simple equilibrium is used to obtain the normal and tangential forces acting on the chamfer land. The chip force and moment equilibrium are satisfied and a realistic elastic/plastic rake face contact situation is incorporated in this approach.

### 4.2.1 Upper-Bound Formulation

Upper-bound models for orthogonal cutting have been examined by DeChiffre (1977), and Rowe and Spick (1967). Perhaps the best-known approach which (essentially) results in an upper-bound is that due to Merchant (1945). In this section, a new upper bound solution is proposed; the physical model and hodograph are shown in Figures 4.1 and 4.2, respectively.

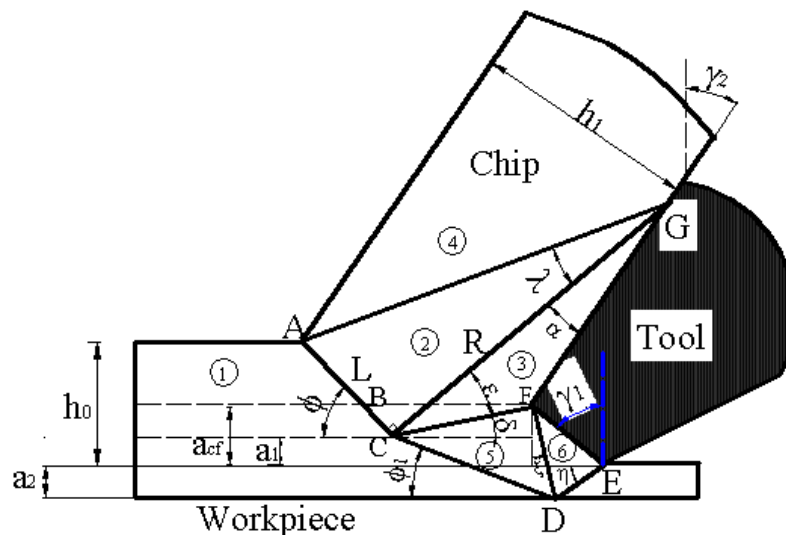
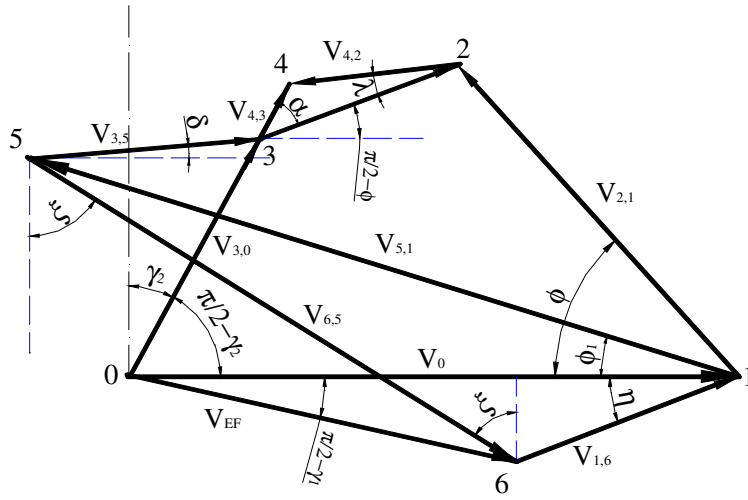


Figure 4.1 Proposed slip-line field for orthogonal cutting chamfer tools

#### 4 The Modeling of Tool Edge Ploughing Force in Milling Operations



**Figure 4.2 Hodograph of the proposed slip-line field**

The chamfer land length (EF) is expressed as  $L_{chmf}$ , and the rake angles for the chamfer land and tool-interface are stated as  $\gamma_1$  and  $\gamma_2$ , respectively. The flow is assumed to occur without a built-up edge or a stable stagnation zone. The uncut chip thickness is  $h_0$ , the chip separation point defined by  $\eta$  and  $\phi_1$ , respectively, the penetration depth under the chamfer land is assumed to be  $a_2$ . The shear plane angle is  $\phi$ . The upper part of this field is the one proposed by Yellowley (1987). The lower part of the slip-line field is an extension of the upper part which reaches the chamfer land, and is consistent with the experimental observation (Challen, Oxley and Doyle 1983; Challen and Oxley 1983 and Kopalinsky and Oxley 1995). Based on force equilibrium, the relationship between  $R$ ,  $L$  and  $\phi$  is given by Yellowley (1987) as

$$\tan(\phi + \beta_s - \gamma_2) = \frac{(1 + \pi/2 - 2\phi) - (R/L)}{1 - (1 + \pi/2 - 2\phi)(R/L)} \quad (4.1)$$

and based upon moment equilibrium of the chip

$$\frac{F_N \cdot z}{L^2} + k \cdot (R/L) - (k/2) \cdot (1 + \pi/2 - 2\phi) \cdot [1 + (R/L)^2] = 0 \quad (4.2)$$

#### 4 The Modeling of Tool Edge Ploughing Force in Milling Operations

in which  $k$  is the shear yield stress of work material,  $\beta_s$  is the angle of friction in elastic contact zone on the rake face,  $F_N$  and  $z$  are the normal component of force acting upon elastic region of the rake face contact and distance between the plastic point B and  $F_N$  respectively, (see Figure 4.3).

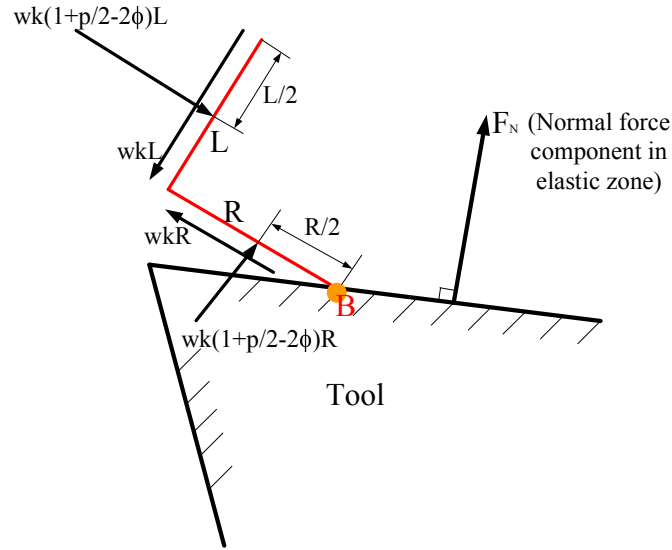


**Figure 4.3 Moment equilibrium of chip**

Assuming a normal stress distribution in the elastic region given by following expression

$$\sigma = const \cdot x^n \quad (4.3)$$

where  $x$  is the distance from the end of the chip-tool contact. Then Eqn. (4.2) is rewritten in the form

$$\frac{F_N}{L^2 \sigma_B} \cdot \frac{n+1}{n+2} + k \cdot (R/L) - (k/2) \cdot (1 + \pi/2 - 2\phi) \cdot [1 + (R/L)^2] = 0 \quad (4.4)$$

in which  $\sigma_B$  is the normal stress at point B.

Based on the proposed slip-line field, the geometry relationships can be written as follows:

#### 4 The Modeling of Tool Edge Ploughing Force in Milling Operations

$$\begin{aligned}
 a_{cf} &= L_{chmf} \cos \gamma_1, L = \frac{h_0}{\sin \phi + (R/L) \cdot (\cos \gamma_2 - \cos \phi)} \\
 \lambda &= \tan^{-1}(L/R), a_1 = h_0 - L \cdot \sin \phi, L_{AC} = L \\
 L_{CG} &= R, L_{AG} = \frac{L}{\sin \lambda}, L_{FG} = \frac{R \cdot \cos \phi - a_{cf} + h_0 - L \cdot \sin \phi}{\cos \gamma_2}, L_{CD} = \frac{a_1 + a_2}{\sin \phi_1} \quad (4.5) \\
 \varepsilon &= \tan^{-1} \left[ \frac{L_{FG} \cdot \sin(\phi - \gamma_2)}{R - L_{FG} \cdot \cos(\phi - \gamma_2)} \right], \delta = \pi/2 - (\phi + \varepsilon), L_{CF} = \frac{L_{FG} \cdot \sin(\phi - \gamma_2)}{\sin \varepsilon},
 \end{aligned}$$

In the previous slip-line field analysis, the angle  $\eta$  is assumed to be friction angle (Shi and Ramalingam 1991; Waldorf et al. 1998 and Fang 2003), which is needed to be given, here there is no need to make an assumption, and the angle  $\eta$  will be determined by the upper-bound optimization method. The formulation of angle  $\eta$  is stated as

$$\eta = \tan^{-1} \left[ \frac{a_2}{L_{CF} \cdot \cos \delta + L_{chmf} \cdot \sin \gamma_1 - (a_1 + a_2) \cdot \cot \phi_1} \right] \quad (4.6)$$

and the angle  $\xi$  is given as

$$\xi = \tan^{-1} \left[ \frac{(a_1 + a_2) \cdot \cot \phi_1 - L_{CF} \cdot \cos \delta}{a_{cf} + a_2} \right] \quad (4.7)$$

Finally the lengths of FD, BG and EF are given as

$$L_{EF} = L_{chmf}, L_{FD} = \frac{a_{cf} + a_2}{\cos \xi}, L_{BG} = R \quad (4.8)$$

It should be noted that the above geometry relation is based on the angles  $\delta$  and  $\xi$  remaining positive; once the angles  $\delta$  or  $\xi$  change the sign, one needs to keep the geometry length positive. In order to obtain the admissible slip-line field, the same idea is applicable to the velocity relationships. Based on the hodograph in Figure 4.2, the bottom part velocities of  $V_{6,0}$  and  $V_{1,6}$  are given as

#### 4 The Modeling of Tool Edge Ploughing Force in Milling Operations

$$V_{1,6} = \frac{V_0 \cos \gamma_1}{\cos(\gamma_1 - \eta)}, V_{6,0} = \frac{V_0 \sin \eta}{\cos(\gamma_1 - \eta)} \quad (4.9)$$

in which  $V_0$  is the cutting velocity. The transition part velocities  $V_{5,1}$ ,  $V_{6,1}$  and  $V_{3,5}$  are given as

$$V_{5,1} = \frac{V_{1,6} \cdot \cos(\xi - \eta)}{\cos(\phi_1 + \xi)}, V_{6,5} = \frac{V_{1,6} \cdot \sin(\phi_1 + \eta)}{\cos(\xi + \phi_1)}, V_{3,5} = \left| \frac{V_{5,1} \cos(\phi_1 - \gamma_2) - V_0 \cos \gamma_2}{\cos(\gamma_2 + \delta)} \right| \quad (4.10)$$

The upper part chip velocity  $V_c$ , shear velocity  $V_s$ , and velocities  $V_{3,1}$ ,  $V_{4,3}$ ,  $V_{4,2}$  and  $V_{2,3}$  are written as

$$\begin{aligned} V_{3,0} &= \frac{V_{5,1} \sin(\phi_1 + \delta) - V_0 \sin \delta}{\cos(\gamma_2 + \delta)} \\ V_{2,3} &= V_0 \sin \phi - V_{3,0} \cos(\phi - \gamma_2), V_{4,3} = \frac{V_{2,3} \sin \lambda}{\sin(\phi + \lambda - \gamma_2)} \\ V_c &= V_{3,0} + V_{4,3} = \frac{V_{5,1} \sin(\phi_1 + \delta) - V_0 \sin \delta}{\cos(\gamma_2 + \delta)} + \frac{V_{2,3} \sin \lambda}{\sin(\phi + \lambda - \gamma_2)} \\ V_s &= V_{2,1} = V_0 \sin \phi + V_{3,1} \sin(\phi - \gamma_2), V_{4,2} = \frac{V_{2,3} \sin(\phi - \gamma_2)}{\sin(\phi + \lambda - \gamma_2)} \end{aligned} \quad (4.11)$$

#### 4.2.2 Optimization Procedure

Having obtained the geometry of an upper bound field and the magnitudes of velocity discontinuities from the associated hodograph, power consumption  $P_T$  can be calculated as

$$\begin{aligned} P_T = F_C V_0 &= wk(L_{AC} \cdot V_s + L_{AG} \cdot V_{4,2} + L_{CG} \cdot V_{2,3} + L_{cd} \cdot V_{5,1} \\ &+ L_{DE} \cdot V_{1,6} + L_{EF} \cdot V_{6,0} + L_{FG} \cdot V_{3,0} + L_{FD} \cdot V_{6,5} + L_{CF} \cdot V_{3,5}) \\ &+ F_{f,elastic} \cdot V_C \end{aligned} \quad (4.12)$$

where  $w$  is the width of cutting,  $F_{f,elastic}$  is the elastic friction force acting on the tool-chip interface, which is given as

#### 4 The Modeling of Tool Edge Ploughing Force in Milling Operations

$$F_{f,elastic} = \{k[(L - p \cdot R) \cdot \cos \phi + (p \cdot L - R) \cdot \sin \phi] \cdot \cos \gamma_2 + k[(p \cdot L - R) \cdot \cos \phi - (L - p \cdot R) \cdot \sin \phi] \cdot \sin \gamma_2\} \cdot \tan \beta_s \quad (4.13)$$

in which

$$p = \left(1 + \frac{\pi}{2} - 2\phi\right) \quad (4.14)$$

For each elastic coefficient of friction the shear angle is incremented and the values of  $R$  and  $L$  are determined from the model, this continues until moment equilibrium is satisfied (Yellowley 1987). There is then a unique solution to the upper part of the field for each elastic coefficient of friction, the energy minimization in essence determines only the position of point D in Figure 4.1, which is depended upon the parameters of  $a_2$  and  $\phi_1$ , once  $a_2$  and  $\phi_1$  are determined, all the slip-line field and associated hodograph are determined. Thus, the upper-bound problem can be mathematically defined as the dual one which seeks the smallest value of  $P_T(a_2, \phi_1)$  as

$$\begin{aligned} \text{Minimize} \quad & P_T(a_2, \phi_1) \\ \text{Subject to:} \quad & 0 < \phi \leq \frac{\pi}{4} \\ & \phi_1 \leq \phi \\ & (h_0 - L \cdot \sin \phi + a_2) \cdot \cot \phi_1 \leq L_{CF} \cos \delta + L_{chmf} \sin \gamma_1 \end{aligned} \quad (4.15a-d)$$

Eqn. (4.15d) is added to guarantee the position of point D allows the construction of the external slip-line field (ABCDE) with a convex geometry.

### 4.2.3 Force Prediction

It has been observed by many researchers that flank wear does not affect the shear angle (Smithy et al. 2001; Song 2006; Spaans 1970; and Huang and Liang 2005);

#### 4 The Modeling of Tool Edge Ploughing Force in Milling Operations

therefore the superposition of force due to force flank wear and shear forces is widely accepted. The forces acting on the elastic region at the tool-interface (shown in Figure 4.4) can be given as

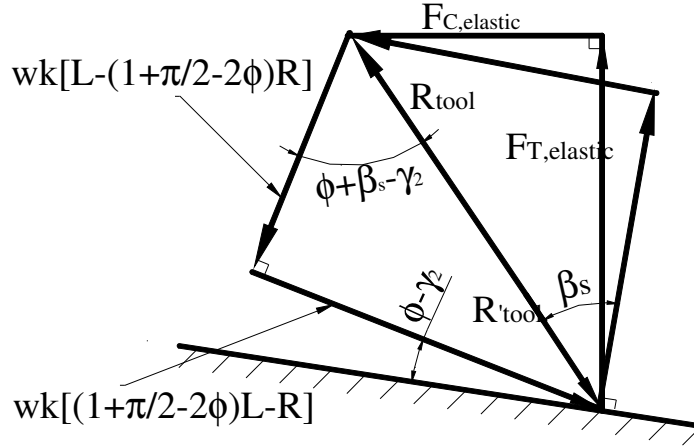


**Figure 4.4 Force equilibrium on the tool-rake face**

$$\begin{aligned} F_{C,elastic} &= wk[(L - p \cdot R) \cdot \cos \phi + (p \cdot L - R) \cdot \sin \phi] \\ F_{T,elastic} &= wk[(p \cdot L - R) \cdot \cos \phi - (L - p \cdot R) \cdot \sin \phi] \end{aligned} \quad (4.16)$$

where

$$p = (1 + \pi/2 - 2\phi) \quad (4.17)$$

$F_{C,elastic}$  and  $F_{T,elastic}$  are the tool-interface elastic forces on the cutting and thrust directions, respectively. The normal stress acting the plastic region FG based on the slip-line field can be stated as

$$\sigma_{N,GF} = \left(1 + \frac{\pi}{2} - 2\gamma_2\right) \quad (4.18)$$

The forces acting on the cutting material by tool are shown in Figure 4.5. The decomposed forces at the region of GF and chamfered land EF to the cutting and thrust directions can be written as

#### 4 The Modeling of Tool Edge Ploughing Force in Milling Operations

$$\begin{aligned} F_{C,GF} &= F_{GF} \cdot \sin \gamma_2 + N_{GF} \cdot \cos \gamma_2 \\ F_{T,GF} &= F_{GF} \cdot \cos \gamma_2 - N_{GF} \cdot \sin \gamma_2 \end{aligned} \quad (4.19)$$

at the contact length of GF, and

$$\begin{aligned} F_{C,EF} &= F_{EF} \cdot \sin \gamma_1 + N_{EF} \cdot \cos \gamma_1 \\ F_{T,EF} &= -F_{GF} \cdot \cos \gamma_1 + N_{EF} \cdot \sin \gamma_1 \end{aligned} \quad (4.20)$$

at the chamfered land EF. Based on the force equilibrium, one can obtain the forces acting on the chamfered land as

$$\begin{aligned} F_{EF} &= wkL_{EF} \\ N_{EF} &= \frac{F_C - F_{C,elastic} - F_{C,GF} - wkL_{EF} \cdot \sin \gamma_1}{\cos \gamma_1} \end{aligned} \quad (4.21)$$

Once the forces acting on the chamfered land are known, the thrust force can be given as

$$F_T = F_{T,elastic} + F_{T,GF} + F_{T,EF} \quad (4.22)$$

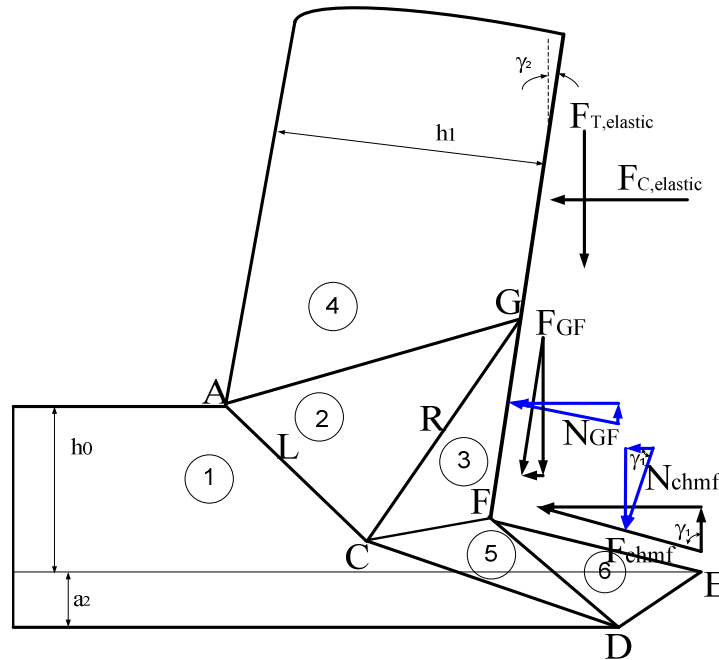


**Figure 4.5 Force equilibrium for chamfered tool**

#### 4.2.4 Adapting the Predictive Model for Radiused Edge Tools

The effective rake angle of the tool is a very important parameter especially for honed tools. Based on the work of Manjunathaiah and Endres (2000), the actual rake angle in the presence of an edge radius or chamfer is quite different from the nominal rake angle  $\gamma$  ground on the tool. The actual rake angle henceforth referred to as the effective rake angle  $\gamma_{avg}$ , can be computed from the relative size of the undeformed chip thickness to the tool edge radius  $h_0/r_e$ . The expressions (Manjunathaiah and Endres 2000) given in Eqn. (4.23) have been used in this thesis to compute the effective rake angle.

$$\gamma_2 = \gamma_{ave} = \tan^{-1} \left[ \frac{(c \cdot h_0 / r_e - 1) \tan \gamma - \sec \gamma + \sin \theta}{c \cdot h_0 / r_e - 1 + \cos \theta} \right] \text{ for } c \cdot h_0 > r_e (1 + \sin \gamma)$$

$$\gamma_2 = \gamma_{ave} = \tan^{-1} \left[ -\frac{\sqrt{(2 - c \cdot h_0 / r_e) \cdot c \cdot h_0 / r_e + \sin \theta}}{c \cdot h_0 / r_e - 1 + \cos \theta} \right] \text{ for } c \cdot h_0 \leq r_e (1 + \sin \gamma)$$
(4.23)

Typically it is assumed that the contact length  $c$  at the tool-interface is twice the undeformed chip thickness (Manjunathaiah and Enres 2000). Hence, the predictive slip-line model incorporated with the round edge tool is shown in Figure 4.6.

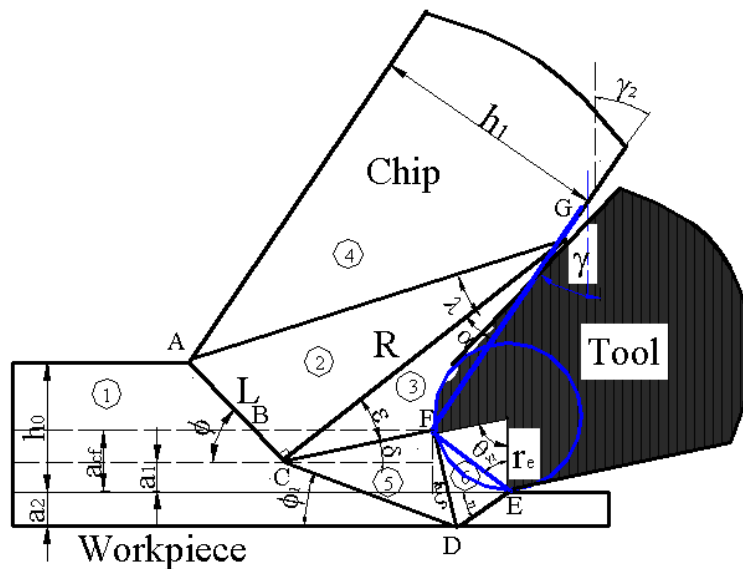


Figure 4.6 Upper bound field for radiused edge

### 4.2.5 Case Studies of Predictive Cutting Model

#### 4.2.5.1 Optimized Upper Bound Geometries

Having assumed that the chamfer length does not influence stresses on the rake face, it is instructive to examine the shape of the flow zones as chamfer width is increased. Consider the case of  $\gamma_1=-70^\circ$ ,  $\gamma_2=0^\circ$ , and  $\beta_s=40^\circ$ , the typical influence of chamfer length with  $L_{chmf}/h_0=0.1$ , 0.3 and 0.5 are plotted in Figures 4.7(a), (b) and (c), respectively. It can be seen that large chamfers exhibit a lower boundary that is almost parallel to the incoming velocity, (indicating an almost stagnant zone) and an apparent increase in the curvature of the leading boundary of the shear plane. The fields for chamfer angle with  $-80^\circ$ ,  $-70^\circ$  and  $-60^\circ$  at the friction angle  $\beta_s=40^\circ$  are plotted in Figures 4.8(a), (b) and (c), respectively. From Figure 4.8, it can be observed that the angle  $\delta$  has negative and increases with the chamfer angle. The optimized flow lines around the chamfer land are similar with Shi and Ramalingam (1991) and experimental observation (Oxley 1989). The latter suggests an increasing hydrostatic stress at the tool edge. The methodology used in this thesis to calculate forces on the chamfer is relatively robust in terms of the potential influence of varying slip-line curvature. To demonstrate this, the expected normal stress levels on the chamfer calculated assuming that the leading slip-line either intersects the rake face at right angles or in the extreme case the effective slip line meets at the angle of intersection of CF and the rake face are examined to see if the final solution is sensitive to this assumption. Figure 4.9 shows that there is remarkably little influence between these extremes.

4 The Modeling of Tool Edge Ploughing Force in Milling Operations

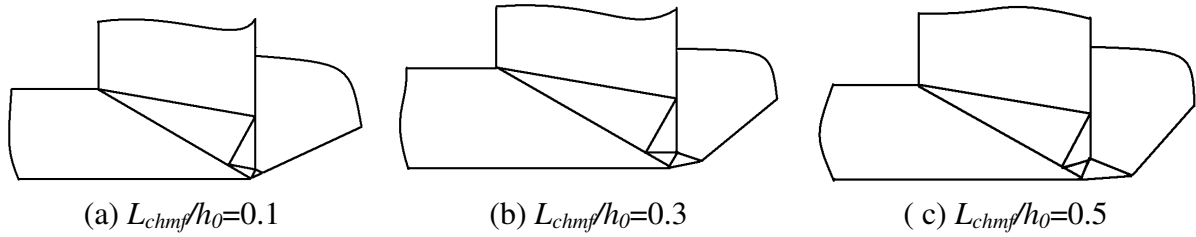


Figure 4.7 Upper bound solutions for the case of  $\gamma_1 = -70^\circ$ ,  $\gamma_2 = 0^\circ$ ,  $\beta_s = 40^\circ$

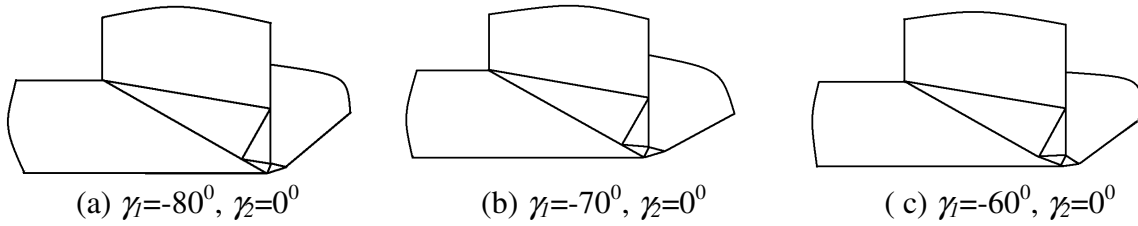


Figure 4.8 Upper bound solutions for different chamfer angles

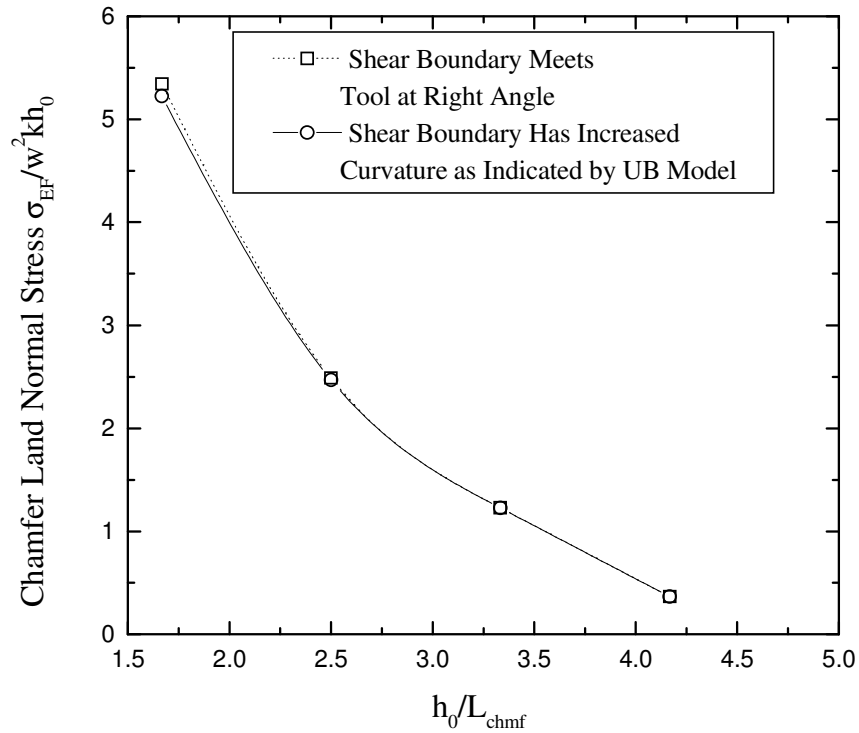
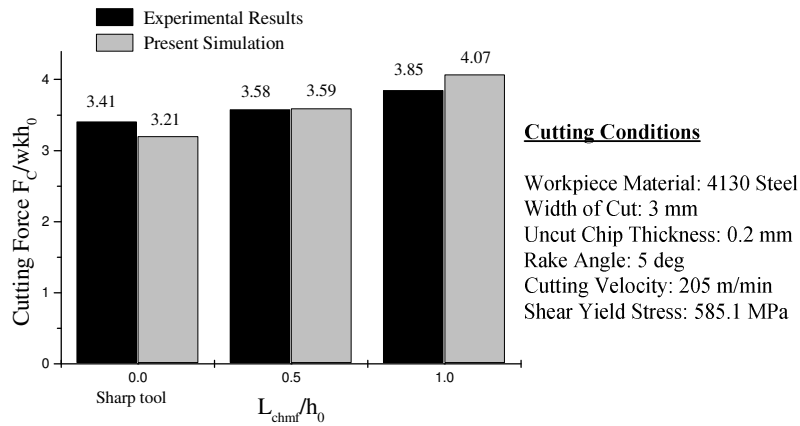


Figure 4.9 Calculation of normal stress on chamfer using two extreme cases of field geometry

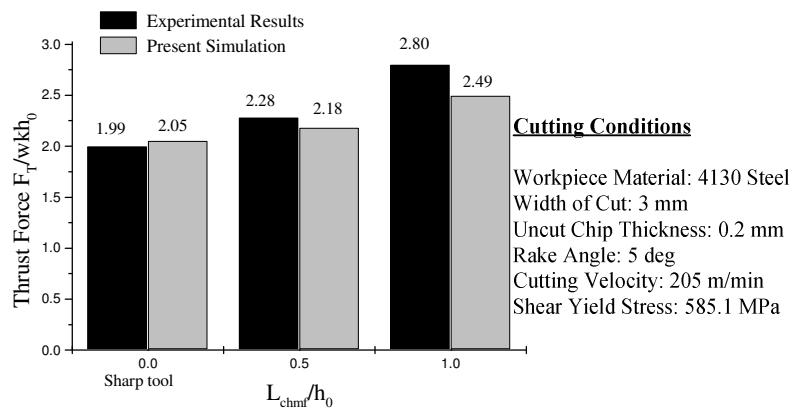
## 4 The Modeling of Tool Edge Ploughing Force in Milling Operations

### 4.2.5.2 Validating the Proposed Model with Experimental Data

The force predictions from the model were compared with recent experimental data. The first series of experiments were conducted by Smithy et al. (2001). The parameters in this predictions are used as  $\gamma_1=-85^0$ ,  $\gamma_2=5^0$  and  $\beta_s=42^0$  (which is the same friction coefficient as Smithy et al. (2001) with  $m_p=0.9$ ). Figures 4.10(a) and (b) show the comparison of the predicted cutting forces with the experimental results given in Smithy et al. (2001). A good agreement is observed between the predictions and the measured values.



(a) Cutting force  $F_C$

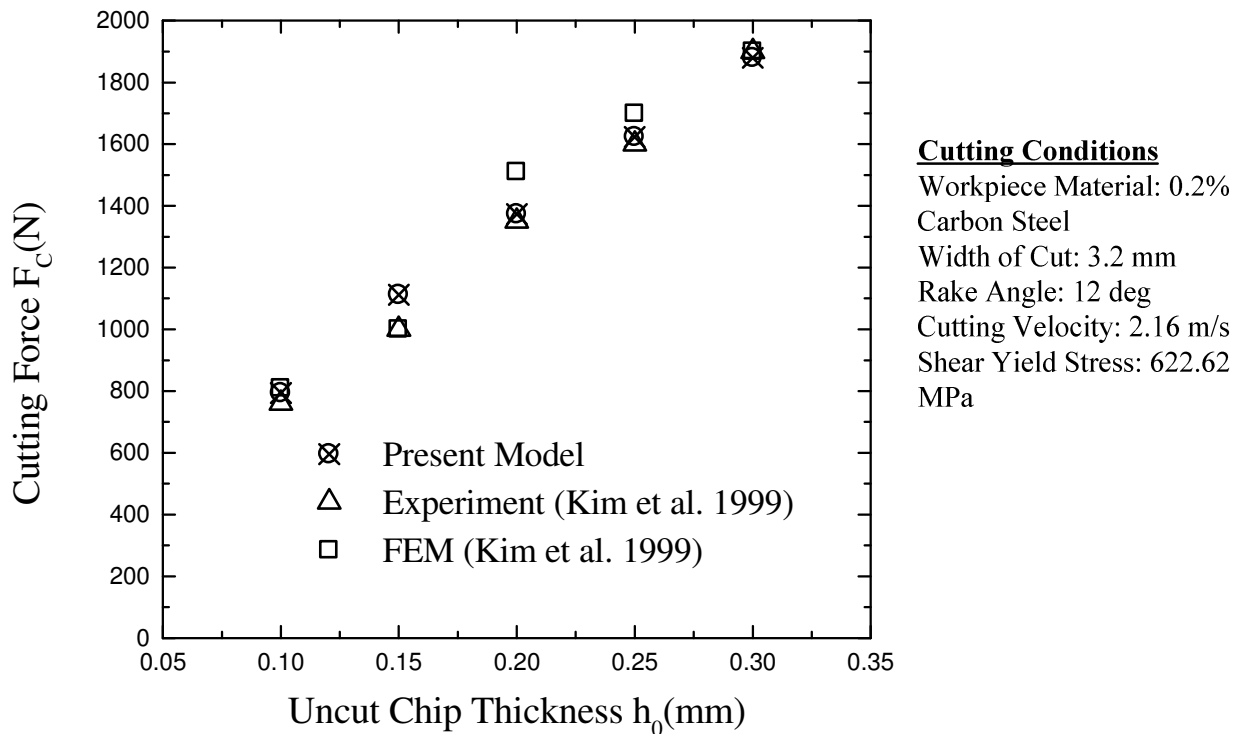


(b) Thrust force  $F_T$

**Figure 4.10 Comparison of predicted cutting forces with experimental results**

#### 4 The Modeling of Tool Edge Ploughing Force in Milling Operations

The second set of experiments concern the cutting of 0.2% carbon steel using a tool with a 0.1 mm radius tool edge and were reported by Kim et al. (1999). In order to characterize the edge radius, the approach suggested by Manjunathaiah and Endres (2000) is used, and the actual critical angle chosen at point (F) is  $30^{\circ}$ . Figures 4.11(a) and (b) present the comparison of the cutting and thrust forces with experiment and FE simulations for various depths of cut. Good correlation is found for the cutting and thrust forces over the entire range of depths of cut tests. Figure 4.12 shows the ratio of thrust force to cutting force. As depth of cut decreases, the ratio increases.



(a) Cutting force  $F_c$

#### 4 The Modeling of Tool Edge Ploughing Force in Milling Operations

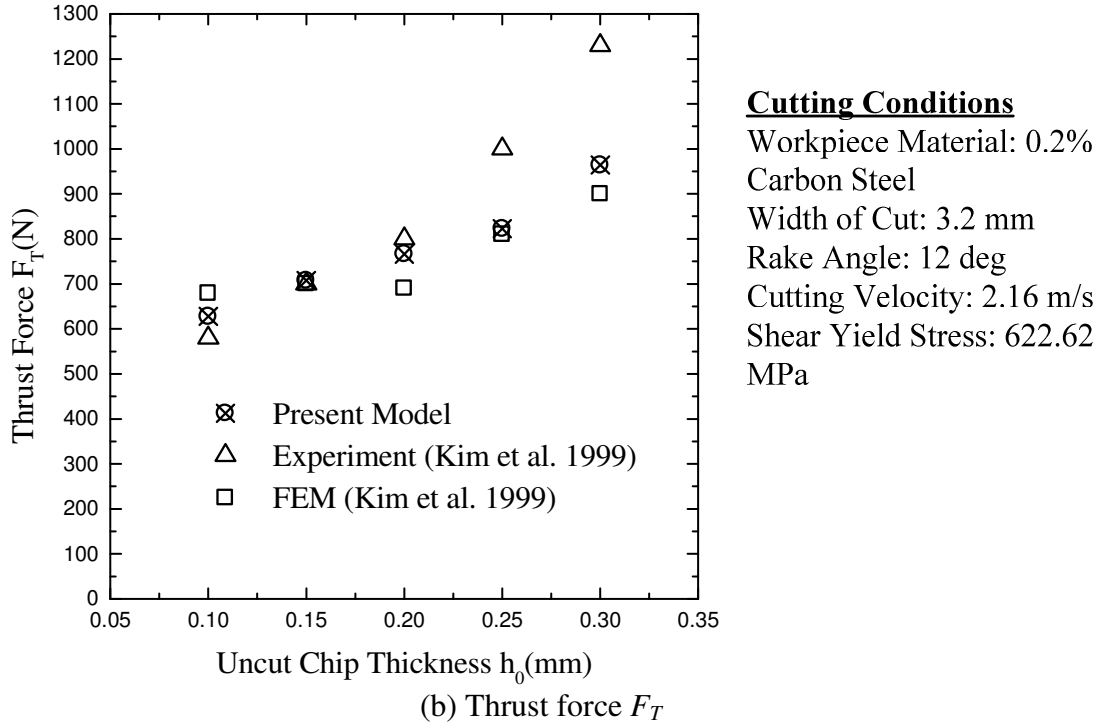


**Figure 4.11** Variation of cutting and thrust forces versus uncut chip thickness

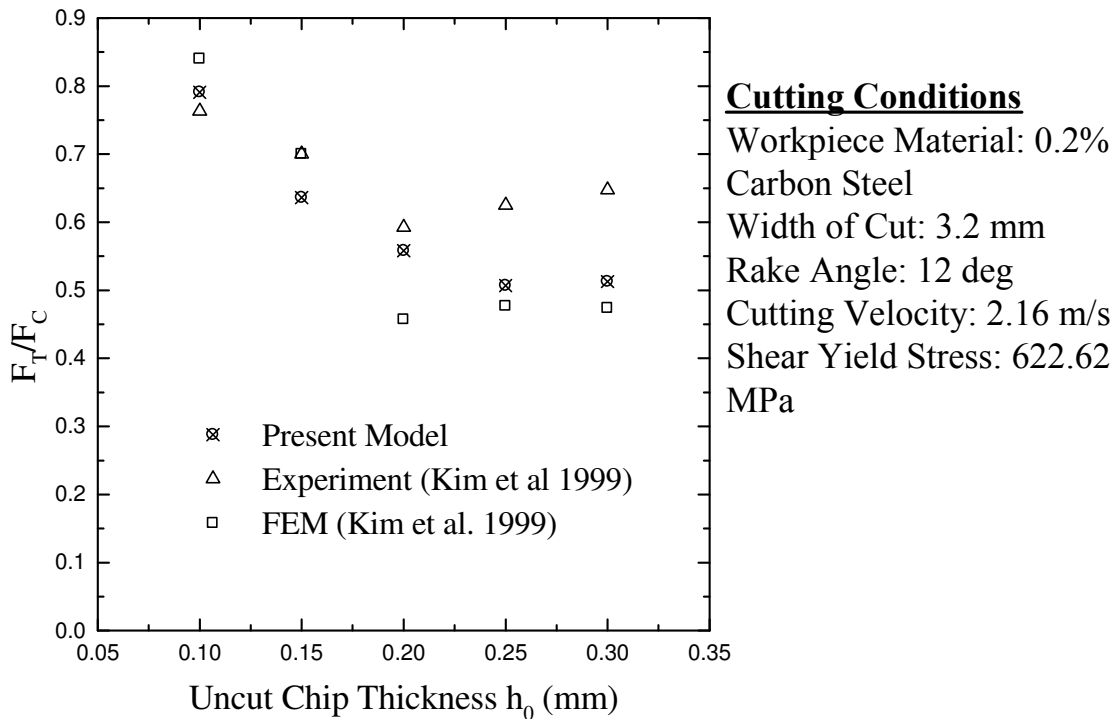


**Figure 4.12** Change in force ratio as uncut chip thickness increases

### 4.2.6 Parameter Studies of Predictive Cutting Model

The validation of the predictive cutting model has been conducted in Section 4.2.5, which shows a good correlation with the experiments. This section attempts to investigate the influences of the chamfer parameters on the cutting forces.

#### 4.2.6.1 Influence of Chamfer Angle on Cutting Forces

The influence of chamfer angle on the cutting forces is investigated here with the consideration of three different rake angles  $\gamma_2$  at  $-10^\circ$ ,  $0^\circ$  and  $10^\circ$ , respectively. The friction angle  $\beta_s$  is taken as  $40^\circ$ . The shear angles for the rake angles at  $-10^\circ$ ,  $0^\circ$  and  $10^\circ$  are calculated as  $24.5^\circ$ ,  $29.5^\circ$  and  $34^\circ$ , respectively. The relations of the normalized cutting force  $F_C$ , and thrust force  $F_T$  with respect to the chamfered angles are given in Figures 4.13, and 4.14, respectively. From Figures 4.13, and 4.14, it can be observed that the cutting force  $F_c$  is decreased as the chamfered angle is increased; while the thrust force  $F_T$  is increased as the chamfer angle is increased.

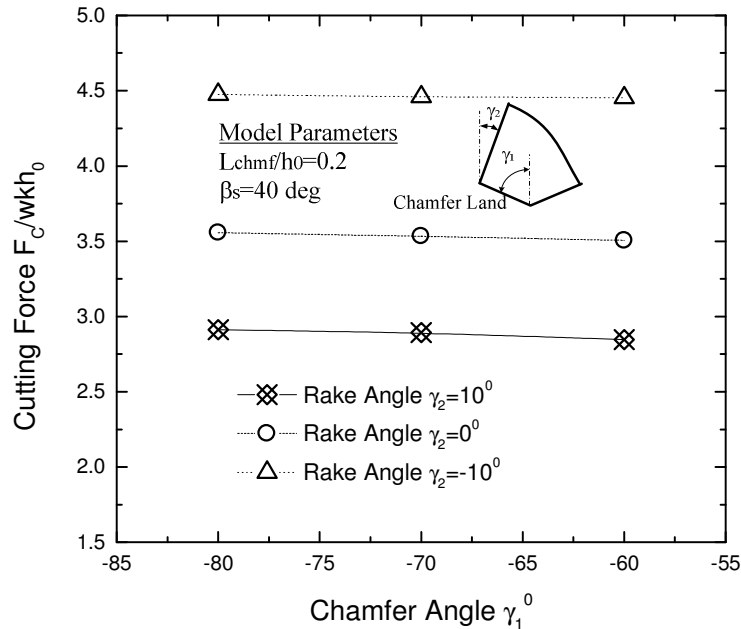


Figure 4.13 Cutting force  $F_c$  versus chamfer angle for the rake angle of  $-10^\circ$ ,  $0^\circ$  and  $10^\circ$

#### 4 The Modeling of Tool Edge Ploughing Force in Milling Operations

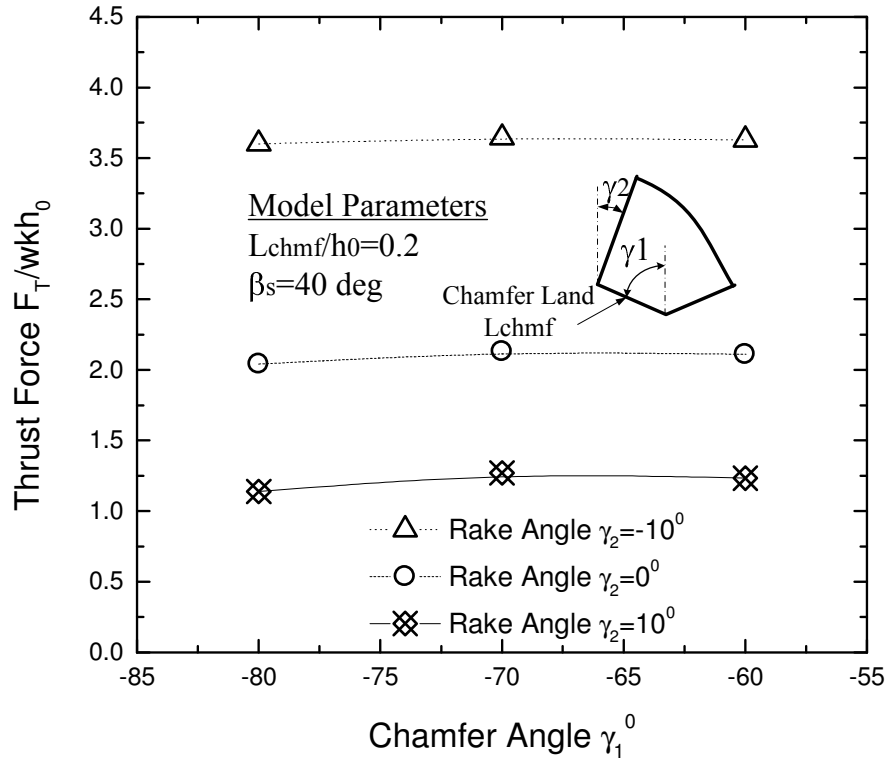
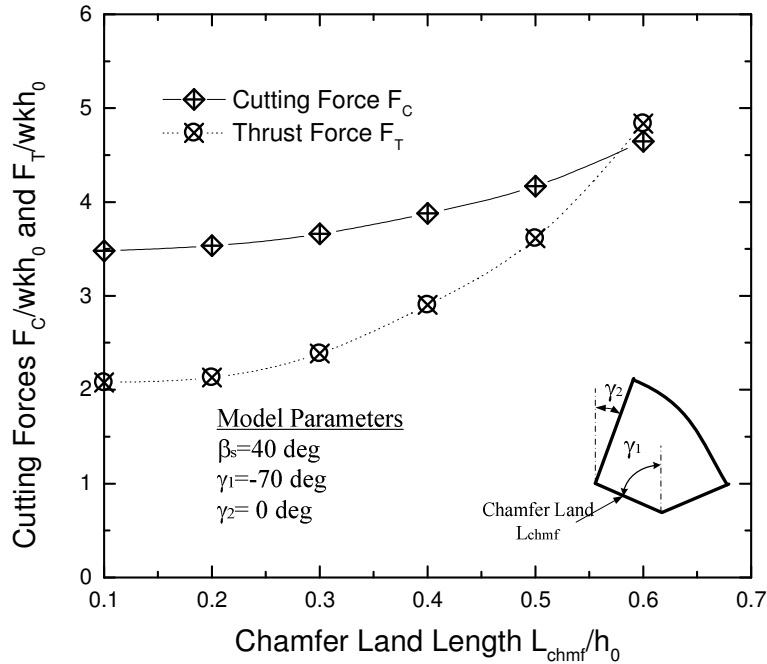


Figure 4.14 Thrust force  $F_T$  versus chamfer angle for the rake angle of  $-10^0$ ,  $0^0$  and  $10^0$

#### 4.2.6.2 Influence of Chamfered Land Length on Cutting Forces

The influence of chamfer length on the cutting forces is examined in this section. The geometry parameters are considered as:  $\gamma_1=-70^0$ ,  $\gamma_2=0^0$  and  $\beta_s=40^0$ , the ratio of chamfer length to the uncut chip thickness is varied in the range of 0.1 to 0.6. Figure 4.15 plots the relationship of normalized cutting forces  $F_C$  and  $F_T$  with respect to the ratio of chamfer land length to the uncut chip thickness, from the figure, it can be seen that the forces  $F_C$  and  $F_T$  are increase in nonlinear fashion with the ratio of chamfer land length to uncut chip thickness.



**Figure 4.15** Variation of cutting force  $F_C$  and thrust force  $F_T$  with respect to chamfer length

### 4.3 Ploughing Models

The ploughing process where majority of workpiece material is displaced without being removed is studied in this section. Two ploughing models which include the effect of build up of a bulge ahead of the tool during sliding are presented to predict the forces during ploughing.

#### 4.3.1 Single Edge Ploughing Model

The single edge ploughing model is based on the wedge indentation model discussed by Rowe and Wetton in respect to grinding, (1969). The wedge is moved to the right with its apex at a constant depth  $h_0$  below the surface, the volume of metal displaced and the height of bulge will increase. In the absence of leakage, the volume displaced will increase by  $l_{slide}h_0$ .

#### 4 The Modeling of Tool Edge Ploughing Force in Milling Operations

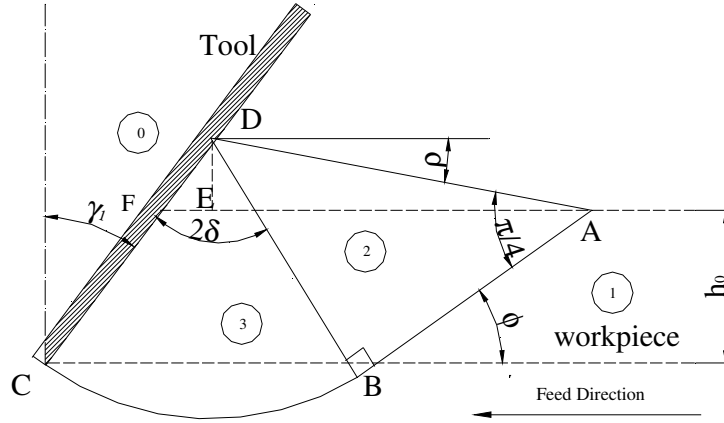


**Figure 4.16 Slip-line field for single edge ploughing model (Rowe and Wetton 1969)**

Based on the proposed slip-line field, the geometry relationships can be given as follows:

$$\delta = \frac{\pi}{8} - \frac{\rho - \gamma_1}{2}, \quad \phi = 2\delta - \gamma_1 \quad (4.24)$$

The angle  $\rho$  can be obtained as Figure 4.16

$$\rho = \sin^{-1} \left( \frac{L \cos \gamma_1 - h_0}{\sqrt{2}L} \right) \quad (4.25)$$

$$L_{CD} = L, L_{BD} = L, L_{AB} = L, L_{AD} = \sqrt{2}L, L_{BC} = 2L \sin \delta \quad (4.26)$$

where  $\gamma_1$  is the rake angle,  $h_0$  the uncut chip thickness,  $L$  the length of fan radius. For the case of sliding distance  $l_{slide}=0$ ,  $L$  is given as

$$L = \frac{h_0}{\cos \gamma_1} \quad (4.27)$$

for the case of sliding distance  $l_{slide}>0$ ,  $L$  can be obtained once one knows the bulge area (DAEF) in the field (shown in Figure 4.16), therefore

$$(L \cdot \cos \gamma_1 - h_0) \sqrt{2L^2 - (L \cdot \cos \gamma_1 - h_0)^2} + (L \cdot \cos \gamma_1 - h_0)^2 \cdot \tan \gamma_1 - 2h_0 \cdot l_{slide} = 0 \quad (4.28)$$

#### 4 The Modeling of Tool Edge Ploughing Force in Milling Operations

The solution should keep the slip-line field convex and correspond to minimum energy consumption. It should be noted that the above geometry relation is based on the angles  $\rho$  and  $\phi$  being positive values.

Based upon the slip-line field, the normal and shear stresses can be given as

$$p(B) = k, \tau(B) = k, p(C) = k(1 + 4\delta), \tau(C) = k \quad (4.29)$$

Therefore the ploughing force acting on the horizontal and vertical directions can be stated as

$$F_C = kL(1 + 4\delta)\cos\gamma_1 + kL\sin\gamma_1, F_T = -kL(1 + 4\delta)\sin\gamma_1 + kL\cos\gamma_1 \quad (4.30)$$

and the ploughing power can be expressed by

$$P = F_C V_0 = kLV_0(1 + 4\delta)\cos\gamma_1 + kLV_0\sin\gamma_1 \quad (4.31)$$

where  $V_0$  is sliding velocity.

#### 4.3.2 Double Edge Ploughing Model

A double edge ploughing model is needed to more accurately simulate the effect of tool edge radius. The proposed slip-line field and hodograph for the double edge ploughing model are given in Figures 4.17 and 4.18, respectively.

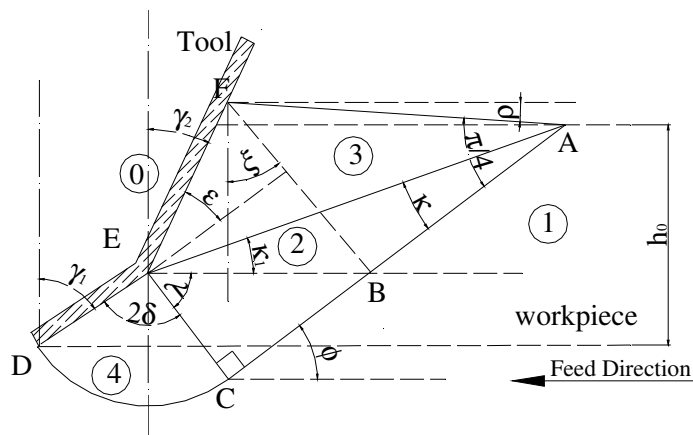
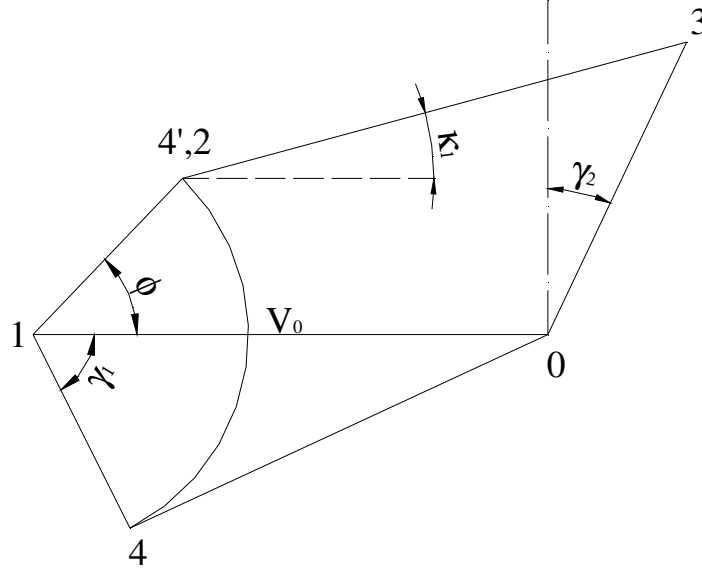


Figure 4.17 Double edge slip-line field

#### 4 The Modeling of Tool Edge Ploughing Force in Milling Operations



**Figure 4.18 Hodograph**

Based on the slip-line field, the geometry relationships are given as follows

$$\xi = 2\delta - \gamma_1, \rho = \frac{\pi}{4} - \phi, \phi = \xi, \varepsilon = \frac{\pi}{2} - \xi - \gamma_2 \quad (4.32)$$

$$\begin{aligned} L_{EC} &= L_{ED}, L_{FI} = L_{EF} \cos(\xi + \gamma_2), L_{EI} = L_{EF} \sin(\xi + \gamma_2), L_{BC} = L_{EI} \\ L_{BF} &= L_{ED} + L_{EF} \cos(\xi + \gamma_2), L_{AB} = L_{BF}, L_{BC} = L_{EI}, L_{AF} = \sqrt{2}L_{BF} \\ L_{AC} &= L_{ED} + L_{EF} \cdot [\sin(\xi + \gamma_2) + \cos(\xi + \gamma_2)] \end{aligned} \quad (4.33)$$

$$\kappa = \tan^{-1}\left(\frac{L_{EC}}{L_{AJ}}\right), \lambda = \tan^{-1}\left(\frac{L_{BC}}{L_{EC}}\right) \quad (4.34)$$

$$\kappa_1 = \frac{\pi}{2} - \kappa - \lambda, L_{AE} = \frac{L_{EC}}{\sin \kappa}$$

and

$$\begin{aligned} L_{EF} &= \frac{h_0 - L_{ED} \cdot \cos \gamma_1 + \sqrt{2}L_{ED} \sin \rho}{\cos \gamma_2 - \sqrt{2} \cos(\xi + \gamma_2) \sin \rho} \quad \text{for sliding distance } l_{slide} = 0 \\ L_{EF} &= \frac{\left( \sqrt{\frac{h_0 l_{slide}}{0.5 \sin 2\rho + 0.5(1 - \cos 2\rho) \cdot \tan \gamma_2}} - L_{ED} \right)}{\cos(\xi + \gamma_2)} \quad \text{for sliding distance } l_{slide} > 0 \end{aligned} \quad (4.35)$$

#### 4 The Modeling of Tool Edge Ploughing Force in Milling Operations

Based upon the hodograph in Figure 4.18, the velocity relationships can be stated

as

$$\begin{aligned} V_{04} &= V_0 \sin \gamma_1, V_{12} = V_0 \cos \gamma_1 \\ V_{03} &= \frac{V_0 \sin \kappa_1 + V_{12} \sin(\phi - \kappa_1)}{\cos(\kappa_1 + \gamma_2)} \\ V_{32} &= \frac{V_0 \cos \gamma_2 - V_{12} \cos(\phi + \gamma_2)}{\cos(\kappa_1 + \gamma_2)}, V_{14} = V_{12} \end{aligned} \quad (4.36)$$

In order to calculate the plastic dissipation of the fan field, a cylindrical-polar coordinate system is adopted. The strain rates in the fan region can be expressed by

$$\dot{\epsilon}_{rr} = \dot{\epsilon}_{\theta\theta} = 0, \dot{\epsilon}_{r\theta} = \frac{1}{2} \frac{V_{14}}{r} \quad (4.37)$$

Then the equivalent strain rate is given as

$$\dot{\epsilon}^p = \sqrt{\frac{2}{3} \dot{\epsilon}_{ij} \dot{\epsilon}_{ij}} = \frac{V_{14}}{\sqrt{3}r} \quad (4.38)$$

Thus the plastic dissipation is

$$\begin{aligned} P_{fan} &= \iint_{\Omega} Y \dot{\epsilon}^p d\Omega + \int_S k[[V]] ds = \int_0^{L_{CD}} \int_0^{2\delta} \sqrt{3}k \frac{V_{14}}{\sqrt{3}r} r dr d\theta + \int_0^{2\delta} kV_{14} d\theta \\ &= kV_{14} \cdot L_{CD} \cdot 4\delta \end{aligned} \quad (4.39)$$

Finally the total power dissipation can be obtained as

$$P = F_C V_0 = kW(L_{ED}V_{04} + 4\delta L_{ED}V_{14} + L_{AC}V_{12} + L_{AE}V_{32} + L_{EF}V_{03}) \quad (4.40)$$

Using the upper-bound technique, the optimization algorithm is stated in the form

as

$$\begin{aligned} &\text{Minimum } F_C \\ &\text{Subject to : } \rho \geq 0, \phi \geq 0, h_0 = \text{constant} \\ &\sin\left(\frac{\pi}{4} + \xi + \gamma_2\right) \geq 0 \end{aligned} \quad (4.41)$$

#### 4 The Modeling of Tool Edge Ploughing Force in Milling Operations

The normal force acting on the ploughing face EF and the vertical ploughing force are then derived as

$$F_N = \frac{F_c - kL_{ED} \sin \gamma_1 - kL_{EF} \sin \gamma_2 - k(1 + 4\delta)L_{ED} \cos \gamma_1}{\cos \gamma_2} \quad (4.42)$$

$$F_T = -k(1 + 4\delta)L_{ED} \sin \gamma_1 - F_N \sin \gamma_2 + kL_{ED} \cos \gamma_1 + kL_{EF} \cos \gamma_2$$

The MAPLE global optimization toolbox (Maple 2010) has been used to solve the above nonlinear equations. In the numerical calculation the accuracy is chosen as  $10^{-9}$  when the minimization of power consuming is satisfied.

#### 4.3.3 Ploughing Model with Rounded Edge Tool

The geometry of rounded edge tools is idealized to achieve a deformation zone and equivalent tool that is made up of straight boundaries. As shown in Figure 4.19, the edge radius is approximated by one and two line segments for the single and double edge model, respectively. The equivalent tool geometry is formulated as follows.

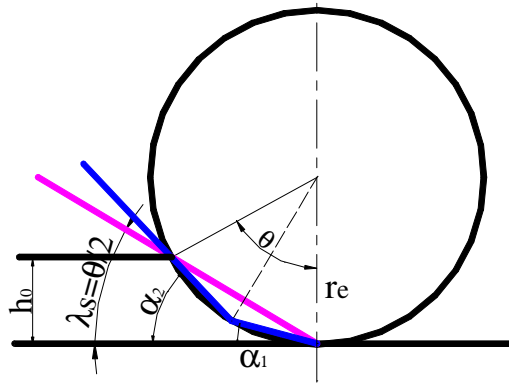


**Figure 4.19 Round edge tool ploughing geometry**

For the single edge model, the ploughing angle is approximated as:

$$\sin \lambda_s = \frac{h_0}{2r_e \sin \lambda_s} \quad (4.43)$$

## 4 The Modeling of Tool Edge Ploughing Force in Milling Operations

where  $r_e$  is the edge radius,  $h_0$  is the uncut chip thickness. Thus the attack angle  $\lambda_s$  can be obtained as

$$\lambda_s = \sin^{-1} \left( \sqrt{\frac{h_0}{2r_e}} \right) \quad (4.44)$$

On the other hand, for double edge ploughing model, the geometry can be derived as

$$\alpha_1 = \frac{\lambda_s}{2}, \alpha_2 = \lambda_s + \tan^{-1} \left[ \frac{1 - \cos \lambda_s}{\sin \lambda_s} \right] \quad (4.45)$$

### 4.3.4 Ploughing Model Applications

#### 4.3.4.1 Effect of Attack Angle

In this section, the effect of attack angle ( $\lambda_s = \pi/2 - \gamma_l$ ) on chip formation has been examined using the single edge ploughing model for the zero sliding distance, ( $l_{slide}=0$ ). The ploughing angle  $\gamma_l$  is changed over what is expected to be a typical range. The resulting values of the specific cutting power are presented in Figure 4.20 and it is clear that the specific power increases very rapidly as the attack angle decreases towards zero.

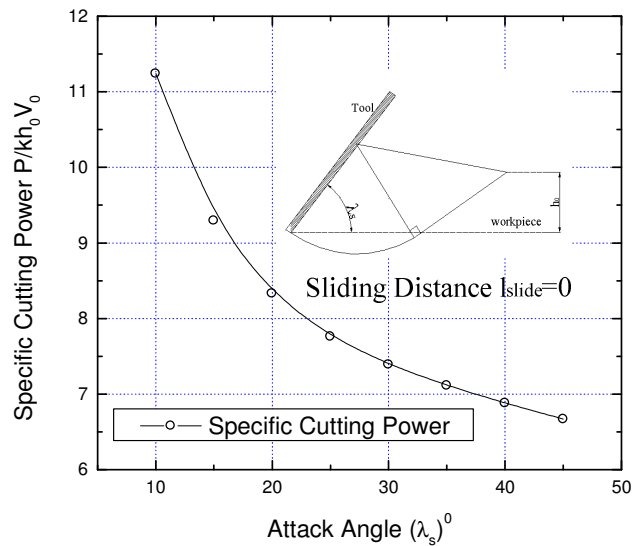
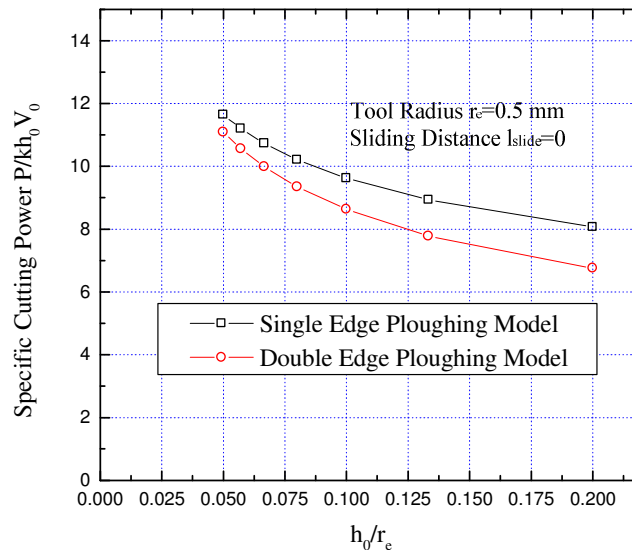


Figure 4.20 Specific cutting power versus attack angle

#### 4.3.4.2 Edge Radius Effects

The ploughing process for a tool having 0.5 mm tool edge radius has been simulated using both the single and double edge models. Figure 4.21 presents the comparison of the specific cutting power consumption using the single edge model and double edge model for various ploughing depths with zero sliding distance. Reasonable agreement is seen for the single edge and double edge models over the range of depths of ploughing testes. As expected, the force increases with increasing depth of ploughing.



**Figure 4.21** Specific ploughing power with respect to ploughing depth

#### 4.4 Transition of Ploughing to Cutting Processes

This section deals with the determination of the transition point from the ploughing process to the cutting processes. It is assumed that when the specific energy of ploughing reaches the critical specific energy of the cutting model (including the edge radius effect), the cutting process occurs. This assumption has been discussed by Felder and Bucaille (2006) who used the Merchant model to determine the critical point.

#### 4.4.1 Effect of Sliding Distance on the Single Edge Ploughing Model

The growth of the frontal bulge pattern as sliding motion proceeds was discussed by Rowe and Wetton (1969). If the wedge is moved to the right with its apex at a constant depth  $h_0$  below the surface, the volume of metal displaced will increase and the height of the bulge will increase, also. In the absence of leakage, the volume displaced will be increased by  $l_{\text{slide}}h_0$ , (for unit width). Figures 4.22, 4.23 and 4.24 plot the specific power with respect to the sliding distance for attack angles of  $\lambda_s=35^\circ$ ,  $\lambda_s=45^\circ$  and  $\lambda_s=55^\circ$ , respectively. The cutting model uses the predictive model (Section 4.2) with zero elastic friction angles. Figures 4.22-4.24 show that, as the attacking angle increases, the ploughing to cutting transformation will occur sooner. Figure 4.25 plots the slip-line field which occurs as the bulge varies in size with different sliding distances, (for a constant attack angle of 30 degrees). Figure 4.26 plots the slip-line field variation with different attack angles and a sliding distance equal to twice the uncut chip thickness.

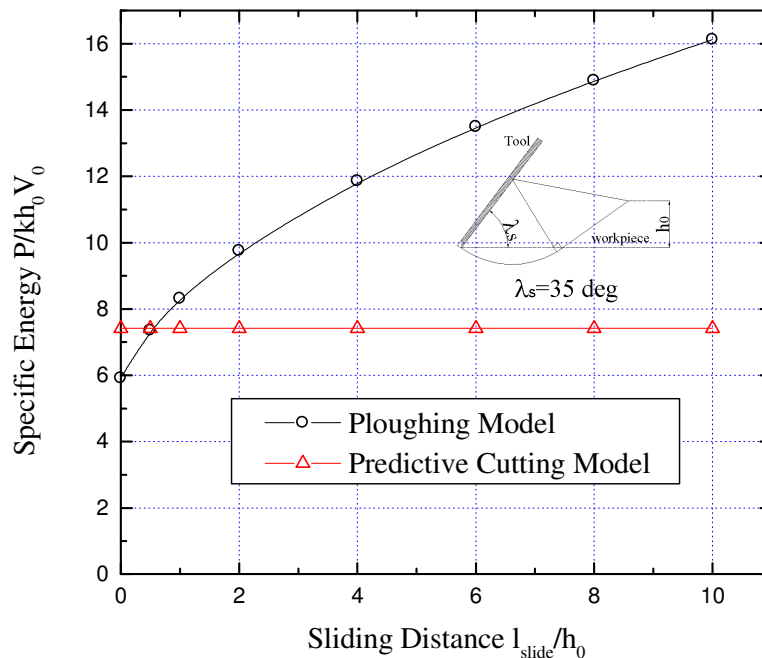


Figure 4.22 Specific power versus sliding distance for attack angle  $\lambda_s=35^\circ$

4 The Modeling of Tool Edge Ploughing Force in Milling Operations

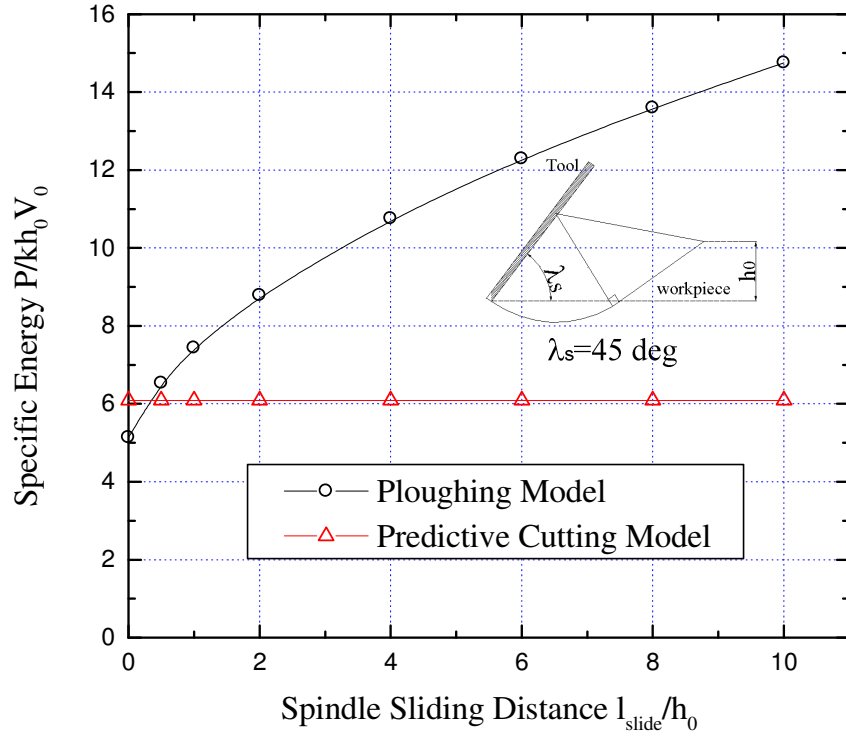


Figure 4.23 Specific power versus sliding distance for attack angle  $\lambda_s=45^\circ$

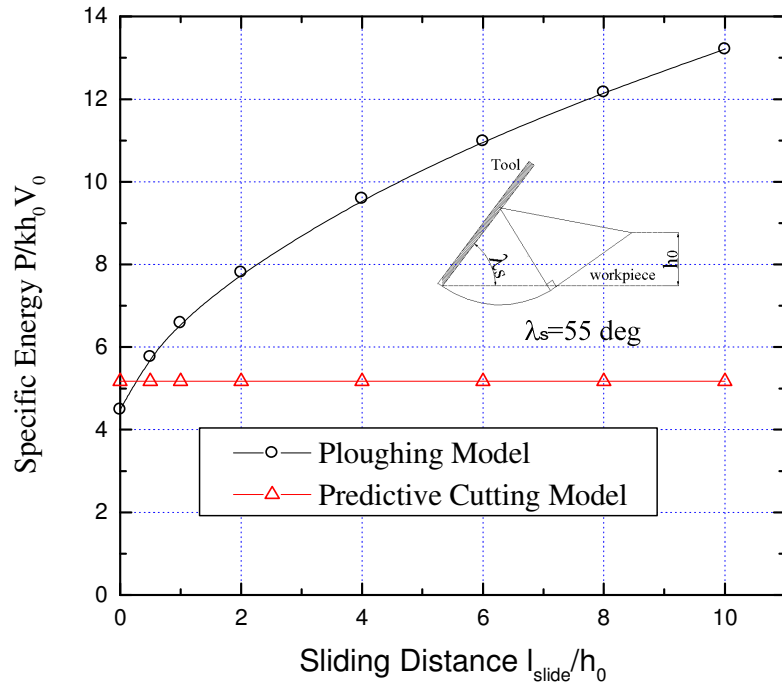
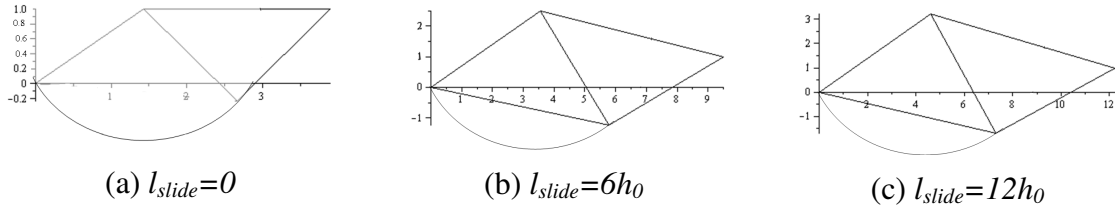
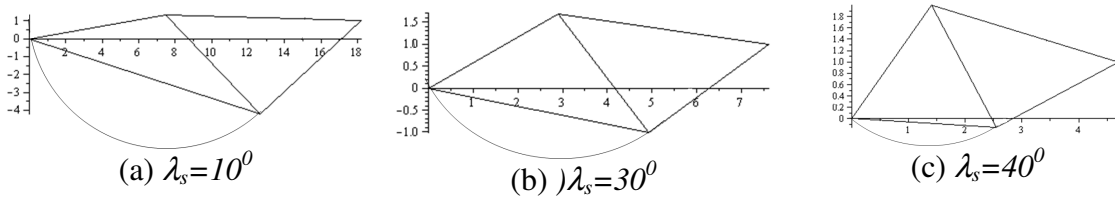


Figure 4.24 Specific power versus sliding distance for attack angle  $\lambda_s=55^\circ$

#### 4 The Modeling of Tool Edge Ploughing Force in Milling Operations



**Figure 4.25 Slip-line field variation with sliding distance for attack angle  $\lambda_s=35^\circ$**



**Figure 4.26 Slip-line field variation with attack angle for sliding distance  $l_{slide}=2h_0$**

#### 4.4.2 Effect of Sliding Distance on Double Edge Ploughing Model

The influence of sliding distance on the energy requirements predicted by the double edge model is examined in this section. Figure 4.27 plots the specific energy with respect to the sliding distance for the case of  $\gamma_1=80^\circ$ ,  $\gamma_2=55^\circ$ ,  $L_{ED}=0.5h_0$ . The result is also compared with the cutting model with a chamfer  $L_{chmf}=0.5$  and  $\beta_s=0$ . From Figure 4.27, it can be seen when sliding distance is approximately equal to the chip thickness, ( $l_{slide}=h_0$ ), the cutting process will occur. Figure 4.28 plots the slip-line field for the case of sliding distances equal to 0 and  $4h_0$ , respectively.

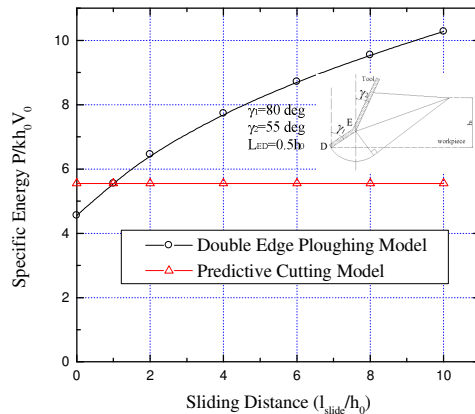


**Figure 4.27 Specific power versus sliding distance for  $\gamma_1=55^\circ$ ,  $\gamma_2=80^\circ$  and  $L_{ED}=0.5 h_0$**

## 4 The Modeling of Tool Edge Ploughing Force in Milling Operations

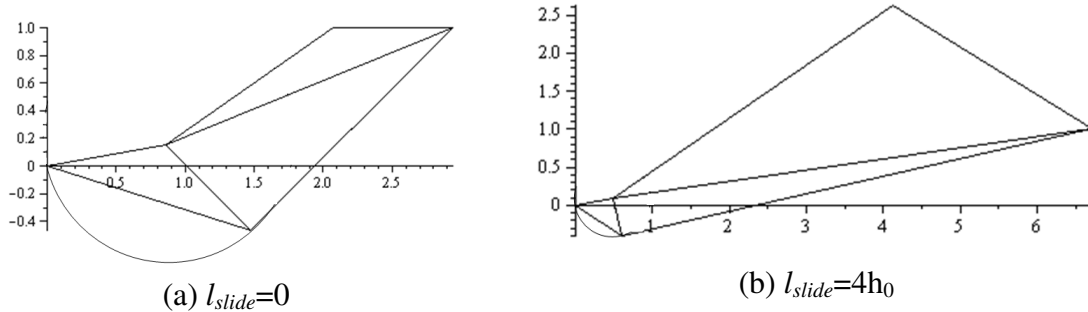


**Figure 4.28 Slip-line field with different sliding distance for ploughing angle  $\gamma_1=55^\circ$ ,  $\gamma_2=80^\circ$**

### 4.4.3 Discussion on the Entry and Exit Milling Processes

The purpose of the preceding simplified analyses has been to demonstrate that the transition from ploughing to cutting is strongly influenced by the sliding distance; there is then no simple formulation of a single critical depth of cut at which the transition will always occur. Previous authors have noticed an abrupt change in the force pattern in cutting particularly in the entry stages of up-milling. They have usually then referred to the chip thickness at which this occurs as the minimum chip thickness, (Chae et al. 1997; Miao et al. 2007; Jun et al. 2006; and Bissacco et al. 2008).

On the other hand, there is little evidence of the same phenomenon occurring in down milling exit conditions where the chip thickness variation is the mirror image to that observed in the entry to up milling. The author believes that this is due to the delay in the ploughing/cutting transition due to the build up that occurs with ploughing distance. In the case of down milling, then at the critical chip thickness, if ploughing begins, it is likely that the process will prefer to revert to cutting as the field develops and that this will continue until a condition is reached that physically precludes cutting, (This will

## 4 The Modeling of Tool Edge Ploughing Force in Milling Operations

depend upon both the effective attack angle, including the bulge and the adhesion or friction properties between chip and tool).

### 4.4.4 Validating Entry and Exit with Worn Tool Milling Operations

Experiments have been conducted previously within the Manufacturing Engineering Laboratory of UBC by Oyawoye (1993); the tests were conducted on an Adcock and Shipley universal milling machine. Cutting forces were measured with a three directional Kistler model 9257A dynamometer. A four tooth 300mm diameter face milling cutter with only one insert was used in these tests and the workpiece was a titanium alloy. (The large diameter of the cutter and large effective approach angle minimize the surface slope seen by the equivalent cutting edge.

To convert the facemilling operation with a non straight cutting edge to an equivalent straight edge orthogonal process the concepts of equivalent chip thickness and effective approach angle are used, (see Yellowley and Lai 1993). The equivalent chip thickness is defined as the uncut area of the chip over the engaged cutting length of the tool insert

$$h_e = S_t a / l_e \quad (4.46)$$

where  $l_e$  is the equivalent length,  $S_t$  is feed per tooth, and  $a$  is the depth of cut. For cutter with a finite nose radius  $r$ , the expression is approximated

$$l_e = \frac{a - r(1 - \sin \psi)}{\cos \psi} + r \left( \frac{\pi}{2} - \psi \right) + \frac{S_t}{2} \quad (4.47)$$

where  $\psi$  is the approach angle. The effective approach angle is given as

$$\psi_e = \tan^{-1} \left( \frac{(a - r(1 - \sin \psi)) \cdot \tan \psi + r \cdot \cos \psi + S_t / 2}{a} \right) \quad (4.48)$$

#### 4 The Modeling of Tool Edge Ploughing Force in Milling Operations

Therefore the measured axial force can be given as

$$F_{Axial} = F_T \cdot \sin \psi_e \quad (4.49)$$

where  $F_T$  is the thrust force.

For the milling processes, the instantaneous chip thickness can be approximated as

$$t_c(\varphi) = h_e \cdot \sin \varphi \quad (4.50)$$

where  $\varphi$  is the angle of immersion.

In the section that follows, the author intends to show that the proposed predictive cutting and ploughing models described earlier are capable in at least a qualitative manner to explain the influence of the cutting/ploughing transition on the force pattern observed with worn tools. At the entry of the cut before the ploughing/cutting critical transition point is reached, the single edge ploughing model is used for the force simulation. The modeling of force in the cutting process which follows the transition is simulated using the chamfer tool model discussed in Section 4.2. The ploughing to cutting transition occurs when cutting is feasible and the energy consumed is less than that due to ploughing, (it should perhaps be noted that energy was always less for cutting when this was feasible in the cases examined here). The forces in the exit “down milling” region are again calculated using the ploughing model; in this case however the process is assumed to operate continuously with the critical value of effective rake angle, (i.e., that above which cutting is feasible).

A comparison of the numerical simulation against the experimental result is shown in Figure 4.29. The plots are fairly close as a result of calibrating the value of shear yield stress for the simulation from the experimental data. The points to be made, however, pertain to the qualitative assessment of the shape of the plots as follows:

#### 4 The Modeling of Tool Edge Ploughing Force in Milling Operations

a) The peak in force versus the later cutting force and point of transition are seen to be in close correspondence.

b) The exit force shows no tendency for the process to revert to ploughing.

Finally it should be noted that the difference in shape of the force during exit and entry are likely due primarily to the inability of the model to include elastic contact forces in these regions.

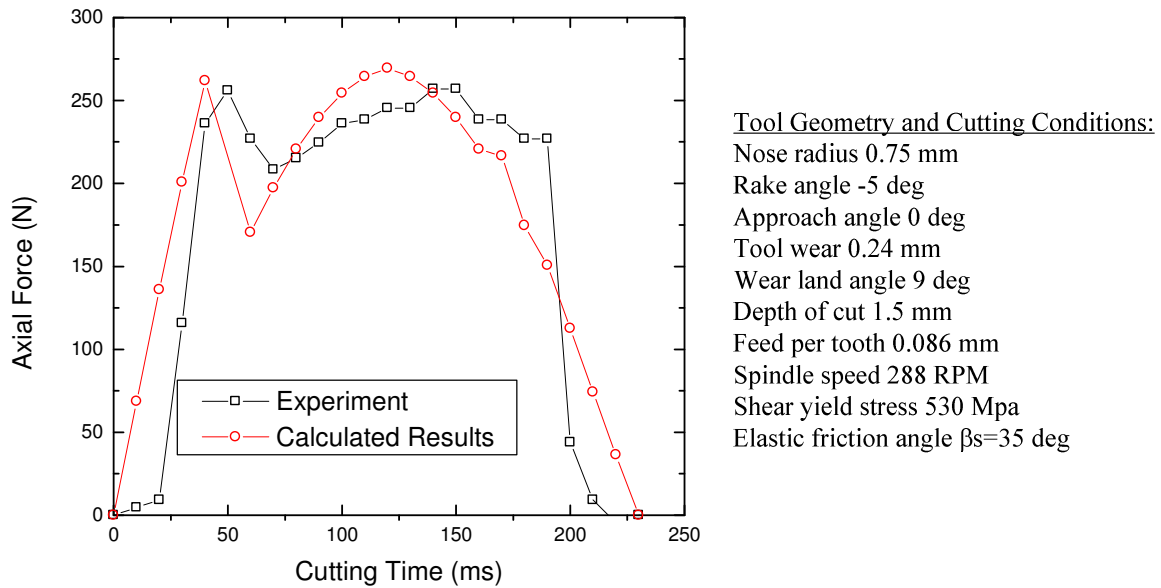


**Figure 4.29 Simulation of micromilling processes**

#### 4.5 Conclusions

The very low chip thickness in milling forces one to examine the basic mechanics of cutting with respect to the incorporation of edge influences into the normal cutting process and in the ploughing process that must inevitably occur before cutting commences.

The major contribution in this chapter is the creation of a new model of orthogonal cutting that incorporates the edge flow processes and can be used to model

#### 4 The Modeling of Tool Edge Ploughing Force in Milling Operations

rounded edge and worn tool forces. It might be noted that the author has not explicitly included the energy required for surface generation. It is believed difficult to do this because the majority of that energy is due to the plastic field accompanying the crack; such work is inevitably related to and already partially accounted for by the plastic flow field included here. The cutting model is novel being an upper bound solution which is based upon a complete slip line field solution on the chip side. One is thus able to guarantee chip equilibrium and maintain realistic rake face boundary conditions while optimizing the field below the tool and ascertaining the likely influence of chamfer, wear or edge roundness on the process at low chip thicknesses. The model does not need extensive calibration, the only unknown is the elastic friction angle and, if forces are required, a mean shear yield stress is also required. The predicted results are in good agreement with the experimental results and FEM simulations.

This chapter also presents two simple fields to model the ploughing process that may be expected in the entry and exit stages of milling with a finite edge radius or wear land. The ploughing models include the effect of sliding distance. It is found that as the tool slides, the energy will continue to rise and it becomes preferable for the process to move. The models have been used as a tool to qualitatively explain the entry and exit force characteristics during milling operations.

## **5 A New Predictive Model for Peripheral Milling Operations**

### **5.1 Introduction**

Milling is one of the most important manufacturing operations; it differs from most other cutting operations in the magnitude of typical chip thickness, the variation in chip thickness, the surface slope at the free surface and the discontinuous nature of the process. Typical milling practice most often leads to widths of cut that are less than cutter radius and hence to relatively few teeth in cut. One may argue that larger widths are much more economic but that is not the normal approach adopted; moreover in finish or semi finish milling this is likely to be the case, even with good practice. The finished surface is then produced most often with just a single tooth in contact and with extremely low chip thickness. It is seen then that where force prediction and material flow patterns are most important than the use of typical force modeling approaches and equations from turning or similar sources are unlikely to be particularly useful. The increasing importance of meso and micromilling operations has led to more interest in such matters, however it needs to be remembered that the conventional milling process will always exhibit similar complexity during the time that the surface is actually being generated.

A lot of attention has been concentrated on the prediction of cutting forces over the last few decades; the mechanistic approach has gained by far the most amount of popularity (Koenigsberger and Sabberwal 1961; Tlusty and MacNeil 1975; Fu et al. 1984). This is because of the simplicity involved in building empirical coefficients in the model which result in accurate force predictions. A mechanistic force model relates cutting forces to uncut chip sectional area through a set of coefficients. These cutting

force coefficients, which are comprised of the specific cutting pressure coefficients and the chip flow angle, are extracted from the measured forces. Two basic calibration approaches are often used in the literature: an empirical parameter fitting approach (Koenigsberger and Sabberwal 1961; Kline et al. 1982; Engin and Altintas 2001), and an orthogonal to oblique transformation approach (Armarego and Deshpande 1991; Budak et al. 1996; Armarego 2000). Generally, both calibration procedures provide only one set of average cutting force coefficients from each cutting tests. In order to obtain a robust application range from the related cutting force model, a great number of tests must be performed for different feeds, depths of cut, etc.

This chapter is concerned with the building of a model of oblique cutting operations which is suited to the analysis of tools with non straight cutting edges and non planar rake faces, (primarily milling, drilling, and tapping operations). The application of the newly developed oblique cutting model (Zou, Yellowley and Seethaler 2009) to the milling processes is described in detail. The model is provided with a suitable material constitutive equation, to allow the consideration of the influence of chip thickness on yield strength and the edge force components are also estimated allowing some degree of confidence at low values of chip thickness. Also the potential influences of surface slope as well as the complex kinematics are examined.

### **5.2 The Development of a Methodology to Estimate Milling Forces**

As described earlier, a theoretical model of the milling process is made difficult by the fact that the milling process creates chip thicknesses that are both small and variable; moreover during surface creation the rate of change of chip thickness is high. The author believes that any theoretical approach must then consider the following:

## 5 A New Predictive Model for Peripheral Milling Operations

- a) The influence of chip thickness on both the shear yield stress in the shear plane and the corresponding normal stress which is influenced by both geometry and work hardening across the shear zone;
- b) The influence of surface slope on the equilibrium value of shear angle;
- c) The estimation of the likely magnitude of edge forces that may be attributed to the flow of the work material under the cutting edge;
- d) For very small chip thickness there should be some mechanism to allow a switch between ploughing and cutting models as well as to estimate forces in the regime;
- e) The helical edge complicates the kinematics of the process and it is not sufficient to simply estimate forces on elemental lengths of edge and then integrate to estimate total forces acting upon the cutter. As the chip flows inward there is evidently additional deformation which, though small, needs to be estimated in any scheme that tries to avoid such issues through calibration rather than through the use of basic physical properties.

The block diagram of the proposed predictive approach is given in Figure 5.1. The basic equations needed to address the concerns enumerated above are outlined in the next sections; following this the overall software model developed to calculate cutting forces is described. Finally, an experimental program and verification of the model are presented in the following chapter.

## 5 A New Predictive Model for Peripheral Milling Operations

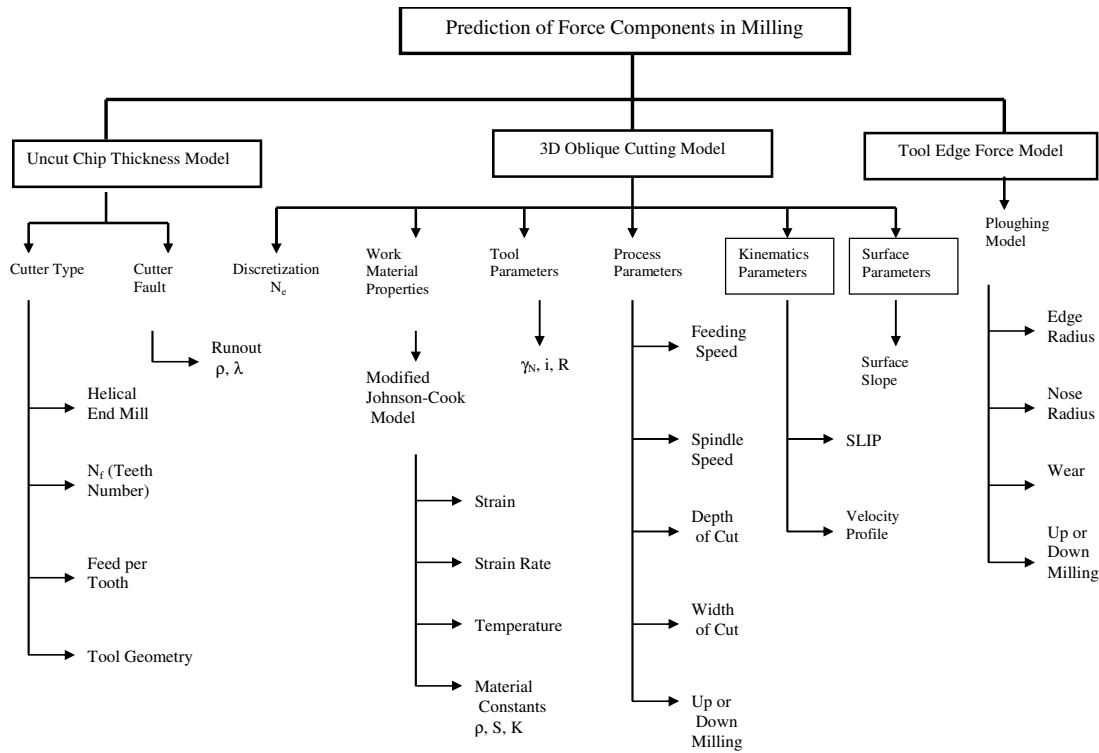


**Figure 5.1 Diagram of predictive model**

### 5.3 The Estimation of Oblique Cutting Forces

The first step in the development of the force model is to estimate the force acting upon an element of cutting edge engaged in an oblique cutting operation with essentially constant chip thickness. This requires the use of a suitable constitutive equation and knowledge of strain, strain rate and temperature, as well as the edge force attributed by the surface generation at the tool edge. This problem is addressed here while later sections address the influence of the remaining process variables on the force components.

#### 5.3.1 Deformation Energy Dissipation on the Shear Plane

The rate of plastic energy dissipation in the shear plane can be expressed as

## 5 A New Predictive Model for Peripheral Milling Operations

$$P_s = F_s V_s = h_0 w V_0 \int_0^{\bar{\epsilon}} \sigma \cdot d\bar{\epsilon} \quad (5.1)$$

where  $\bar{\epsilon}$  is the equivalent oblique cutting plastic strain, which can be written as (Atkins 2006)

$$\bar{\epsilon} = \frac{\gamma_{oblique}}{\sqrt{3}} = \frac{\cot \gamma_N + \tan(\phi_N - \gamma_N)}{\sqrt{3} \cos \eta_s} \quad (5.2)$$

According to the Johnson-Cook model, the von Misses flow stress  $\sigma$ , is given by (Jaspers and Dautzenberg 2002)

$$\sigma = (A + B\epsilon^n) \left[ 1 + C_m \ln \left( \frac{\dot{\epsilon}}{\dot{\epsilon}_0} \right) \right] (1 - T^{*m}) \quad (5.3)$$

where  $\dot{\epsilon}/\dot{\epsilon}_0$  is the dimensionless strain rate for  $\dot{\epsilon}_0 = 1.0s^{-1}$  and  $A$ ,  $B$ ,  $C_m$ ,  $n$ , and  $m$  are material constants. The shear strain rate is estimated as follows

$$\dot{\epsilon} = \frac{\dot{\gamma}_{oblique}}{\sqrt{3}} = \frac{V_s}{\sqrt{3} \cdot \Delta y} = Const \frac{V_s}{\sqrt{3} l_{shear}} \quad (5.4)$$

where  $\Delta y$  is the width of the shear zone, which is assumed to have a constant relationship with shear plane length ( $l_{shear}$ ).

The relationship between the absolute temperature  $T$  and thermal softening term  $T^*$  is expressed as

$$T^* = (T - T_{room}) / (T_{melt} - T_{room}) \quad (5.5)$$

where  $T_{room}$  and  $T_{melt}$  are the room temperature and the melting point of the specific alloy, respectively. The Johnson-Cook model assumes the slope of the flow stress curve to be independently affected by strain, strain rate and temperature represented by the terms in each set of brackets.

## 5 A New Predictive Model for Peripheral Milling Operations

Substituting Eqn. (5.3) into Eqn. (5.1), the rate of plastic energy dissipation in the shear plane can be derived as

$$P_s = h_0 w V_0 \left[ A \bar{\epsilon} + \frac{B}{n+1} \bar{\epsilon}^{n+1} \right] \cdot \left[ 1 + C_m \ln \dot{\bar{\epsilon}}^* \right] \cdot \left[ 1 - T^{*m} \right] \quad (5.6)$$

The increased temperature in the shear zone can be calculated as follows (Loewen and Shaw 1954, Lei et al. 1999)

$$\Delta T = x \frac{P_s}{\rho S} (1 - \eta) = x \frac{\int \sigma d\bar{\epsilon}}{\rho S} \xi \quad (5.7)$$

where  $x$  is the ratio of plastic energy converted to heat, and  $\xi = 1 - \eta$  is the fraction of the heat remaining in shear zone. According to Lei et al. (1999),  $\xi$  can be estimated from the expression

$$\xi = \frac{1}{1 + 1.328 \sqrt{\frac{\gamma_{oblique} K}{\rho S V_0 h_0}}} \quad (5.8)$$

where  $\rho$ ,  $S$  and  $K$  are the workpiece material density, specific heat, and thermal conductivity, respectively.

### 5.3.2 Friction Energy Dissipation at the Tool-chip Interface

The rate of energy dissipated by friction at the tool-chip interface can be written as

$$P_f = F_f \cdot V_c \quad (5.9)$$

where  $F_f$  is the friction force. The shear velocity  $V_s$  and chip velocity  $V_c$  can be given in terms of the *SLIP* on the rake face in the oblique cutting process (Zou, Yellowley and Seethaler 2009)

## 5 A New Predictive Model for Peripheral Milling Operations

$$V_{cn} = \frac{V_0 \cos i \cdot \sin \phi_N}{\cos(\phi_N - \gamma_N)}, \quad V_{ct} = (1 - SLIP) \cdot V_0 \cdot \sin i \quad (5.10)$$

$$V_{sn} = \frac{V_0 \cos i \cdot \cos \gamma_N}{\cos(\phi_N - \gamma_N)}, \quad V_{st} = SLIP \cdot V_0 \cdot \sin i$$

and

$$V_c = (V_{cn}^2 + V_{ct}^2)^{\frac{1}{2}}, \quad V_s = (V_{sn}^2 + V_{st}^2)^{\frac{1}{2}} \quad (5.11)$$

$$\eta_s = \tan^{-1}\left(\frac{V_{st}}{V_{sn}}\right), \quad \eta_c = \tan^{-1}\left(\frac{V_{ct}}{V_{cn}}\right)$$

where  $\phi_N$  is the normal shear angle,  $\gamma_N$  the normal rake angle,  $\eta_s$  the shear plane flow angle, and  $\eta_c$  the chip flow angle, shown in Figure 5.2.

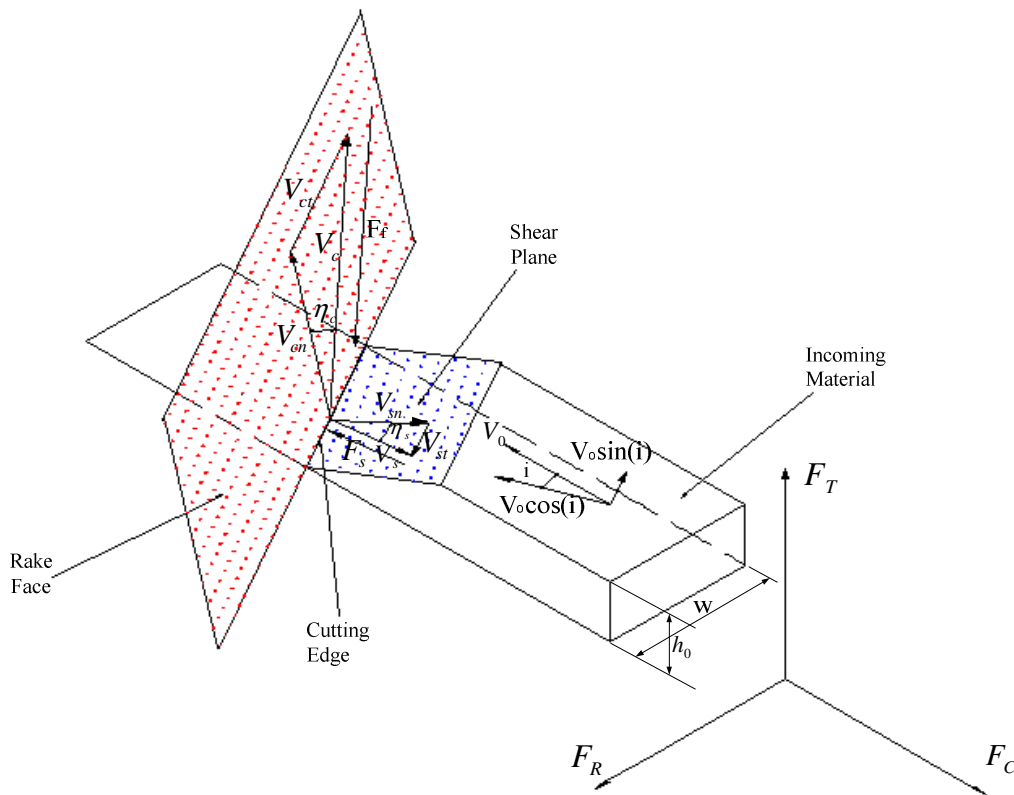


**Figure 5.2** Coordinate system of oblique cutting

The total internal work rate is given by the summation of Eqns. (5.6) and (5.9). The external work rate is given by  $F_c V_0$ . Thus, the energy equation for oblique cutting is given as

$$F_c V_0 = h_0 w V_0 \left[ A \bar{\epsilon} + \frac{B}{n+1} \bar{\epsilon}^{n+1} \right] \cdot [1 + C_m \ln \dot{\bar{\epsilon}}^*] \cdot [1 - T^{*m}] + F_f V_c \quad (5.12)$$

### 5.4 The Influence of Work Hardening on the Average Normal Stress in the Shear Plane

The influence of work hardening on the average normal stress in the shear plane is estimated based on the application of force equilibrium in the normal shear plane as shown in Figure 5.3.

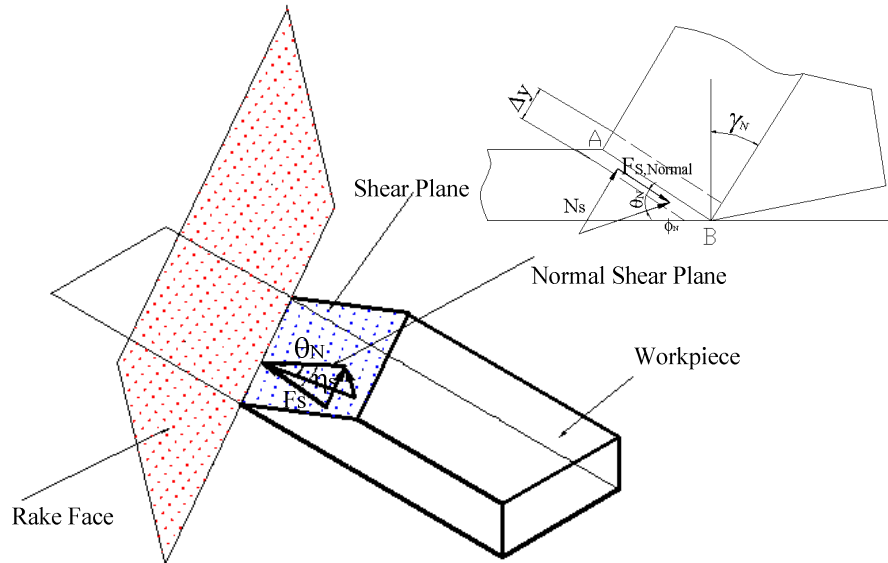


**Figure 5.3 Normal shear plane for oblique cutting**

The angle  $\theta_N$  between the shear force and the normal force on the normal shear plane is calculated as follows (Lin et al. 1982, Oxley 1989)

## 5 A New Predictive Model for Peripheral Milling Operations

$$\tan \theta_N = 1 + 2 \left( \frac{\pi}{4} - \phi_N \right) - \left( \frac{\Delta k^N}{\Delta s_{2N}} \right)_{AB} \frac{l_{AB}^N}{2k_{AB}^N} \quad (5.13)$$

where  $\left( \frac{\Delta k^N}{\Delta s_{2N}} \right)_{AB}$  is the variation of the shear flow stress across the width at the parallel

sided shear zone (Oxley 1989). This term is evaluated in the following manner:

$$\left( \frac{dk^N}{ds_{2N}} \right)_{AB} = \left( \frac{dk^N}{d\gamma^N} \right)_{AB} \cdot \left( \frac{d\gamma^N}{dt} \right)_{AB} \cdot \left( \frac{dt}{ds_{2N}} \right)_{AB} \quad (5.14)$$

where

$$l^N = \frac{h_0}{\sin \phi_N}, \quad V_s^N = \frac{V_0 \cos i \cdot \cos \gamma_N}{\cos(\phi_N - \gamma_N)} \quad (5.15)$$

$\gamma_N$  is the rake angle. The strain along the normal shear plane is given as (Oxley 1989, Lin et al. 1982)

$$\epsilon_{AB}^N = \frac{1}{2\sqrt{3}} \frac{\cos \gamma_N}{\sin \phi_N \cdot \cos(\phi_N - \gamma_N)} \quad (5.16)$$

The strain rate along the shear zone AB is given as

$$\dot{\epsilon}_{AB}^N = Const \frac{V_{sn}}{\sqrt{3}l^N} \quad (5.17)$$

Therefore, the shear flow stress along AB using the Johnson-Cook model can be written as

$$\sigma_{AB}^N = \left( A + B \epsilon_{AB}^N \right) \cdot \left[ 1 + C_m \ln \left( \frac{\dot{\epsilon}_{AB}^N}{\dot{\epsilon}_0} \right) \right] \cdot \left( 1 - T_{AB}^{*m} \right) \quad (5.18)$$

Each of the above terms may be evaluated independently. The derivatives in Eqn. (5.14) can be expressed as

## 5 A New Predictive Model for Peripheral Milling Operations

$$\begin{aligned} \left( \frac{dk^N}{d\gamma^N} \right)_{AB} &= \frac{d(\sigma_{AB}^N / \sqrt{3})}{d(\sqrt{3}\epsilon_{AB}^N)} = \frac{1}{3} \frac{d\sigma_{AB}^N}{d\epsilon_{AB}^N}, \quad \left( \frac{dt}{ds_{2N}} \right)_{AB} = \frac{1}{V_0 \cos i \cdot \sin \phi_N} \\ \left( \frac{d\gamma^N}{dt} \right)_{AB} \left( \frac{dt}{ds_{2N}} \right)_{AB} &= \text{Const} \frac{V_{sn}}{l^N} \frac{1}{V_0 \cos i \cdot \sin \phi_N} \end{aligned} \quad (5.19)$$

Then

$$\left( \frac{\Delta k^N}{\Delta s_{2N}} \right)_{AB} \frac{l^N}{2k_{AB}^N} = \text{Const} \cdot n_{eqv} \quad (5.20)$$

where

$$n_{eq} = \left( \frac{d\sigma_{AB}^N}{d\epsilon_{AB}^N} \right) \left( \frac{\epsilon_{AB}^N}{\sigma_{AB}^N} \right) = (c_1 + c_2 \cdot c_3) \cdot \left( \frac{\epsilon_{AB}^N}{\sigma_{AB}^N} \right) \quad (5.21)$$

in which

$$\begin{aligned} c_1 &= nB\epsilon_{AB}^{N \ n-1} \left( 1 + C_m \ln \frac{\dot{\epsilon}_{AB}^N}{\dot{\epsilon}_0} \right) \cdot \left( \frac{T_{melt} - T_{AB}}{T_{melt} - T_{room}} \right)^m \\ c_2 &= (A + B\epsilon_{AB}^{N \ n}) \cdot \left( 1 + C_m \ln \frac{\dot{\epsilon}_{AB}^N}{\dot{\epsilon}_0} \right) \cdot \left( \frac{-m(T_{AB}^*)^{m-1}}{T_{melt} - T_{room}} \right) \\ c_3 &= \left( \frac{\partial T}{\partial \epsilon} \right)_{AB} = \frac{T_u - T_l}{2\epsilon_{AB}^N} \end{aligned} \quad (5.22)$$

where  $T_u$  and  $T_l$  are the temperatures at the upper and lower boundaries along the normal shear plane, respectively.  $T_u$  and  $T_l$  can be obtained by substituting the strain and strain rate at the upper and lower boundary of shear zone as well as the Johnson-Cook model into Eqn. (5.7). Thus the normal friction angle can be given as

$$\beta_N = \theta_N - \phi_N + \gamma_N \quad (5.23)$$

and the friction angle along the chip flow direction is

$$\beta = \tan^{-1} \left( \frac{\tan \beta_N}{\cos \eta_c} \right) \quad (5.24)$$

where  $\eta_c$  is the chip flow angle.

### 5.5 The Estimation of Edge Force Components

The edge force occurring in orthogonal cutting analysis is discussed in Chapter 4, the orthogonal edge forces need to be transformed into a three-dimensional coordinate system. It is assumed that the orthogonal edge forces act on the velocity plane in this case. The velocity rake angle is given as

$$\tan \gamma_v = \frac{\tan \gamma_N}{\cos i} \quad (5.25)$$

Then the orthogonal cutting force,  $F'_{CE}$ , and thrust force,  $F'_{TE}$ , become the 3D force,  $F_{CE}$  and  $F_{TE}$ , respectively, which can be expressed

$$\begin{cases} F_{CE} = F'_{CE} \\ F_{TE} = F'_{TE} \\ F_{RE} = 0 \end{cases} \quad \text{for } h_0 \geq h_{\min} \quad (5.26)$$

where  $h_{\min}$  is the minimum chip thickness. As discussed previously, when the uncut chip thickness is less than the minimum chip thickness at the entry or exit region, the total forces are mainly caused by either the ploughing processes (entry) or the high negative rake cutting process (exit). The 2D ploughing forces should also be transformed to the force components in oblique cutting as

$$\begin{cases} F_{CE} = F'_{CP} \\ F_{TE} = F'_{TP} \\ F_{RE} = 0 \end{cases} \quad \text{entry,} \quad \text{or} \quad \begin{cases} F_{CE} = F'_{CH} \\ F_{TE} = F'_{TH} \\ F_{RE} = 0 \end{cases} \quad \text{exit for } h_0 < h_{\min} \quad (5.27)$$

where  $F'_{CP}$  and  $F'_{TP}$  are the ploughing forces at the entry process, while  $F'_{CH}$  and  $F'_{TH}$  are the high negative rake cutting forces occurring at the exit process.

## 5.6 The Effect of Work Surface Slope

The effect of surface slope on milling has been studied by Pandey and Shen (1972) and Altintas (1986). Pandey and Shan (1972) examined the slope change due to the advancement of shear plane, while Altintas (1986) only considered the chip thickness variation. The work surface slope caused by both the relative angle of the tool edge and the free end of the shear plane as well as the variation of uncut chip thickness is examined in this section. The relationship between the surface slope and shear angle is examined as well.

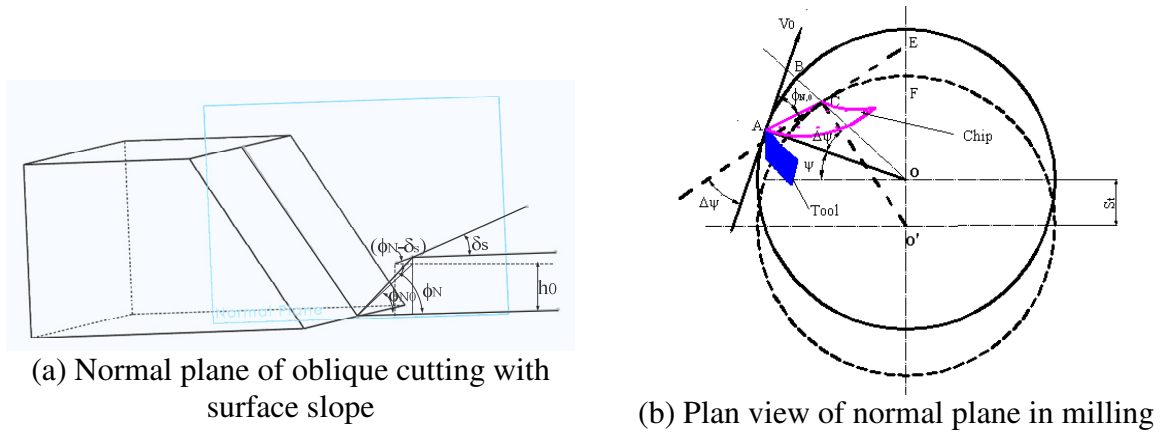
### 5.6.1 Surface Slope Formations

Figure 5.4 shows the surface slope change caused by the relative position of the tool edge and the free end of the shear plane during up milling operations. At the tooth rotation angle  $\psi$ , the work material is assumed to be sheared along the plane AC and the corresponding shear angle is represented by  $\phi_{N0}$ . The uncut chip thickness at the point of cutting is BC. Surface slope caused by the curvature of the workpiece is represented by  $\Delta\psi$ , which is a function of the cutter diameter and feedrate in milling operations, and can be approximated as

$$\Delta\psi \approx \frac{S_t \sin \psi \cdot \cot \phi_{N0}}{R} \quad (5.28)$$

On the other hand, the surface slope caused by the variation of uncut chip thickness ( $h = S_t \sin \psi$ ) can be derived as

$$\lambda = \tan^{-1} \frac{dh}{ds} = \tan^{-1} \left( \frac{d(S_t \sin \psi)}{R d\psi} \right) = \tan^{-1} \left( \frac{S_t \cos \psi}{R} \right) \approx \frac{S_t \cos \psi}{R} \quad (5.29)$$



**Figure 5.4 Slope variation in milling**

Therefore the total surface slope  $\delta_s$  in milling can be taken a simple summation of Eqn. (5.27) and (5.28)

$$\delta_s = \Delta\psi + \lambda = \frac{S_r}{R} [\sin\psi \cdot \cot\phi_{N0} + \cos\psi] \quad (5.30)$$

In wave removing, it is generally assumed that the shear angle is a linear function of work surface slope, i.e.

$$\phi_N = \phi_{N0} + C_s \cdot \delta_s \quad (5.31)$$

where  $\phi_{N0}$  is the normal shear angle when the work surface slope  $\delta_s$  is zero and  $C_s$  is a constant. Shaw and Sanghani (1963) performed experiments to measure shear angle during the cutting of a wavy surface and indicated that a  $C_s$  of close to unity results. Wallace and Andrew (1965) found the value of  $C_s$  to be 0.75 from their wave removing experiments. The purpose of the following analysis is to investigate the influence of surface slope variation on the shear angle. Two cases are examined: 1) frictionless orthogonal cutting, and 2) oblique cutting process.

### 5.6.2 Frictionless Orthogonal Cutting

The geometry of the orthogonal cutting model having surface slope  $\delta_s$  is shown in Figure 5.5. From Figure 5.5, the geometry relationship can be written as

$$\frac{l_s}{\sin(\pi/2 + \delta_s)} = \frac{l_s}{\cos \delta_s} = \frac{h_0}{\sin(\phi - \delta_s)} \quad (5.32)$$

Then the shear plane length is given by

$$l_s = \frac{h_0 \cos \delta_s}{\sin(\phi - \delta_s)} \quad (5.33)$$

The total cutting power for the frictionless case is given by

$$P = F_s V_s = k l_s w V_0 \frac{\cos \gamma}{\sin(\phi - \gamma)} = \frac{k \cos \delta_s \cos \gamma}{\sin(\phi - \delta_s) \sin(\phi - \gamma)} h_0 w V_0 \quad (5.34)$$

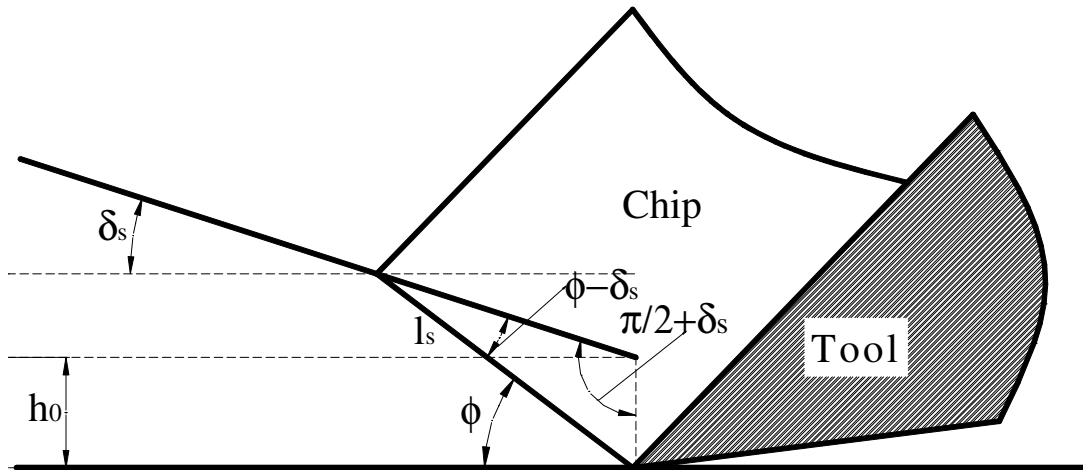


Figure 5.5 Orthogonal model with surface slope

The derivative of  $P$  with respect to  $\phi$ , yields

$$\frac{dP}{d\phi} = \cos \delta_s \cdot \cos \gamma \cdot [\sin(2\phi - \delta_s - \gamma)] = 0 \quad (5.35)$$

The relationship of shear angle with surface slope can be stated as

$$2\phi - \delta_s - \gamma = 0 \quad (5.36)$$

Thus,  $C_s$  for the frictionless case is equal to 0.5, i.e.

$$C_s = 0.5 \quad (5.37)$$

### 5.6.3 Oblique Cutting Model

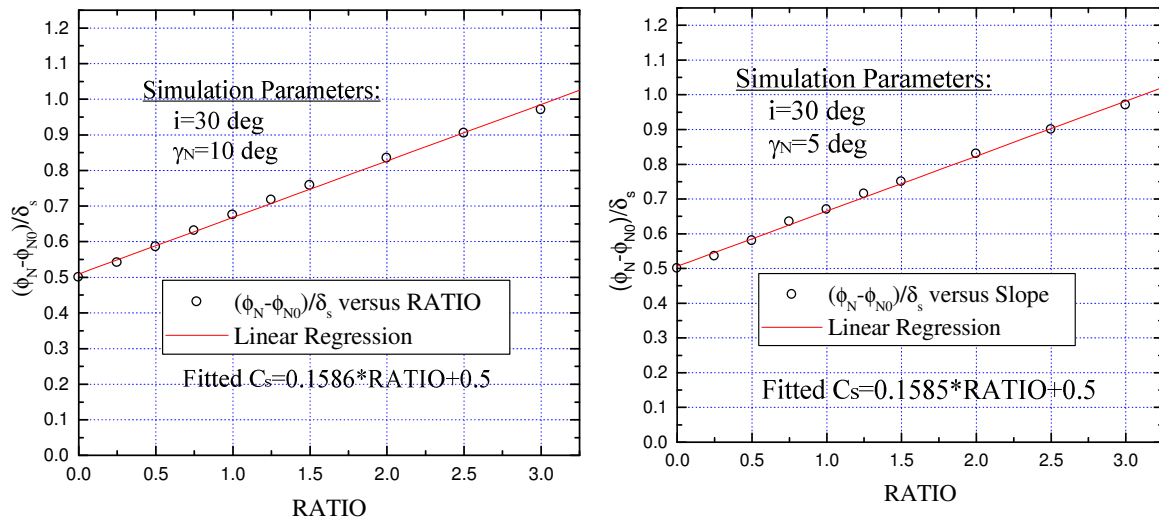
The power consumed in oblique cutting is given by

$$P = kA_s V_s + k \cdot \text{RATIO} \cdot A_s \cdot V_c \quad (5.38)$$

where  $A_s$  is the area of the shear plane having a surface slope

$$A_s = \frac{h_0 w \cdot \cos \delta_s}{\sin(\phi_N - \delta_s) \cdot \cos i} \quad (5.39)$$

Further, if one adopts the optimization algorithms developed for the oblique cutting process (Zou, Yellowley and Seethaler 2009), the relationship between the shear angle change with respect to slope) and  $\text{RATIO}$  is easily calculated. The result is shown in Figure 5.6 for an inclination angle of 30 degrees.



(a)  $i=30^0, \gamma_N=10^0$

(b)  $i=30^0, \gamma_N=5^0$

**Figure 5.6 Shear angle relationship with  $\text{RATIO}$**

It can be observed from Figures 5.6 (a) and (b) that the linear fitted parameter  $C_s$  changes very little for both  $\gamma_N=10^0$  and  $\gamma_N=5^0$ , which can be approximated as

$$C_s = 0.159 \cdot \text{RATIO} + 0.5 \quad (5.40)$$

## 5.7 Force Prediction Based on the Shear Plane Forces

After one obtains the work surface slope, the shear force along the shear plane can be rewritten in the form

$$F_s = \frac{kwh_0 \cos \delta_s}{\cos i \cdot \sin(\phi_N - \delta_s)} \quad (5.41)$$

where  $\phi_N$  is the normal shear angle given by Eqn. (5.31). The normal resultant angle  $\theta_N$  and mean nominal friction angle  $\beta_N$  based on Oxley's machining theory (see Section 5.2) are

$$\begin{aligned} \theta_N &= \tan^{-1} \left[ 1 + 2 \left( \frac{\pi}{4} - \phi_N + \delta_s \right) - \text{Const} \cdot n_{eqv} \right] \\ \beta_N &= \theta_N - \phi_N + \gamma_N \end{aligned} \quad (5.42)$$

The friction angle along the chip flow direction is

$$\beta = \tan^{-1} \left( \frac{\tan \beta_N}{\cos \eta_c} \right) \quad (5.43)$$

Thus the resultant force  $R_{tool}$  can be obtained based on the force balance between the shear plane and the tool rake face as follows

$$R_{tool} = \frac{F_s \cos \eta_s}{\cos \beta \cdot [\cos(\phi_N - \gamma_N) - \tan \beta \cdot \cos \eta_c \cdot \sin(\phi_N - \gamma_N)]} \quad (5.44)$$

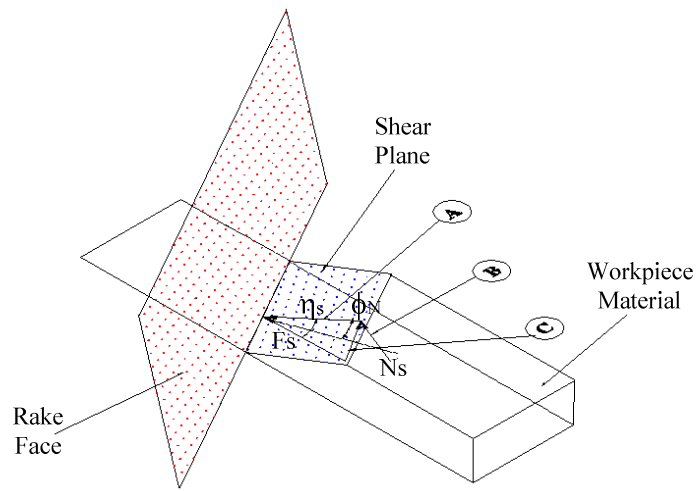
Based on the force balance on the plane perpendicular to the normal shear plane, the normal force in the shear plane can be derived as

## 5 A New Predictive Model for Peripheral Milling Operations

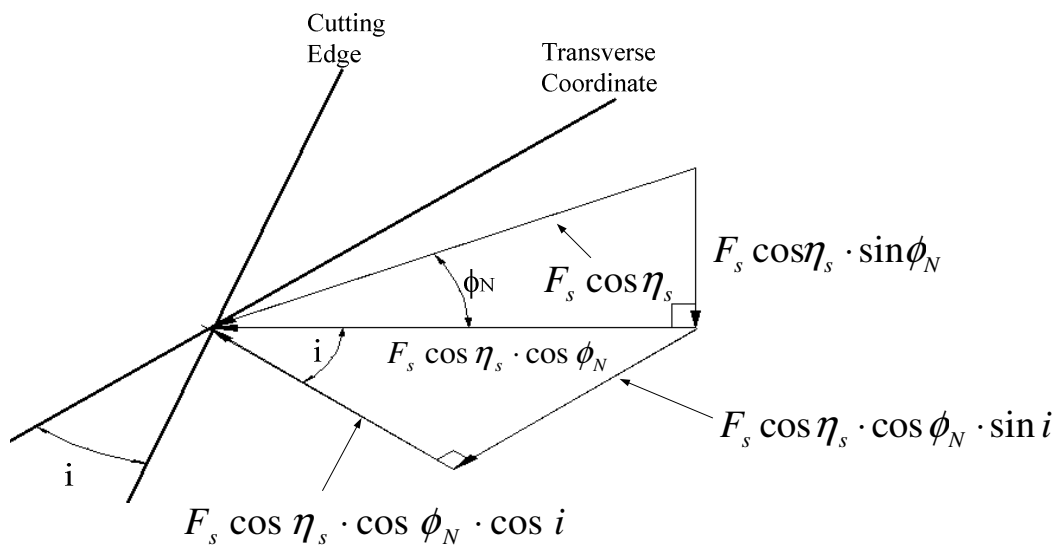
$$\begin{aligned}
 N_s &= F_s \cos \eta_s \tan \theta_N \\
 &= R_{tool} \cdot \cos \beta \cdot [\sin(\phi_N - \gamma_N) + \tan \beta \cdot \cos \eta_c \cdot \cos(\phi_N - \gamma_N)]
 \end{aligned}
 \tag{5.45}$$

The force diagram at the shear plane is shown in Figure 5.7 and the global force based on the shear plane can be given as

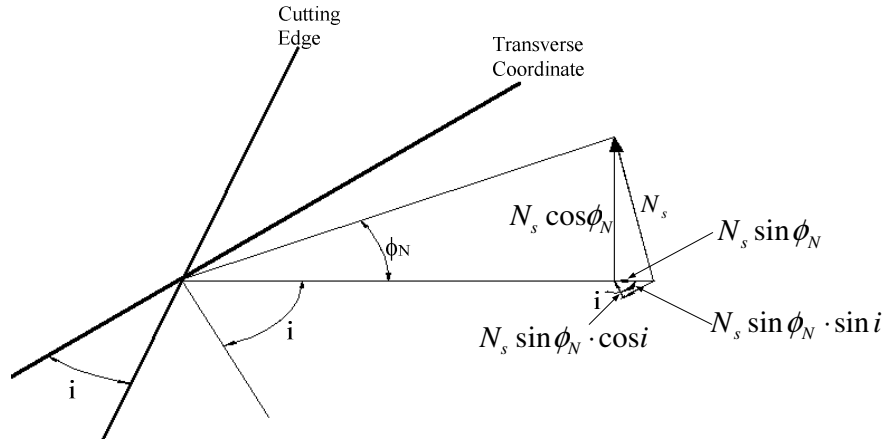
$$\begin{aligned}
 F_C &= F_s \sin \eta_s \cdot \sin i + F_s \cos \eta_s \cdot \cos \phi_N \cdot \cos i + N_s \sin \phi_N \cdot \cos i \\
 F_T &= N_s \cos \phi_N - F_s \cos \eta_s \cdot \sin \phi_N \\
 F_R &= F_s \sin \eta_s \cdot \cos i - F_s \cos \eta_s \cdot \cos \phi_N \cdot \sin i - N_s \sin \phi_N \cdot \sin i
 \end{aligned}
 \tag{5.46}$$



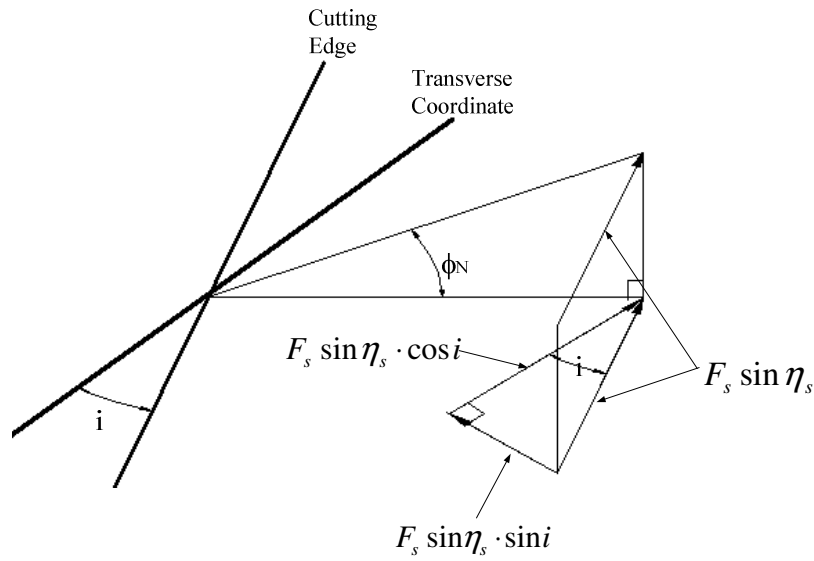
(a) 3-D shear plane forces



(b) Shear force perpendicular to cutting edge (Part A)



(c) Shear plane normal force (Part B)



(d) Shear force parallel to cutting edge (Part C)

**Figure 5.7 Force diagram for the shear plane**

## 5.8 Kinematics of Helical End Milling Tools

This section is concerned with the integration of the previous material into a model that is suited to the analysis of tools with helical cutting edges and non-planar rake faces, (primarily milling, drilling, and tapping operations).

### 5.8.1 Coordinate System and Velocity Relationship

The helical flute cutter coordinate system and the corresponding oblique cutting coordinate system are shown in Figure 5.8. The coordinate transformation matrix for the coordinate  $(x, y, z)$  to the coordinate  $(x', y', z')$  can be obtained through two angular transformations:

1) Rotate along the  $x$  axis with angle  $i$ ; the transformation matrix can be written as

$$R_x(i) = \begin{bmatrix} 1 & 0 & 0 \\ 0 & \cos i & -\sin i \\ 0 & \sin i & \cos i \end{bmatrix} \quad (5.47)$$

2) Rotate along  $y$  axis with angle  $\gamma_N$ ; the transformation matrix can be written as

$$R_y(\gamma_N) = \begin{bmatrix} \cos \gamma_N & 0 & \sin \gamma_N \\ 0 & 1 & 0 \\ -\sin \gamma_N & 0 & \cos \gamma_N \end{bmatrix} \quad (5.48)$$

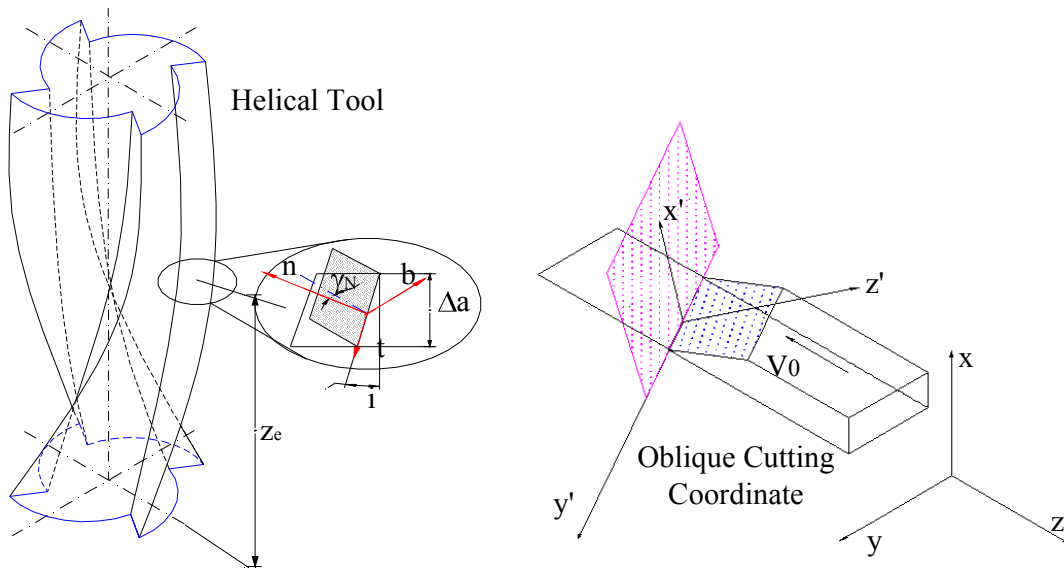


**Figure 5.8 Geometry of helical tool system**

Thus the coordinate transformation from  $(x, y, z)$  to  $(x', y', z')$  can be written as

$$\begin{aligned}
 \begin{Bmatrix} u_{x'} \\ u_{y'} \\ u_{z'} \end{Bmatrix} &= [R_y(\gamma_N)]^T \cdot [R_x(i)]^T = \begin{bmatrix} \cos \gamma_N & 0 & -\sin \gamma_N \\ 0 & 1 & 0 \\ \sin \gamma_N & 0 & \cos \gamma_N \end{bmatrix} \begin{bmatrix} 1 & 0 & 0 \\ 0 & \cos i & \sin i \\ 0 & -\sin i & \cos i \end{bmatrix} \begin{Bmatrix} u_x \\ u_y \\ u_z \end{Bmatrix} \\
 &= \begin{bmatrix} \cos \gamma_N & \sin \gamma_N \cdot \sin i & -\sin \gamma_N \cdot \cos i \\ 0 & \cos i & \sin i \\ \sin \gamma_N & -\cos \gamma_N \cdot \sin i & \cos \gamma_N \cdot \cos i \end{bmatrix} \begin{Bmatrix} u_x \\ u_y \\ u_z \end{Bmatrix}
 \end{aligned} \tag{5.49}$$

where  $\gamma_N$  is the normal rake angle, and  $i$  the inclination angle. Coordinates  $x$ ,  $y$ , and  $z$  denote the uncut chip plane and coordinates  $x'$ ,  $y'$ , and  $z'$  denote the rake face coordinate system. Considering the velocity field along the tool radius direction ( $u_r$ ) and along the tangential direction on helical surface ( $u_t$ ), the velocity relationship based on the above-defined coordinate systems is expressed as

$$\begin{cases} u_x = u_r \\ u_{y'} = u_t \\ u_{z'} = 0 \end{cases} \tag{5.50}$$

and

$$\begin{cases} u_t = -V_{ct} \\ u_{x'} = V_{cn} \end{cases} \tag{5.51}$$

in which  $V_{cn}$ ,  $V_{ct}$ ,  $V_{sn}$  and  $V_{st}$  are the velocities of straight edge oblique cutting in the rake face and shear plane, respectively. They can be written as (Zou, Yellowley and Seethaler 2009)

$$\begin{cases} V_{cn} = \frac{\sin \phi_N \cdot \cos i}{\cos(\phi_N - \gamma_N)} V_0 \\ V_{ct} = (1 - SLIP) \cdot V_0 \cdot \sin i \end{cases} \tag{5.52}$$

and

$$\begin{cases} V_{sn} = \frac{\cos \gamma_N \cdot \cos i}{\cos(\phi_N - \gamma_N)} V_0 \\ V_{st} = SLIP \cdot V_0 \cdot \sin i \end{cases} \tag{5.53}$$

where  $V_0$  is the magnitude of the incoming velocity. Based on the Eqns.5.49, 5.50 and 5.51, the following relations can be obtained

$$\begin{aligned} u_{x'} &= V_{cn} = \cos \gamma_N \cdot u_r + \sin \gamma_N \cdot \sin i \cdot u_y - \sin \gamma_N \cdot \cos i \cdot u_z \\ u_{y'} &= u_t = \cos i \cdot u_y + \sin i \cdot u_z \\ u_{z'} &= \sin \gamma_N \cdot u_r - \cos \gamma_N \cdot \sin i \cdot u_y + \cos \gamma_N \cdot \cos i \cdot u_z = 0 \end{aligned} \quad (5.54)$$

Solving Eqn. (5.54), the velocities  $u_y$  and  $u_z$  are given by

$$\begin{aligned} u_y &= \frac{u_t - \sin i \cdot u_z}{\cos i} \\ u_z &= \frac{\cos \gamma_N \cdot \tan i \cdot u_t - \sin \gamma_N \cdot u_r}{\cos \gamma_N \cdot \cos i + \cos \gamma_N \cdot \tan i \cdot \sin i} \end{aligned} \quad (5.55)$$

Substituting Eqn. (5.55) into Eqn. (5.49), the relationship of  $u_{x'}$  and  $u_r$  is derived as

$$\begin{aligned} u_{x'} &= u_r \cdot \cos \gamma_N + \sin \gamma_N \cdot \tan i \cdot u_t \\ &\quad - \frac{\sin \gamma_N \cdot \sin i \cdot \tan^2 i}{\cos i + \tan i \cdot \sin i} u_t \\ &\quad - \frac{\sin \gamma_N \cdot \cos i \cdot \tan i}{\cos i + \tan i \cdot \sin i} u_t \\ &\quad + \frac{\sin^2 \gamma_N \cdot \sin i \cdot \tan i}{\cos \gamma_N \cdot \cos i + \cos \gamma_N \cdot \tan i \cdot \sin i} u_r \\ &\quad + \frac{\sin^2 \gamma_N \cdot \cos i}{\cos \gamma_N \cdot \cos i + \cos \gamma_N \cdot \tan i \cdot \sin i} u_r \end{aligned} \quad (5.56)$$

Simplifying Eqn. (5.56), the relationship of  $u_{x'}$  and  $u_r$  is obtained as

$$u_{x'} = u_r \left( \cos \gamma_N + \frac{\sin^2(\gamma_N)}{\cos \gamma_N} \right) = \frac{u_r}{\cos \gamma_N} \quad (5.57)$$

## 5.8.2 Helical Tool Velocity Profile

The basic geometry of helical pitch during the milling process is shown in Figure 5.9.

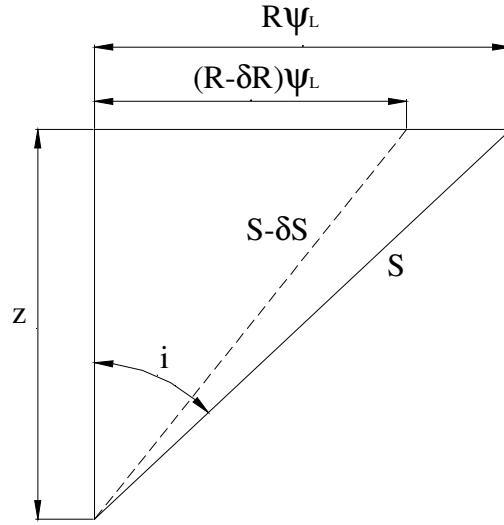


**Figure 5.9 Basic geometry of helical pitch**

From Figure 5.9, the helical pitch relationship can be written as

$$[S - \delta S]^2 = S^2 + [\delta R \cdot \psi_L]^2 - 2S \cdot \delta R \cdot \psi_L \cdot \sin i \quad (5.58)$$

where pitch rotation angle is

$$\psi_L = \frac{z}{R} \tan i \quad (5.59)$$

Simplifying Eqn. (5.58), the following relationship can be obtained as

$$\frac{dS}{dt} = u_r \cdot \psi_L \cdot \sin i \quad (5.60)$$

Satisfaction of the condition of Eqn. (5.60) requires the velocity profile to be in the form

$$\begin{aligned} u_r &= C_1 \\ u_t &= (C_2 + C_3 \cdot \psi_L) \end{aligned} \quad (5.61)$$

where  $C_1$ ,  $C_2$  and  $C_3$  are constants.  $\psi_L$  is the angle of global rotation;  $u_r$  and  $u_t$  denote the velocity in radial and tangential direction to the helix curve, respectively. It is noted that

the direction of tangential velocity defined in Figure 5.8 is opposite to the chip sliding direction; therefore, Eqn. (5.60) can be rewritten in the form of

$$\frac{dS}{dt} = -(u_{t1} - u_{t0}) \quad (5.62)$$

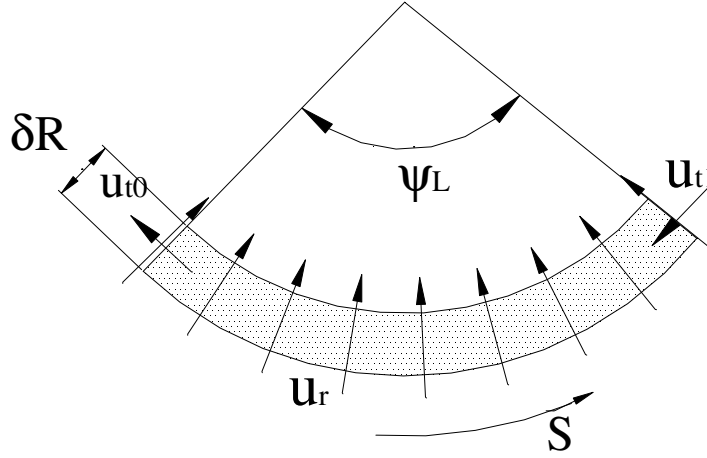


**Figure 5.10 Tangential velocity of the segment**

where  $u_{t0}$ , and  $u_{t1}$  are the tangential velocities at the start and the end of the segment shown in Figure 5.10. Substituting Eqn. (5.62) into Eqn. (5.60) yields

$$u_r = -\frac{1}{\psi_L \cdot \sin i} [u_{t1} - u_{t0}] \quad (5.63)$$

The helical tool boundary velocity conditions are given by

$$\begin{aligned} u_{t0} &= C_2 \\ u_{t1} &= C_2 + C_3 \cdot \psi_L \end{aligned} \quad (5.64)$$

Substituting Eqns. (5.61) and (5.64) into Eqn. (5.63), the relationship between  $C_1$  and  $C_3$  is derived as

$$C_3 = -C_1 \cdot \sin i \quad (5.65)$$

Based upon Eqn. (5.57), the velocity  $u_{x'}$  is obtained

$$u_{x'} = \frac{C_1}{\cos \gamma_N} \quad (5.66)$$

Thus the parameter  $C_1$  is written as

$$C_1 = V_{cn} \cdot \cos \gamma_N \quad (5.67)$$

Then the parameter  $C_3$  is derived as

$$C_3 = -C_1 \sin i = -V_{cn} \cdot \cos \gamma_N \cdot \sin i \quad (5.68)$$

After the constant parameters  $C_1$  and  $C_3$  are determined, the only unknown is  $C_2$ . Considering the constant velocity gradient in tangential direction, it should have a height that meets the straight edge oblique cutting velocity  $((1 - SLIP) \cdot \sin i \cdot V_0)$  along the tangential direction, that height is defined as  $z_h$  with a rotational angle  $\psi_h = z_h \tan i / R$ .

Thus, using Eqn. (5.51) together with the relationship mentioned above yields

$$C_2 + C_3 \frac{z_h}{R} \tan i = -(1 - SLIP) \cdot V_0 \sin i \quad (5.69)$$

Then the parameter  $C_2$  is derived as

$$C_2 = -(1 - SLIP) \cdot V_0 \sin i + \frac{z_h}{R} V_{cn} \cdot \cos \gamma_N \frac{\sin^2(i)}{\cos i} \quad (5.70)$$

Finally, the radial and tangential velocities are written as

$$\begin{aligned} u_r &= V_{cn} \cos \gamma_N \\ u_t &= -\left\{ (1 - SLIP) V_0 \sin i - V_{cn} \cdot \cos \gamma_N \frac{\sin^2(i)}{\cos i} \cdot \frac{z_h}{R} \right\} - V_{cn} \cdot \cos \gamma_N \cdot \sin i \cdot \psi_L \end{aligned} \quad (5.71)$$

Substituting Eqn. (5.71) into Eqn. (5.52), the velocity field on the rake face can be derived as

$$\begin{aligned} V_{cn} &= \frac{\sin \phi_N \cdot \cos i}{\cos(\phi_N - \gamma_N)} V_0 \\ V_{ct} &= \left\{ (1 - SLIP) V_0 \sin i - V_{cn} \cdot \cos \gamma_N \cdot \frac{\sin^2(i)}{\cos i} \cdot \frac{z_h}{R} \right\} + V_{cn} \cdot \cos \gamma_N \cdot \sin i \cdot \psi_L \end{aligned} \quad (5.72)$$

The tangential velocity in the shear plane can be obtained by

$$V_{st} + V_{ct} = V_0 \sin i \quad (5.73)$$

Then the velocity field in the shear plane can be derived as

$$V_{sn} = \frac{\cos \gamma_N \cdot \cos i}{\cos(\phi_N - \gamma_N)} V_0 \quad (5.74)$$

$$V_{st} = \left\{ SLIP \cdot V_0 \sin i + V_{cn} \cdot \cos \gamma_N \frac{\sin^2(i)}{\cos i} \cdot \frac{z_h}{R} \right\} - V_{cn} \cdot \cos \gamma_N \cdot \sin i \cdot \psi_L$$

### 5.8.3 Continuous Shear

The plan view of a chip is given in Figure 5.11.  $R$  is the chip radius and  $\delta R$  is the change of radius.

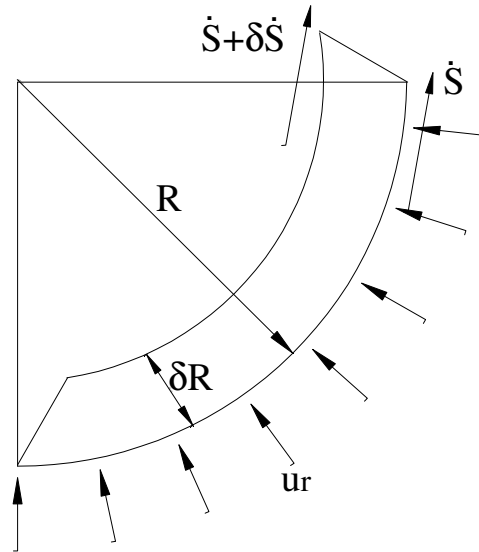


Figure 5.11 Plan view of chip

Since the velocity in radial direction ( $u_r$ ) is constant, there is no velocity jump on radial lines, but there is velocity change in the circumferential direction. The chip arc length change at radius  $(R - \delta R)$  can be given as

## 5 A New Predictive Model for Peripheral Milling Operations

$$\dot{S} + \delta\dot{S} = u_r \cdot \sin i \cdot \left( \frac{R}{R - \delta R} \right) \cdot \psi_L \quad (5.75)$$

Eqn. (5.75) can be rewritten as

$$(R - \delta R)(\dot{S} + \delta\dot{S}) = u_r \cdot \sin i \cdot R \cdot \psi_L \quad (5.76)$$

or

$$\delta\dot{S} = \delta R \frac{\dot{S}}{R} \quad (5.77)$$

Thus  $\dot{S}$  changes linearly with radius. If the inside chip radius is  $R_i$  and the outside chip radius is  $R_o$ , the change of  $\dot{S}$  along the chip can be written as

$$\Delta[\dot{S}] = u_r \cdot \sin i \cdot \frac{R_o}{R_i} \cdot \psi_L \quad (5.78)$$

Then the volume shear power can be given as

$$P_{shear} = \Delta[\dot{S}] \cdot k \cdot h_{av} \cdot R_o \cdot \psi_L \quad (5.79)$$

where  $h_{av}$  is the average chip thickness.

### 5.8.4 Special Case: Frictionless

As discussed in Section 3.3.1, in the case of  $SLIP$  being zero, the complete solution of basic oblique cutting parameters is given by

$$SLIP = 0, \quad RATIO = 0, \quad 2\phi_N - \gamma_N = \frac{\pi}{2} \quad (5.80)$$

The power can be written as

$$P = \int k \cdot |V_s| \cdot dA_s \quad (5.81)$$

where

## 5 A New Predictive Model for Peripheral Milling Operations

$$|V_s| = \sqrt{V_{sn}^2 + V_{st}^2} = V_{sn} \left[ 1 + \frac{1}{2} \left( \frac{V_{st}}{V_{sn}} \right)^2 \right] \quad (5.82)$$

$$dA_s = \frac{R \cdot S_t}{\sin \phi_N \cdot \sin i} d\phi, \quad d\phi = \frac{\tan i}{R} dz$$

For the frictionless case, the tangential velocity profile is linear and asymmetric along the depth of cut, the mean value of the velocity being at the mid depth

$$V_{st} = \frac{V_{cn} \cos \gamma_N \cdot \sin^2(i)}{R \cdot \cos i} \left[ \frac{a}{2} - z \right] \quad (5.83)$$

Then the power can be written as

$$P = \frac{kS_t V_{sn}}{\sin \phi_N \cdot \cos i} \int_0^a \left[ 1 + \frac{\cos^2(\gamma_N) \cdot \sin^4(i)}{2R^2 \cdot \cos^2(i)} \left( \frac{V_{cn}}{V_{sn}} \right)^2 \left( \frac{a}{2} - z \right)^2 \right] dz = \bar{P} + \tilde{P} \quad (5.84)$$

where

$$\frac{V_{cn}}{V_{sn}} = \frac{\sin \phi_N}{\cos \gamma_N}, \quad \bar{P} = \frac{kS_t a V_{sn}}{\sin \phi_N \cdot \cos i} \quad (5.85)$$

where  $\bar{P}$  is the power with the constant velocity profile, and  $\tilde{P}$  is the extra power related the linearly changed tangential velocity as

$$\begin{aligned} \tilde{P} &= \frac{kS_t V_{sn}}{\sin \phi_N \cdot \cos i} \frac{\cos^2(\gamma_N) \cdot \sin^4(i)}{2R \cdot \cos^2(i)} \left( \frac{V_{cn}}{V_{sn}} \right)^2 \int_0^a \left( \frac{a^2}{4} - az + z^2 \right) dz \\ &= \frac{kS_t V_{sn} \cos^2(\gamma_N) \cdot \tan^3(i) \cdot \sin i \cdot a^3}{24R^2 \sin \phi_N} \left( \frac{V_{cn}}{V_{sn}} \right)^2 = \frac{1}{24R^2} kS_t V_{sn} a^3 \sin \phi_N \cdot \tan^3(i) \cdot \sin i \end{aligned} \quad (5.86)$$

Figure 5.12 plots the power versus depth of cut and helical angle for the case of  $\gamma_N = 0^\circ$ ,  $D = 1/16$  inch. Figure 5.13 plots the cutting power with respect to radius  $R$  and helical angle  $i$  for the case of  $\gamma_N = 0^\circ$ ,  $a = 1.0$  mm. From Figures 5.12 and 5.13, it can be observed that the power consumption is increased with an increased depth of cut or helical angle, but decreased with an increased tool diameter. In other words, for the

## 5 A New Predictive Model for Peripheral Milling Operations

large depths of cut and small diameter tools the kinematics will have a significant influence on the helical tool milling operation.

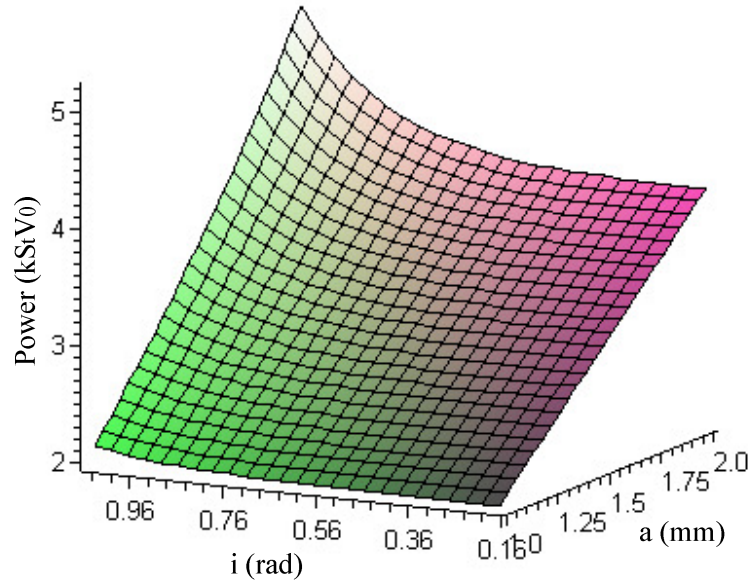


**Figure 5.12** Power change versus depth of cut  $a$  and helical angle  $i$

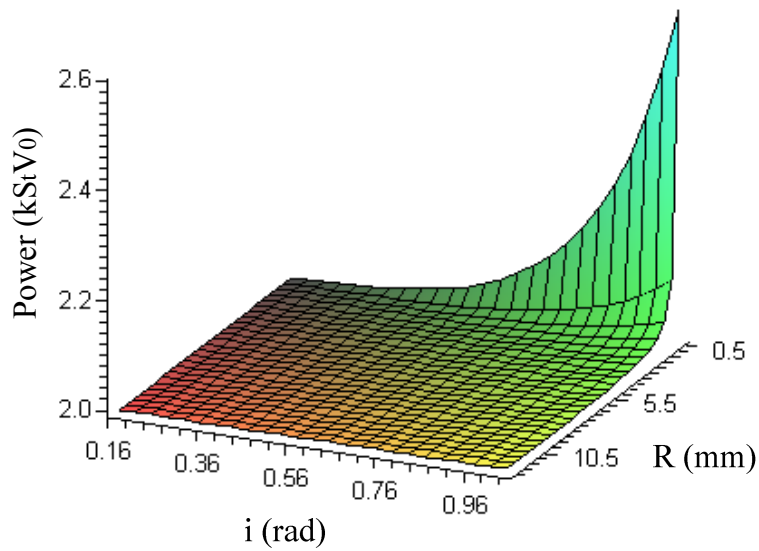


**Figure 5.13** Power change versus tool radius  $R$  and helical angle  $i$

## **5.9 Cutting Force Prediction for a General Helical Tooth Milling**

### **Cutter**

In order to incorporate the above-mentioned physical processes in the model, a numerical approach is developed in this thesis. The velocity field is assumed to be constant along the radial direction and linear along the tangential direction. An external optimization process determines the velocity profile. Then the velocity profile is taken as an input for the further computations. Five steps are employed in the proposed methodology:

- 1) The position of the individual incremental helical cutting edges are calculated by cutting edge discretization;
- 2) The uncut chip thickness is calculated by performing the coordinate transformation;
- 3) The velocity profile (constant along the radial direction, linear along the tangential direction) is determined by the optimization processes;
- 4) The flow stress and edge force are calculated based on the local oblique cutting system and the new velocity profile;
- 5) The resulting cutting force is estimated by using the shear plane prediction methodology plus extra continuous shear caused by kinematics constraint.

The chip formation process and elementary geometry of a helical toothed milling cutter are shown in Figure 5.14.

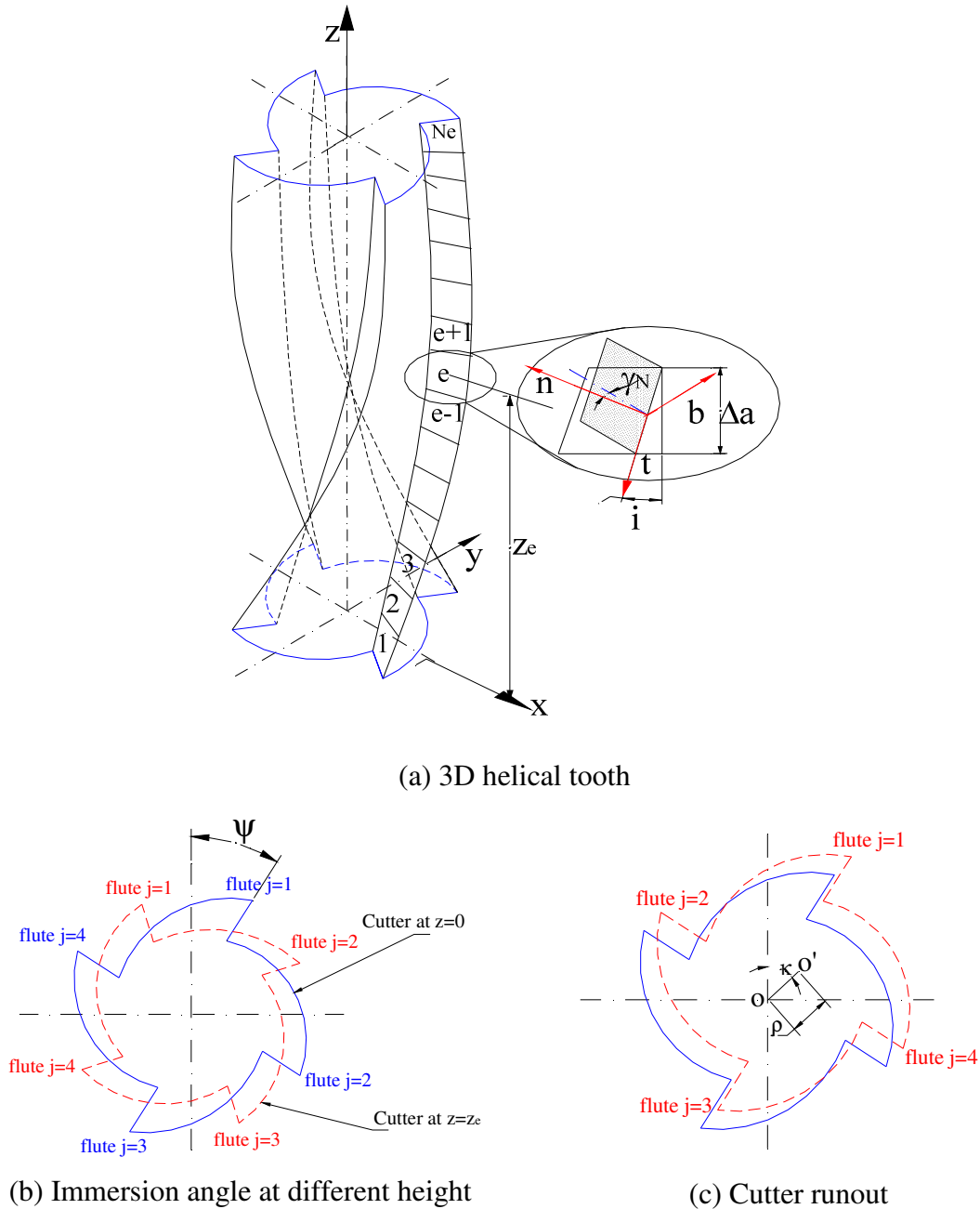


**Figure 5.14 Geometry of helical tooth**

The helical tool has  $N_f$  flutes and  $N_e$  discrete elements are created on each flute. Each element ( $e$ ) can be considered as an elemental oblique cutting edge which has a width of  $\Delta a$ , a normal rake angle  $\gamma_N$ , an inclination angle  $i$ , and the three local coordinates ( $n, t, b$ ). It is assumed that the position of the middle section of the element is the height

of the element ( $z_e$ ). The uncut chip thickness, immersion angle and height of each element are given as

$$\begin{aligned} h_j(z_e) &= m_j S_t \sin \psi_j(z_e) + R_j(z_e) - R_{j-m_j}(z_e) \\ \psi_j(z_e) &= \psi - \frac{2\pi \cdot (j-1)}{N_f} - \frac{z_e}{R} \tan i, \quad z_e = \frac{\Delta z}{2} + (e-1)\Delta z \end{aligned} \quad (5.87)$$

where  $S_t$  is the feed per tooth,  $m_j$  means that the current tooth or flute ( $j$ ) is removing the material left by the  $m_j^{\text{th}}$  tooth (Sutherland and DeVor 1986, Wang and Chang 2003, and Wang and Huang 2004), and

$$R_j(z_e) = R + \rho \cdot \cos \left[ \kappa - \frac{z_e}{R} \tan i - \frac{2(j-1)\pi}{N_f} \right] \quad (5.88)$$

where  $\rho$  and  $\kappa$  are the magnitude and angle shift of runout (shown in Figure 5.13c). By resolving Eqns. (5.88) and (5.87) together, Eqn. (5.87) can be rewritten as

$$h_j(z_e) = m_j S_t \sin \psi_j(z_e) + \left[ -2m_j \rho \sin \left( \frac{m_j \pi}{N_f} \right) \cdot \sin \left( \kappa - \frac{z_e}{R} \tan i - \frac{(2j - m_j - 2)\pi}{N_f} \right) \right] \quad (5.89)$$

The kinematics constraint assumed for helical tools requires that the chip flow velocity is constant along the radial direction and linear changing along the tangential direction. The velocity fields in the rake face and the shear plane for element (e) are given as (see Section 5.8)

$$\begin{aligned} V_{cn}^e &= \frac{\sin \phi_N \cdot \cos i}{\cos(\phi_N - \gamma_N)} V_0 \\ V_{ct}^e &= (1 - SLIP) \cdot V_0 \sin i - V_{cn}^e \cos \gamma_N \frac{\sin^2(i)}{\cos i} \left( \frac{z_h}{R} - \frac{z_e}{R} \right) \end{aligned} \quad (5.90)$$

$$\begin{aligned} V_{sn}^e &= \frac{\cos \gamma_N \cdot \cos i}{\cos(\phi_N - \gamma_N)} V_0 \\ V_{st}^e &= SLIP \cdot V_0 \sin i + V_{cn}^e \cos \gamma_N \frac{\sin^2(i)}{\cos i} \left( \frac{z_h}{R} - \frac{z_e}{R} \right) \end{aligned} \quad (5.91)$$

## 5 A New Predictive Model for Peripheral Milling Operations

The power consumption is expressed as (see Chapter 3 and Section 5.8.3)

$$P = \sum_{e=1}^{N_e} \left( k^e V_s^e A_s^e + \frac{SLIP}{1-SLIP} \frac{V_c^e}{V_s^e} k^e V_c^e A_s^e + P_{shear}^e \right) \quad (5.92)$$

where  $A_s^e$  is the shear plane area for element  $e$

$$A_s^e = \frac{h_j(z_e)\Delta a}{\sin \phi_N \cdot \cos i} \quad (5.93)$$

The velocity profile is obtained by minimizing the power consumption. However, Eqn. (5.92) is a highly nonlinear function that is difficult to solve directly and the highly nonlinear effect will not affect the velocity profile (see Section 5.8) significantly. For simplicity then, it is assumed that the shear yield stress and shear angle may be assumed constant at an average value for the incut flute. An external optimization algorithm is then used to determine the velocity profile. After obtaining the velocity profile and uncut chip thickness, the shear yield stress can be determined exactly from the Johnson-Cook model for each individual element, and then the shear force at the shear plane including the extra continuous shear caused by kinematics constraint for element ( $e$ ) can be given as

$$F_s^e = \frac{k^e \Delta a h_j(z_e) \cos \delta_s^e}{\cos i \cdot \sin(\phi_N - \delta_s^e)} + \frac{P_{shear}^e}{V_0} \frac{\cos i \cdot \cos \phi_N}{\cos \eta_s^e} \quad (5.94)$$

in which the shear angle  $\phi_N$  can be obtained from centerline milling tests with the same feedrate expressed in Section 6.4. Then following the procedures discussed in Sections 5.5 and 5.7, the oblique cutting forces acting on each element ( $e$ ) can be derived as

$$\begin{cases} F_C^e(j) = F_{CS}^e(j) + F_{CE}^e(j) \\ F_T^e(j) = F_{TS}^e(j) + F_{TE}^e(j) \\ F_R^e(j) = F_{RS}^e(j) + F_{RE}^e(j) \end{cases} \quad (5.95)$$

## 5 A New Predictive Model for Peripheral Milling Operations

It is noted that when the element (e) is at the entry or the exit region, the forces  $F_{CS}^e(j), F_{TS}^e(j), F_{RS}^e(j)$  will be set to zero and only the edge forces ( $F_{CE}^e(j), F_{TE}^e(j), F_{RE}^e(j)$ ) are left and calculated by Eqn. (5.27). Then the oblique cutting forces in each element in the local principal directions (C, T, R) shown in Figure 5.14a are transformed to the global elemental forces in x, y and z directions as

$$\begin{Bmatrix} F_x^e(j) \\ F_y^e(j) \\ F_z^e(j) \end{Bmatrix} = \begin{bmatrix} \cos \psi_j(z^e) & \sin \psi_j(z^e) & 0 \\ -\sin \psi_j(z^e) & \cos \psi_j(z^e) & 0 \\ 0 & 0 & 1 \end{bmatrix} \begin{Bmatrix} F_C^e(j) \\ F_T^e(j) \\ F_R^e(j) \end{Bmatrix} \quad (5.96)$$

These forces must now be summed for each edge  $j$  of the elementary disk and for each elementary disk along the engaged length of flute on each tooth of the milling cutter. The instantaneous forces on the whole cutter are a function of mill angular position  $\psi$  and given by

$$\begin{Bmatrix} F_x(\psi) \\ F_y(\psi) \\ F_z(\psi) \end{Bmatrix} = \begin{Bmatrix} \sum_{j=1}^{N_f} \sum_{e=1}^{N_e} F_x^e(j) \\ \sum_{j=1}^{N_f} \sum_{e=1}^{N_e} F_y^e(j) \\ \sum_{j=1}^{N_f} \sum_{e=1}^{N_e} F_z^e(j) \end{Bmatrix} \quad (5.97)$$

### 5.10 Conclusions

The mathematical formulations for the analysis of peripheral milling operations are presented. The Johnson-Cook constitutive model is used to allow the consideration of chip thickness, strain, strain rate, work hardening and temperature on yield strength and normal stress on the shear plane. The ploughing force model for orthogonal cutting developed in Chapter 4 is applied for the prediction of edge forces which are resolved

## 5 A New Predictive Model for Peripheral Milling Operations

from the velocity plane to provide the required oblique force components. A new approach for the consideration of surface slope on the shear angle and cutting forces is presented and the influence of slope on shear angle and forces are investigated. An improved but still simple kinematic arrangement that satisfies the plastic incompressibility for the helical tool is proposed. The model allows the prediction of the influence of helical angle, radius and depth on the degree of constraint and provides estimates of the additional energy requirements in the process.

## **6 Experimental Validation of the Predictive Model**

### **6.1 Introduction**

A GUI-based Matlab program based on the theoretical formulations presented in Chapter 5 has been developed to estimate forces in the milling process using helical toothed cutters. In order to verify the model and to estimate the overall predictive capability of the model, it is necessary to assess the model qualitatively and quantitatively with respect to experimental results. This chapter describes a series of experiments with different workpiece materials, tool diameters, milling types, and a wide range of feeding velocities which allow the examination of the accuracy of the proposed model. The edge radius of the cutters used in the experiments has been measured using a scanning electron microscope (SEM) to allow edge forces to be estimated, and an innovative algorithm is used to identify the constitutive parameters of the work materials using a central cut milling test. The proposed algorithm does not need shear angle data for calibration, relying instead on the measured force data. This chapter also presents the constitutive equations and primary shear zone parameter identifications for steel, titanium alloy and aluminum alloy workpieces.

### **6.2 Experimental Setup**

All experiments were conducted on a vertical milling machine center using end mills and dry cutting. The three orthogonal milling force components were measured using a three component dynamometer which incorporates piezoelectric load cells; signals were low pass filtered with a cutoff frequency of 200 Hz and data was recorded at

## 6 Experimental Validation of the Predictive Model

sampling rates ranging from  $1 \times 10^4$  (1/s) to  $2.5 \times 10^4$  (1/s) using a Tektronix Oscilloscope. The testing program included the use of 3 workpiece materials with very different physical properties. The tests examined both up and down milling operations; additional tests used centerline face milling to reduce the variation in chip thickness and to maintain surface slope at a lower value (note centerline milling also allows easier identification of tool position). The cutters used were HSS end mills to cut an aluminum alloy and solid carbide end mills with TiN coating to cut a titanium alloy and high strength steel. The cutter diameters varied from 3/16 inch to 1/2 inch and the feedrates were chosen to best allow the identification of physical parameters while avoiding tool edge or shank breakage. It should be noted that the use of small end mills on the hardened steel led to the adoption of small feeds and in this case cutters have a single edge (of two) ground away to avoid the need to deal with cutter runout in the identification procedure. The range of experiments, tools and workpiece materials are shown in Table 6.1, a full list of experiments is given in Appendix A.

**Table 6.1 The range of cutting tests undertaken**

Workpiece Material	Tool Manufacturer	Cutter Diameter (in)	Feeding Velocity (in/min)	Cutting Type	Uncut Chip Thickness (mm/per tooth)	Spindle Speed (RPM)
Aluminum Alloy	Niagara Cutter: High Speed Steel	1/2	1.28 -7.9	Up/Down /Center/ Slotting	0.01626-0.10033	1000
Titanium Alloy	SGS Tools: Solid Carbide TiN Coated	3/8	0.75-4.4	Up/Down/ Center	0.01656-0.09718	575
Titanium Alloy	SGS Tools: Solid Carbide TiN Coated	3/16	0.75-2.56	Up/Down/ Center	0.00827-0.0282	1152
Steel	SGS Tools: Solid Carbide TiN Coated	3/8	0.75-3.95	Slotting	0.0191-0.10033	1000

### 6.3 Edge Radius Measurement

Cutting tool edges are critical to cutting performance (Filiz et al. 2007). Edge sizes range from microscale (including cutting tools for plastic web materials and diamond tools for precision applications) to mesoscale for traditional cutting tool inserts (Aramchareon et al. 2008). In this thesis, three types of helical end-milling cutters (1/2 inch HSS end mill cutter with helical angle 30 deg, 3/8 inch solid carbide coated TiN end milling cutter with 30 deg helical angle and 3/16 inch solid carbide coated TiN end milling cutter with 30 deg helical angle) have been measured using the scanning electron microscope (SEM). The cutters have been cut on a diamond-slicing machine and encapsulated in an epoxy resin using a mould cylinder. Before examining under the microscope, the samples were polished using abrasive paper in four stages (P180, P400, P600 and P1200 grades) and finally polished by 6  $\mu\text{m}$  and 1  $\mu\text{m}$  diamond grinding as shown in Figure 6.2. Detailed information regarding cutters A-E is given in Table 6.2.

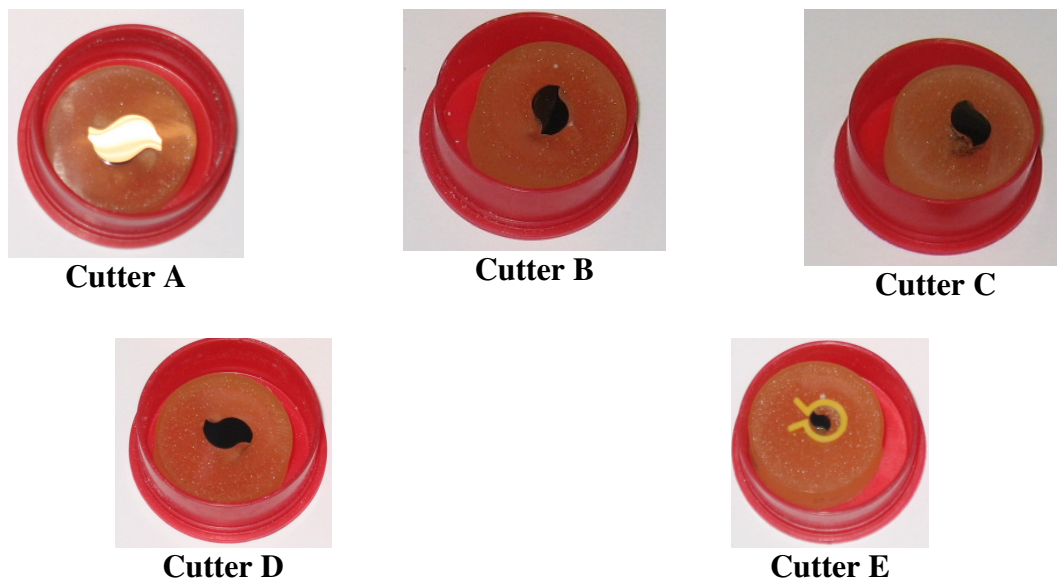


**Figure 6.1 Mounted cutter samples**

## 6 Experimental Validation of the Predictive Model

**Table 6.2 Cutter information**

Cutter Type	Manufacture Company	Tool Material	Tool Diameter	Number of Teeth	Helix Angle	Radial Rake Angle
Cutter A	Niagara Cutter	HSS	1/2 inch	2	30 <sup>0</sup>	10 <sup>0</sup>
Cutter B	SGS Tools	Solid Carbide TiN Coated	3/8 inch	2	30 <sup>0</sup>	5 <sup>0</sup>
Cutter C	SGS Tools	Solid Carbide TiN Coated	3/8 inch	2	30 <sup>0</sup>	5 <sup>0</sup>
Cutter D	SGS Tools	Solid Carbide TiN Coated	3/8 inch	1	30 <sup>0</sup>	5 <sup>0</sup>
Cutter E	SGS Tools	Solid Carbide TiN Coated	3/16 inch	2	30 <sup>0</sup>	5 <sup>0</sup>

Note: In Cutter D one tooth is ground away and only one tooth left

Figures 6.2-6.6 show the SEM images of the HSS cutter used to cut the aluminum alloy, the 3/8” SGS carbide coated cutter used to cut the titanium alloy and steel, and the 3/16” SGS carbide coated cutter used to cut the titanium alloy, respectively. The cutting operations and the measured edge radiuses are given in Table 6.3.

**Table 6.3 The cutting operations and measured edge radii**

Cutter Type	Tool Diameter (inch)	Cutting Operations	Mean Edge Radii (µm)
Cutter A	1/2	Aluminum Alloy (Table AA.1) (Up/Down/Center)	3.425
Cutter B	3/8	Titanium Alloy Table AA.2: Test 1-5), (Center Cut)	5.3026
Cutter C	3/8	Titanium Alloy (Table AA.2: Test 6-10), (Up/Down Milling)	6.6332
Cutter D	3/8	Steel (Table AA.4: Test 1-6) (Slotting)	4.4873
Cutter E	3/16	Titanium Alloy (Table AA.3: Test 1-12), (Up/Down/Center)	3.5473

## 6 Experimental Validation of the Predictive Model

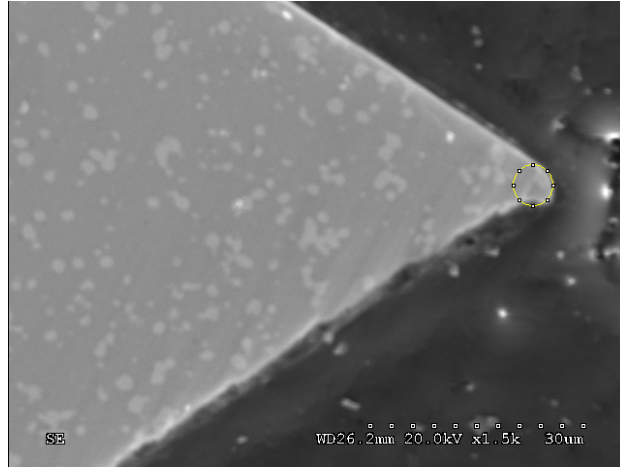


**Figure 6.2 SEM image for Cutter A**

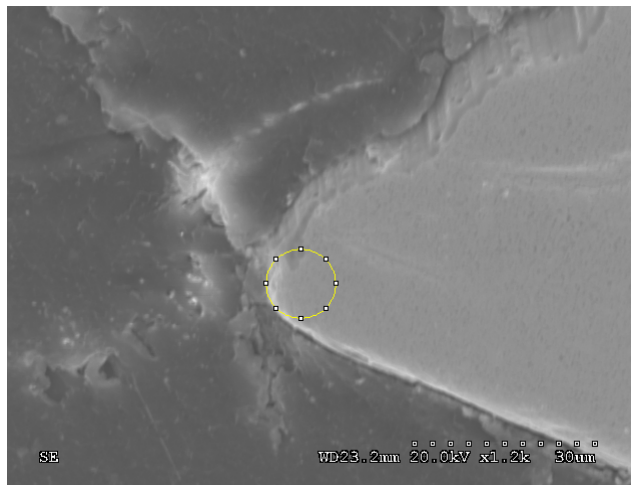


**Figure 6.3 SEM image for Cutter B**

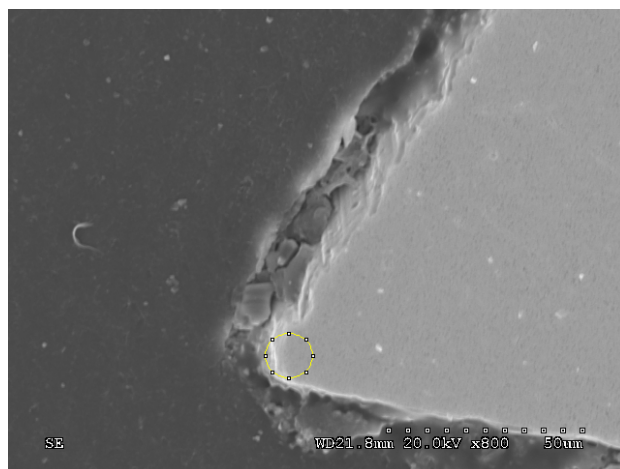


**Figure 6.4 SEM image for Cutter C**

6 Experimental Validation of the Predictive Model

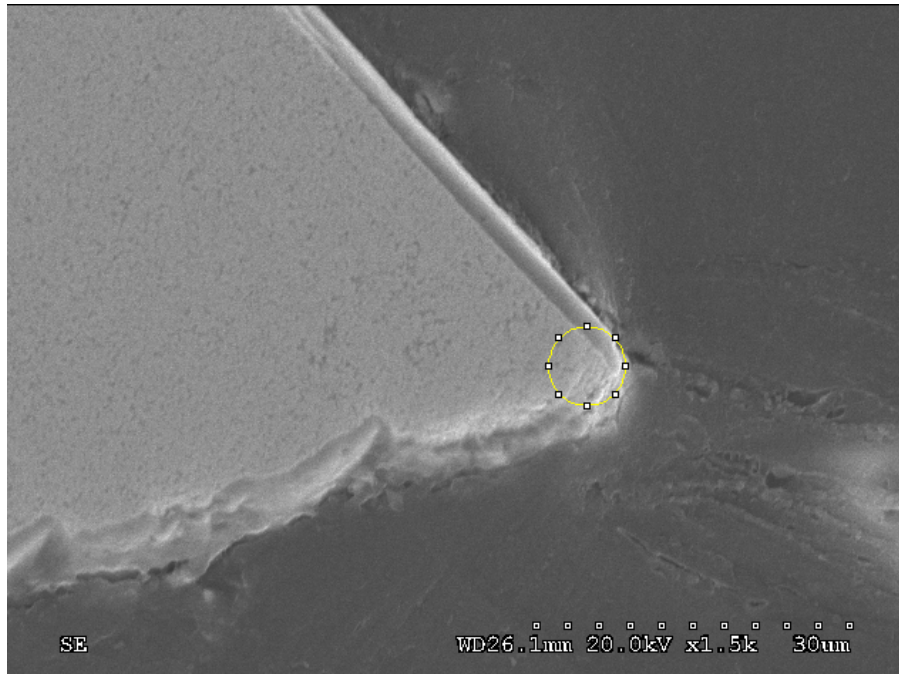


Figure 6.5 SEM image for Cutter D

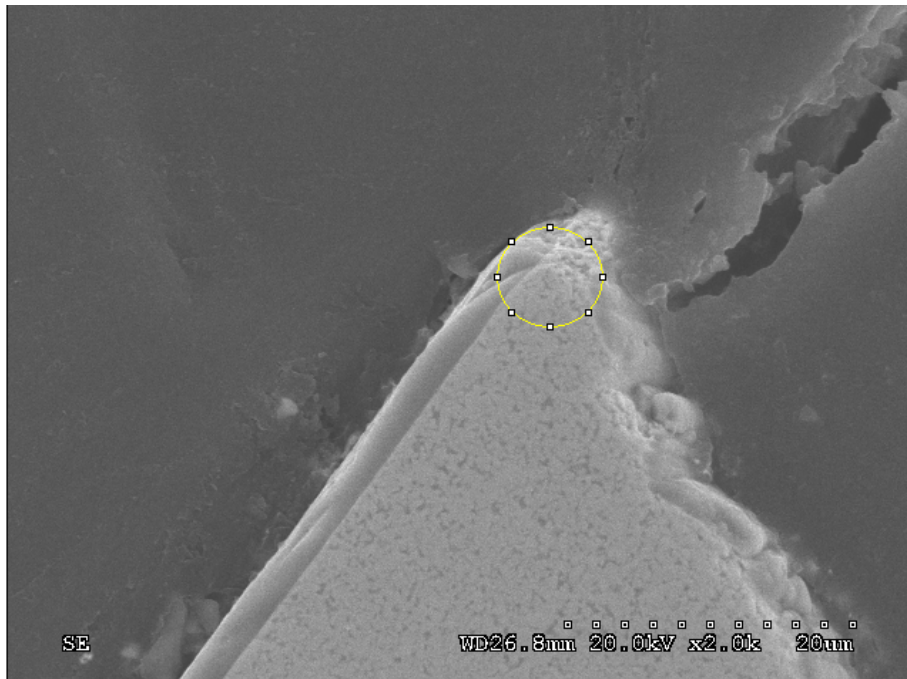


Figure 6.6 SEM image for Cutter E

### 6.4 Identification of the Constitutive Parameters

The advantage of using a constitutive model over following a purely empirical method is that, for a known material, the experimental data required to determine the dependence of flow stress on temperature, strain and strain rate can be dramatically reduced. Ideally, theoretical relationships derived from the physical processes at the atomic level should be used to describe the macroscopic flow behavior of material. However, a soundly based theoretical approach of good accuracy is still some way from being realized (Jaspers and Dautzenberg 2002). Consequently, it is inevitable that one must be satisfied with an empirical model of the material behavior itself. In this thesis, the Johnson-Cook constitutive model has been selected as the basis for the prediction of material yield strength and work hardening over the shear plane.

The values of the constants in the constitutive equation are available in the literature for conditions approaching those found in metal cutting. To allow for material variations due to slight changes in composition, structure and treatment, it is assumed that the Johnson-Cook constitutive parameters,  $(m, n, C_m)$  are the same as those quoted in the literature but that parameters  $A$  and  $B$  within the term  $(A + B\varepsilon^n)$  may be scaled. This methodology will maintain the relationships between the variables but vary the magnitude of shear yield stress. The identification process is carried out using the one set of forces collected at the center point of a centered face milling cut. The process adopted for identification minimizes the errors due to “timing” of the force signal; it minimizes edge force components by using the largest chip thickness during the cut and eliminates some of the error due to slope considerations. The identified process is based on the largest feed of central cut, the uncut chip thickness is more than an order of magnitude

## 6 Experimental Validation of the Predictive Model

larger than the edge radius in all of these tests therefore the edge force effect to the total force will be limited. Based upon the measured three forces for large feed, the forces acting on the rake face (shown in Figure 6.7) are given as

$$\begin{cases} F_{fr} = [F_C \cos i + F_R \sin i] \cdot \sin \gamma_N + F_T \cos \gamma_N \\ F_{ft} = F_C \sin i - F_R \cos i \\ N = [F_C \cos i + F_R \sin i] \cdot \cos \gamma_N - F_T \sin \gamma_N \end{cases} \quad (6.1)$$

The friction force  $F_f$  and chip flow angle can then be obtained as

$$F_f = \sqrt{F_{fr}^2 + F_{ft}^2}, \quad \eta_c = \tan^{-1} \left[ \frac{F_{ft}}{F_{fr}} \right] \quad (6.2)$$

Based on the work of Zou, Yellowley and Seethaler (2009), the kinematic parameter  $SLIP$  is given as

$$SLIP = 1.0928 - 0.47799 \left( \frac{\eta_c}{i} \right) - 0.53039 \left( \frac{\eta_c}{i} \right)^2 \quad (6.3)$$

The normal shear angle is then estimated based on the energy minimization of the oblique cutting processes discussed in Section 5.3 as

$$P = h_0 w V_0 \left[ A \bar{\epsilon} + \frac{B}{n+1} \bar{\epsilon}^{n+1} \right] \cdot [1 + C_m \ln \dot{\bar{\epsilon}}^*] \cdot [1 - T^{*m}] + F_f V_c \quad (6.4)$$

In order to apply the optimization technique, the constitutive parameters are selected from the literature for the initial step, the parameters in the following steps use the parameters obtained from the previous step. The cutting velocity is

$$V_0 = \pi D \cdot \Omega \cdot 25.4 / 60000 \quad (6.5)$$

where  $D$ : diameter of tool (inch);  $\Omega$ : spindle speed (rev/min);  $V_0$ : cutting velocity (m/s). The model of helical tool kinematics adopted here requires that the chip velocity is constant along the radial direction and changes linearly along the tangential direction (see

## 6 Experimental Validation of the Predictive Model

Section 5.7). After obtaining the normal shear angle, the forces acting on the shear plane (shown in Figure 6.7) may be calculated as follows

$$\begin{cases} F_{sr} = [F_C \cos i + F_R \sin i] \cdot \cos \phi_N - F_T \sin \phi_N \\ F_{st} = -F_C \sin i + F_R \cos i \\ N_s = [F_C \cos i + F_R \sin i] \cdot \sin \phi_N + F_T \cos \phi_N \end{cases} \quad (6.6)$$

Then the total shear force and the shear flow angle can be given as

$$F_s = \sqrt{F_{st}^2 + F_{sr}^2}, \quad \eta_s = \tan^{-1} \left[ \frac{F_{st}}{F_{sr}} \right] \quad (6.7)$$

So the shear yield stress and normal pressure on the shear plane are

$$k_{AB} = \frac{F_s}{A_s} = \frac{F_s \sin \phi_N \cdot \cos i}{wh_0}, \quad \bar{p}_{AB} = \frac{N_s}{A_s} = \frac{N_s \sin \phi_N \cdot \cos i}{wh_0} \quad (6.8)$$

The mean inplane stress and the normal stress at point A on the shear plane are estimated as (Oxley 1989)

$$\bar{p}_{AB} = \frac{p_A + p_B}{2}, \quad p_A = k_{AB} \left[ 1 + 2 \left( \frac{\pi}{4} - \phi_N + \delta_s \right) \right] \quad (6.9)$$

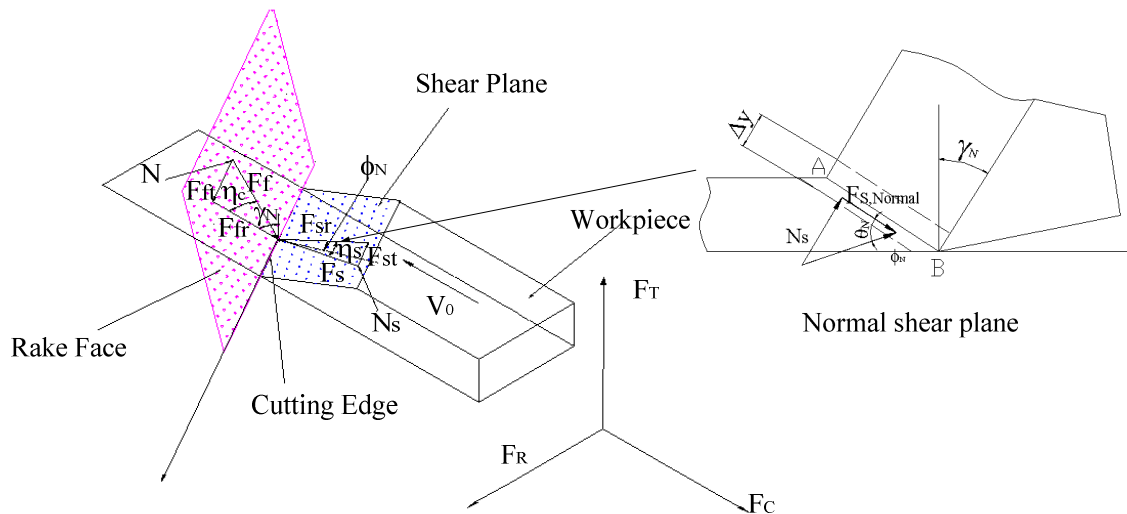


**Figure 6.7 Forces acting on the rake face and shear plane**

## 6 Experimental Validation of the Predictive Model

Therefore, from Eqns. (6.8) and (6.9), the pressure at point B can be obtained as

$$p_B = \frac{2N_s \sin \phi_N \cdot \cos i}{wh_0} - p_A \quad (6.10)$$

Applying force equilibrium along AB, the following relations result (Oxley 1989)

$$dp = \frac{dk_{AB}}{ds_{2N}} ds_{1N} \quad (6.11)$$

where  $s_{1N}$  and  $s_{2N}$  are the slip-line length along AB and the width of the zone at the normal plane. By substituting Eqn. (5.21) into Eqn. (6.11), the following relationship can be derived as

$$p_A - p_B = 2Const \times n_{eq} \times k_{AB} \quad (6.12)$$

where  $p_A$  and  $p_B$  are the hydrostatic stresses at points A and B, respectively. Then the value *Const* is obtained as

$$Const = \frac{k_{AB} \left[ 1 + 2 \left( \frac{\pi}{4} - \phi_N + \delta_s \right) \right] - \frac{N_s \sin \phi_N \cdot \cos i}{wh_0}}{n_{eq} k_{AB}} \quad (6.13)$$

The optimization technique used to identify these parameters is then phrased as

$$\begin{aligned} & \text{Minimum } k_{AB}^{measure} - k_{AB} \\ & \text{Subject to : } \text{abs}(Const - Const^{measure}) \leq \text{Accuracy} \end{aligned} \quad (6.14)$$

where the shear yield stress  $k_{ab}$  is calculated based on the strain, strain rate and temperature.

It is noted that during the first iteration it is not necessary to consider the edge force effect on the large feed. In order to predict the constitutive parameters and shear angle accurately, the edge force effect can be considered in the following iteration rounds. The edge forces at large feed are approximated based on the methodology

## 6 Experimental Validation of the Predictive Model

discussed in Chapter 4 and Section 5.5 as well as the shear yield stress obtained from Eqn. (6.14). Then the measured forces with edge forces subtracted are used for the following round of identification procedures, (i.e.,  $F_C$ ,  $F_R$ , and  $F_T$  are replaced by  $(F_C - F_{CE})$ ,  $(F_R - F_{RE})$ , and  $(F_T - F_{TE})$ , respectively). The whole identification process stops when the required accuracy of shear angle is obtained, (i.e.,  $abs(\phi_N^j - \phi_N^{j-1}) \leq \phi_\epsilon$ , where  $\phi_\epsilon$  is the prescribed shear angle accuracy). The above methodology avoids the need for shear angle data, relying instead on experimental force data for calibration and an internal optimization routine to find the normal shear angle. This is important since actual milling operations do not yield chip geometries which may be analyzed for shear angle.

Three materials, AL-6061 T6, Ti-6AL-V4 and AISI 4140 Steel have been tested in the milling experiments. The material properties are given in Table 6.4.

**Table 6.4 Workpiece material properties**

Material	Al-6061-T6 (Johnson et al. 1996)	Ti-6Al-4V (Meyer and Kleponis 2001)	AISI 4140 Steel (Arrazola et al. 2008)
Thermal Conductivity (K)	167 (w/m-K)	7.3 (w/m-K)	46 (w/m-K)
Specific Heat (S)	896 (J/kg- <sup>0</sup> C)	580 (J/kg- <sup>0</sup> C)	450 (J/kg- <sup>0</sup> C)
Melting Temperature ( $T_{melt}$ )	582 ( <sup>0</sup> C)	1605 ( <sup>0</sup> C)	1460 ( <sup>0</sup> C)
Young Modulus (E)	68.9GPa)	113.8 (GPa)	210 (GPa)
Poisson Ratio ( $\nu$ )	0.33	0.342	0.3
Density ( $\rho$ )	2700 (kg/m <sup>3</sup> )	4430 (kg/m <sup>3</sup> )	7862 (kg/m <sup>3</sup> )

The forces measured at the midpoint of a large feed central cut are shown in Table 6.5. Based on the measured forces, shear angles expected to be 25.6<sup>0</sup>, 23.7<sup>0</sup>, and 24.9<sup>0</sup> for the cutting of aluminum alloy, titanium alloy and steel, respectively. As mentioned previously, the identification process is conducted to keep the Johnson-Cook constitutive parameters, ( $m$ ,  $n$ ,  $C_m$ ), the same as found in previous literature (Johnson et al. 1996, Meyer and Kleponis 2001, and Arrazola et al. 2008 for aluminum alloy, titanium alloy,

## 6 Experimental Validation of the Predictive Model

and steel, respectively), on the other hand the magnitude of  $(A + B\varepsilon^n)$  is allowed to vary to fit the experimental data. The identified Johnson-Cook parameters, width of shear zone and thermal transfer fraction are given in Table 6.6.

**Table 6.5 The measured forces at the midpoint of central cuts**

Material	Cutting Operation	Measured Forces		
		$F_C$ (N)	$F_T$ (N)	$F_R$ (N)
Aluminum Alloy	Table AA.1: Test 5	195.1	122.4	27.1
Titanium Alloy	Table AA.2: Test 5	351.2	235.3	114.8
Steel	Table AA.4: Test 6	276.4	111.9	40.9

**Table 6.6 Identified J-C constitutive parameters for aluminum alloy, titanium alloy and steel**

Johnson-Cook Constitutive Equation Parameters	Identified Parameters for Aluminum Alloy	Identified Parameters for Titanium Alloy	Identified Parameters for Steel
$A$ (MPa)	422.5	728.6	648.3
$B$ (MPa)	148.7	279.8	832.6
$C_m$	0.002	0.012	0.0137
$n$	0.42	0.34	0.2092
$m$	1.34	0.8	0.807
$const$	7.47	7.95	7.94
$x$	0.681	0.692	0.801

Based on the parameters determined for the Johnson-Cook equation, the cutting forces are predicted using the oblique cutting force model (described in Chapter 5) and compared with the measured cutting forces in centerline milling operations. The comparison between calculated and measured forces is shown in Figures 6.8-6.10 for aluminum alloy, titanium alloy and steel, respectively. It is noted that the calculated ploughing force has been subtracted from the measured force and that the calculated force does not include the ploughing component. The force versus chip thickness is

## 6 Experimental Validation of the Predictive Model

concave and so any attempt to use a linear relationship on the full force to estimate the edge forces will lead to an overestimate. The shear angles predicted for the centerline milling operations are shown in Figures 6.11-6.13 for aluminum alloy, titanium alloy and steel, respectively. It can be observed that the shear angle decreases with a reduction in uncut chip thickness.

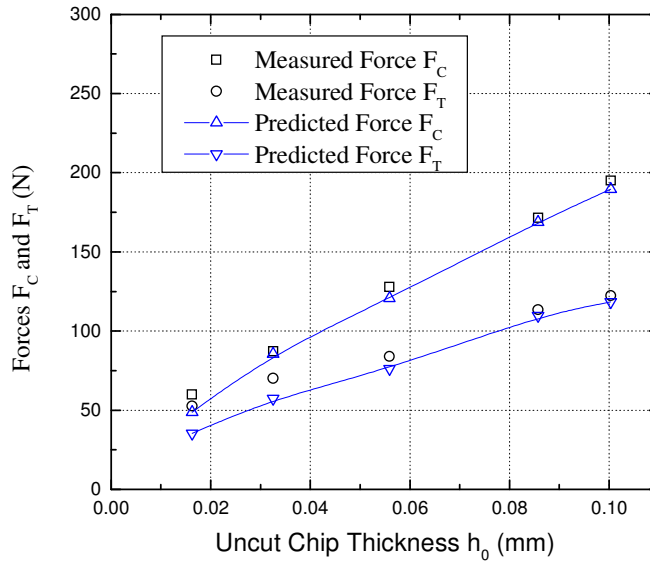


**Figure 6.8 Centerline cutting force comparison as feedrate changes for central cutting aluminum alloy (cutter A)**

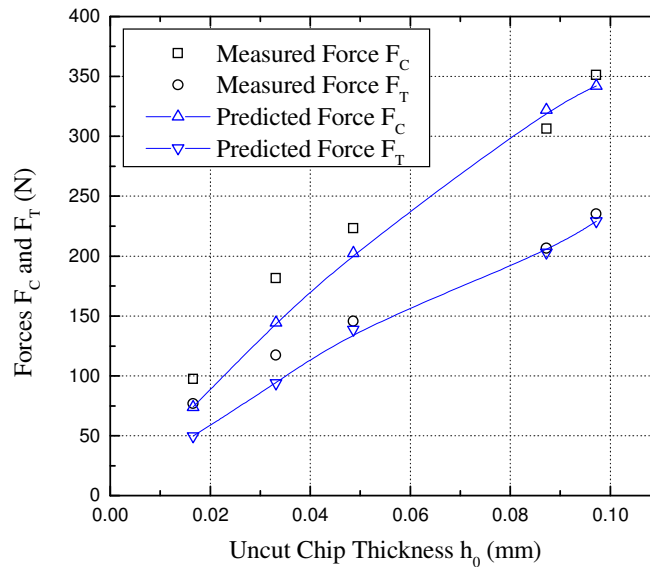


**Figure 6.9 Centerline cutting force comparison as feedrate changes for central cutting titanium alloy (cutter B)**

## 6 Experimental Validation of the Predictive Model

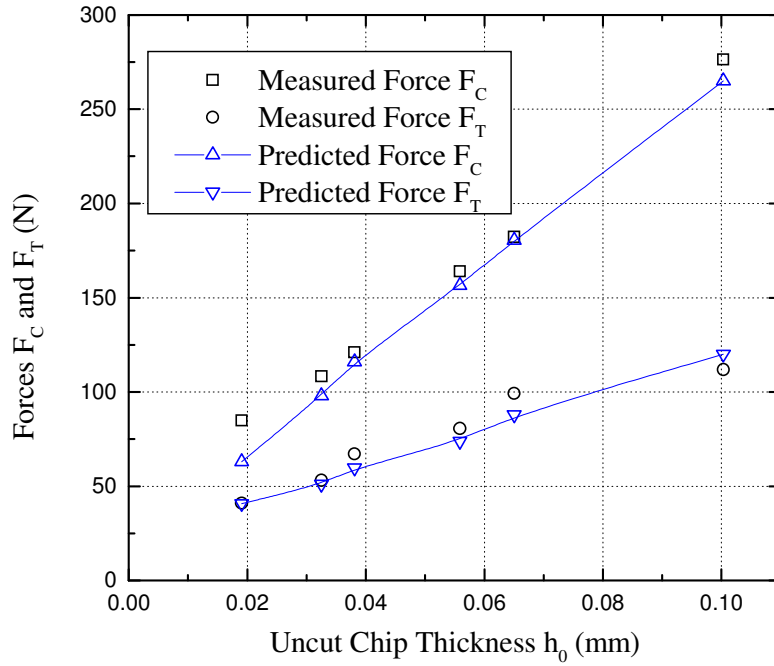


**Figure 6.10 Centerline cutting force as feedrate changes for slotting of steel (cutter D)**

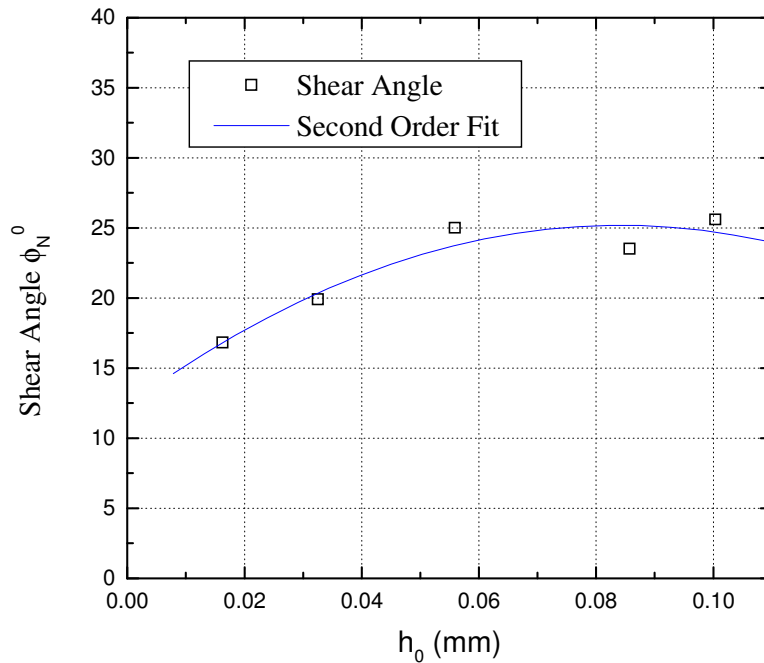


**Figure 6.11 Predicted shear angle versus uncut chip thickness for central cutting aluminum alloy (cutter A)**

## 6 Experimental Validation of the Predictive Model

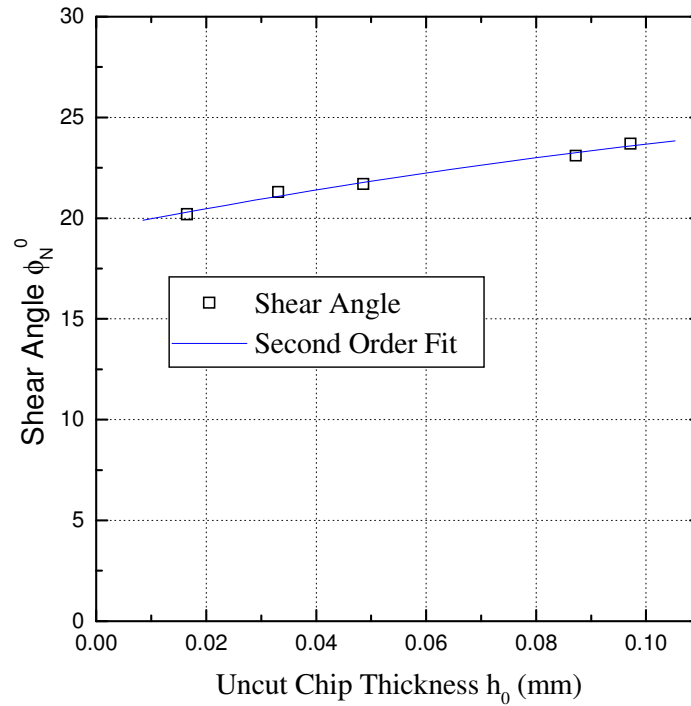


**Figure 6.12 Predicted shear angle versus uncut chip thickness for central cutting titanium alloy (cutter B)**

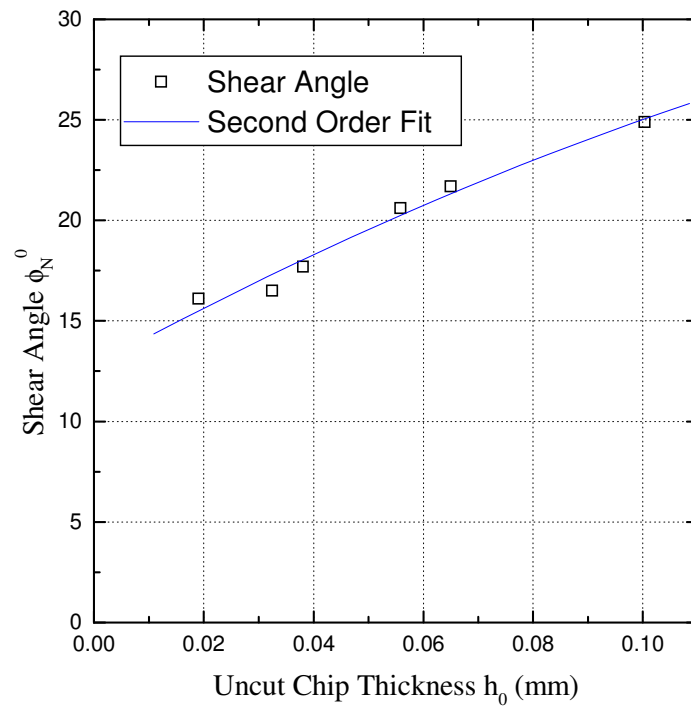


**Figure 6.13 Predicted shear angle versus uncut chip thickness for slotting steel (cutter D)**

## 6.5 Detailed Validation of the Proposed Model

The results predicted by the proposed model are compared with the experimental test results in this section. (The details of the test have been described earlier in this chapter and a full list of tests is given in Appendix A). It is known that the kinematic constraint imposed by the helical tooth is a minor factor in almost all practical operations and especially here where axial depths are relatively low. The author has simplified the process by approximating the expected change in velocity along the edge for constant shear angle and yield stress using the UB method described earlier. The estimated velocity profile is then input to the general force calculation method discussed in Chapter 5. Figures 6.14-6.17 show the estimated single flute radial and tangential velocity components for cutting aluminum alloy (Cutter A), titanium alloy (Cutter B and C), titanium alloy (Cutter E), and steel (Cutter D), respectively. The dashed black line represents the radial velocity component; the solid blue line represents the expected tangential component of velocity for a straight edge oblique cutting process, while the dotted red line represents the tangential component of velocity along the helical tool cutting edges (the component changes linearly along the helix cutting edge as dictated by Eqn (5.71). The incoming velocities for cutting aluminum alloy (Cutter A), titanium alloy (Cutter B and C), titanium alloy (Cutter E), and steel (Cutter D) are 0.665 m/s, 0.2868 m/s, 0.2872 m/s and 0.4987 m/s, respectively. The ratios of constant tangential velocity versus radial velocity for the cutting aluminum alloy (Cutter A), titanium alloy (Cutter B and C), titanium alloy (Cutter E), and steel (Cutter D) are 0.6013, 0.4010, 0.6886, and 0.5503, respectively. The following sections present the complete force validation results. It should be noted that runout is not considered.

## 6 Experimental Validation of the Predictive Model

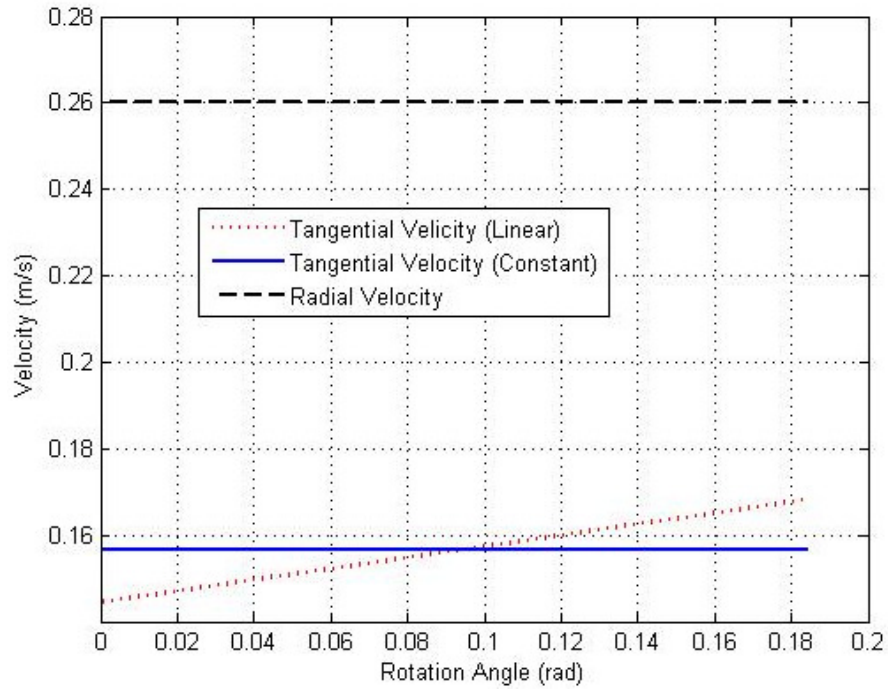


**Figure 6.14** Velocity profile for cutting aluminum alloy (Cutter A)

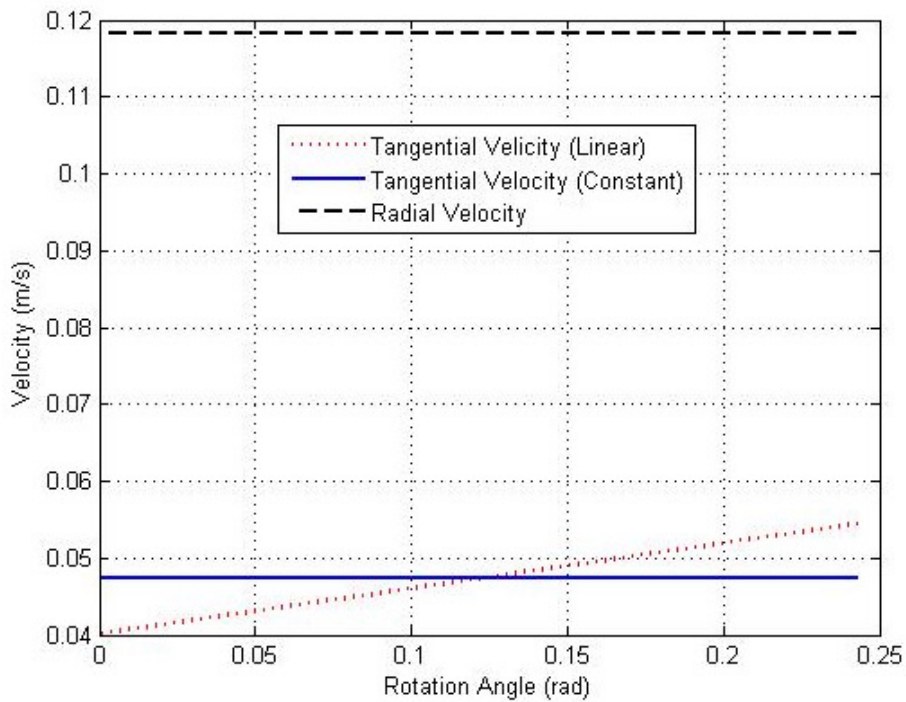


**Figure 6.15** Velocity profile for cutting titanium alloy (Cutter B and C)

## 6 Experimental Validation of the Predictive Model

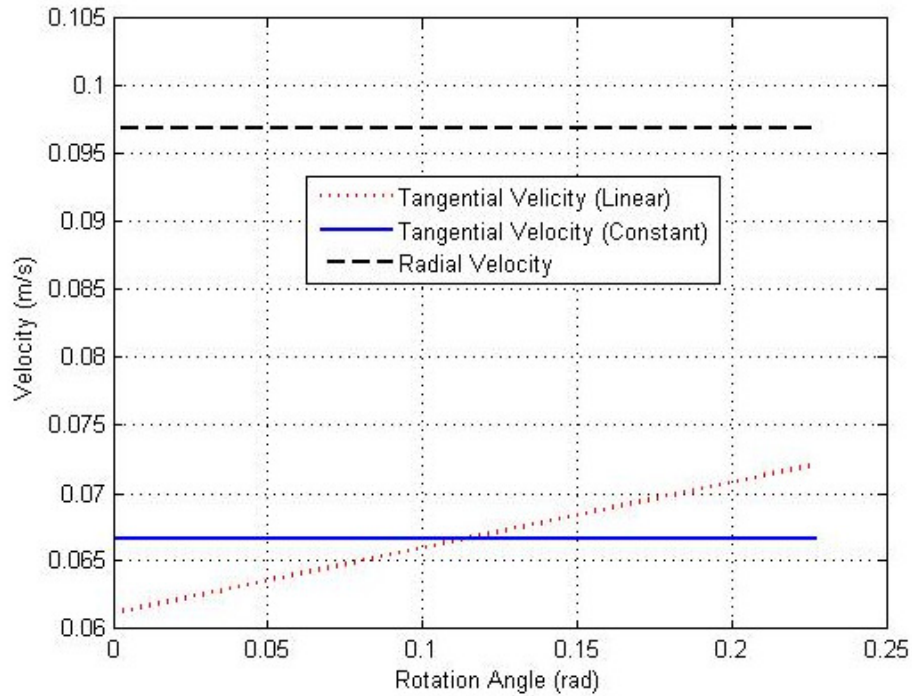


**Figure 6.16** Velocity profile for cutting titanium alloy (Cutter E)

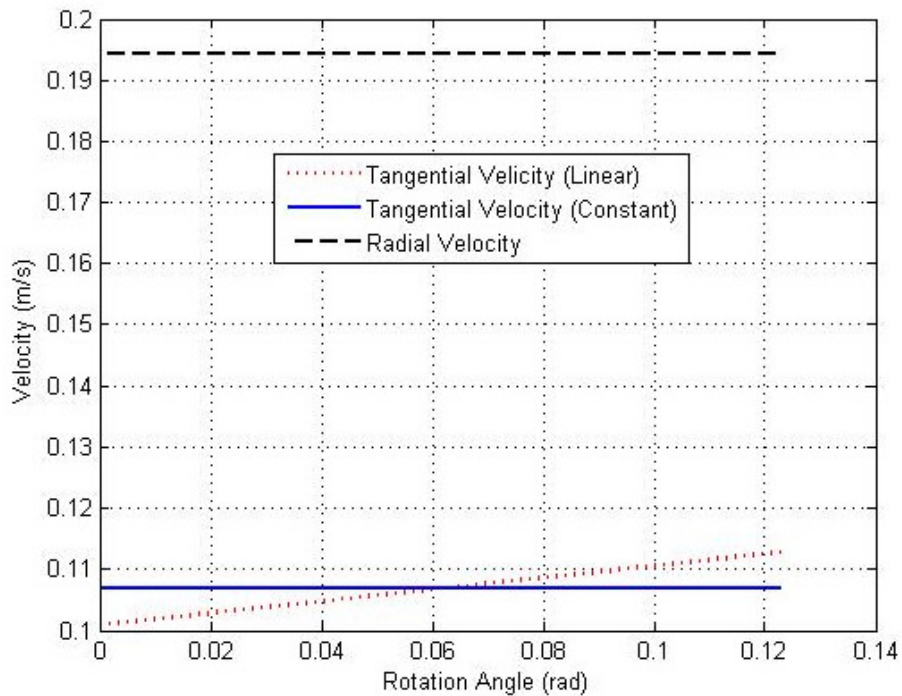


**Figure 6.17** Velocity profile for cutting steel (Cutter D)

### 6.5.1 Validating Simulation Results for Aluminum Alloy

The tests were all conducted using cutter A and cover a wide range of feeds and a variety of milling modes. The test conditions were selected so as to allow the assessment of the influence of the second order effects that have been included in this model but are rarely addressed by other authors within actual model development. The force measurements are presented in Figures 6.18-6.28 which portray the feeding and normal forces  $F_x$  and  $F_y$  as a function of cutter rotational angle in up milling, down milling, and central cut modes. A good agreement between the predictive model (all force component modules included) and experimental results is found excepting in those cases where the feeding velocity is very low, ( $V_f=1.28$  in/min), and runout distorts the expected result.

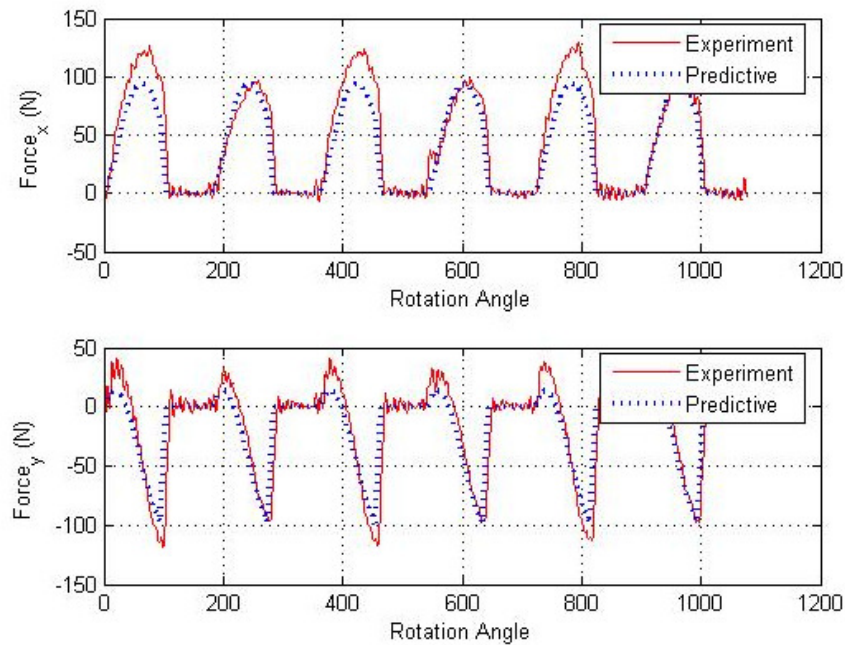


**Figure 6.18 Measured and predicted forces  $F_x$  and  $F_y$  for up milling of aluminum alloy ( $V_f=3.95$  in/min, Cutter A)**

## 6 Experimental Validation of the Predictive Model

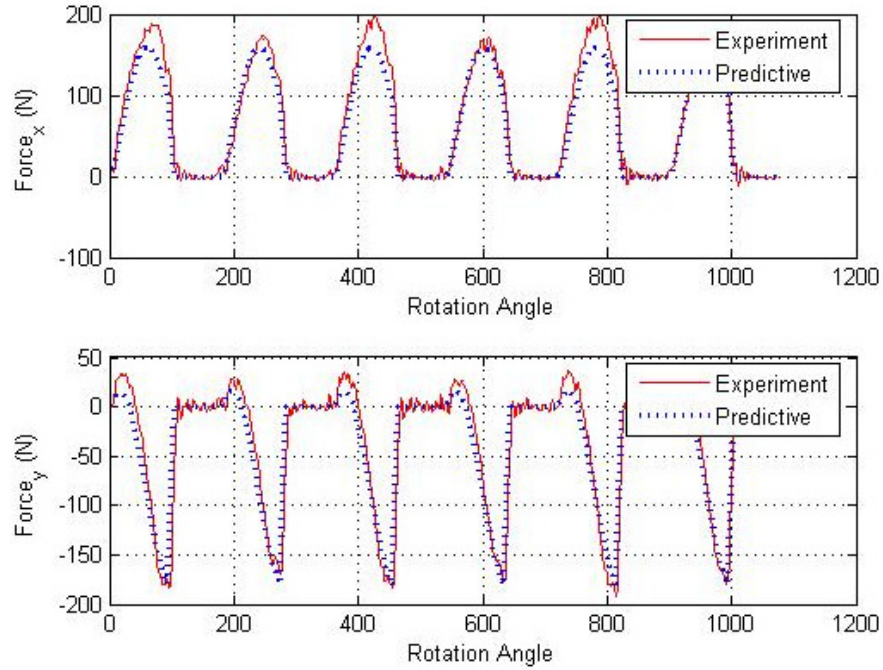


**Figure 6.19 Measured and predicted forces  $F_x$  and  $F_y$  for up milling of aluminum alloy ( $V_f=7.9$  in/min, Cutter A)**

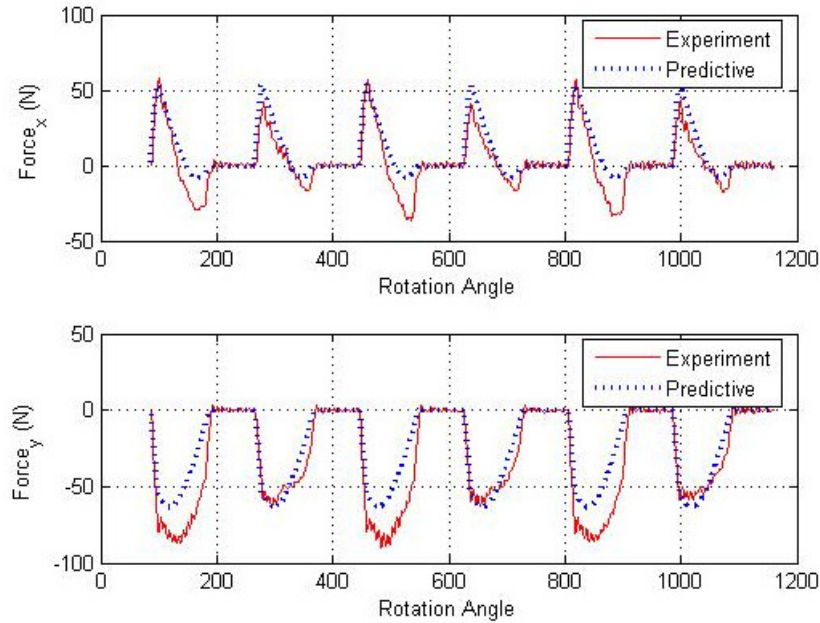


**Figure 6.20 Measured and predicted force  $F_x$  and  $F_y$  for down milling of aluminum alloy ( $V_f=1.28$  in/min, Cutter A)**

## 6 Experimental Validation of the Predictive Model

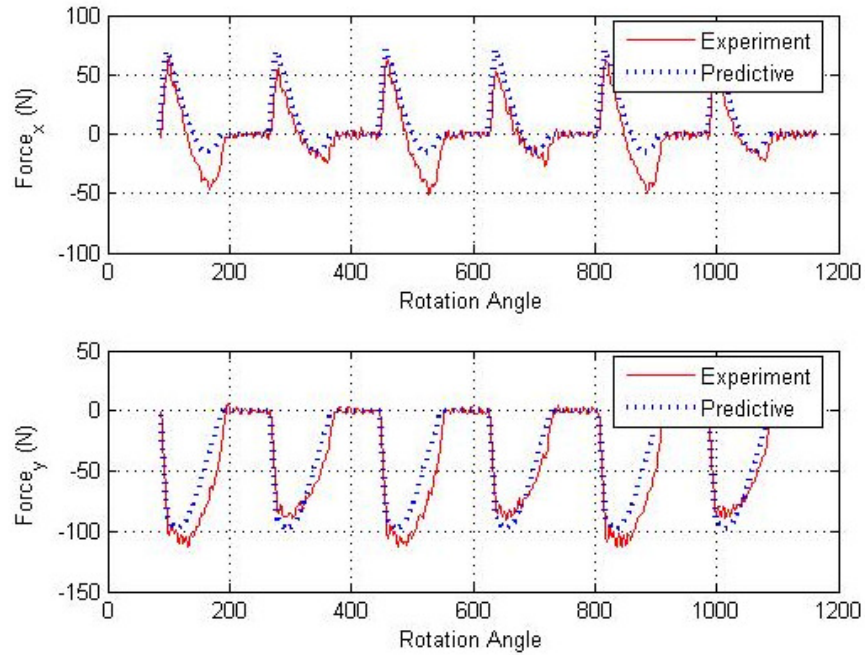


**Figure 6.21 Measured and predicted force  $F_x$  and  $F_y$  for down milling of aluminum alloy ( $V_f=2.56$  in/min, Cutter A)**

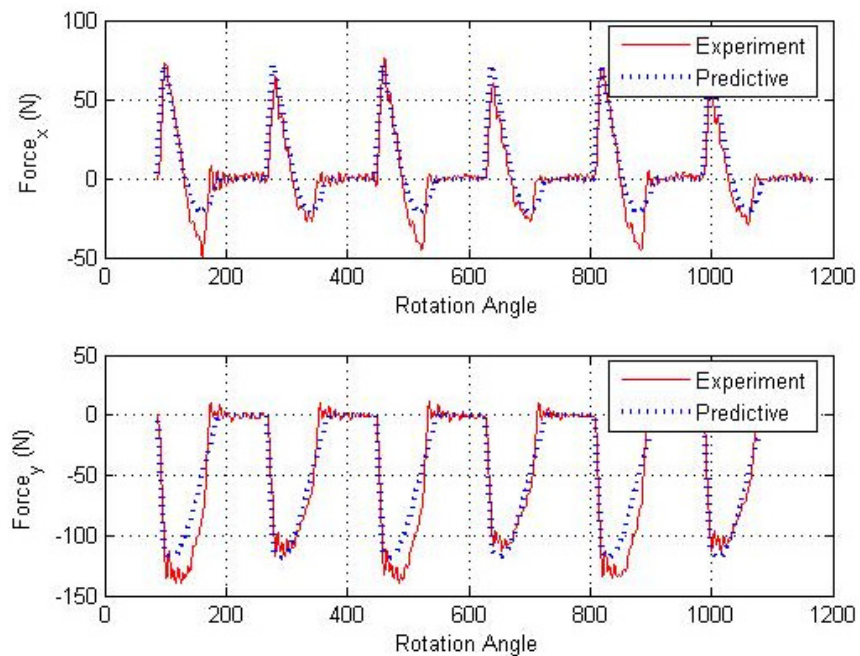


**Figure 6.22 Measured and predicted force  $F_x$  and  $F_y$  for down milling of aluminum alloy ( $V_f=3.95$  in/min, Cutter A)**

## 6 Experimental Validation of the Predictive Model

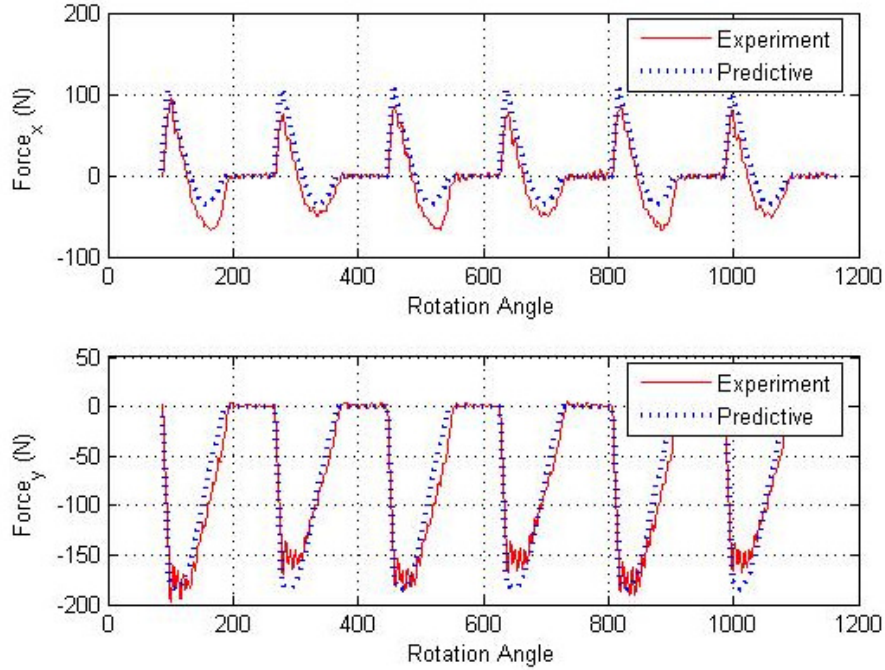


**Figure 6.23 Measured and predicted force  $F_x$  and  $F_y$  for down milling of aluminum alloy ( $V_f=6.75$  in/min, Cutter A)**

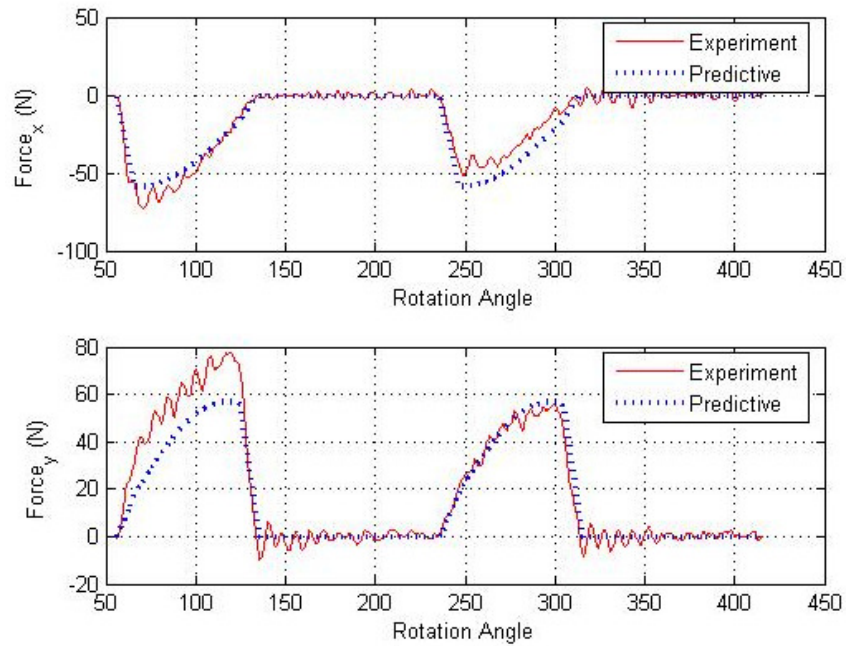


**Figure 6.24 Measured and predicted forces  $F_x$  and  $F_y$  for central cutting aluminum alloy ( $V_f=1.28$  in/min, Cutter A)**

## 6 Experimental Validation of the Predictive Model

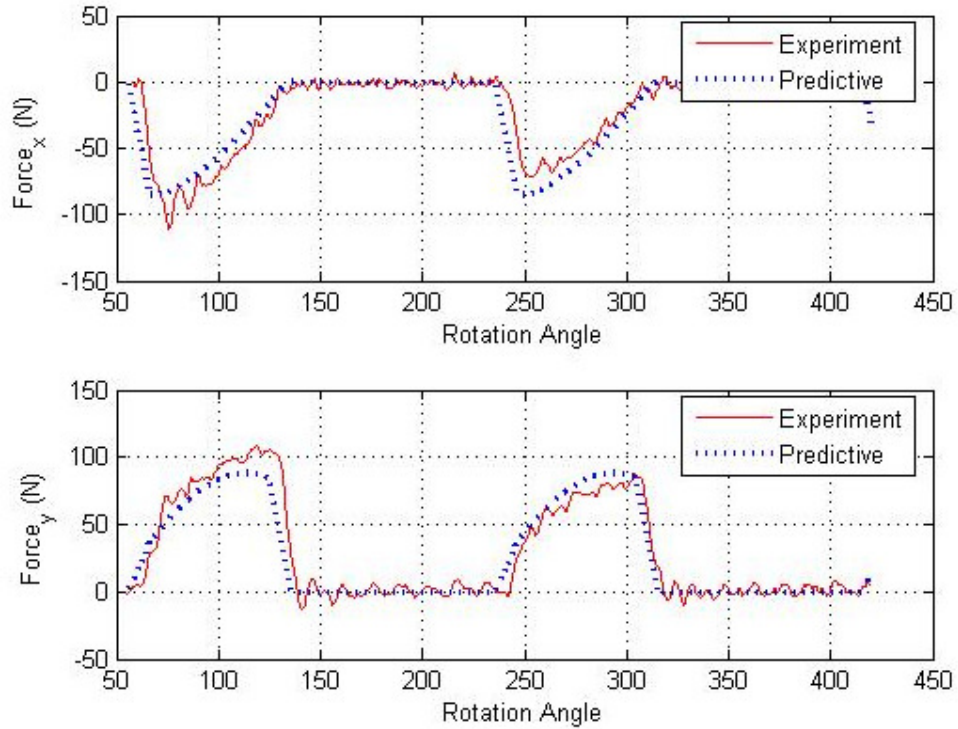


**Figure 6.25 Measured and predicted forces  $F_x$  and  $F_y$  for central cutting aluminum alloy ( $V_f=2.56$  in/min, Cutter A)**

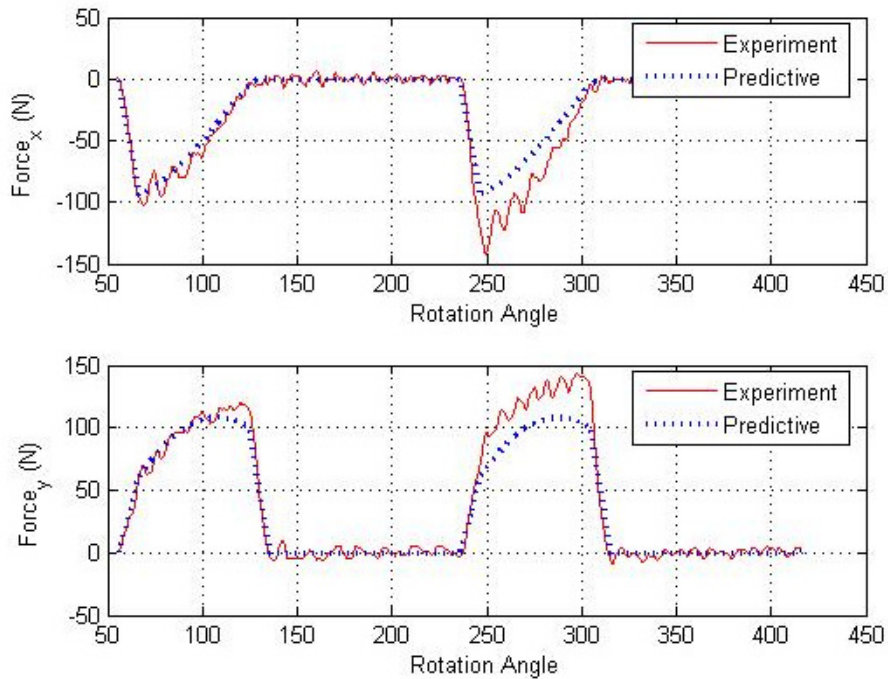


**Figure 6.26 Measured and predicted forces  $F_x$  and  $F_y$  for central cutting aluminum alloy ( $V_f=4.4$  in/min, Cutter A)**

## 6 Experimental Validation of the Predictive Model

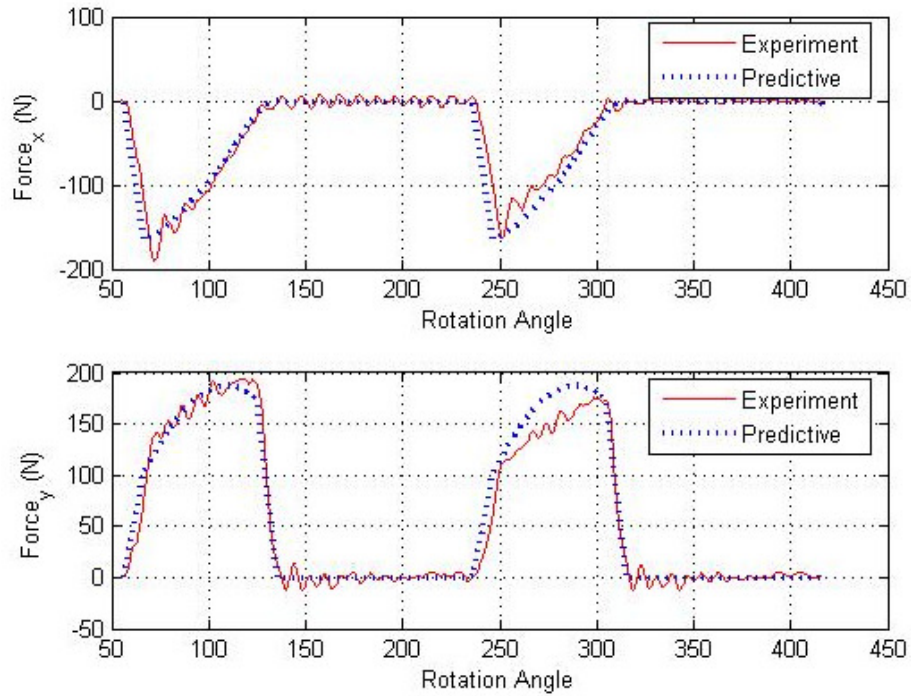


**Figure 6.27 Measured and predicted forces  $F_x$  and  $F_y$  for central cutting aluminum alloy ( $V_f=6.75$  in/min, Cutter A)**

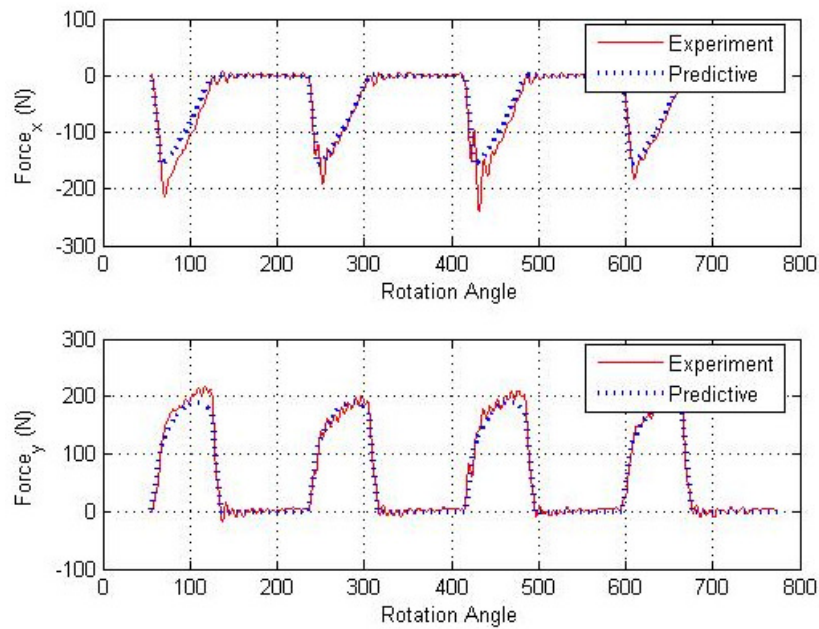


**Figure 6.28 Measured and predicted forces  $F_x$  and  $F_y$  for central cutting aluminum alloy ( $V_f=7.9$  in/min, Cutter A)**

## 6 Experimental Validation of the Predictive Model

To investigate the importance of the ploughing effect, force predictions with and without considering the ploughing force are shown in Figures 6.29 and 6.30 for feeds of  $V_f=1.28$  in/min and 2.56 in/min respectively in the central cut operations. The figures confirm the strong influence of ploughing force; these of course are especially significant at low feed.

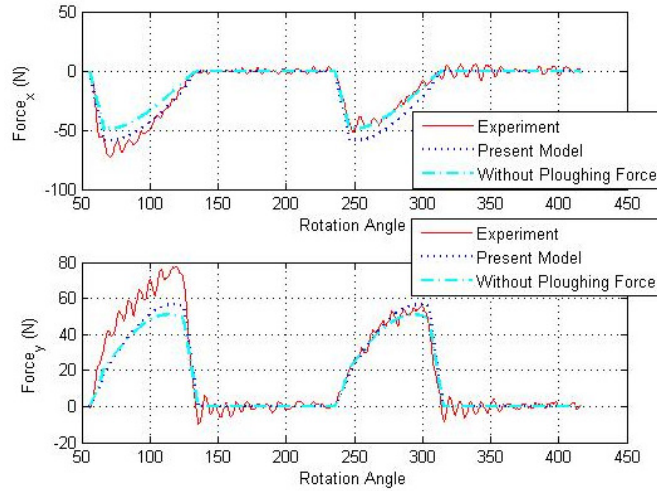


**Figure 6.29 Force comparison with and without considering ploughing force on central cutting aluminum alloy ( $V_f=1.28$  in/min, Cutter A)**

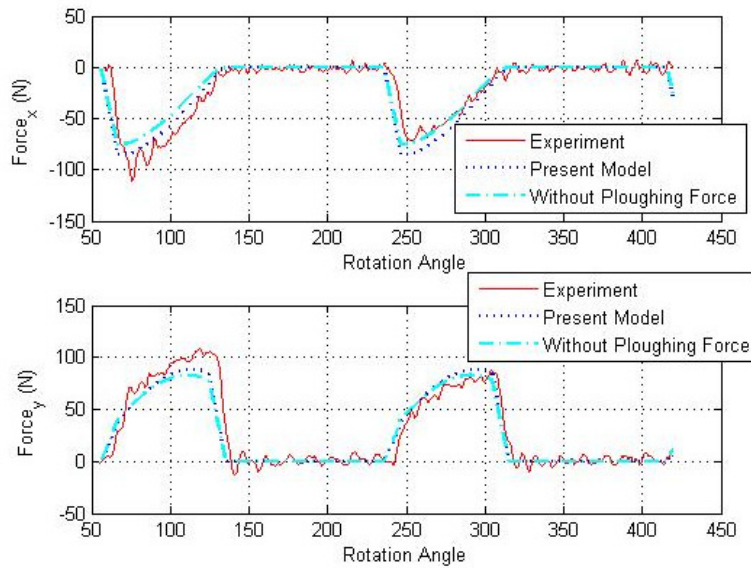


**Figure 6.30 Force comparison with and without considering ploughing force on central cutting aluminum alloy ( $V_f=2.56$  in/min, Cutter A)**

## 6 Experimental Validation of the Predictive Model

The influence of surface slope variation on the cutting forces is shown in Figures 6.31 and 6.32 for both central cutting and up milling of aluminum alloy at a feed  $V_f=7.9$  in/min. It can be seen that the surface slope changes both the force magnitude and shape.

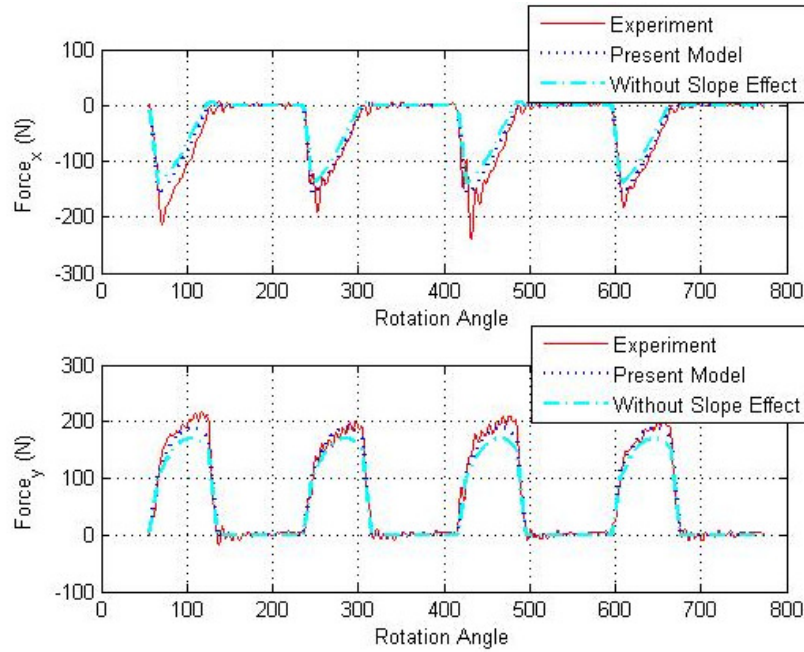


**Figure 6.31 Force comparison with and without considering slope effect on central cutting aluminum alloy ( $V_f=7.9$  in/min, Cutter A)**

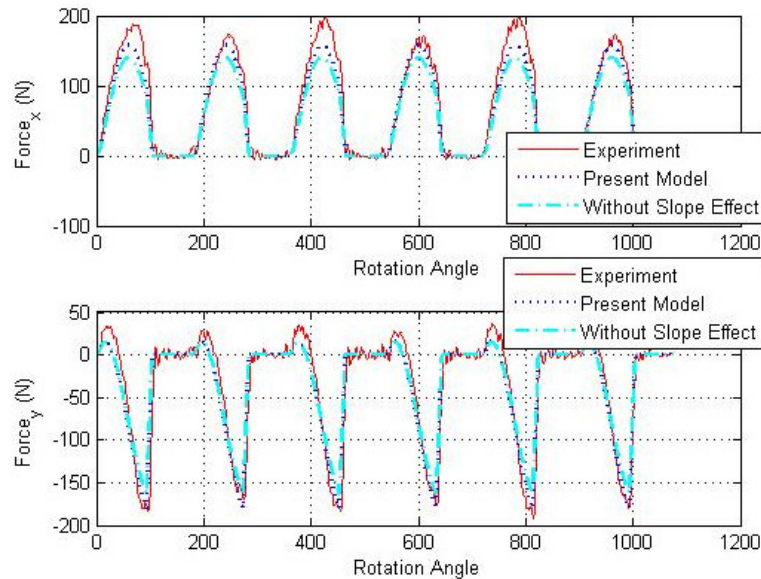


**Figure 6.32 Force comparison with and without considering slope effect on up milling aluminum alloy ( $V_f=7.9$  in/min, Cutter A)**

## 6 Experimental Validation of the Predictive Model

Figure 6.33 shows the force comparison between the experimental data and the predicted results for slotting aluminum alloy at the feeding speeds 2.2 in/min and 4.4 in/min. It should be noted that in this case, there is a jump in depth from 0.05 inch to 0.165 inch at the center of the cut. This depth jump means that there is a kinematics change around the jump locations, which can be used to further validate the accuracy of the proposed predictive model. As expected, a good agreement can be observed for these two cutting processes.

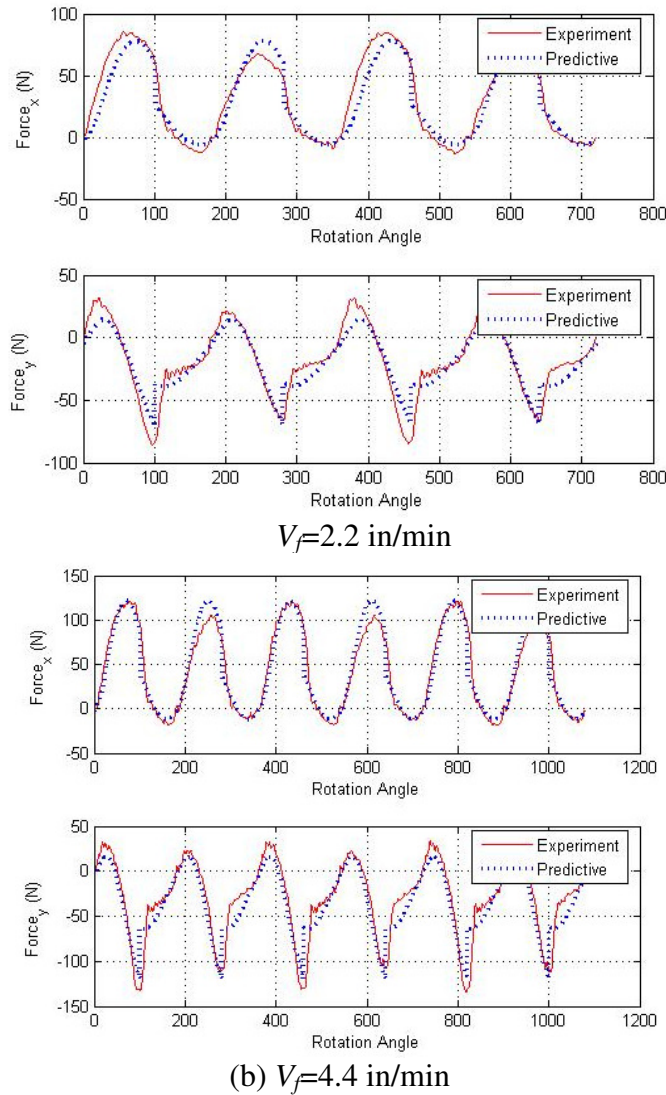


**Figure 6.33 Measured and predicted forces  $F_x$  and  $F_y$  for slotting (center jump of depth of cut) aluminum alloy at different feeding velocities (Cutter A)**

### 6.5.2 Validating Simulation Results for Titanium Alloy with 3/8" SGS

#### Cutter

Experiments were conducted at a spindle speed 575 RPM and included down milling, up milling and central cutting of the titanium alloy at five different feed rates ranging from 0.75 in/min to 4.4 in/min. Figures 6.34-6.44 plot the force comparison between the predicted results and measured values. The dotted line indicates the predictions made from the present model; the solid line represents the experimental results. Overall, the present model is shown to accurately predict the cutting forces in both x and y directions.

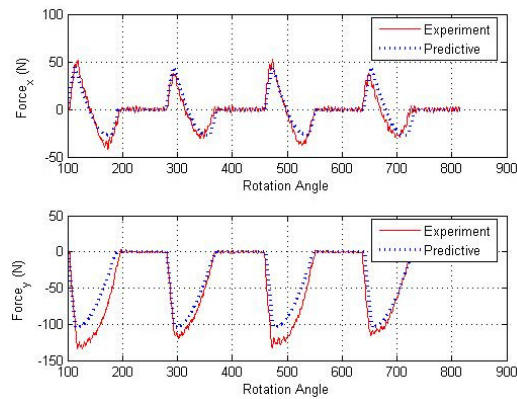


**Figure 6.34 Measured and predicted forces  $F_x$  and  $F_y$  for down milling of titanium alloy ( $V_f=0.75$  in/min, Cutter C)**

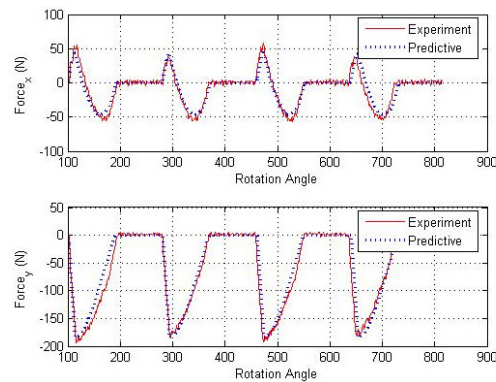


**Figure 6.35 Measured and predicted forces  $F_x$  and  $F_y$  for down milling of titanium alloy ( $V_f=1.5$  in/min, Cutter C)**

## 6 Experimental Validation of the Predictive Model

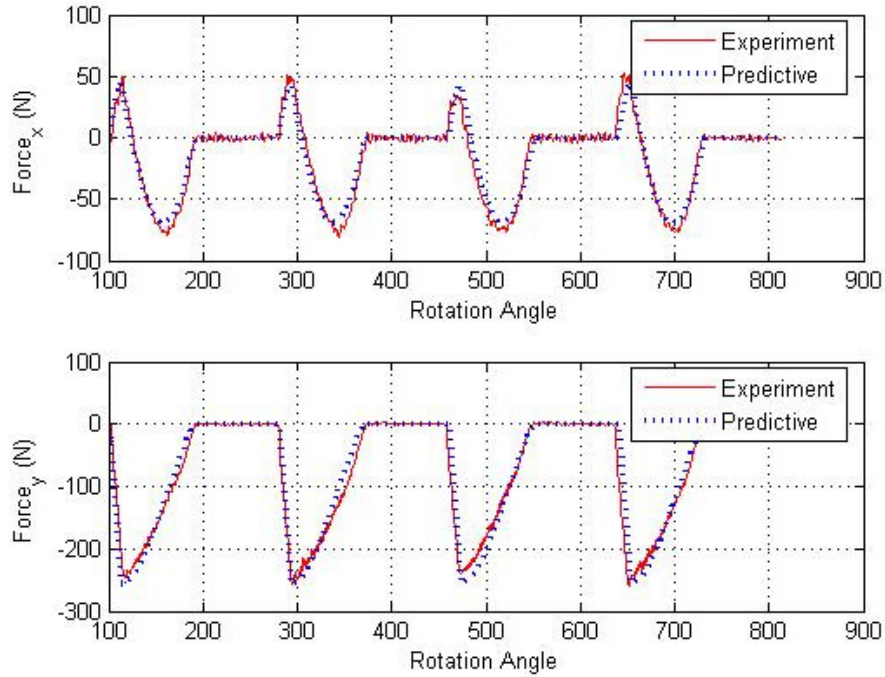


**Figure 6.36 Measured and predicted forces  $F_x$  and  $F_y$  for down milling of titanium alloy ( $V_f=2.2$  in/min, Cutter C)**

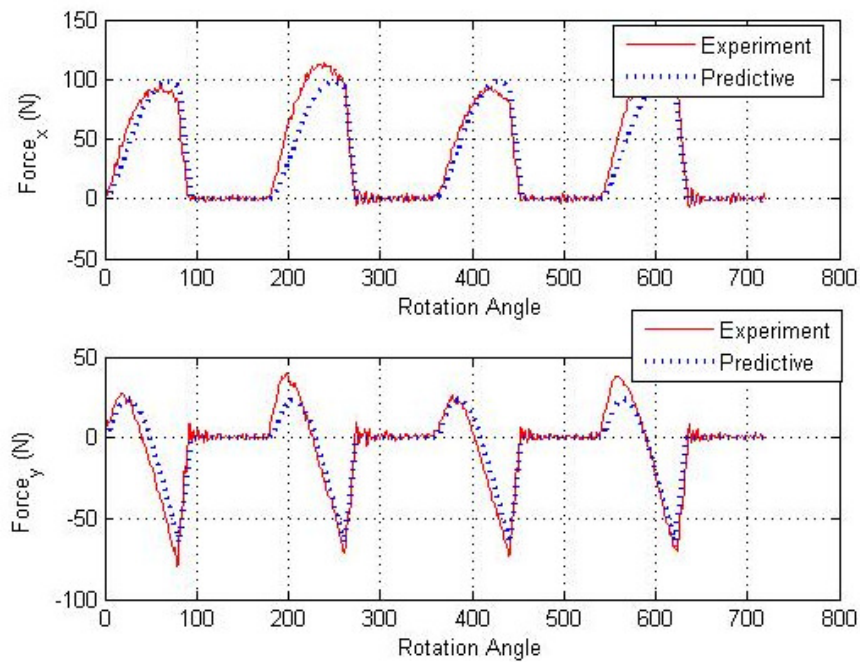


**Figure 6.37 Measured and predicted forces  $F_x$  and  $F_y$  for up milling of titanium alloy ( $V_f=0.75$  in/min, Cutter C)**

## 6 Experimental Validation of the Predictive Model

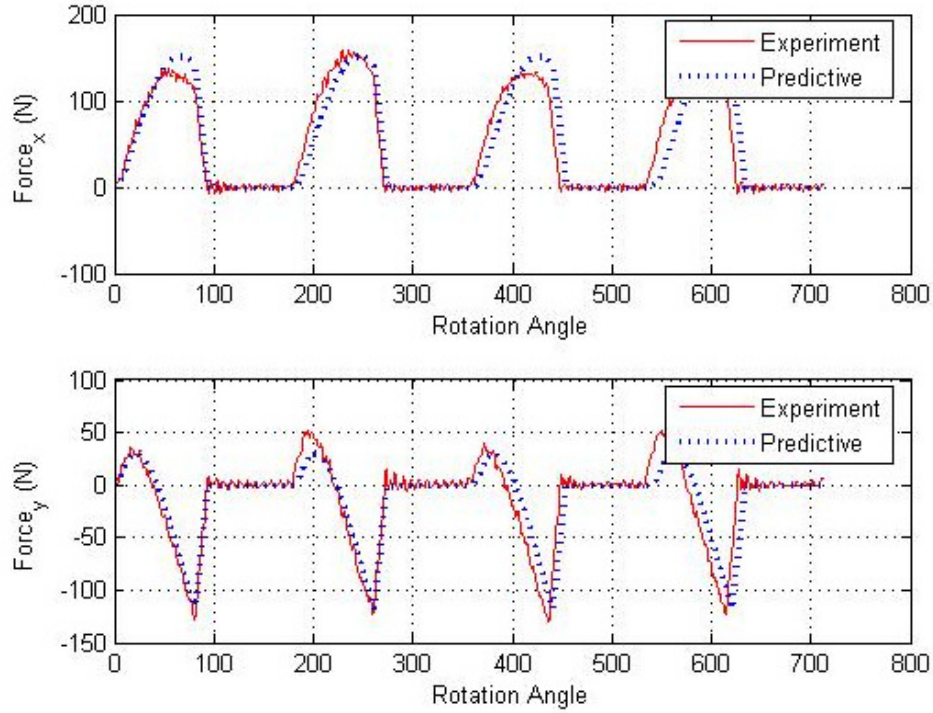


**Figure 6.38 Measured and predicted forces  $F_x$  and  $F_y$  for up milling of titanium alloy ( $V_f=1.5$  in/min, Cutter C)**

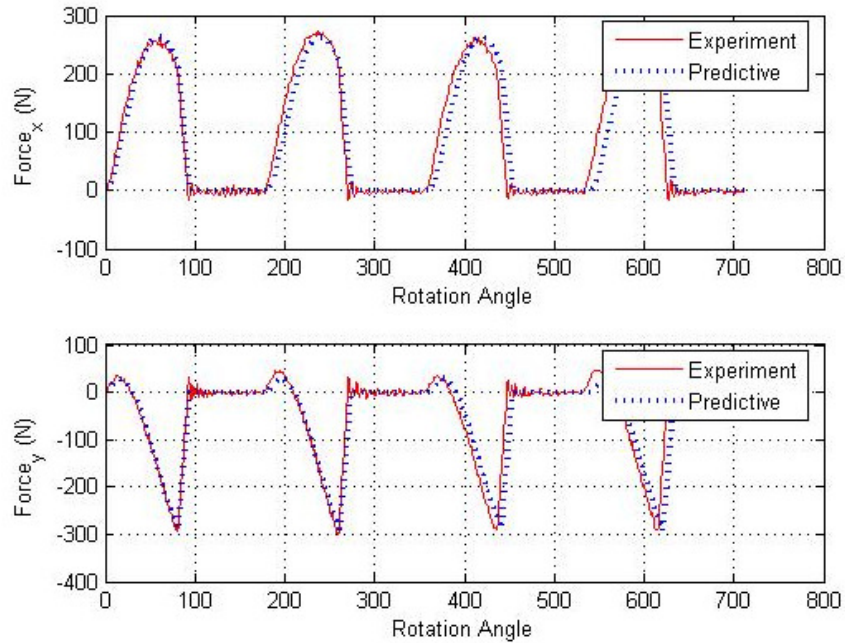


**Figure 6.39 Measured and predicted forces  $F_x$  and  $F_y$  for up milling of titanium alloy ( $V_f=4.4$  in/min, Cutter C)**

## 6 Experimental Validation of the Predictive Model

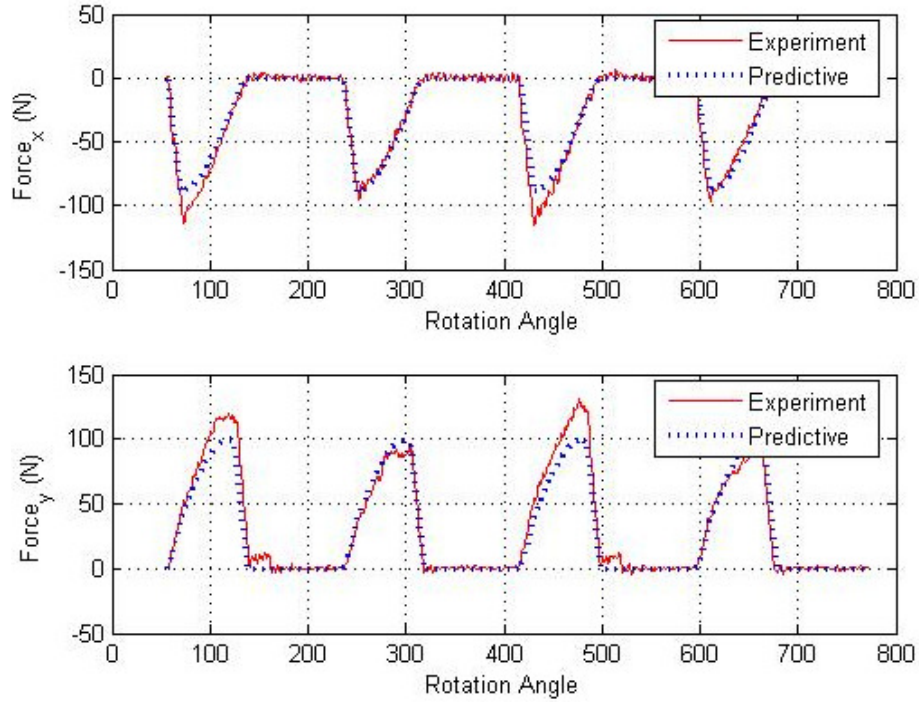


**Figure 6.40 Measured and predicted forces  $F_x$  and  $F_y$  for central cutting titanium alloy ( $V_f=0.75$  in/min, Cutter B)**

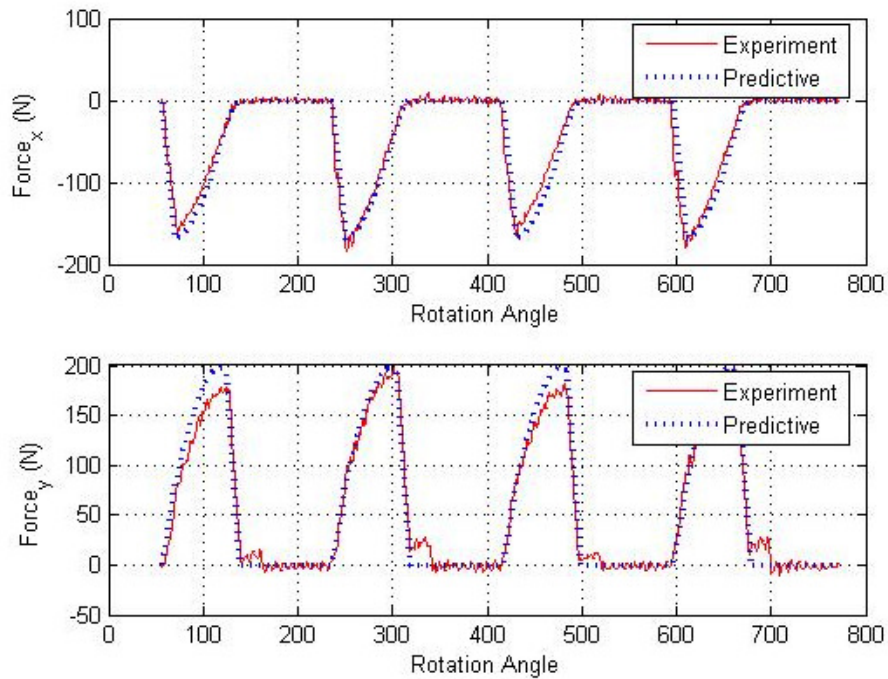


**Figure 6.41 Measured and predicted forces  $F_x$  and  $F_y$  for central cutting titanium alloy ( $V_f=1.5$  in/min, Cutter B)**

## 6 Experimental Validation of the Predictive Model

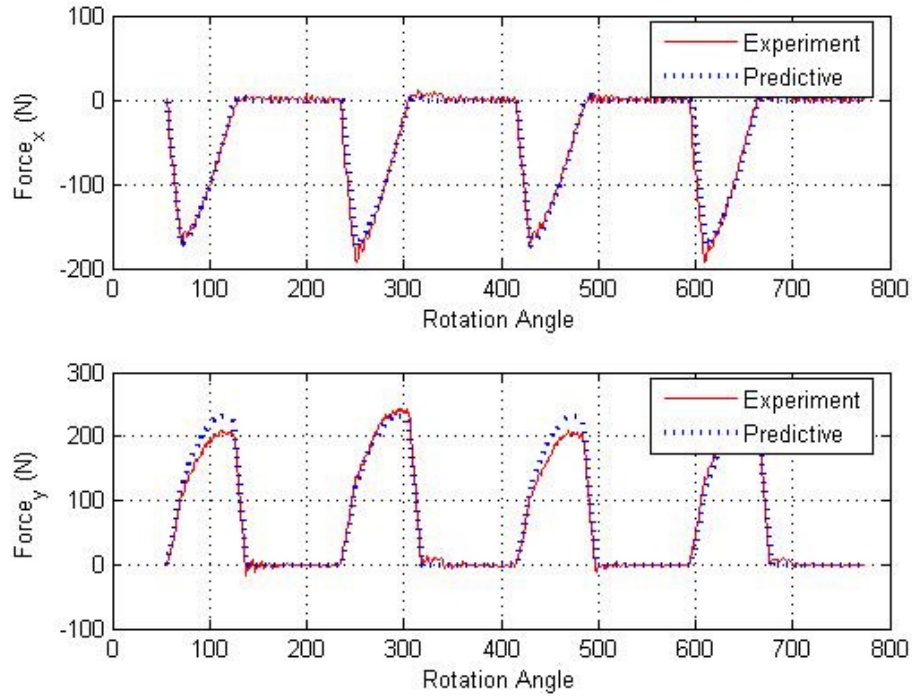


**Figure 6.42 Measured and predicted forces  $F_x$  and  $F_y$  for central cutting titanium alloy ( $V_f=2.2$  in/min, Cutter B)**

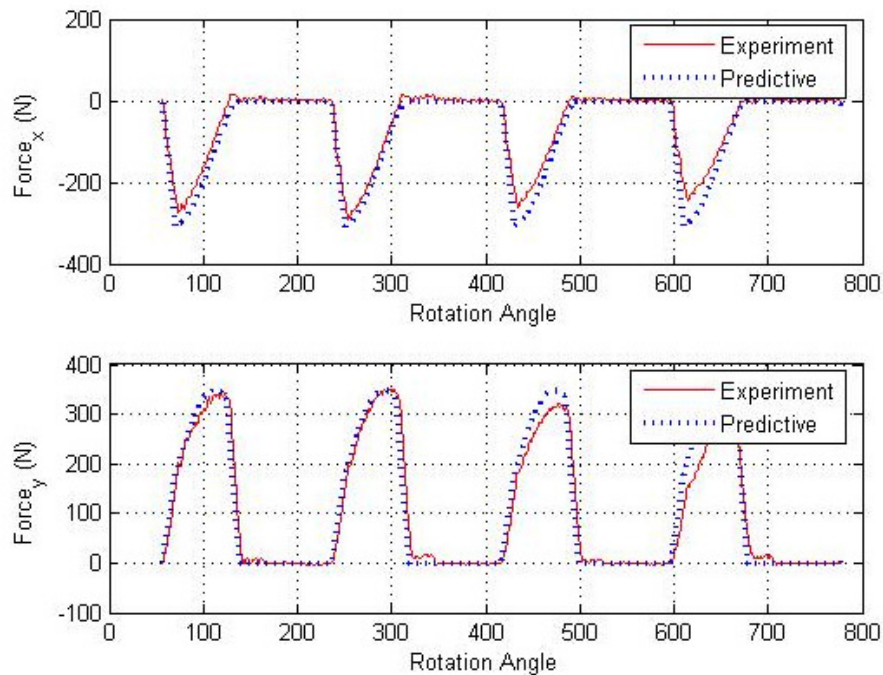


**Figure 6.43 Measured and predicted forces  $F_x$  and  $F_y$  for central cutting titanium alloy ( $V_f=3.95$  in/min, Cutter B)**

## 6 Experimental Validation of the Predictive Model

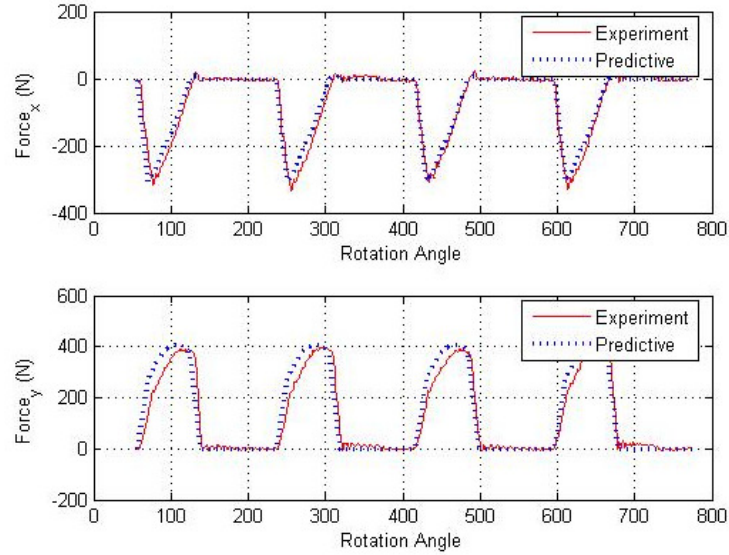


**Figure 6.44 Measured and predicted forces  $F_x$  and  $F_y$  for central cutting titanium alloy ( $V_f=4.4$  in/min, Cutter B)**

The predicted contributions of ploughing force to overall force in milling operations have been investigated. The predicted forces for up milling, down milling, and central cutting of titanium alloy at a low feed of  $V_f=0.75$  in/min are shown in Figures 6.45, 6.46 and 6.47, respectively. The solid line in these figures represents the measured forces, the dotted line indicates the force prediction including the ploughing forces, and the dashed line indicates the predicted results without considering the ploughing forces. The figures confirm the strong influence of ploughing force at low feed. The proposed upper bound model does an excellent job of accounting for the additional forces due to ploughing. The slope effect was examined previously for the high feed  $V_f=4.4$  in/min in up milling and central cutting, it is interesting to compare the influence of slope at the lower feed and to contrast this with the influence of ploughing force. Figures 6.48 and 6.49 show the predicted results with and without considering the slope effect. It can be

## 6 Experimental Validation of the Predictive Model

seen that the surface slope does influence the overall shape of the force magnitude, but to a much lesser extent than the ploughing effect at these low chip thicknesses.

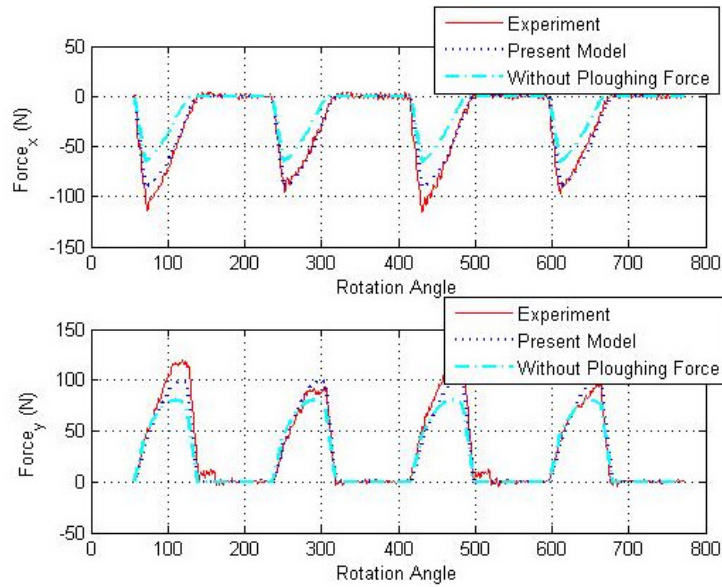


**Figure 6.45 Force comparison with and without considering ploughing force for central cutting titanium alloy ( $V_f=0.75$  in/min, Cutter B)**

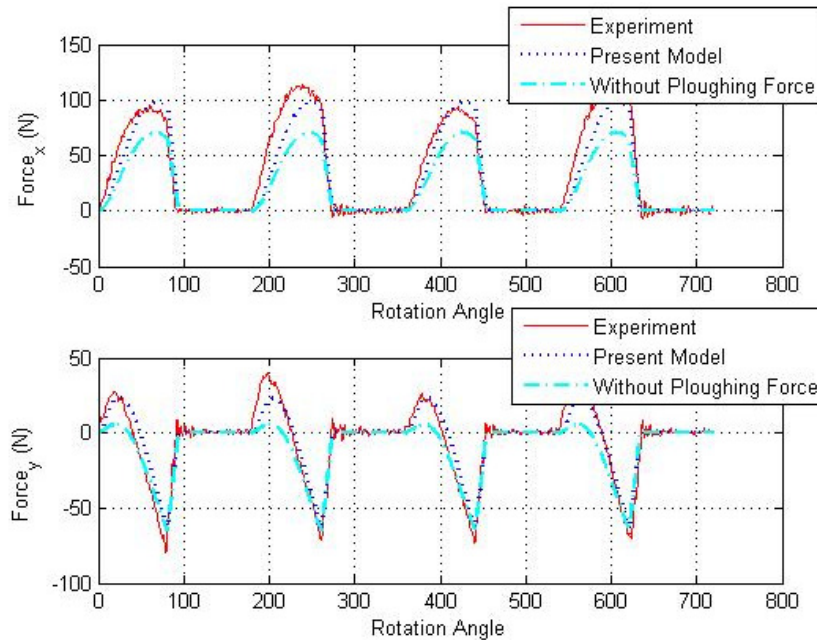


**Figure 6.46 Force comparison with and without considering ploughing force for up milling of titanium alloy ( $V_f=0.75$  in/min, Cutter C)**

## 6 Experimental Validation of the Predictive Model

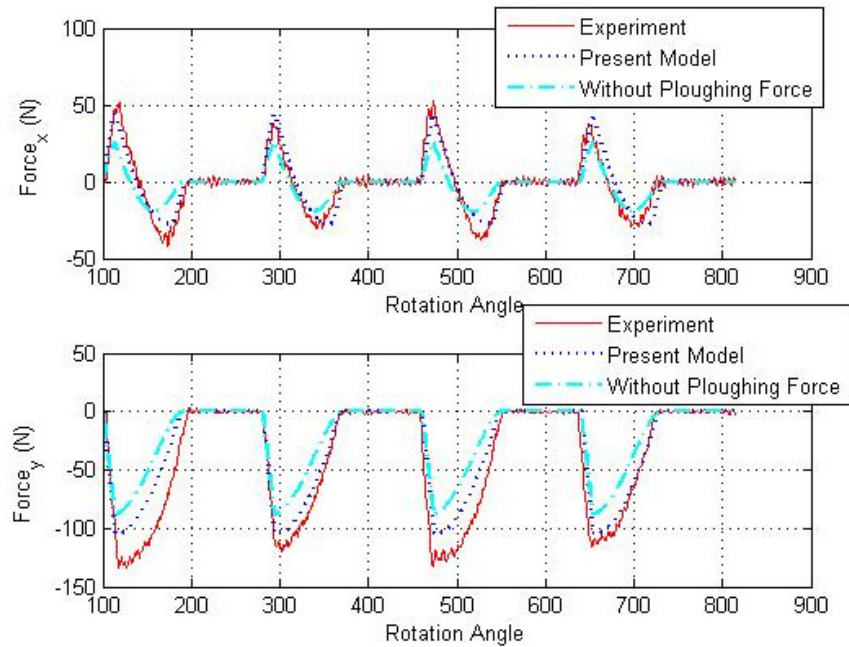


**Figure 6.47** Force comparison with and without considering ploughing force for down milling of titanium alloy ( $V_f=0.75$  in/min, Cutter C)

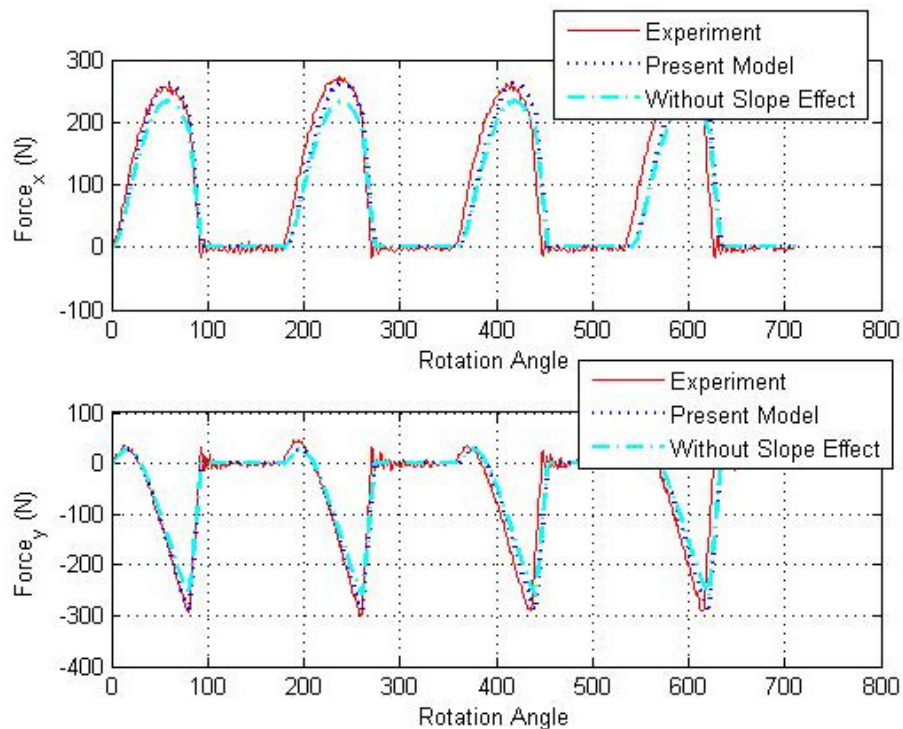


**Figure 6.48** Force comparison with and without considering slope effect for up milling of titanium alloy ( $V_f=4.4$  in/min, Cutter C)

## 6 Experimental Validation of the Predictive Model

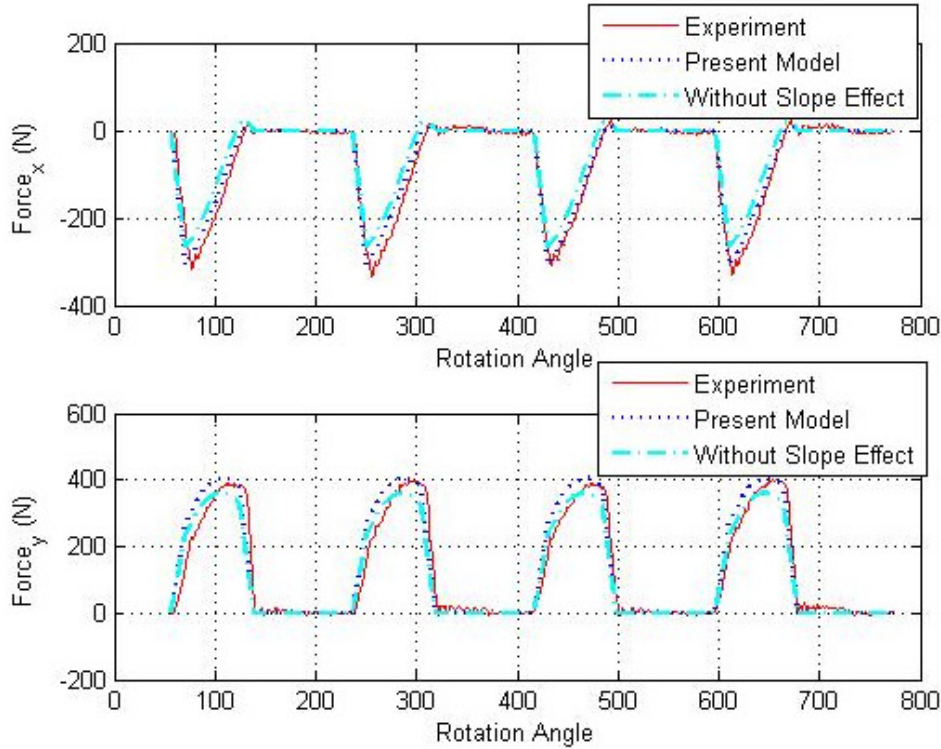


**Figure 6.49 Force comparison with and without considering slope effect for central cutting titanium alloy ( $V_f=4.4$  in/min, Cutter B)**

### 6.5.3 Validating Simulation Results for Titanium Alloy with 3/16" SGS

#### Cutter

The identified constitutive parameters of titanium alloy are now used in the predictions of cutting forces for the data collected (Table AA.3) using a 2 teeth 3/16 inch SGS Ti-N coated carbide end mill cutter (Cutter E). In order to keep the same cutting velocity with the 3/8 inch SGS cutter, the spindle speed is doubled from the 3/8" tool tests to 1152 RPM for 3/16" cutter. The tool edge radius for 3/16" cutter is  $r_e=3.5473 \mu\text{m}$ . Figures 6.50-6.61 show the comparison of the predicted results with measured values for the up milling, down milling and central cutting of titanium alloy. These comparisons clearly show that the predictions are in good agreement with the experiments; there is an

## 6 Experimental Validation of the Predictive Model

obvious but slight difference between the measured and the predicted cutting force that is caused by the tool run-out.

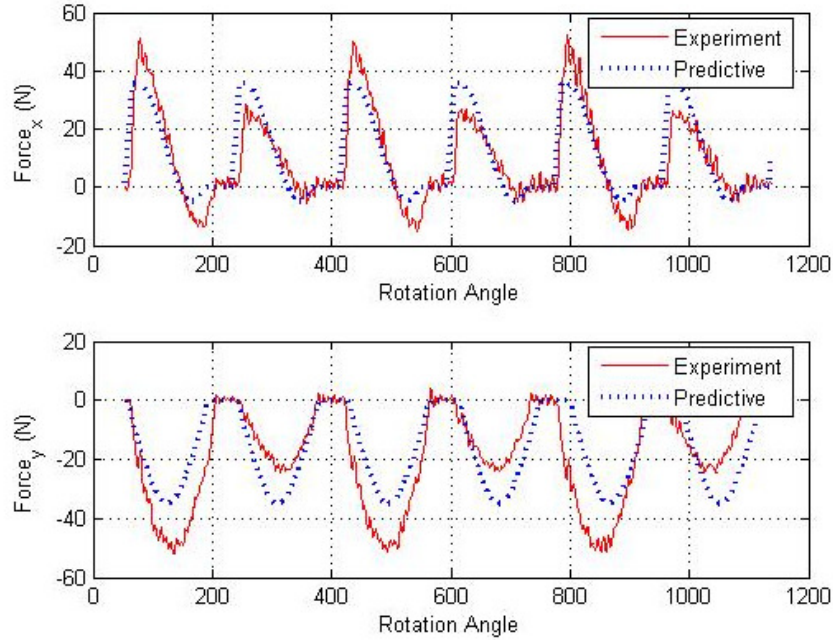


**Figure 6.50 Measured and predicted forces  $F_x$  and  $F_y$  for down milling of titanium alloy ( $V_f=0.75$  in/min, Cutter E)**

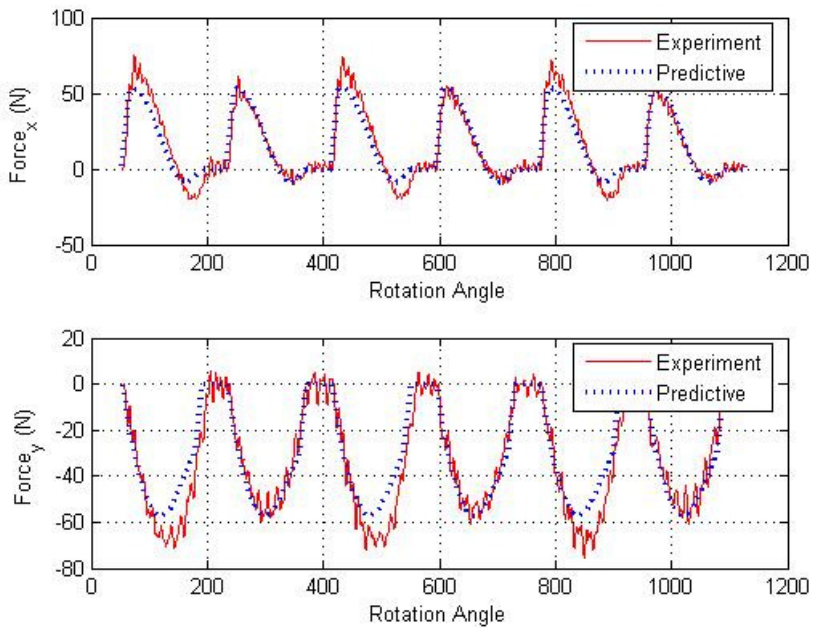


**Figure 6.51 Measured and predicted forces  $F_x$  and  $F_y$  for down milling of titanium alloy ( $V_f=1.5$  in/min, Cutter E)**

## 6 Experimental Validation of the Predictive Model

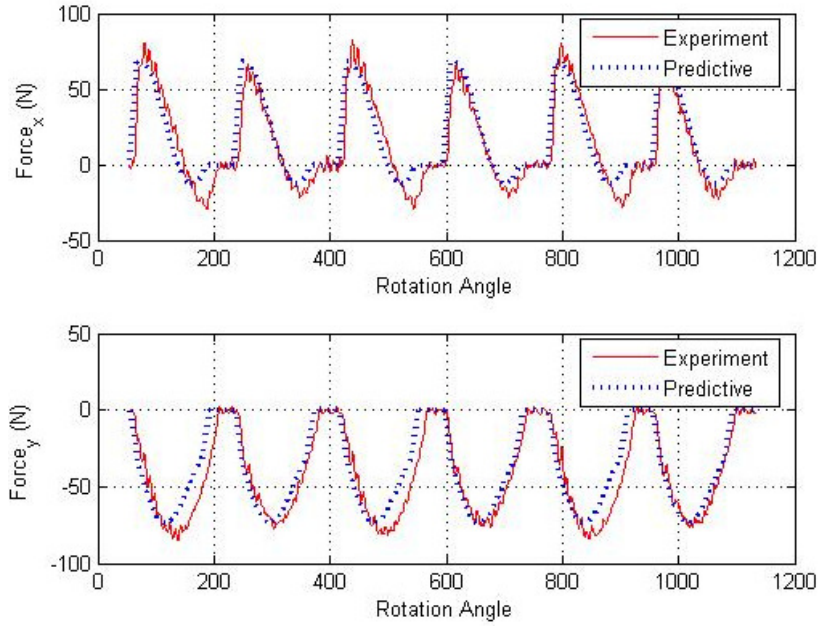


**Figure 6.52 Measured and predicted forces  $F_x$  and  $F_y$  for down milling of titanium alloy ( $V_f=2.2$  in/min, Cutter E)**

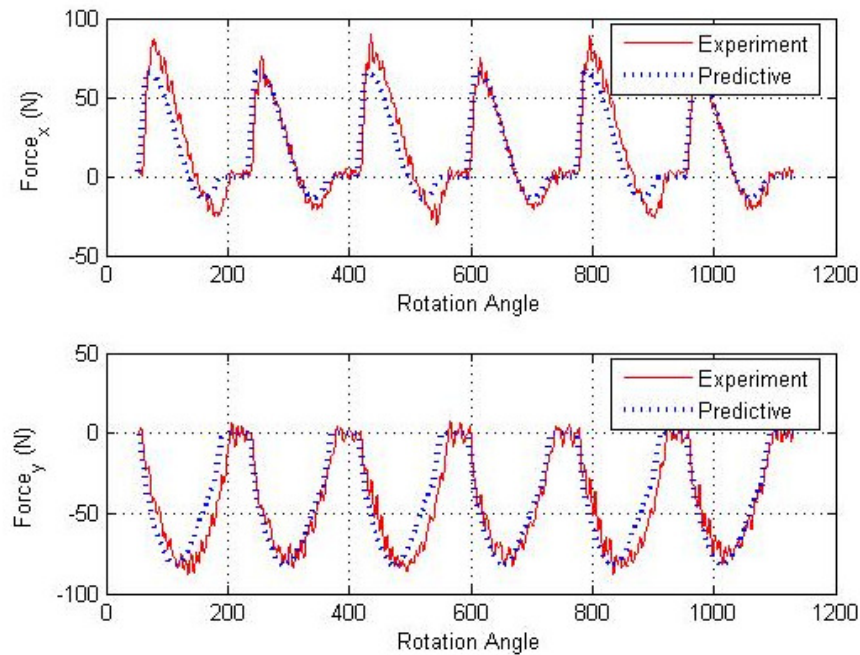


**Figure 6.53 Measured and predicted forces  $F_x$  and  $F_y$  for down milling of titanium alloy ( $V_f=2.56$  in/min, Cutter E)**

## 6 Experimental Validation of the Predictive Model

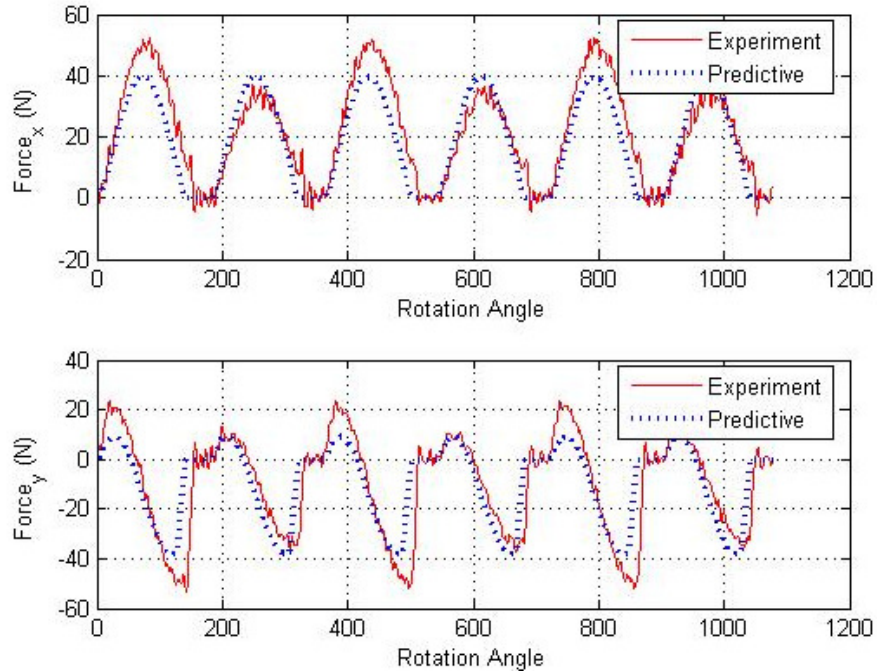


**Figure 6.54** Measured and predicted forces  $F_x$  and  $F_y$  for up milling of titanium alloy ( $V_f=1.5$  in/min, Cutter E)

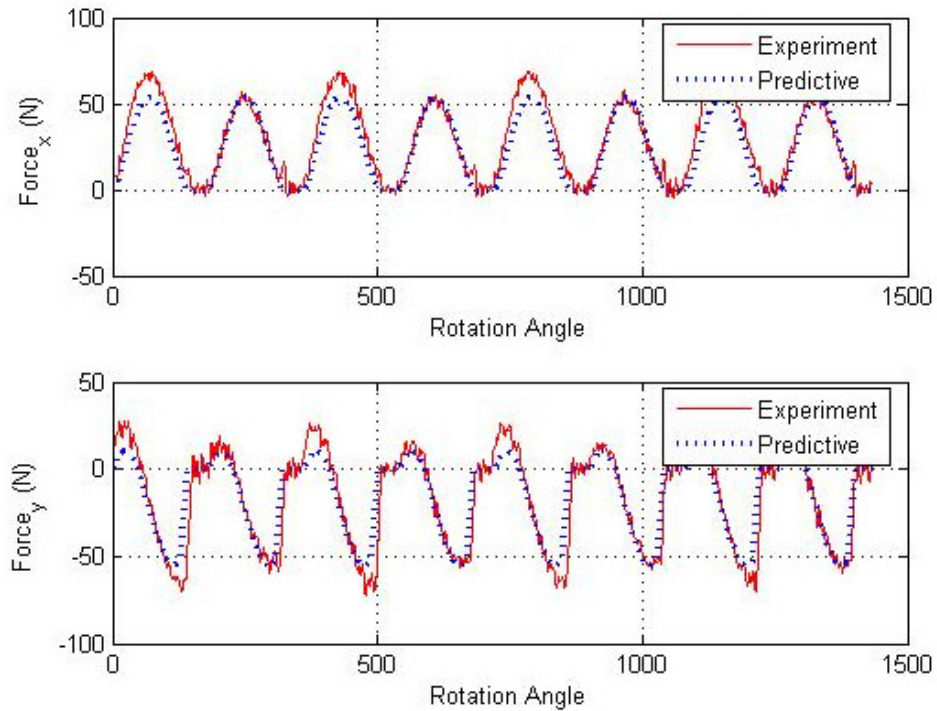


**Figure 6.55** Measured and predicted forces  $F_x$  and  $F_y$  for up milling of titanium alloy ( $V_f=1.5$  in/min, Cutter E)

## 6 Experimental Validation of the Predictive Model

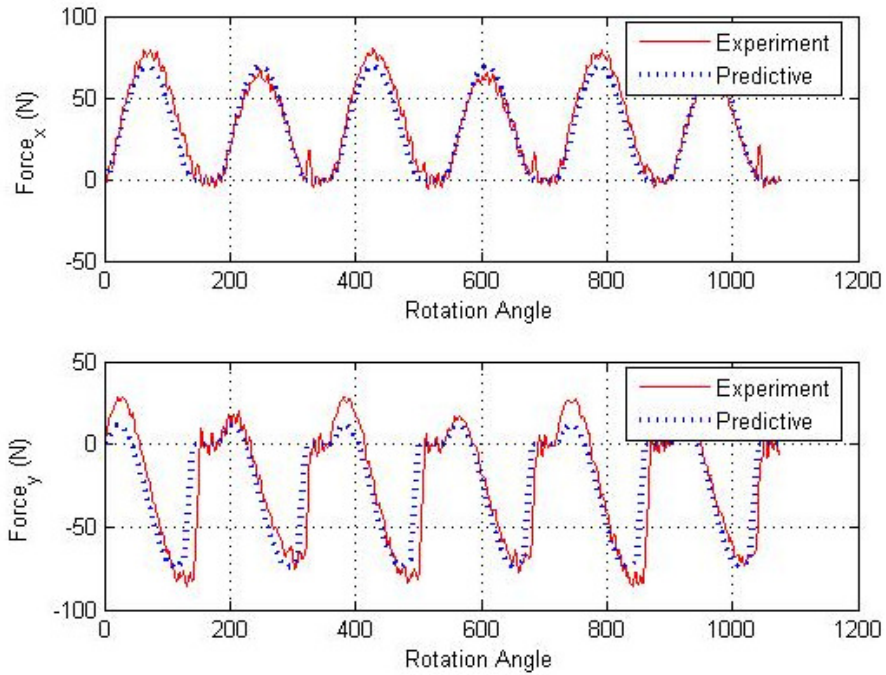


**Figure 6.56** Measured and predicted forces  $F_x$  and  $F_y$  for up milling of titanium alloy ( $V_f=2.2$  in/min, Cutter E)

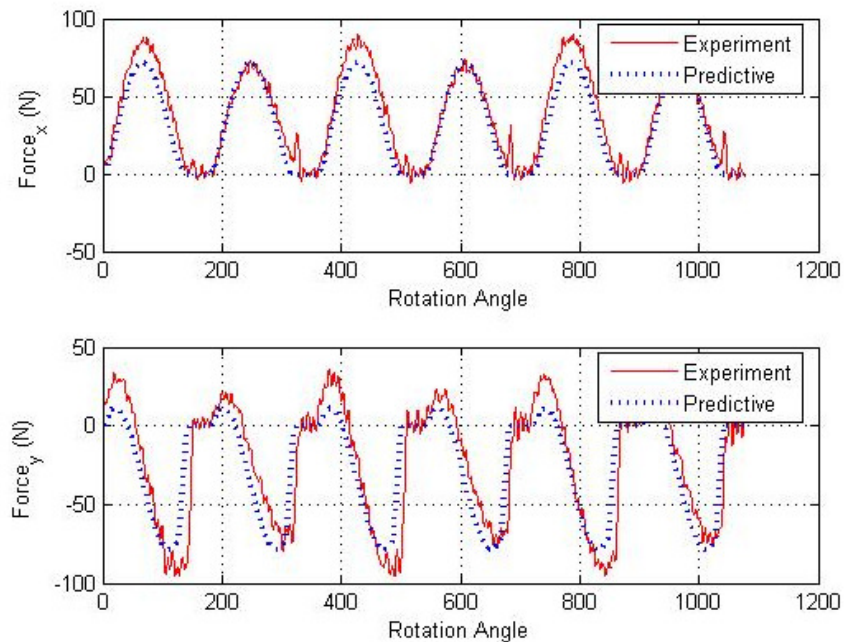


**Figure 6.57** Measured and predicted forces  $F_x$  and  $F_y$  for up milling of titanium alloy ( $V_f=2.56$  in/min, Cutter E)

## 6 Experimental Validation of the Predictive Model

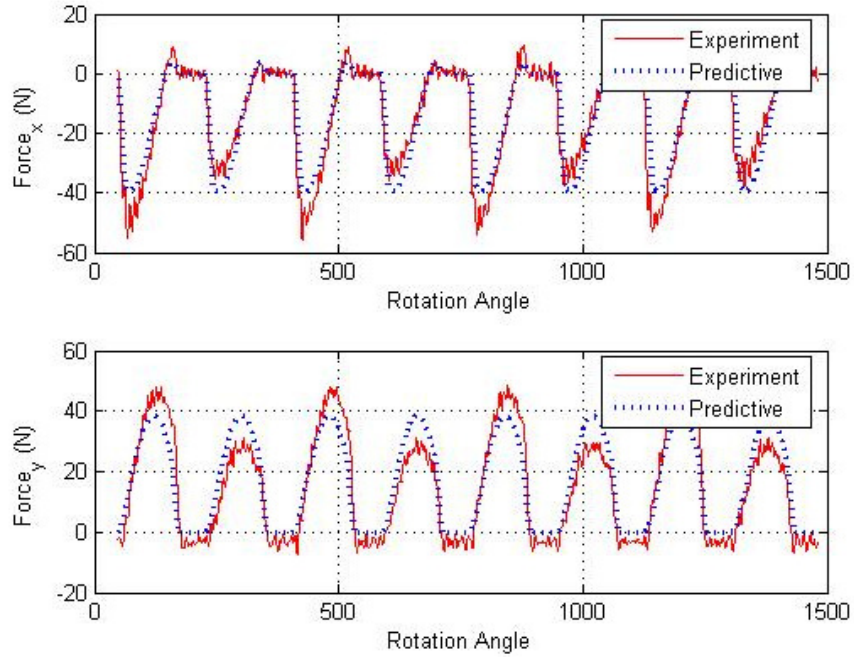


**Figure 6.58** Measured and predicted forces  $F_x$  and  $F_y$  for central cutting titanium alloy ( $V_f=0.75$  in/min, Cutter E)

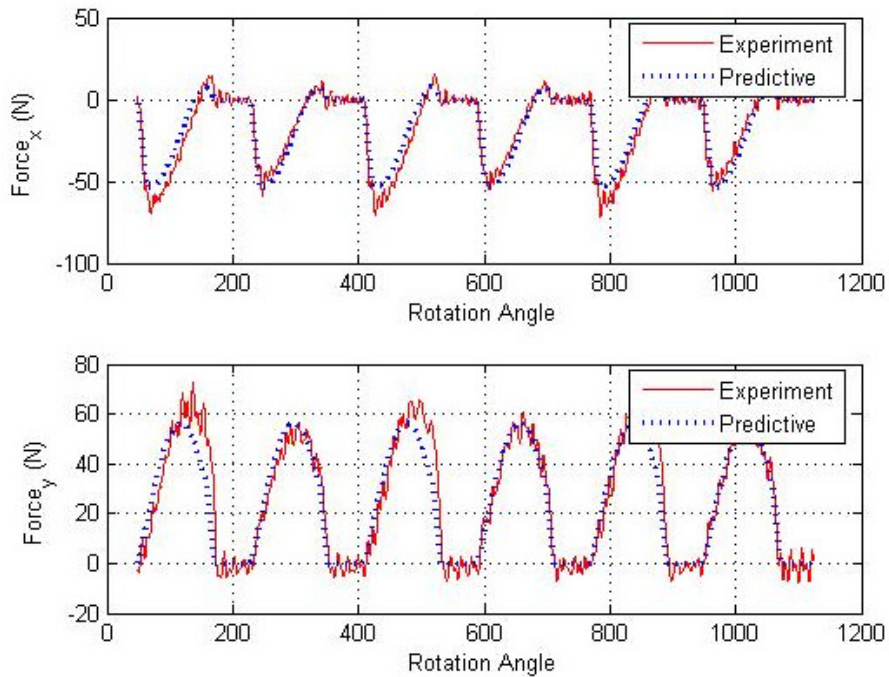


**Figure 6.59** Measured and predicted forces  $F_x$  and  $F_y$  for central cutting titanium alloy ( $V_f=1.5$  in/min, Cutter E)

## 6 Experimental Validation of the Predictive Model

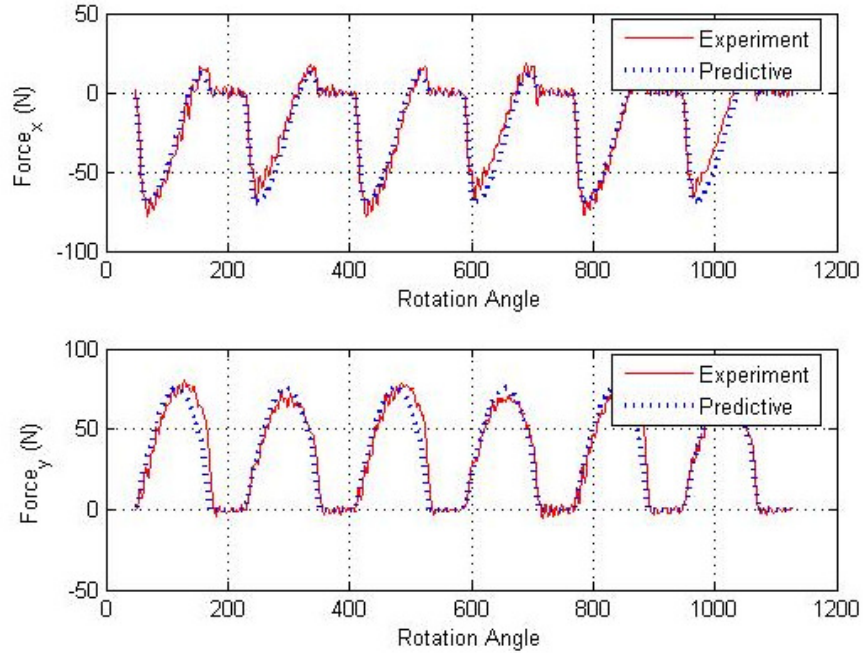


**Figure 6.60** Measured and predicted forces  $F_x$  and  $F_y$  for central cutting titanium alloy ( $V_f=2.2$  in/min, Cutter E)

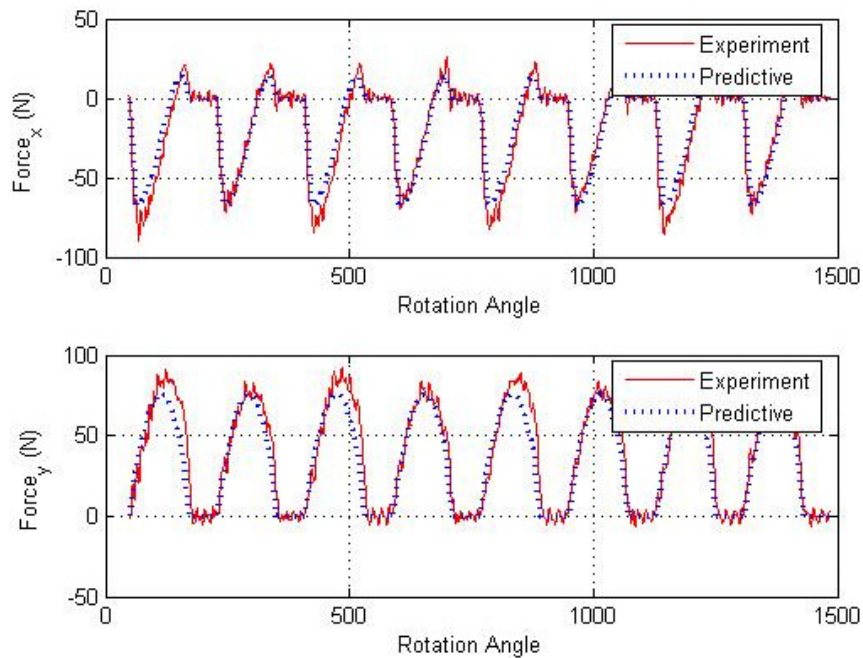


**Figure 6.61** Measured and predicted forces  $F_x$  and  $F_y$  for central cutting titanium alloy ( $V_f=2.56$  in/min, Cutter E)

## 6 Experimental Validation of the Predictive Model

Figures 6.62-6.64 show the force comparisons between the measured values and the predicted results when the ploughing force is neglected at the relatively low feed of  $V_f=0.75$  in/min. The red solid line indicates the measured forces, the blue dotted line represents the predicted forces including the ploughing force, and the cyan dash-dotted line represents the predicted forces neglecting the ploughing force. There is a large error when the ploughing component is neglected (generally greater than 15%). Figures 6.65-6.67 show the force components  $F_x$  and  $F_y$  as a function of rotation angle at the higher feeding velocity of  $V_f=2.56$  in/min, for the down milling, up milling, and central cutting of the titanium alloy. It is expected that there is a larger range of slope here with the smaller diameter tool. The slope effect is examined in these three figures and as expected, the figures clearly show that the surface slope has a significant influence on the shape of the force profiles.

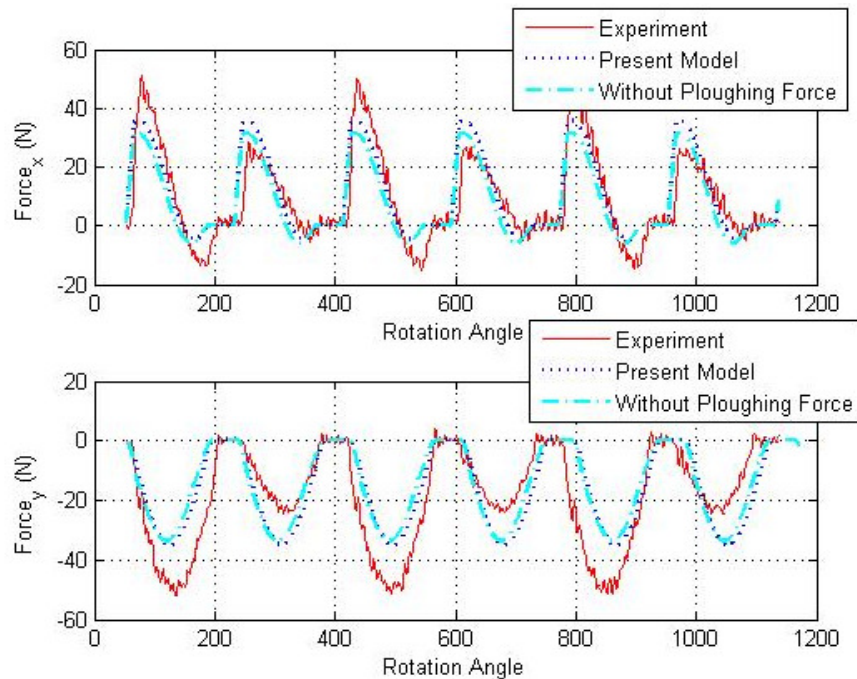


**Figure 6.62 Comparison of the predicted forces with and without considering ploughing force for down milling of titanium alloy ( $V_f=0.75$  in/min, Cutter E)**

## 6 Experimental Validation of the Predictive Model

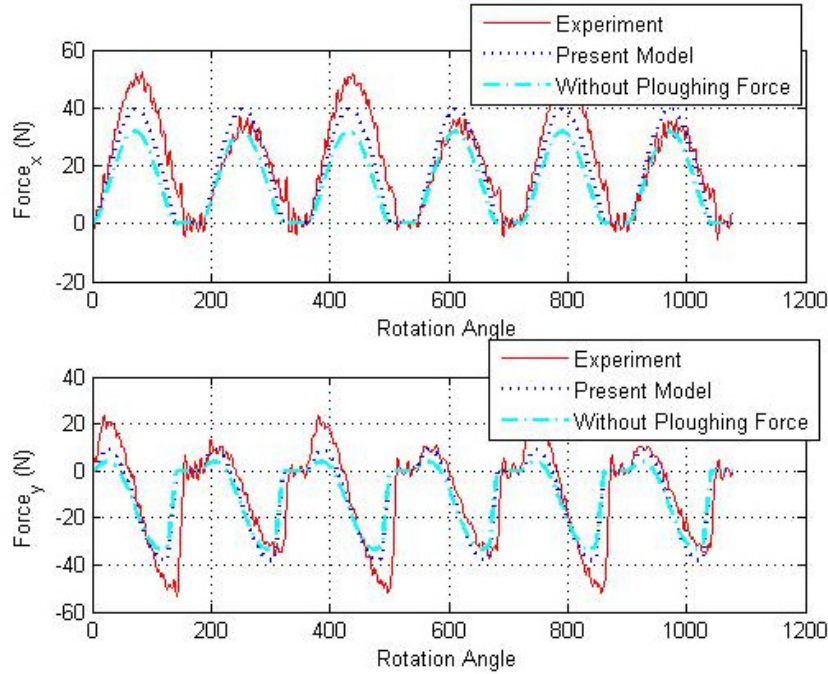


**Figure 6.63** Comparison of the predicted forces with and without considering ploughing force for up milling of titanium alloy ( $V_f=0.75$  in/min, Cutter E)

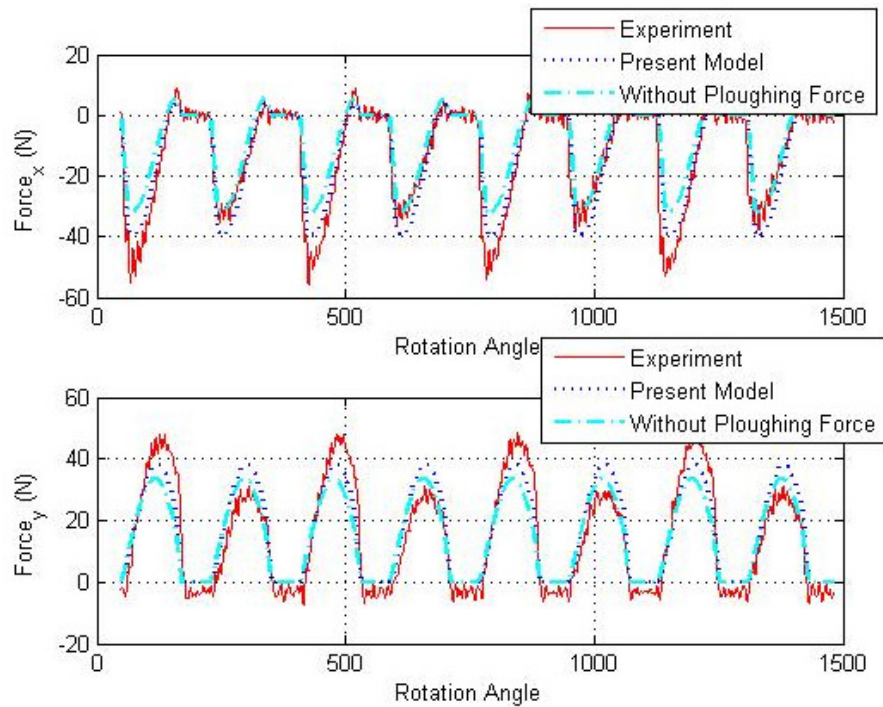


**Figure 6.64** Comparison of the predicted forces with and without considering ploughing force for central cutting titanium alloy ( $V_f=0.75$  in/min, Cutter E)

## 6 Experimental Validation of the Predictive Model

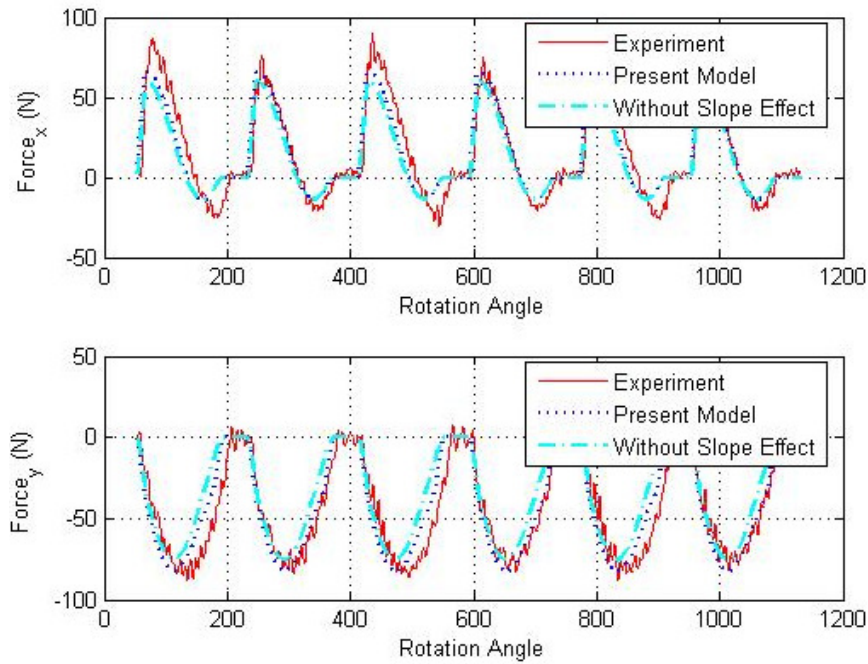


**Figure 6.65** Comparison of the predicted forces with and without considering slope effect for down milling of titanium alloy ( $V_f=2.56$  in/min, Cutter E)

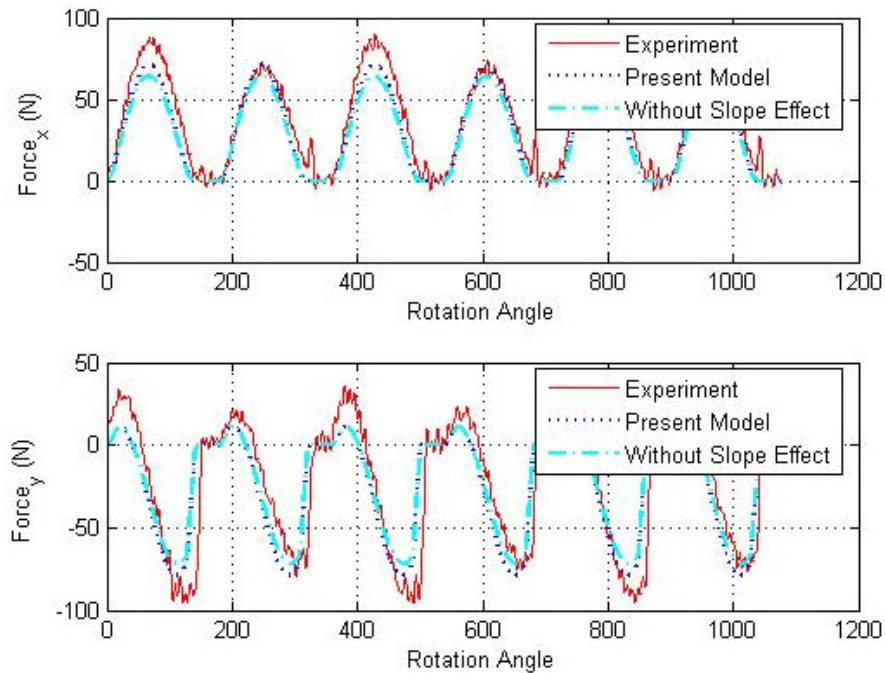


**Figure 6.66** Comparison of the predicted forces with and without considering slope effect for up milling of titanium alloy ( $V_f=2.56$  in/min, Cutter E)

## 6 Experimental Validation of the Predictive Model

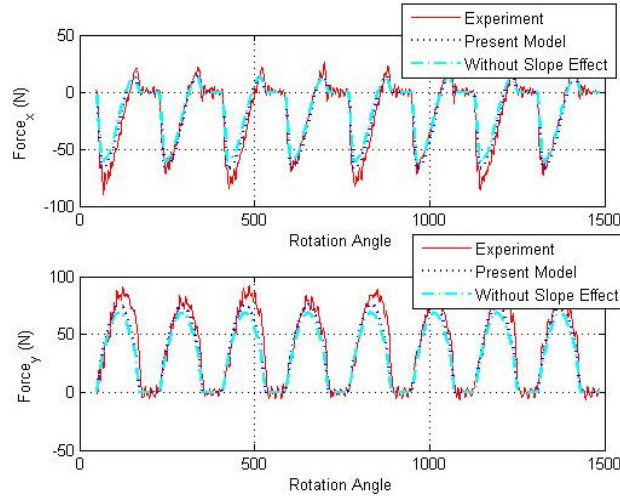


**Figure 6.67 Comparison of the predicted forces with and without considering slope effect for central cutting titanium alloy ( $V_f=2.56$  in/min, Cutter E)**

To show the relative influence of the chip “crowding” that results from the kinematic constraint, the author has calculated cutter forces at the larger feed ( $V_f=2.56$  in/min) for two cases. The first being the case where it is assumed there is no constraint and the tangential component of velocity is constant, the second where the constraint is acknowledged and an appropriate linear variation in tangential velocity applied. Figures 6.68-6.70 show the resulting force predictions and it is seen that the kinematic constraint changes the force shape, but does not make a large amount in magnitude.

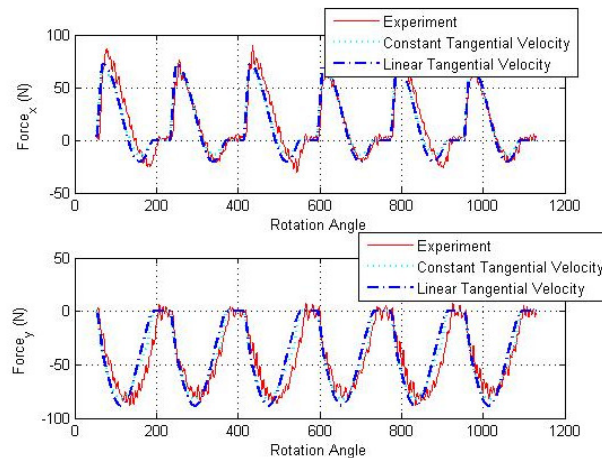


**Figure 6.68 Comparison of the effect of velocity profile for down milling of titanium alloy ( $V_f=2.56$  in/min, Cutter E)**

## 6 Experimental Validation of the Predictive Model

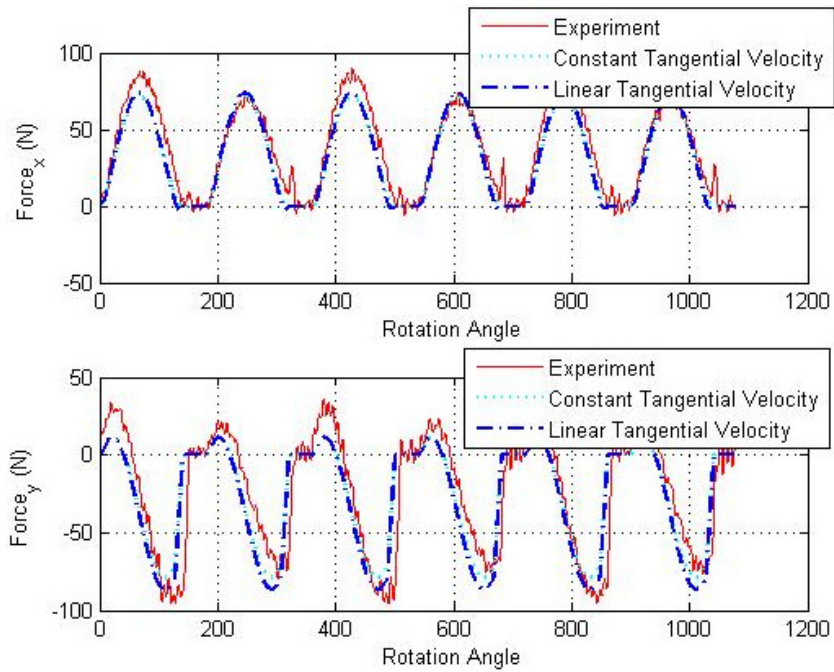


**Figure 6.69** Comparison of the effect of velocity profile for up milling of titanium alloy ( $V_f=2.56$  in/min, Cutter E)

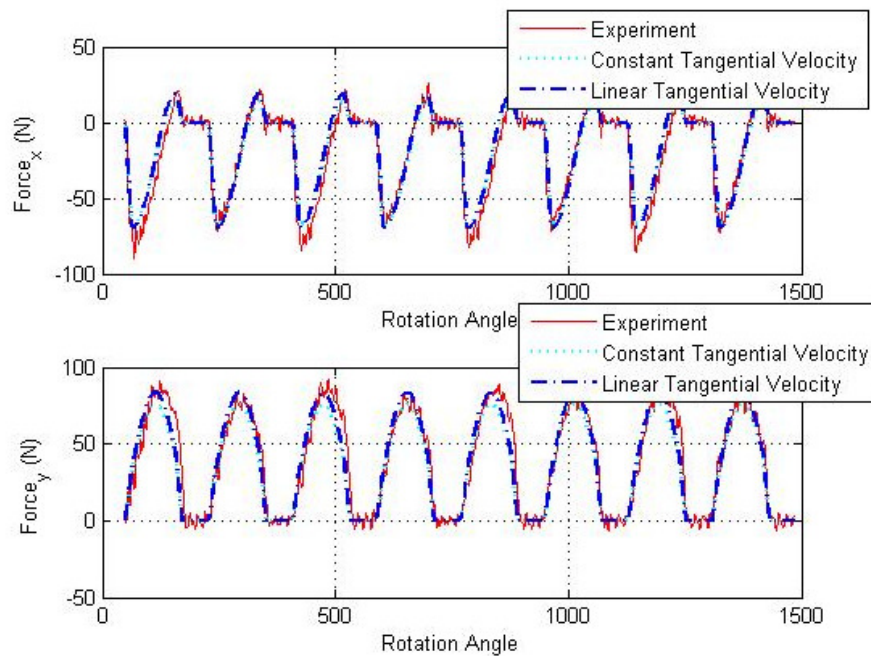


**Figure 6.70** Comparison of the effect of velocity profile for central cutting titanium alloy ( $V_f=2.56$  in/min, Cutter E)

### 6.5.4 Validating Simulation Results for Steel

As seen in Sections 6.5.1-6.5.3 cutter runout has a very large influence on force at feeding velocities. Since the steel workpiece dictated very small chip thicknesses, then to avoid the problem of runout, the cutter had one tooth ground down to ensure that only a single tooth was in cut. All tests were performed with 3/8 inch SGS end milling cutters (Cutter D) with a spindle speed 1000 RPM. The work material is AISI 4140 steel and the feed ranges from 0.75 in/min to 3.95 in/min as shown in Table AA.4. The measured edge radius and the identified constitutive parameters are given in Tables 6.3 and 6.5 respectively. A comparison of the predicted forces with experimental results for the feeds varying from 0.75 in/min to 3.95 in/min is given in Figures 6.71-6.76. The red solid line indicates the experimental results, while the blue dotted line represents the results predicted by the present model. From these comparisons between the measured and predicted cutting forces, it was confirmed that the proposed cutting force model could effectively predict the cutting forces in helical milling operations.

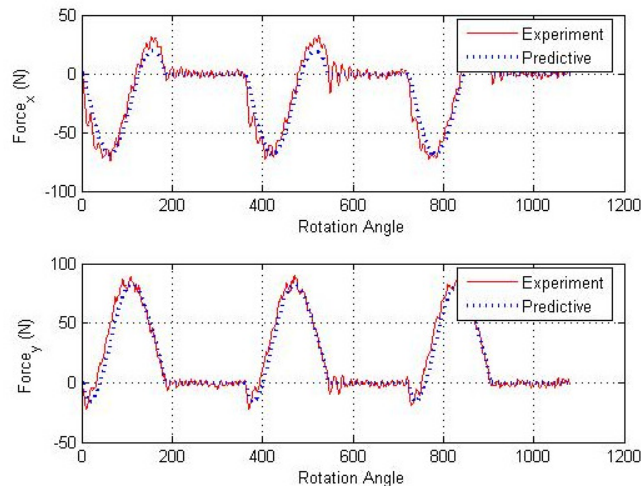


**Figure 6.71 Measured and predicted forces  $F_x$  and  $F_y$  for slotting of steel ( $V_f=0.75$  in/min, Cutter D)**

## 6 Experimental Validation of the Predictive Model

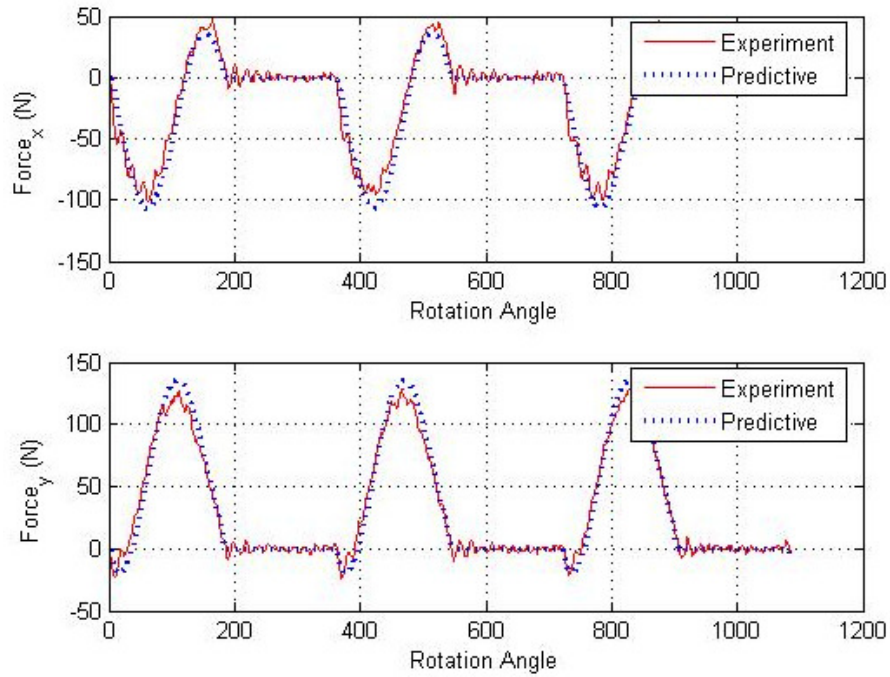


**Figure 6.72 Measured and predicted forces  $F_x$  and  $F_y$  for slotting of steel ( $V_f=1.28$  in/min, Cutter D)**

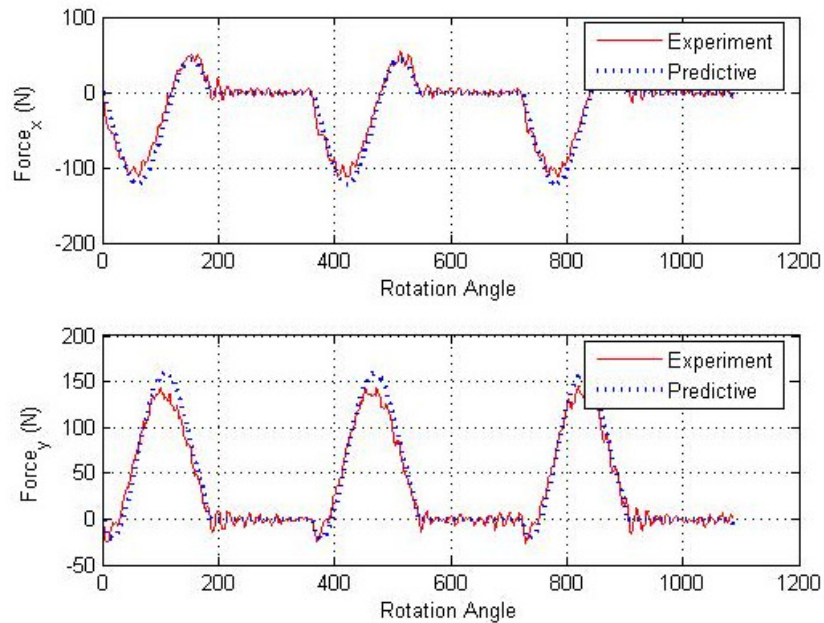


**Figure 6.73 Measured and predicted forces  $F_x$  and  $F_y$  for slotting of steel ( $V_f=1.5$  in/min, Cutter D)**

## 6 Experimental Validation of the Predictive Model

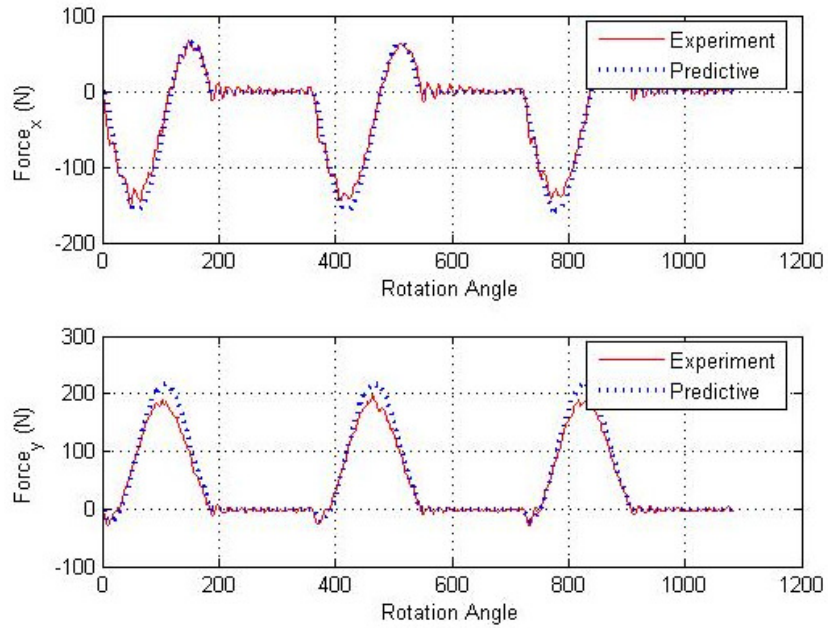


**Figure 6.74 Measured and predicted forces  $F_x$  and  $F_y$  for slotting of steel ( $V_f=2.2$  in/min, Cutter D)**

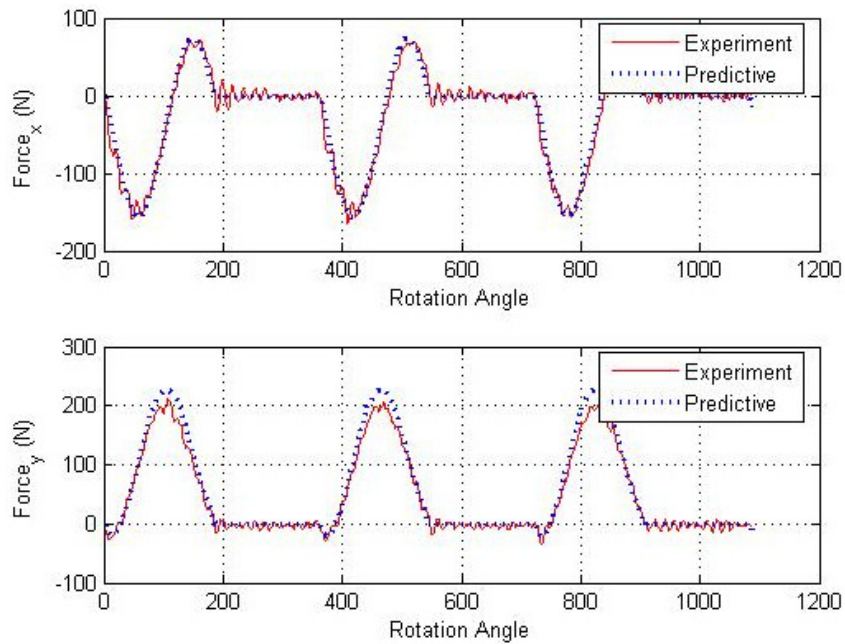


**Figure 6.75 Measured and predicted forces  $F_x$  and  $F_y$  for slotting of steel ( $V_f=2.56$  in/min, Cutter D)**

## 6 Experimental Validation of the Predictive Model

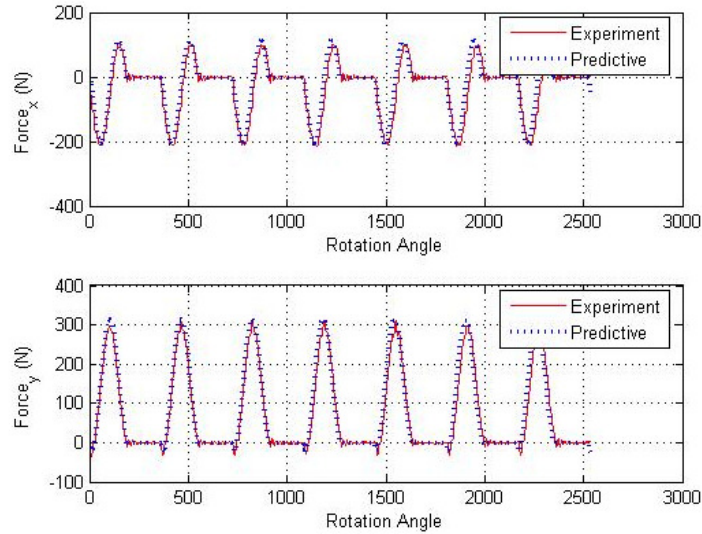


**Figure 6.76 Measured and predicted forces  $F_x$  and  $F_y$  for slotting of steel ( $V_f=3.95$  in/min, Cutter D)**

Again for illustration, force predictions are made by neglecting the ploughing force. Figure 6.77 shows the force comparison with the present model, neglecting the ploughing component, and the corresponding experimental values for the low feed  $V_f=0.75$  in/min. The figure clearly confirms the significant influence of ploughing effect at low feed.

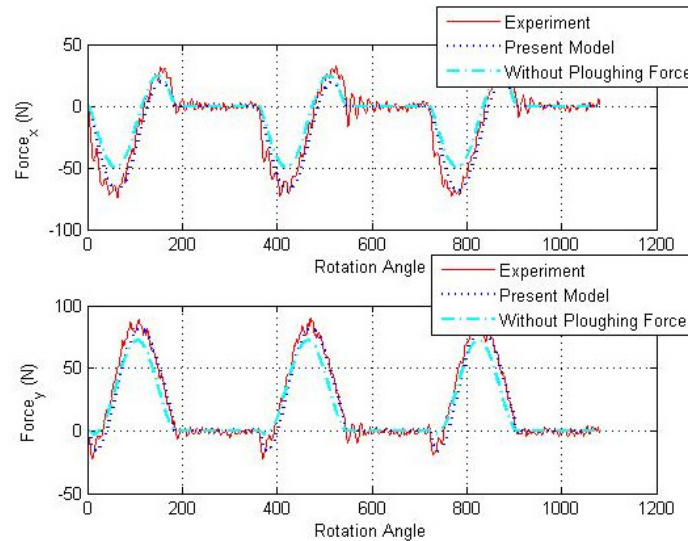


**Figure 6.77 Comparison of force prediction with and without considering edge force for slotting of steel ( $V_f=0.75$  in/min, Cutter D)**

### 6.6 Conclusions

Milling operations present small varying chip thickness, they have relatively large cutting edge radii and the edges are generally non-straight. The practical parameters in milling then dictate that any approach to modeling should include the variation in yield stress and normal stresses on the shear plane as well as the influence of ploughing forces at the edge. The author also suspected that the surface slope induced in the process and the kinematic constraint imposed by the helical tooth form should be investigated further. The experimental work described in this chapter has shown that the material model and ploughing force model appear to work well when compared to a wide range of practical data. Differences due to the influence of surface slope (more pronounced at lower radii) have also been identified and illustrated. The influence of kinematic constraint over the range of parameters studied has been shown to be relatively small.

## **7 Conclusions**

### **7.1 Dissertation Overview**

This thesis presents a theoretical modeling methodology to allow the prediction of cutting forces in typical milling operations with multiple helical teeth. The approach is based upon the fundamental physics of cutting and makes an effort to include many of the more complex and second order influences that are normally neglected. The author begins with the analysis of the basic oblique cutting process in an attempt to provide a base which avoids the necessity of defining equivalent orthogonal geometries and to provide a simple energy based model that can be used on an element by element basis along the flute of the cutter. The oblique cutting model development was critical to the work since it allows predictions of shear angle and the extraction of material parameters directly from milling operations; this is a major advantage over methods which require separate tests with straight edged tools at identical conditions. The integrated force model is based upon a fairly traditional approach to the calculation of cutting conditions and the estimation of the material properties which are expected at these conditions. To this base is added a consideration of ploughing forces, a simplified analysis of the influence of “chip crowding” induced by the kinematics of the process, a simple model of the influence of slope and finally consideration is given to the expected transitions between cutting and ploughing at very low chip thicknesses.

Despite using as much basic material information as possible, the model still needs calibration on specific work-tool pairs. To minimize this process, the author has developed and tested an innovative identification methodology that combines the central

cutting milling tests and an optimization algorithm to determine the flow stress data, and other required process information. Finally, the model has been integrated within a simple GUI based modeling package to allow easy calculation of forces in practical processes and a comparison with experimental data has been conducted to prove the validity of the approach.

### 7.2 Major Contributions

The main contributions of this research to the modeling of helical end milling operations can be summarized as follows:

1. A new upper bound model for oblique cutting has been developed. The analysis replaces the normal variables of chip flow angle and apparent coefficient of friction with basic variables relating to the kinematics (*SLIP*) and forces in the two main deformation zones, (*RATIO*). The relationship of *SLIP* and *RATIO* is easily found through force equilibrium, thus avoiding any assumptions regarding rake face stress or the ratio of the stresses in the shear plane.

2. The upper-bound method coupled with the predictive method developed by Yellowley (1987) has been applied to the analysis of chamfered and rounded edge tools. The model utilizes an upper bound approach combined with primary and secondary boundaries that guarantee both force and moment equilibrium of the chip. The model does not need extensive calibration, the only unknown is the elastic friction angle and if forces are required a mean shear yield stress is also needed. The calculated results are in general agreement with the experimental observations.

3. The characteristics of the ploughing process and the ploughing/cutting transition have been studied in this thesis. Single edge and double edge ploughing models

## 7 Conclusions

based on slip line fields for wedge indentation have been developed and a transition formulation of ploughing to cutting process based on force equilibrium and critical specific energy has been developed.

4. The author has investigated the influence of the total surface slope on forces in milling operations. A relationship between the shear angle, surface slope and the force parameter *RATIO* has been derived.

5. A new, kinematically admissible, velocity field that satisfies the incompressibility criterion has been developed for helical end mills. This leads to changes in predicted forces that are normally neglected but can be significant for very small tool diameters and high helical angles.

6. An innovative algorithm is developed for the identification of material constitutive equation as a function of strain, strain rate and temperature. The model avoids the need for shear angle data, relying instead on experimental force data for calibration and an internal optimization routine to find the normal shear angle.

7. The helical tool force model including the new oblique cutting methodology, the ploughing model and cutting/ploughing transition, surface slope, kinematics constraint, and a suitable constitutive equation has been integrated within a GUI based modeling package to allow easy calculation of forces in practical applications.

## Bibliography

- Albrecht, P., 1960. New developments in the theory of metal cutting process: part I-the ploughing process in metal cutting, *Journal of Engineering for Industry, Trans. ASME*, 82, 348-357.
- Altintas, Y., 1986. Process Monitoring and Tool Breakage Recognition in Milling, Ph.D Thesis, McMaster University, Hamilton, Ontario, Canada.
- Aramcharoen, A., Mativenga, P. T., Yang, S., Cooke, K. E., and Teer, D. G., 2008. Evaluation and selection of hard coating for micro milling of hardened tool steel, *Int. J. of Machine Tools and Manufacture*, 42, 1578-1584.
- Armarego, E. J. A., 2000. The unified-generalized mechanics of cutting approach-a step towards a house of predictive performance models for machining operations, *Machining Science and Technology*, 4, 319-362.
- Armarego, E. J. A., Wang, J., Deshpande, N. P., 1995. Computer-aided predictive cutting model for forces in face milling allowing for tooth runout, *Annals of CIRP*, 44, 43-49.
- Armarego, E. J. A., and Brown, R. H., 1969. *The Machining of Metals*, Englewood Cliffs, N. J., Prentice-Hall.
- Armarego, E. J. A., and Deshpande, N. P., 1991. Computerized end-milling force predictions with cutting models allowing eccentricity and cutter deflection, *CIRP Annals*, 40, 25-29.
- Arrazola, P. J., Ugarte, D., and Dominguez, X., 2008. A new approach for the friction identification during machining through the use of finite element modeling, *Int. J. of Machine Tools and Manufacture*, 48, 173-183.
- Arsecularatne, J. A., 1997. On tool-chip interface stress distributions, ploughing force and size effect in machining, *Int. J. of Machine Tools and Manufacture*, 37(2), 885-899.
- Atkins, A. G., 2003. Modelling metal cutting using modern ductile fracture mechanics: quantitative explanations for some longstanding problems, *Int. J. of Mechanical Science*, 45, 373-396.
- Atkins, A. G., 2005. Toughness and cutting: a new way of simultaneously determining ductile fracture toughness and strength, *Engineering Fracture Mechanics*, 72, 849-860.

## Bibliography

- Atkins, A. G., 2006. Toughness and oblique metal cutting, *Trans. ASME, J. of Manufacturing Science and Engineering*, 128, 775-786.
- Bissacco, G., Hansen, H. N., and Slunsky, J., 2008. Modelling the cutting edge radius size effect for force prediction in micromilling, *CIRP Annals-Manufacture Technology*, 57, 113-116.
- Bower, A. F., 2010. *Applied Mechanics of Solids*, CRC Press, Boca Raton, FL.
- Boothroyd, G., 1965. *Fundamentals of Metal Machining*, Pitman Press, Bath (UK).
- Brown, R. H., and Armarego, E. J. A., 1964. Oblique machining with a single cutting edge, *Int. J. Mach. Tool Des. Res.*, 4, 9-25.
- Budak, E., Altintas, Y., and Armarego, E. J. A., 1996. Prediction of milling force coefficients from orthogonal cutting data, *Trans. ASME, J. of Manufacturing Science and Engineering*, 118, 216-224.
- Cannolly, R., and Rubenstein, C., 1968. The mechanics of continuous chip formation in orthogonal cutting, *Int. J. Mach. Tool Des. Res.*, 8, 159-187.
- Chae J., Park, S. S., Freiheit T., 2006. Investigation of micro-cutting operations, *Int. J. of Machine Tools and Manufacture*, 46, 313-332.
- Challen, J. M., Oxley, P. L. B., and Doyle, E. D., 1983. The effect of strain hardening on the critical angle for abrasive (chip formulation) wear, *Wear*, 88, 1-12.
- Challen, J. M. and Oxley, P. L. B., 1983. Slip-line fields for explaining the mechanics of polishing and related processes, *Int. J. of Mechanical Science*, 26(6-8), 403-418.
- Chang, C. S., 1998. Turning of stainless steel with worn tools having chamfered main cutting edges, *Int. J. of Machine Tools and Manufacture*, 38, 291-313.
- Chiou, C. H., Hong, M. S., and Ehmann, K. F., 2005. Instantaneous shear plane based cutting force model for end milling, *Journal of Materials Processing Technology*, 170, 164-180.
- Collins, I. F., 1968. The algebraic-geometry of slip-line fields with applications to boundary value problems, *Proc. Roy. Soc. Ser. A.*, 303, 317-338.
- Collins, I. F., 1970. Compression of a rigid perfectly-plastic strip between parallel rotating smooth dies, *Q. J. Mech. Appl. Math.*, 23, 329-348.
- DeChifre, L. D., 1977. Mechanics of metal cutting and cutting fluid action, *Int. J. of Machine Tools Design and Research*, 17, 225-234.

## Bibliography

- Dewhurst, P., 1978. On the non-uniqueness of the machining process, Proc. of Royal Society of London, Series A, 360, 587-610.
- Dewhurst, P., and Collins, I. F., 1973. A matrix technique for constructing slip-line field solutions to a class of plane strain plasticity problems, Int. J. for Numerical Methods in Engineering, 7, 357-378.
- Endres, W. J., DeVor, R. E., and Kapoor, S. G., 1995. A dual-mechanism approach to the prediction of machining forces, part 1: model development, Journal of Engineering for Industry, Trans. ASME, 117, 526-533.
- Engin, E., Altintas, Y., 2001. Mechanics and dynamics of general milling cutters. Part I: helical end mills, Int. J. of Machine Tools and Manufacture, 41, 2195-2212.
- Ewing, D. J. F., 1967. A series-method for constructing plastic slip-line fields, J. of the Mechanics and Physics of Solids, 15, 105-114.
- Fang, N., 2003. Slip-line modeling of machining with a rounded edge tool-part I: numerical model and theory, J. of the Mechanics and Physics of Solids, 51, 715-742.
- Fang, N., Jawahir, I. S., and Oxley, P. L. B., 2001. A universal slip-line model with non-unique solutions for machining with curled chip formation and a restricted contact tool, Int. J. of Mechanical Science, 43, 557-580.
- Felder, E., Bucaille, J. L., 2006. Mechanical analysis of the scratching of metals and polymers with conical indenters at moderate and large strains, Tribology International, 39, 70-87.
- Feng, H. Y., and Su, N., 2001. A mechanistic cutting force model for 3D ball-end milling, Trans. ASME, J. of Manufacturing Science and Engineering, 123, 23-29.
- Filiz, S., Caroline, M. C., Matthew, B. W., Ozdoganlar, O. B., 2007. An experimental investigation of micro-machinability of copper 101 using tungsten carbide micro-endmills, Int. J. of Machine Tools and Manufacture, 47, 1088-1100.
- Finnie, I., 1956. Review of the metal cutting theories of the past hundred years, Mech. Engng, 78, 715-721.
- Fuh, K. H., Chang, C. S., 1995. Prediction of the cutting forces for chamfered main cutting edge tools, Int. J. of Machine Tools and Manufacture, 35(11), 1559-1586.
- Fu, H. J., DeVor, R. E., and Kapoor, S. G., 1984. A mechanistic model for the prediction of the force system in face milling operations, Journal of Engineering for Industry, 106, 81-88.

## Bibliography

- Guo, Y. B., Wen, Q., and Horstemeyer, M. F., 2005. An internal state variable plasticity-based approach to determine dynamic loading history effects on material property in manufacturing processes, *Int. J. of Mechanical Science*, 47, 1423-1441.
- Gygax, P. E., 1980. Cutting dynamics and process-structure interactions applied to milling, *Wear*, 62, 161-184.
- Huang, Y., and Liang, S.Y., 2005. Modeling of cutting forces under hard turning conditions considering tool wear effect, *Trans. ASME, J. of Manufacturing Science and Engineering*, 127, 262-270.
- Hu, R. S., Mathew, P., and Oxley, P. L. B., 1986. Allowing for end cutting edge effects in predicting forces in bar turning with oblique machining conditions, *Proc. Instn. Mech. Engrs.*, 200, 89-99.
- Iwata, K., Osakada, K., Terasaka, Y., 1984. Process modeling of orthogonal cutting by the rigid-plastic finite element method, *Trans. ASME, Journal of Engineering Materials and Technology*, 106, 132-137.
- Jaspers, S. P. F. C., Dautzenberg, J. H., 2002. Material behaviour in conditions similar to metal cutting: flow stress in the primary shear zone, *Journal of Materials Processing Technology*, 122, 322-330.
- Johnson, W., 1962. Some slip-line fields for swaging or expanding indenting, extruding and machining for tools with curved dies, *Int. J. of Mechanical Science*, 4, 323-347.
- Johnson, W., 1967. Cutting with tools having a rounded edge: some theoretical considerations, *Annals of the CIRP*, 14, 315-319.
- Johnson, G. R., Stryk, R. A., Holmquist, T. J., and Beissel, S. R., 1996. User Instruction for the 1996 Version of the EPIC Code, Alliant Techsystems Inc.
- Jun, M. B. G., Liu, X., DeVor, R. E., and Kapoor, S. G., 2006. Investigation of the dynamics of microend milling-Part I: model development, *Trans. ASME, J. of Manufacturing Science and Engineering*, 128, 893-900.
- Kapoor, S. G., DeVor, R. E., Zhu, R., Gajjala, R., Parakkal, G., Smithy, D., 1998. Development of mechanistic models for the prediction of machining performance: model building methodology, *Machining Science and Technology*, 2(2), 213-238.
- Kim, K. W., Lee, W. Y., and Sin, H. C., 1999. A finite-element analysis of machining with the tool edge considered, *Journal of Materials Processing Technology*, 86, 45-55.

## Bibliography

- Kline, W. A., DeVor, R. E., Lindberg, J. R., 1982. Prediction of cutting forces in end milling with application to cornering cuts, *Int. J. Mech. Design Res*, 22, 7-22.
- Koenigsberger, F., and Sabberwal, A., 1961. An investigation into the cutting force pulsations during milling operations, *Int. J. Mech. Design Res*, 1, 15–31.
- Komanduri, R., Chandrasekaran, N., Ratt, L. M., 1998. Effect of tool geometry in nanometric cutting: a molecular dynamics simulation approach, *Wear*, 219, 84-97.
- Kopalinsky, E. M. and Oxley, P. L. B., 1995. Explaining the mechanics of metallic sliding friction and wear in terms of slipline field models of asperity deformation, *Wear*, 190, 145-154.
- Kronenberg, M., 1966. *Machining Science and Application*, Pergamon Press, Oxford, UK.
- Kudo, H., 1965. Some new slip-line solutions for two-dimensional steady-state machining, *Int. J. of Mechanical Science*, 7, 43-55.
- Lau, W. S., and Rubenstein, C., 1983. The mechanics of continuous chip formation in oblique cutting in the absence of chip distortion. Part 2. comparison of experimental data with deductions from theory, *Int. J. Mach. Tool Des. Res.*, 23, 21-37.
- Lee, E. H., and Shaffer, B. W., 1951. The theory of plasticity applied to a problem of machining, *J. of Applied Mechanics*, 18, 405-413.
- Lei, S., Shin, Y. C., and Incropera, F. P., 1999. Material constitutive modeling under high strain rates and temperatures through orthogonal machining tests, *Trans. ASME, J. of Manufacturing Science and Engineering*, 121, 577-585.
- Li, H., and Shin, Y. C., 2006. A comprehensive dynamic end milling simulation model, *Trans. ASME, J. of Manufacturing Science and Engineering*, 128, 86-95.
- Lin, G. C. I., 1978. Prediction of cutting force and chip geometry in oblique machining from flow stress properties and cutting conditions, *J. Mach. Tools Des. Res.*, 18, 117-130.
- Lin, G. C. I, Mathaw, P., Oxley, P. L. B., Watson, A. R., 1982. Predicting cutting forces for oblique machining conditions, *Proc. Inst. Mech. Eng. (London)*, 196, 141-148.
- Lin, G. C. I., and Oxley, P. L. B., 1972. Mechanics of oblique machining: predicting chip geometry and cutting force from work material and cutting conditions, *Proc. Instn. Mech. Engrs.*, 186, 813-820.

## Bibliography

- Liu, X., DeVor, R. E., Kapoor, S. G., Ehman, K. F., 2004. The mechanics of machining at the micro scale: assessment of the current state of the science, *Trans. ASME, J. of Manufacturing Science and Engineering*, 126, 666-678.
- Liu X., DeVor R. E., Kapoor S. G., 2006. An analytical model for the prediction of minimum chip thickness in micromachining, *Trans. ASME, J. of Manufacturing Science and Engineering* , 128, 474-481.
- Liu, X., DeVor, R. E., Kapoor, S. G., 2007. Model-based analysis of the surface generation in microendmilling-Part I: model development, *Trans. ASME, J. of Manufacturing Science and Engineering*, 129, 453-460.
- Lowen, E. G., and Shaw, M. C., 1954. On the analysis of cutting-tool temperature, *Trans. ASME*, 76, 217-231.
- Lucca, D. A., and Seo, Y. W., 1993. Effect of tool edge geometry on energy dissipation in ultraprecision machining, *CIRP Annals*, 42(1), 83-86.
- Maity, K. P., and Das, N. S., 2001. A class of slipline field solutions for metal machining with slipping and sticking contact at the chip-tool interface, *Int. J. of Mechanical Science*, 43, 2435-2452.
- Manjunathaiah, J., and Endres, W. J., 2000. A new model analysis of orthogonal machining with an edge-radiused tool, *Trans. ASME, J. of Manufacturing Science and Engineering*, 122, 384-390.
- Maple, 2010. <http://www.maplesoft.com/products/maple>, Maplesoft, a division of Waterloo Maple Inc.
- Martellotti, M. E., 1941. An analysis of the milling process, *Transactions of the ASME*, 677-700.
- Martellotti, M. E., 1944. An analysis of the milling process, part II-down milling, *Transactions of the ASME*, 233-251.
- Masuko, M., 1953. Fundamental research on metal cutting (1<sup>st</sup> report), a new analysis of cutting forces, *Transactions of the Japan Society of Mechanical Engineers*, 19, 32-39.
- Merchant, M. E., 1944. Basic mechanics of the metal-cutting process, *J. of Applied Mechanics*, 66, 168-175.
- Merchant, M. E., 1945. Mechanics of the metal cutting process I. Orthogonal cutting and a type 2 chip, *Journal of Applied Physics*, 16(5), 267-275.

## Bibliography

- Merchant, M. E., 1945. Mechanics of the metal cutting process II. Plasticity conditions in orthogonal cutting, *Journal of Applied Physics*, 16 (6), 318-324.
- Meyer, H. W. J., Kleponis, D. S., 2001. Modelling the high strain rate behavior of titanium undergoing ballistic impact and penetration, *International Journal of Impact Engineering*, 26, 509-521.
- Miao, J. C., Chen, G. L., Lai, X. M., Li, H. T., Li, C. F., 2007. Review of dynamic issues in micro-end-milling, *Int. J. Adv. Manuf. Technol.*, 31, 897-904.
- Mittal, R. N., and Juneja, B. L., 1982. Effect of stress distribution on the shear angle  $\phi$  in controlled contact orthogonal cutting, *Int. J. Mach. Des. Res.*, 22(2), 87-96.
- Morcos, W. A., 1972. Contribution to the mechanics of free oblique continuous cutting, *Int. J. Prod. Res.*, 10, 365-377.
- Moufki, A., Dudzinski, D., Molinari, A., and Rausch, M., 2000. Thermoviscoplastic modelling of oblique cutting: forces and chip flow predictions, *Int. J. of Mechanical Science*, 42, 1205-1232.
- Moufki, A., Devillez, A., Dudzinski, D., and Molinari, A., 2004. Thermomechanical modelling of oblique cutting and experimental validation, *Int. J. of Machine Tools and Manufacture*, 44, 971-989.
- Movahhedy, M. R., Altintas, Y. and Gadala, M. S., 2002. Numerical analysis of metal cutting with chamfered and blunt tools, *Trans. ASME, J. of Manufacturing Science and Engineering*, 124, 178-188.
- Ng, E.G., Ei-Wardany, T. I., Dumitrescu, M., and Elbestawi, A., 2002. Physics-based simulation of high speed machining, *Machining Science and Technology*, 6(3), 301-329.
- Oldknow, K. D., 2004. Dynamically Reconfigurable Machining Systems, Ph.D Thesis, The University of British Columbia.
- Oxley, P. L. B., 1961. A strain-hardening solution for the “shear angle” in orthogonal metal cutting, *Int. J. of Mechanical Science*, 3, 68-79.
- Oxley, P.L.B., and Hatton, P. A., 1963. Shear angle solution based on experimental shear zone and tool-chip interface stress distributions, *Int. J. of Mechanical Science*, vol. 5, 41-55.
- Oxley, P. L. B., and Hastings, W. F., 1976. Minimum work as a possible criterion for determining the frictional conditions at the tool/chip interface in machining, *Philosophical Trans. of the Royal Society of London, Series A. Mathematical and Physical Science*, 282 (1310), 565-584.

## Bibliography

- Oxley, P. L. B., 1989. *The Mechanics of Machining: An Analytical Approach to Assessing Machinability*, E. Horwood, Chichester, England.
- Oyawoye, O. A., 1993. *An Investigation into Tool-wear and Phenomena Influencing Tool-life in Milling*, M.A.Sc Thesis, The University of British Columbia.
- Ozel, T., Zeren, E., 2004. Determination of work material flow stress and friction for FEA of machining using orthogonal cutting tests, *Journal of Materials Processing Technology*, 153/154, 1019-1025.
- Ozel, T., and Zeren, E., 2006. A methodology to determine work material flow stress and tool-chip interfacial friction properties by using analysis of machining, *Trans. ASME, J. of Manufacturing Science and Engineering*, 128, 119-129.
- Pal, A. K., and Koenigsberger, F., 1968. Some aspects of the oblique cutting process, *Int. J. Mach. Tools Des. Res.*, 8, 45-57.
- Palmer, W. B., and Yeo, P. C. K., 1963. Metal flow near the tool point during orthogonal cutting with a blunt tool, *Proc. 4<sup>th</sup> Int. MTDR Conference*, 61-71.
- Pandey, P. C., Shan, H. S., 1972. Analysis of cutting forces in peripheral and face milling operations, *Int. J. Prod. Res.*, 10(4), 379-391.
- Pantale, O., Bacaria, J. L., Dalverny, O., Rakotomalala, R., and Caperaa, S., 2004. 2D and 3D numerical models of metal cutting with damage effect, *Comput. Methods Appl. Mech. Engrg.*, 193, 4383-4399.
- Patel, Y., Blackman, B. R. K., and Williams, J. G., 2009. Determining fracture toughness from cutting tests on polymers, *Engineering Fracture Mechanics*, 76, 2711-2730.
- Piispanen, V., 1937. Lastunmuodostumisen teoriaa, *Teknillinen Aikakauslehti*, 27, 315-322.
- Ranganath, S., Campbell, A. B., Gorkiewicz, D. W., 2007. A model to calibrate and predict force in machining with honed cutting tools or inserts, *Int. J. of Machine Tools and Manufacture*, 47, 820-840.
- Ren, H., and Altintas, Y., 2000. Mechanics of machining with chamfered tools, *Trans. ASME, J. of Manufacturing Science and Engineering*, 122, 650-659.
- Rowe, G. W., and Spick, P. T., 1967. A new approach to determination of the shear-plane angle in machining, *Trans. ASME, Journal of Engineering for Industry*, 89, 530-538.

## Bibliography

- Rowe, G. W., and Wetton, A. G., 1969. Theoretical considerations in the grinding of metals, *Journal of the Institute of Metal*, 97,193-200.
- Russell, J. K., and Brown, R. H., 1966. The measurement of chip flow direction, *Int. J. Mach. Tool Des. Res.*, 6, 129-138.
- Rubenstein, C., 1983. The mechanics of continuous chip formation in oblique cutting in the absence of chip distortion. Part I. Theory, *Int. J. Mach. Tool Des. Res.*, 23, 11-20.
- Sartkulvanich, P., Koppka, F., and Altan, T., 2004. Determination of flow stress for metal cutting simulation-a progress report, *Journal of Materials Processing Technology*, 146(1), 61-71.
- Sartkuvanich, P., Altan, T., and Soehner, J., 2005. Flow stress data for finite element simulations in metal cutting: A progress report on MADAMS, *Machining Science and Technology*, 9, 271-288.
- Sedeh, A. A. H., Madhavan, V., and Bagr, B., 2002. Upper bound analysis of oblique cutting with nose radius tools, *Int. J. of Machine Tools and Manufacture*, 42, 1081-1094.
- Sedeh, A. A. H., Madhavan, V., and Bagr, B., 2003. Upper bound analysis of oblique cutting: improved method of calculating the friction area, *Int. J. of Machine Tools and Manufacture*, 43, 485-492.
- Sedeh, A. A.H., and Madhavan, V., 2004. Upper bound of turning using sharp corner tools, *Machine Science and Technology*, 8, 277-303.
- Seethaler, R. J., 1997. *Integrated Planning, Monitoring, and Control of Milling Operations*, Ph.D. Thesis, The University of British Columbia, Vancouver, Canada.
- Seethaler, R. J., and Yellowley, I., 1997. An upper-bound cutting model for oblique cutting tools with a nose radius, *Int. J. of Machine Tools and Manufacture*, 37, 119-134.
- Seethaler, R. J., and Yellowley, I., 1999. The identification of radial runout in milling operations, *Trans. ASME, J. of Manufacturing Science and Engineering*, 121, 524-531.
- Shamoto, E., and Altintas, Y., 1999. Prediction of shear angle in oblique cutting with maximum shear stress and minimum energy principles, *J. of Manufact. Sci. and Eng.*, 121, 399-407.

## Bibliography

- Shaw, M. C., Cook, N. H., and Smith, P. A., 1952. The mechanics of three-dimensional cutting operations, *Trans. of ASME*, 74, 1055-1064.
- Shaw, M. C., 1997. *Metal Cutting Principles*, Oxford Publications, New York.
- Shaw, M. C., Sanghani, R. S., 1963. Cutting characteristics with variable undeformed chip thickness, *CIRP Annal*, 12, 240-246.
- Shi, J, and Liu, C. R., 2004. The influence of material models on finite element simulation of machining, *Trans. ASME, J. of Manufacturing Science and Engineering*, 126, 849-857.
- Shi, T., and Ramalingam, S., 1991. Slip-line solution for orthogonal cutting with a chip breaker and flank wear, *Int. J. Mech. Sci.*, 33(9), 689-704.
- Smithey, D. W., Kapoor, S. G., and DeVor, R. E., 2001. A new mechanistic model for predicting worn tool cutting forces, *Machining Science and Technology*, 5, 23-42.
- Song, W., 2006. *Development of Predictive Force Models for Classical Orthogonal and Oblique Cutting and Turning Operations Incorporating Tool Flank Wear Effects*, Ph.D Thesis, Queensland University of Technology, Australia.
- Spaans, C., 1970. The mechanics of oblique cutting, taking into account the forces on the clearance face, *Int. J. Mach. Tool Des. Res.*, 10, 213-220.
- Stabler, G. V., 1951. The basic nomenclature of cutting tools, *Proceeding of the Institution of Mechanical Engineers*, 165, 14-21.
- Stephenson, D. A., Wu, S. M., 1988. Computer models for the mechanics of three-dimensional cutting processes-Part I: theory and numerical method, *J. Eng. Ind.*, 36, 32-37.
- Stephenson, D. A., Agapiou, J.S., 2006. *Metal Cutting Theory and Practice*, Boca Raton, CRC Press.
- Subbiah, S., 2006. *Some Investigations of Scaling Effects in Micro-Cutting*, Ph.D Thesis, Georgia Institute of Technology.
- Sutherland, J.W., and DeVor, R. E., 1986. An improved method for cutting force and surface error prediction in flexible end milling systems, *Journal of Engineering for Industry, Trans. ASME*, 108, 269-279.
- Tai, C. C., Fuh, K. H., 1994. A predictive force model in ball-end milling including eccentricity effects, *Int. J. of Machine Tools and Manufacture*, 34 (7), 1559-1586.

## Bibliography

- Thrusty, J., and MacNeil, P., 1975. Dynamics of cutting in end milling, *Annals of the CIRP*, 24(1), 213-221.
- Uriarte, L., Azcarate, S., Herrero, A., de Lacalle, L. N. P., and Lamikiz, A., 2008. Mechanistic modeling of the micro end milling operation, *Proc. IMechE, Part B: J. Engineering Manufacture*, 222, 23-33.
- Usui, E., and Hoshi, K., 1963. Slip-line fields in metal machining with involve centered fans, *Proc. of International Production Engineering Research Conference*, Pittsburgh: ASME, pp. 61-71.
- Usui, E., Hirota, A., and Masuko, M., 1978. Analytical prediction of three dimensional cutting process, part 1. basic cutting model and energy approach, *Trans. ASME, J. of Eng. for Industry*, 100, 222-228.
- Usui, E., and Hirota, A., 1978. Analytical prediction of three dimensional cutting process, part 2. chip formation and cutting force with conventional single-point tool, *Trans. ASME, J. of Eng. for Industry*, 100, 229-235.
- Vinuvinod, P. K., and Jin, W. L., 1995. Three-dimensional cutting force analysis based on the lower boundary of the shear zone. Part 1: Single edge oblique cutting, *Int. J. of Machine Tools and Manufacture*, 36(3), 307-323.
- Waldorf, D. J., DeVor, R. E., and Kapoor, S. G., 1998. Slip-line field for ploughing during orthogonal cutting, *Trans. ASME, J. of Manufacturing Science and Engineering*, 120, 693-698.
- Wallace, R. W., and Andrew, C., 1965. Machining forces: some effects of removing a wavy surface, *J. of Mech. Eng. Sci.*, 7, 43-45.
- Wang, M. Y., Chang, H. Y., 2003. A simulated shape error for end milling AL6061-T6, *Int. J. Adv. Manuf. Technol.*, 22, 689-696.
- Wang, J. J. J., and Huang, C. Y., 2004. A force-model-based approach to estimating cutter axis offset in ball end milling, *Int. J. Adv. Manuf. Technol*, 24, 910-918.
- Wang, S. M., Chiou, C. H., and Cheng, Y. M., 2004. An improved dynamic cutting force for end-milling process, *Journal of Materials Processing Technology*, 148, 317-327.
- Williams, J. G., Patel, Y., and Blackman, B. R. K., 2010. A fracture mechanics analysis of cutting and machining, *Engineering Fracture Mechanics*, 77, 293-308.
- Wyeth, D. J., 2008. An investigation into the mechanics of cutting using data from orthogonal cutting Nylon 66, *Int. J. of Machine Tools and Manufacture*, 48, 896-904.

## Bibliography

- Yellowley, I., 1983. The influence of work hardening on the mechanics of orthogonal cutting with zero rake angle, *International Journal of Machining Tools Des. Res.*, 23(4), 181-189.
- Yellowley, I., 1985. Observations on the mean values of forces, torque and specific power in the peripheral milling process, *Int. J. Mach. Tools Des. Res.*, 25(4), 337-346.
- Yellowley, I., 1987. A simple predictive model of orthogonal metal cutting, *Int. J. of Machine Tools and Manufacture*, 27(3), 357-365.
- Yellowley, I., 1988. A note on the significance of the quasi-mean resultant force and the modeling of instantaneous torque and forces in peripheral milling operations, *Journal of Engineering for Industry*, 110, 300-303.
- Yellowley, I., Hosepyan, Y. and Oyawaye, O., 1992. The identification of machining conditions and tracking of tool wear in milling using machining forces, ASME, Winter Annual Meeting.
- Yellowley, I., and Lai, C. T., 1993. The use of force ratios in the tracking of tool wear in turning, ASME, *J. Eng. for Ind.*, 115, 370-372.
- Zhang, H. T., Liu, P. D. and Hu, R. S., 1991. A three-zone model and solution of shear angle in orthogonal machining, *Wear*, 143, 29-43.
- Zheng, L., Li, Y., and Liang, S. Y., 1997. A generalized model of milling forces, *Int. J. Adv. Manuf. Technol.*, 14, 160-171.
- Zorev, N. N., 1966. *Metal Cutting Mechanics*, Oxford: Pergamon Press.
- Zou, G. P., Yellowley, I., and Seethaler, R. J., 2009. A new approach to the modeling of oblique cutting processes, *Int. J. of Machine Tools and Manufacture*, 49, 701-707.
- Zou, G. P., Yellowley, I., and Seethaler, R. J., 2010. The extension of a simple predictive model for orthogonal cutting to include flow below the cutting edge, 36 MATADOR Conf., Manchester, UK.

# Appendices

## Appendix A: Experimental Tests

Full list of experimental tests for aluminum alloy, titanium alloy and steel are given in Table AA.1-AA.4.

**Table AA.1 Milling tests for aluminum alloy**

Test No.	Milling Type	Tool Diameter (in)	Feed Velocity (in/min)	Spindle Speed (RPM)	Depth of Cut $a$ (in)	Width of Cut $w$ (in)
1	Center Cut	1/2	1.28	1000	0.08	0.283
2	Center Cut	1/2	2.56	1000	0.08	0.283
3	Center Cut	1/2	4.4	1000	0.08	0.283
4	Center Cut	1/2	6.75	1000	0.08	0.283
5	Center Cut	1/2	7.9	1000	0.08	0.283
6	Slotting	1/2	2.2	1000	$a_1=0.05,$ $a_2=0.165$	—
7	Slotting	1/2	4.4	1000	$a_1=0.05,$ $a_2=0.165$	—
8	Down Milling	1/2	3.95	1000	0.08	0.266
9	Down Milling	1/2	2.56	1000	0.08	0.266
10	Down Milling	1/2	1.28	1000	0.08	0.266
11	Down Milling	1/2	6.75	1000	0.08	0.266
12	Up Milling	1/2	7.9	1000	0.08	0.266
13	Up Milling	1/2	3.95	1000	0.08	0.266

Note for test 6 and 7, the depth of cut jump at the center of slotting.

**Table AA.2 Milling tests for titanium alloy with 2 teeth 3/8" end mill cutter**

Test No.	Milling Type	Tool Diameter (in)	Feed Velocity (in/min)	Spindle Speed (RPM)	Depth of Cut $a$ (in)	Width of Cut $w$ (in)
1	Center Cut	3/8	2.2	575	0.08	0.21
2	Center Cut	3/8	0.75	575	0.08	0.21
3	Center Cut	3/8	1.5	575	0.08	0.21
4	Center Cut	3/8	3.95	575	0.08	0.21
5	Center Cut	3/8	4.4	575	0.08	0.21
6	Down Milling	3/8	0.75	575	0.073	0.154
7	Down Milling	3/8	1.5	575	0.073	0.154
8	Down Milling	3/8	2.2	575	0.073	0.154
9	Up Milling	3/8	1.5	575	0.073	0.158
10	Up Milling	3/8	0.75	575	0.073	0.158

**Table AA.3 Milling tests for titanium alloy with 2 teeth 3/16” end mill cutter**

Test No.	Milling Type	Tool Diameter (in)	Feed Velocity (in/min)	Spindle Speed (RPM)	Depth of Cut $a$ (in)	Width of Cut $w$ (in)
1	Down Milling	3/16	0.75	1152	0.037	0.1482
2	Down Milling	3/16	1.5	1152	0.037	0.1482
3	Down Milling	3/16	2.2	1152	0.037	0.1482
4	Down Milling	3/16	2.56	1152	0.037	0.1482
5	Up Milling	3/16	2.56	1152	0.037	0.152
6	Up Milling	3/16	2.2	1152	0.037	0.152
7	Up Milling	3/16	1.5	1152	0.037	0.152
8	Up Milling	3/16	0.75	1152	0.037	0.152
9	Central Cut	3/16	0.75	1152	0.037	$w_1=0.08675$ $w_2=0.06275$
10	Central Cut	3/16	1.5	1152	0.037	$w_1=0.08675$ $w_2=0.06275$
11	Central Cut	3/16	2.2	1152	0.037	$w_1=0.08675$ $w_2=0.06275$
12	Central Cut	3/16	2.56	1152	0.037	$w_1=0.08675$ $w_2=0.06275$

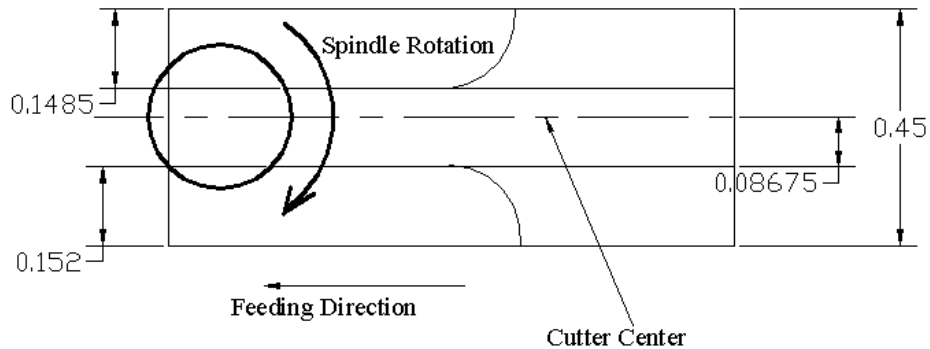


**Figure AA.1 Geometry of central cutting titanium alloy by 3/16” end mill cutter**

**Table AA.4 Milling tests for AISI 4140 steel**

Test No.	Milling Type	Tool Diameter (in)	Feed Velocity (in/min)	Spindle Speed (RPM)	Depth of Cut $a$ (in)	Width of Cut $w$ (in)
1	Slotting	3/8 (One Tooth)	0.75	1000	0.04	3/8
2	Slotting	3/8 (One Tooth)	1.28	1000	0.04	3/8
3	Slotting	3/8 (One Tooth)	1.5	1000	0.04	3/8
4	Slotting	3/8 (One Tooth)	2.2	1000	0.04	3/8
5	Slotting	3/8 (One Tooth)	2.56	1000	0.04	3/8
6	Slotting	3/8 (One Tooth)	3.95	1000	0.04	3/8

**Appendix B: Dynamometer Calibration**

The dynamometer calibration procedure was performed at the Manufacturing Engineering Laboratory of UBC. The 3D dynamometer linked to three charge amplifiers (Kistler Model 5004) was mounted at the XY motion table developed by Oldknow 2004. The cutting forces were measured by the Tektronix TDS 2024B scope. The measured data was postprocessed by using the MATLAB program. The load was applied through a wheel and linked by small diameter strong plastic wire mounted at the Bridgeport machine in order to reduce the friction effect in the calibration processes. The piezotransducer sensitivity and cross sensitivity were identified by using a Sensortronics 60001-256 load cell. The identified parameters of the charge amplifier for  $x$ ,  $y$  and  $z$  directions are given in Table AB.1.

**Table AB.1 Identified parameters used for charge amplifiers (Kistler Model 5004)**

Parameter	$x$	$y$	$z$
Mechanical Unit (N/V)	20	20	20
Sensitivity Range	1-11	1-11	1-11
Sensitivity (mV/N)	86	86	73

A series of incremental loads ranging from 5.8 N to 85 N were applied as steady weight through the plastic wire. Figures AB.1-AB.3 plot the calibration of the dynamometer in  $x$ ,  $y$  and  $z$  directions, respectively. The response of the dynamometer is quite linear in all three directions. The calibrated relationships of the force and measured voltage for the  $x$ ,  $y$  and  $z$  direction are stated as following

## Appendices

$$\begin{cases} F_x(N) = 18.95 \cdot V + 0.2091 \\ F_y(N) = 19.077 \cdot V + 0.1018 \\ F_z(N) = 19.133 \cdot V + 0.1284 \end{cases} \quad (\text{AB.1})$$

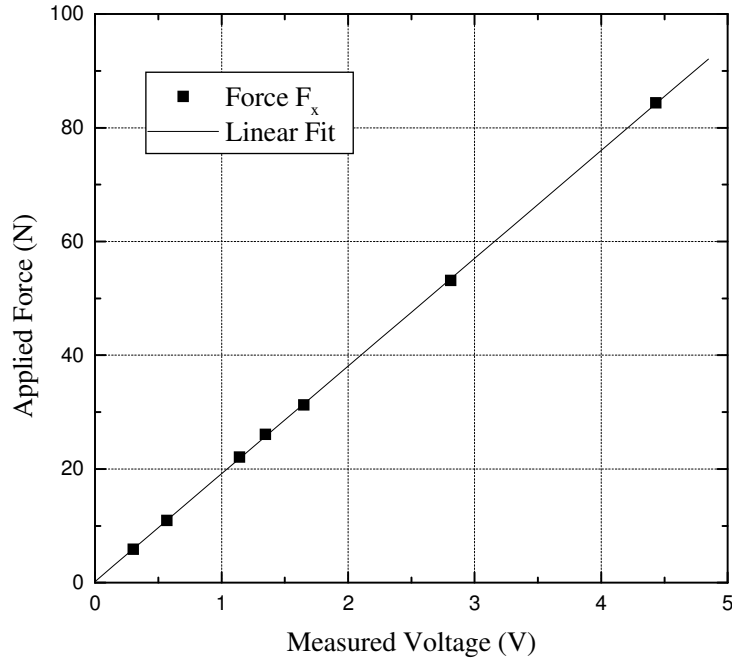


**Figure AB.1 Calibration of the dynamometer in x direction**

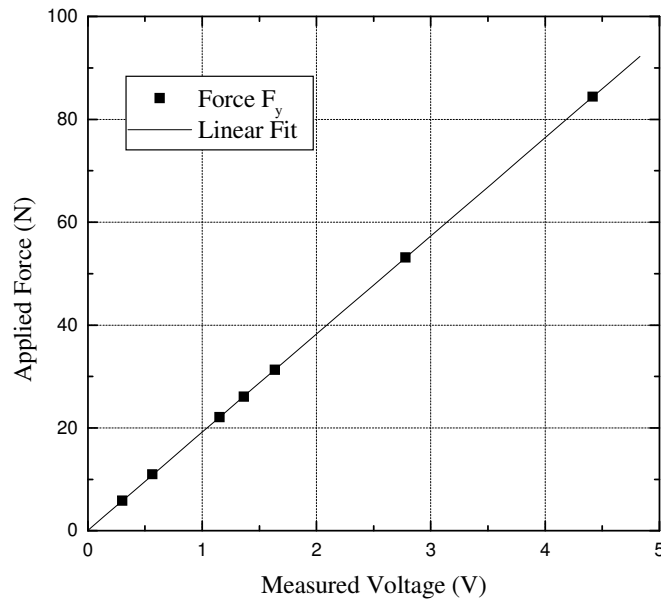


**Figure AB.2 Calibration of dynamometer in y direction**

## Appendices

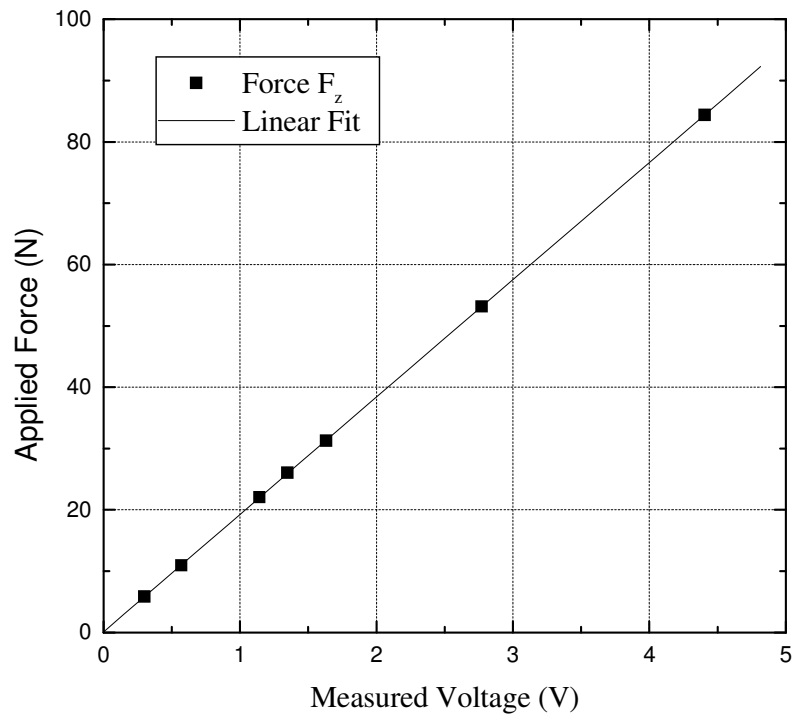


**Figure AB.3 Calibration of dynamometer in z direction**